Structure of Turbulent Boundary Layers and Surface Pressure Fluctuations on a Patch of Large Roughness Elements

Max T. Rusche

Thesis submitted to the Faculty of the
Virginia Polytechnic Institute and State University
in partial fulfillment of the requirements for the degree of

Master of Science
in
Aerospace Engineering

Roger L. Simpson, Chair
William J. Devenport
Joseph A. Schetz

July 28, 2011
Blacksburg, Virginia

Keywords: turbulence, roughness, surface pressure, velocity spectra, boundary layer

Structure of Turbulent Boundary Layers and Surface Pressure Fluctuations on a Patch of Large Roughness Elements

Max T. Rusche

(ABSTRACT)

Measurements were made in a zero pressure gradient turbulent boundary layer over two roughness patches containing hemispherical and cubical elements. The elements were 3 mm in height and spaced 16.5 mm apart in an array containing 7 streamwise rows and 6 spanwise columns for a total of 42 elements per patch. The boundary layer thickness was approximately 60 mm, so the ratio of element height to that thickness was a large amount at $k/\delta = 1/20$. A three velocity component laser Doppler velocimeter measured instantaneous velocities. Mean flow and turbulence statistics were calculated as well velocity energy spectra. Surface pressure fluctuations were measured using a two-microphone subtraction method.

The results show that hemispherical elements produce larger turbulence quantities in their wakes compared to the cubes. This is due to the hemispheres having a frontal area nearly 60% larger than that of the cubes. The turbulence levels behind the hemispheres is a maximum behind the first streamwise row of elements, and decreases afterwards. The cubical elements maintain a nearly constant amount of turbulence in their wake, signifying little interaction between cubical elements. Surface pressure fluctuations vary little in the streamwise direction of the patches. The hemispherical elements produce a larger sound pressure level behind them than the cube elements do. Velocity spectra results show large normal stress energy for regions at and below the element height. The energy for locations high in the boundary layer increases as the flow moves downstream. Coherency plots show that there is a large correlation between the turbulent structure and production of shear stress at the roughness height. Any measurements taken at or below the roughness height are highly correlated under 10 kHz, while locations higher in the boundary layer are correlated under 2 kHz.

This work was supported by the US Office of Naval Research under N00014-06-1-0671, Dr. Ki-Han Kim, Program Manager.

Acknowledgments

I would like to thank my advisor, Dr. Roger Simpson, for his guidance and support throughout my M.S. program. His experience has taught me how to be a better researcher, and I am grateful for all of his help. I would also like to thank the other members of my committee, Dr. William Devenport and Dr. Joseph Schetz, for their input on my thesis and defense.

I am grateful to my parents for their support throughout my education. Thank you to my friends and family for the encouragement to finish my graduate program.

My fellow coworkers have helped me considerably throughout the past two years. Thank you to Andrew Hopkins, Nathaniel Varano, and Joe Derlaga for their assistance getting me up to speed with the DAQ systems. Thank you to Gwibo Byun for all of the little problems that he helped me out with. Thank you to Dr. Todd Lowe for being an excellent source of information as well as a great mentor. I also thank the entire Virginia Tech AOE department staff for their help in the office and machine shop.

Finally, I would like to acknowledge the support of the Office of Naval Research and Program Manager Dr. Ki-Han Kim. This work was supported by Grant N00014-06-1-0671.

Contents

List of Abbreviations

$\bar{U}$	Mean velocity
$\bar{u}$	Mean velocity fluctuation
δ	Boundary layer thickness
δ	Uncertainty
λ	Ratio of frontal area to planform area
μ	Dynamic viscosity
ν	Kinematic viscosity
$\overline{u^2}, \overline{v^2}, \overline{w^2}$	Reynolds normal stresses
$\overline{uv}, \overline{uw}, \overline{vw}$	Reynolds shear stresses
Φ	Spectral density of surface pressure fluctuations
ϕ	Calibration angle
ρ	Density
$\vec{e}$	Measurement direction vector
A_f	Frontal area
A_p	Planform surface area
p	Pressure
p_a	Pressure contribution from acoustic waves of the tunnel
p_t	Pressure contribution from the turbulent flow
x_m	Uncertainty of the mean

CNC	Computer numerical control
DAQ	Data acquisition
DOP	Dioctyl phtlatate
E	Velocity spectral energy
f	Frequency
k	Roughness height
LDV	Laser Doppler velocimetry
N	Number of samples
PMT	Photo-multiplier tube
S	Fringe spacing
SNR	Signal to noise ratio
SPL	Sound pressure level
t	Time
TKE	Turbulent kinetic energy
U	Instantaneous velocity
u	Instantaneous velocity fluctuation
x	Reference coordinate in the streamwise direction
y	Reference coordinate in the wall-normal direction
z	Reference soordinate in the spanwise direction

List of Figures

List of Tables

Chapter 1

Introduction

1.1 Previous Research

Smooth wall turbulent boundary layers encountering a step change in roughness immediately begin to transition towards a rough wall boundary layer. The effects of this roughness change are not immediately felt by the entire boundary layer, and instead, a separate "inner layer" is formed. This inner layer grows as the flow continues downstream of the change in wall conditions. The inner layer contains turbulent flow determined by the new boundary conditions of the roughness. The "outer layer" contains flow and turbulence characteristics of the upstream boundary layer in front of the roughness step. This outer layer experiences much larger time scales than flow closer to the wall, and therefore will only respond to the step change after ten or more boundary layer thicknesses, as found by Antonia and Luxton [3] and Smits et al. [19].

The response of the boundary layer greatly depends on the size of the roughness compared to the boundary layer thickness. If the roughness is sufficiently small enough ($k/\delta < 1/50$), Jimenez [10] concludes that the roughness effects will be confined to the inner portion of the boundary layer and the outer layer will be similar to the outer layer

of a smooth wall boundary layer in non-dimensional scaling terms. This statement was studied further and confirmed by Schulz and Flack [17] for small roughnesses over a wide range of Reynolds number. However, if the roughness elements are large in comparison to the boundary layer thickness, they will have a direct effect on the semi-logarithmic mean velocity profile. The semi-logarithmic region contains most of the turbulent energy production and mean shear stresses of the boundary layer, and when roughness elements block parts of this region, the flow cannot be expect to retain normal wall turbulence characteristics. In the case of this study, the roughness elements are very large, and the blockage ratio k/δ is on the order of 1/20. Due to the large size of the elements in this study, the flow is better described as passing over "obstacles".

The "inner layer" created due to a surface roughness was first discussed by Elliott [6] and further studied by Panofsky and Townsend [15][21]. Their primary focus was the inner layer of the Earth's atmospheric boundary layer. Experiments on the growth of the inner layer were conducted by Antonia and Luxton [3][4] as well as Andreopoulos and Wood [2]. Antonia and Luxton found that when plotting the streamwise velocity component U versus the square root of the wall distance, $y^{1/2}$, the inner and outer layer data points created two straight lines with different slopes. The intersection of these two lines, or the "joint", was a good estimate of the inner layer thickness. The results of the inner layer growth for this study will be compared to those of Antonia and Luxton [4].

Previous research similar to that in this study has been done by other members of this research group. Bennington [5] studied the turbulent structure behind single elements of various shapes, including a hemisphere and cube. His research depicts the development of a horseshoe vortex in front of all roughness elements which induces downwash toward the wall behind the element. Bennington also studied the sweeping motion behind the element, the turbulent triple products, and made comparisons between elements with smooth edges and sharp edges. Stewart [20] and Varano [22] studied the effect of long fetches of sparsely spaced roughness elements. Stewart's roughness elements included Gaussian shaped elements as well as cylinders, while Varano studied sparsely spaced

hemispheres.

Rasnick [16] studied the far field noise created by the roughness patches contained in this crrent study as well as other cases in a wall jet flow. For the 6x7 patches included in this current study, he found that the cubical roughness elements produced significantly more far field noise than the hemispheres. The cubes create large disturbances to their perpendicular faces obstructing the flow. With the hemispheres, the lack of a perpendicular face and sharp edges significantly reduces the amount of noise, even if the hemispheres have a larger frontal area. Rasnick also found that the cubes each produced a similar amount of far field noise on their own. That is, he studied different numbers of cubes in different rectangular arrays, and found that as more elements were added (up until the large 6x7 array), the amount of noise produced by the patch increased proportionally. He concluded that the cubes have little interaction with each other when it comes to producing the far field noise.

Alexander et al. [1] also studied the far field noise of the 6x7 cubical and hemispherical patches. He also found that the cubical elements produced significantly more far-field noise than the hemispheres. He also studied the wall pressure fluctuations for the roughness patches, as is also done in this study. His conclusion was that the radiated far-field noise cannot be related to the surface pressure field because the noise is produced on the surface of the roughness elements. His surface pressure fluctuation results will be compared in this current study to examine the differences between his wall-jet flow and the current wind tunnel flow.

Yang and Wang [23] have done large eddy simulations of turbulent boundary layers over roughness patches containing cubical, hemispherical, and cylindrical elements that are similar to those in this study. They found that the impingement of fluid on the perpendicular upstream face of the cubical elements created large amounts of noise. The edge-induced unsteady flow separations and vortex shedding over the top edge of the cubes created significantly more noise than the hemispherical elements.

1.2 Scope of this Research

The goal of this research is to obtain laser Doppler velocimeter flow field measurements as well as surface pressure fluctuation measurements on the same roughness elements that Rasnick, Alexander, and Yang and Wang have already studied. Rasnick and Alexander produced surface pressure fluctuation and far field noise results using a wall-jet wind tunnel facility. Their roughness patches had the exact same geometry as the roughness patches included in this study. The results from this study can be compared to theirs to examine differences between the zero pressure gradient turbulent boundary layer produced by the wind tunnel used in this study, and the wall-jet boundary layer produced by their anechoic facility. The results of this study will also be compared to the work of Yang and Wang. Flow field measurements from the LDV in this wind tunnel can be compared to the large eddy simulations for a boundary layer and free-stream flow.

Chapter 2

Apparatus and Instrumentation

2.1 Laser Doppler Velocimeter

2.1.1 LDV Principles

Laser Doppler Velocimetry is a technique that unobtrusively measures the velocity of micron-sized particles in fluids. The simplest explanation of LDV is that two coherent, collimated, and single color laser beams intersect to form a fringe pattern of constructing and deconstructing light waves. Seed particles that are small enough to follow the the fluid flow pass into this fringe pattern and scatter light at a certain frequency. The frequency of these flashes and the distance between the fringes are proportional to the velocity compoenent of the particle perpindicular to the fringes.

A three component LDV system is used for this research. The formula for this system is

given as

$$\vec{u}\begin{bmatrix} \vec{e_1} \\ \vec{e_2} \\ \vec{e_2} \end{bmatrix} = \begin{bmatrix} f_1 s_1 \\ f_2 s_2 \\ f_3 s_3 \end{bmatrix} \tag{2.1}$$

where $\vec{u}$ is the velocity vector of the particle, $\vec{e_i}$ is the measurement direction vector for each laser beam pair, f_i is the frequency of the scattered light flashes, and s_i is the fringe spacing for each beam pair. Solving for the instantaneous velocity vector of the particle can be done by taking the inverse of the beam measurement direction matrix. The beam direction matrix and fringe spacing must be determined by a calibration describe in Section 2.1.4.

One problem with the simple LDV setup is that there can be a sign ambiguity with the particle velocities. A particle will create the same scattered signal if it passes through the stationary fringes forwards or backwards. To correct this, one laser beam of each beam pair is frequency shifted using a Bragg cell modulated at a given frequency. The shift results in a small change in wavelength of the laser beam, and causes the fringe pattern to move. This means a particle moving through the measurement volume will create a higher frequency when moving forward, a lower frequency when moving backward, and a frequency equal to the Bragg cell shift when stationary. During post processing, the Bragg cell frequency is subtracted from the data to obtain the felocity produced frequency signals.

2.1.2 Long System

The 'Long System' is the name of the LDV system used for this research. The Long System was designed by Dr. Semih Ölcmen[14] and used by Drs. Jacob George[7], Andrew

Hopkins[9], and Nathaniel Varano [22]. Hopkins and Varano made modifications from Ölcmen's design that allowed the probe to be used on the ceiling of the Small AOE Boundary Layer Wind tunnel. The system consists of an optical table, probe, and receiving table.

Optical Table

The optical table is used to condition the laser beams before sending them to the probe head. The system uses one 5 Watt Coherent Innova I90 C-5 argon-ion laser. The laser is fitted with an etelon and therefore only emits green (514.5 nm) beams. Out of the laser head, the beam is split into two seperate beams, each of which go through separate Bragg cells operated at different frequencies. One beam is split using a 60 MHz Bragg cell. The other beam is split first using a 40 MHz Bragg cell. The unshifted beam coming out of the 40 MHz bragg cell is then split again using an 80 MHz Bragg cell. The use of these Bragg cells creates 5 separate beams which are sent to the probe head. The Bragg cell power supplies are adjusted so that the beams of each pair have equal power. The five beams are focused into a 4 μm diameter polarization preserving fiber optic cable (Alcoa-Fujikura SM8-P-4/125-ST/NY-9000). A Newport Single-Mode Fiber Coupler is used to hold the fibers at a certain angle. It is necessary for the beams to enter the fiber at the proper angle to ensure the polarization preserving attributes of the fiber work properly.

Probe Head

The probe head consists of two transmitting heads and a receiving lens. The heads contain five 6 mm focal length plano-convex lenses for each beam and two 88.3 mm focal length plano-convex lenses for each head. Each head has its own set of linear stages to allow for fine adjustment during laser alignment. The receiving lens assembly contains two Thor Labs achromat lenses, one with focal length 200 mm and the other 250 mm. Further information about modifications to the receiving assembly can be found in Varano[22].

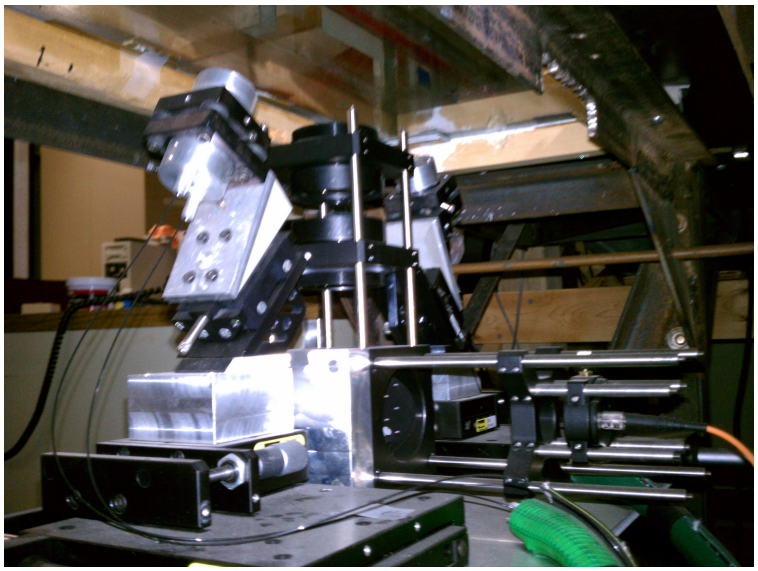

Figure 2.1: LDV probe head

The 60 MHz shifted beam and an unshifted beam enters one of the heads to create one beam pair. The 40 MHz shifted, 80 MHz shifted, and other unshifted beam enter the second head to create two more beam pairs. The measurement volume size for this setup was estimated by Hopkins and Varano to be 80 μm in the streamwise and spanwise directions and 405μm in the wall normal direction.

A receiving fiber of 62.5μm diameter carries the measured light signals from the probe head to the receiving table.

Receiving Table

The light signal from the receiving fiber first passes through an interference narrow bandpass filter to eliminate any contamination from other wavelengths of light. The light the passes into a photomultiplier tube (PMT), which creates a current from the light signals. The PMT is powered by a Brandenburg model 477 power supply. A Sonoma Instrument model 315 amplifier takes the current from the PMT and amplifies it into a voltage signal. This signal is lowpass filtered at 100 MHz and highpass filtered at 5 MHz. This eliminates

any noise from outside of the measurement spectrum. The PMT tube and power supply are subject to various sources of electronic noise which can have a large effect on data given the weak currents produced by the PMT tube. Aluminum foil is used as shielding to mitigate any noise entering the system.

Data Acquisition

After amplification and filtering, the voltage signal is recorded by a Strategic Test board (model UF.258). This DAQ card is located in a standard PC operating Windows XP. The Strategic Test board samples at 250 megasamples/second. The data are recorded using Labview software. Labview only records bursts that pass a certain voltage threshold called the trigger level. The use of triggered data reduces the amount of storage space necessary per point of data, and quickens the data reduction process. A second DAQ card is required to record the timestamp of each triggered burst. A National Instruments 5112 board is connected to the 'trigger out' port of the Strategic test board. The Labview code incorporates this second DAQ card to record the timestamp of each burst.

For the velocity spectra measurements, a very high data rate must be attained. The triggered data method above does not provide this, so data is measured continuously in 0.54 second windows. The DAQ card can sample at 250 MS/s for 0.54 seconds before its internal memory is full. It then dumps all of the data onto a hard drive. This process takes about 8 seconds from recording the data to storing it to a hard drive before the next batch of data is collected. A total of 30 seconds of data was recorded for each velocity spectra data point.

Data Processing

The continuous and triggered data are processed in the same way. A fast Fourier transform is run on each burst's time signal to determine the frequency content of that signal.

The Bragg frequency for each beam pair is subtracted out before storing the data. Also stored with the data is the signal to noise ratio (SNR_1). To reduce the amount of noise in the signal, the bursts are clipped so that only good bursts above a certain SNR_1 ratio and within a certain frequency band are kept. This is depicted in Figure 2.2. A user-defined noise floor is selected first, and then a frequency window is created based on any noise spikes. Bursts are only kept above the noise floor and inside the window, removing any bursts due to noise in the data.

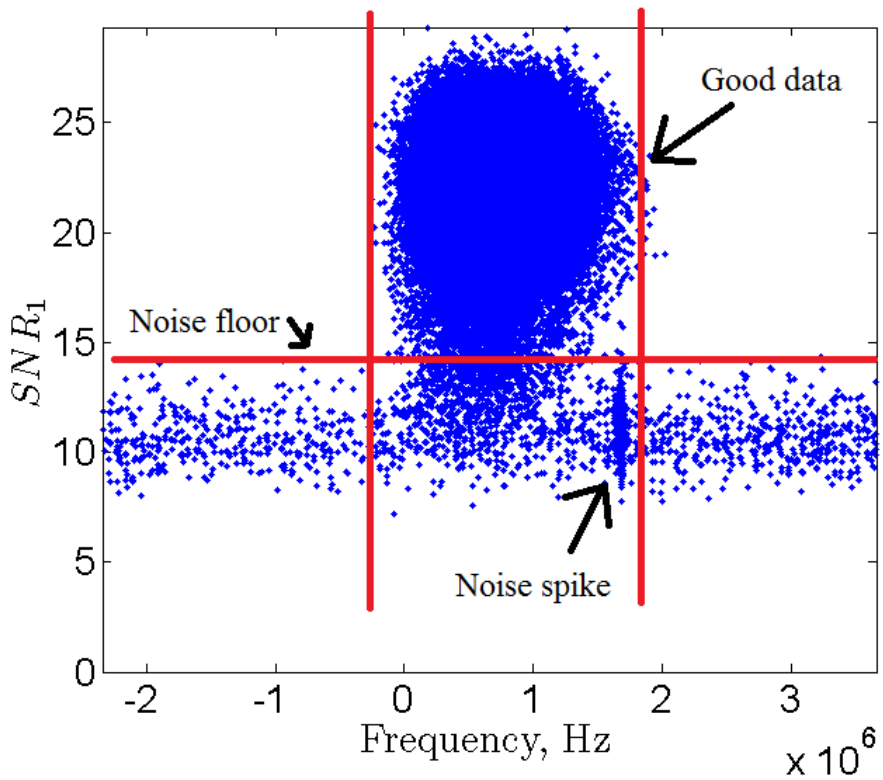

Figure 2.2: LDV bursts plotted on SNR_1 versus frequency. Bursts located above the noise floor and inside the frequency window are kept for further processing.

After frequency clipping, the burst frequencies are multiplied by the fringe spacing and the inverse of the beam direction matrix to give the three instantaneous components of the velocity vector. These data are processed again by clipping the outer edge of a velocity histogram. The data points that are outliers on the velocity histogram are removed from the set. This is shown in Figure 2.3. The user defines a window where only bursts with a

velocity inside that window are kept.

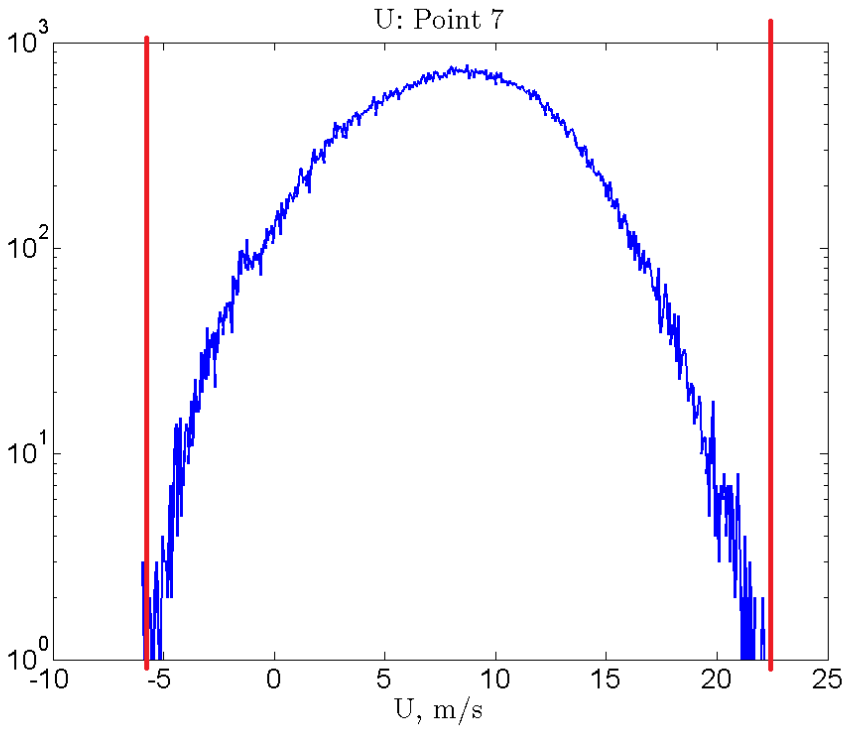

Figure 2.3: Histogram of LDV burst samples vs. velocity. A user-defined window clips any bursts outside the window to remove outliers from the histogram.

2.1.3 Measurement of Beam Directions

The laser beam directions are measured by taking two photographs of a piece of plain white plain affixed to the tunnel floor. The beams shine onto the paper and show up as dots in the photographs. The LDV probe head is then traversed in the vertical direction and the laser dots move on the paper. The change in position of the dots is measured from the two photographs. The paper has a streamwise and spanwise scale on it so that proper distances can be measured using a MATLAB script. Knowledge of the change in vertical distance Δy, as well as the measured change in the streamwise Δx and spanwise Δz, allows for the creation of the beam direction matrix.

2.1.4 Calibration

A novel calibration devised by Hopkins and Varano was used to measure the fringe spacing of the LDV system. The method utilizes the rotation stage that the probe head sits on. The probe head is rotated to a precisely known angle and a measurement of the flow is taken. The probe is rotated to a second angle and another measurement is taken. The calibration flow velocity of the tunnel is measured using a Pitot-static probe. Equation (2.1) can be rearranged such that:

$$(\cos\phi\frac{e_x}{S} + \sin\phi\frac{e_z}{S}) = \frac{\bar{f}}{U_p} \tag{2.2}$$

$$\begin{bmatrix} \cos\phi_1 & \sin\phi_1 \\ \cos\phi_2 & \sin\phi_2 \end{bmatrix} \begin{bmatrix} e_x/S \\ e_z/S \end{bmatrix} = \begin{bmatrix} \bar{f}_1/U_p \\ \bar{f}_2/U_p \end{bmatrix} \tag{2.3}$$

Where ϕ_1 and ϕ_2 are the rotation angles of the rotary stage, e_x and e_z are the components of the measurement direction vector, $\bar{f}_1$ and $\bar{f}_2$ are the measured frequencies at each rotation angle, and U_p is the calibration velocity measured from the Pitot probe.

This system of equations is solved for the two values, e_x/S and e_z/S. The identity $e_x^2 + e_y^2 + e_z^2 = 1$ is used to solve for the fringe spacing.

$$S = \left[\frac{1 - e_y^2}{(e_x/S)^2 + (e_z/S)^2}\right]^{1/2} \tag{2.4}$$

This method of calibration only utilizes the measurement direction component in the wall normal direction. This greatly reduces the uncertainty of the fringe spacing calibration. Further analysis of the uncertainy improvement over the previous calibration method can be found in Varano[22].

2.1.5 LDV Uncertainty

The two main sources of uncertainty for a laser Doppler velocimeter system are the uncertainties in the frequency measurement and the fringe spacing measurement. The basic equation that defines the flow velocity for a LDV system is:

$$\vec{U} \cdot \hat{e}_i = f_i S_i \tag{2.5}$$

where $i = 1, 2, 3$ for the different measurement directions. The uncertainty of the flow velocity is therefore:

$$\delta U = \sqrt{(S\delta f)^2 + (f\delta S)^2} \tag{2.6}$$

The uncertainty in the frequency, δf, is limited by the noise levels experienced in a certain system. For this particular LDV, Shinpaugh et al.[18] estimate the 95% uncertainty as $\delta f = 0.1/D$, where D is the burst duration. The burst duration is is the measurement volume size divided by the flow velocity component. The measurement volume for the Long System is 80 microns, and a typical flow is 28 m/s. This results in a 95% frequency uncertainty of $\delta f = \pm 35kHz$. Long System fringe spacings are approximately 11 microns, so the contribution to the flow velocity uncertainty from the frequency uncertainty, $S\delta f$, is approximately 0.385 m/s. This uncertainty is difficult to improve upon without upgrading the electronics of a certain system.

Equation (2.4) shows the formula to measure the fringe spacing. The uncertainty in the fringe spacing measurement relies on data measured from the calibration procedure: the two mean frequencies, two rotation angles, calibration velocity, and the measurement

Beam Pair	Uncertainty $\delta S(\mu m)$
40 MHz	0.0342
60 MHz	0.0327
80 MHz	0.0276

Table 2.1: Fringe Spacing Uncertainties

direction vector uncertainty in the y direction.

$$\delta S = \left[\left(\frac{\partial S}{\partial \phi_1} \delta \phi \right)^2 + \left(\frac{\partial S}{\partial \phi_2} \delta \phi \right)^2 + \left(\frac{\partial S}{\partial \bar{f}_1} \delta \bar{f} \right)^2 + \left(\frac{\partial S}{\partial \bar{f}_2} \delta \bar{f} \right)^2 + \left(\frac{\partial S}{\partial U_p} \delta U_p \right)^2 + \left(\frac{\partial S}{\partial e_y} \delta e_y \right)^2 \right]^{1/2} \tag{2.7}$$

The uncertainty in the calibration angles is $\delta\phi = 0.005°$. The uncertainty in the mean frequency measurement is $\delta\bar{f} = 111Hz$ and the uncertainty in the calibration velocity is $\delta U_p = 0.061m/s$. Plugging in typical values for the Long system produces the fringe spacing uncertainties shown in Table 2.1.

The calculations for the uncertainty in the fringe spacing are done using MATLAB's Symbolic Toolbox. The software is capable of quickly calculating the partial derivatives associated with these uncertaintly measurements. Then the numerical values are input into the symbolic equations to return the uncertainty values.

The contribution of the fringe spacing uncertainty to the flow velocity is approximately $f\delta S = 0.0265m/s$. This value is considerably lower than the contribution from the frequency uncertainty. The frequency uncertainty will dominate the uncertainty of the instantaneous measured velocity. However, many samples are taken for these LDV measurements, and therefore an uncertainty in the mean should be calculated. This uncertainty in the mean is calculated as $\delta x_m = 1.96\delta x/\sqrt{N}$. For a typical LDV measurement, approximately 50,000 independent samples were taken. This large amount of samples drastically reduces the uncertainty in the mean velocity measurements.

Quantity	Uncertainty
δU	± 0.342 m/s
δV	± 0.598 m/s
δW	± 0.439 m/s
$\delta \bar{U}$	± 0.091 m/s
$\delta \bar{V}$	± 0.161 m/s
$\delta \bar{W}$	± 0.013 m/s
$\delta u'$	± 0.354 m/s
$\delta v'$	± 0.619 m/s
$\delta w'$	± 0.439 m/s
$\delta \bar{u'}$	± 0.0016 m/s
$\delta \bar{v'}$	± 0.0028 m/s
$\delta \bar{w'}$	± 0.0020 m/s

Table 2.2: Velocity Uncertainty Quantities

In Table 2.2, the uncertainty values for various velocity quantities are provided.

Comparisons between measurements of the Long System on a flat plate are presented in AppendixB.

2.1.6 Seeding

DOP

The LDV system is seeded using atomized dioctyl phthalate (DOP). Pressurized air is forced through Laskin nozzles which are located in a sealed pressurized container full of liquid DOP. The Laskin nozzles produce small pockets of air and vaporized seed. Different amounts of seeding levels can be attained by using different air pressures. The vaporized seed exits the pressure container and enters another container called an im-

Figure 2.4: The DOP seeder system. The pressure pot containing Laskin nozzles and liquid DOP is located on the right. Particles travel from the pressure pot into the impactor can located on the left. Particles leave the impactor can and are introduced into the plenum of the wind tunnel.

pactor can. The impactor can forces the seed to quickly change direction as it flows into the container. This quick change causes larger DOP particles to impact on the container side and fall to the bottom of the container due to their momemtum. The use of an impactor can reduces the amount of large particles flowing into the wind tunnel. The seed particles are then introduced into the plenum chamber of the Small Boundary Layer Wind Tunnel. This DOP seeder system is depicted in Figure 2.4.

Olive Oil

For velocity spectra results, a very high data rate is required. The DOP seeding system did not produce enough seed particles, so an olive oil seeder was used instead. A LaVision Aerosol Generator (item number 1108926) was used for this purpose. At its maximum ouput, the generator can produce up to 200 billion olive oil particles per second in the 1-1.5 micron size range.

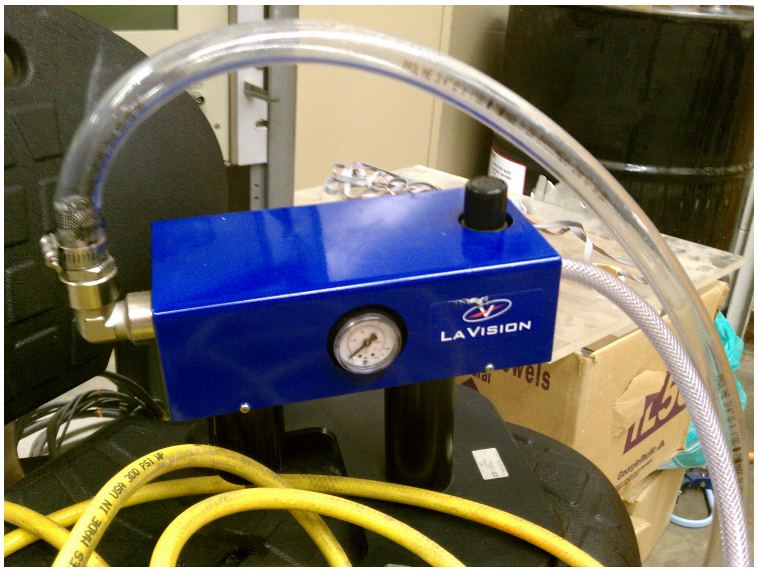

Figure 2.5: A LaVision olive oil seeder system.

2.1.7 Traverse

The Long System probe head is approximately 25 pounds and must be positioned accurately down to the scale of microns. To do this, thre Velmex BiSlide Positioning Slides are used to traverse the system in three directions. Each slide can hold 300 pound loads with a resolution of 0.005$\pm$0.0025 mm. The slides are driven by three Slo-Syn stepper motors (type M092-FD-447). The motors are controlled by a Velmex VP9000 controller which is connected to the PC and integrated into the Labview software. An additional encoder was added to the wall-normal slide to ensure further accuracy with this component. An Acu-Rite ENC 150 encoder with an accuracy of 3 μm was connected to a Quick-Chek digital readout to accurately determine changes in the vertical direction. Further information about the support structure for the probe head can be found in Varano[22].

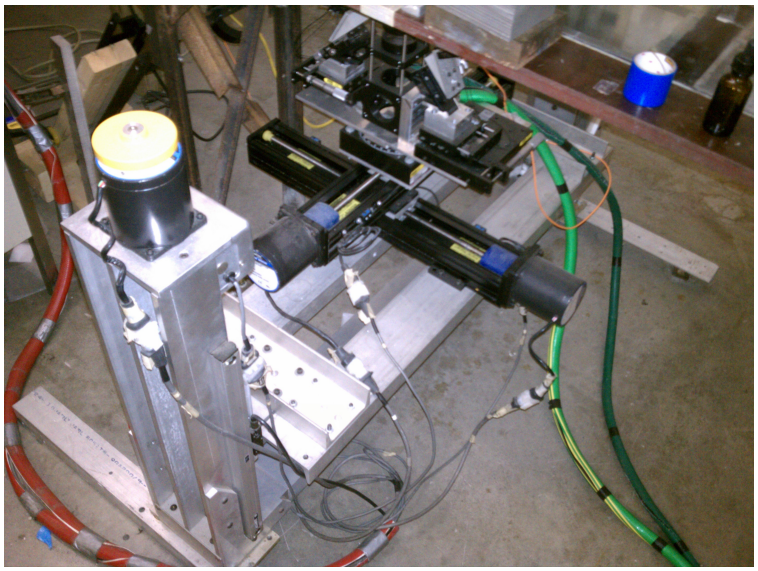

Figure 2.6: Three Velmex BiSlide positioning slides create the traverse system for the LDV. The stepper motors have high accuracy for precision LDV measurements.

2.2 Small AOE Boundary Layer Wind Tunnel

Measurements were made in the Small AOE Boundary Layer Wind Tunnel located in the basement of Randolph Hall at Virginia Tech. Extensive details about the tunnel can be found in Bennington [5]. The test section is 200 cm long with a cross-section of that is 10 cm high and 24 cm wide. The test section roof and side walls are made of plexiglass. The roof is removable and adjustable allowing for control of the pressure gradient along the test section length. The roof is sealed using tape during testing to eliminate any leaks. The tunnel speed is controlled by a butterfly valve located before the blower and plenum chamber. Experiments for this research were done around a free-stream velocity of 26.5 m/s. The tunnel ceiling and floor have port holes for Pitot probe access. The Pitot probe uses a liquid manometer to measure the dynamic pressure of the flow. The floor of the tunnel is cut where the measurements were made to place a 71 cm long piece of float glass. This glass allows access for the LDV system. It must be cleaned regularly due to seeding particles settling on the floor of the tunnel. The hatch that contains the roughness elements is removed to clean this surface.

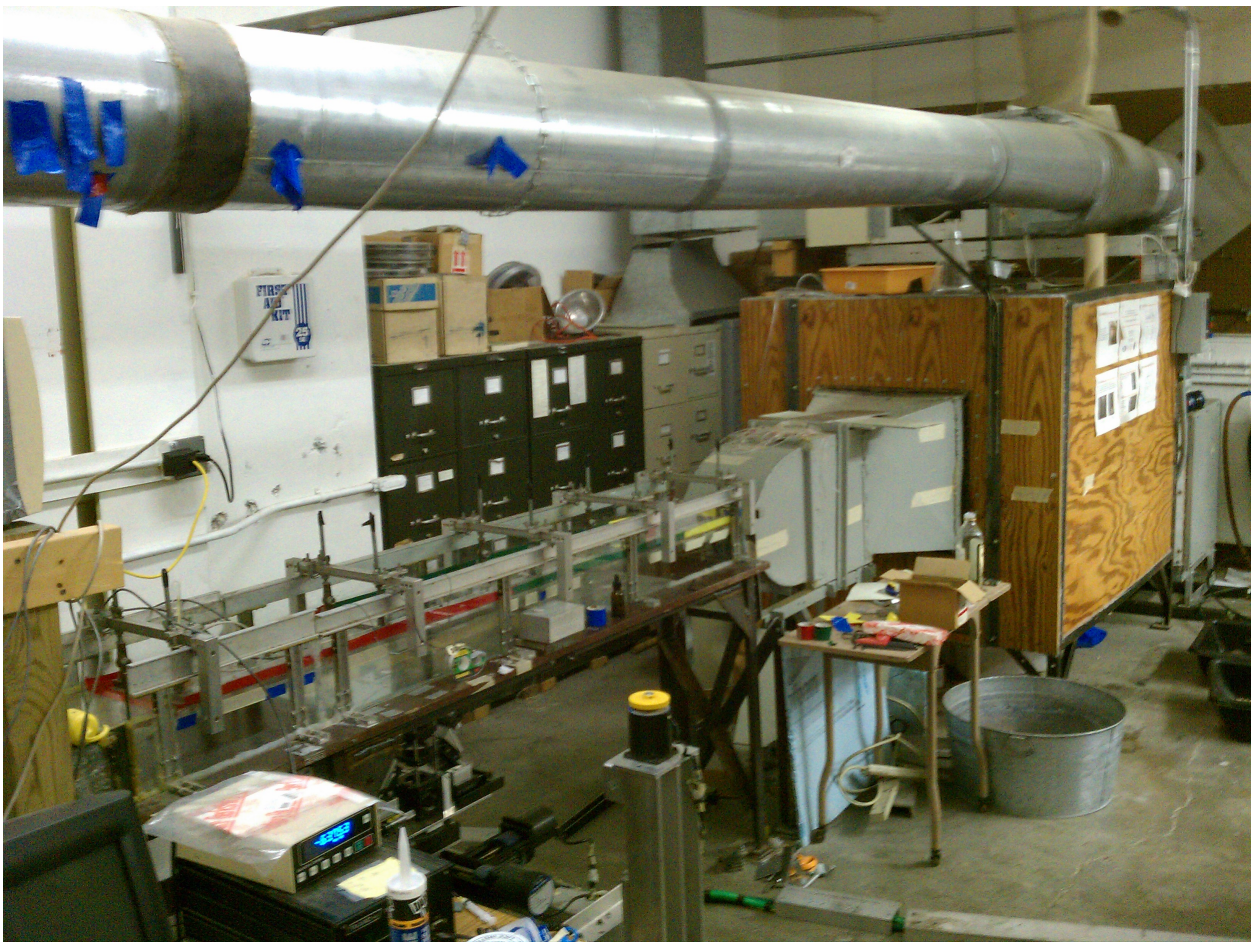

Figure 2.7: The Small AOE Boundary Layer Wind Tunnel. The plenum chamber is the large wooden box to the right of the photograph. The test section is the plexiglas channel, and the close-loop air return is located above the test section in the large metal duct.

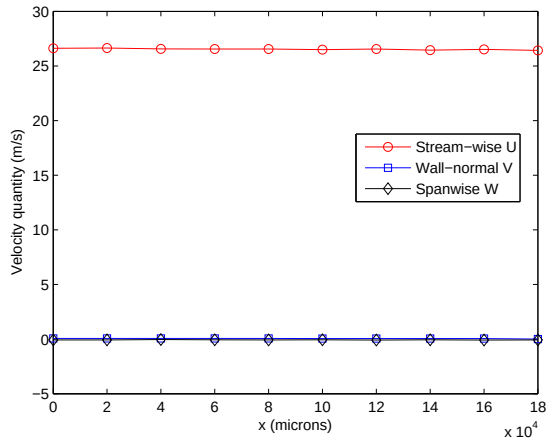

Figure 2.8: Velocity profiles taken in the stream-wise direction of the wind tunnel to ensure a zero pressure gradient flow

The boundary layer is tripped at the beginning of the test section using two 0.125 inch square rods spanning the width of the test section. These two rods are placed 2 inches apart, and a piece of Norton 20-grit sandpaper is placed between them. This trip produced a 43 mm thick boundary layer about 1 meter downstream. Bennington[5] states that there is a 12 cm wide region in the center of the wind tunnel where the boundary layers from the side walls have no effect. All measurements were made within this region.

LDV measurements are made in the streamwise direction to ensure that the tunnel creates a zero-pressure gradient. First, a Pitot probe is used to roughly create a zero-pressure gradient, and then the LDV measurements are made and analyzed. The tunnel ceiling is adjusted to create a zero-pressure gradient flow. One of these LDV measurements is show in Figure2.8.

2.3 Microphones

Surface pressure fluctuation measurements were made for both of the roughness patches using equipment and measurement techniques proven by Goody[8], Hopkins[9], and

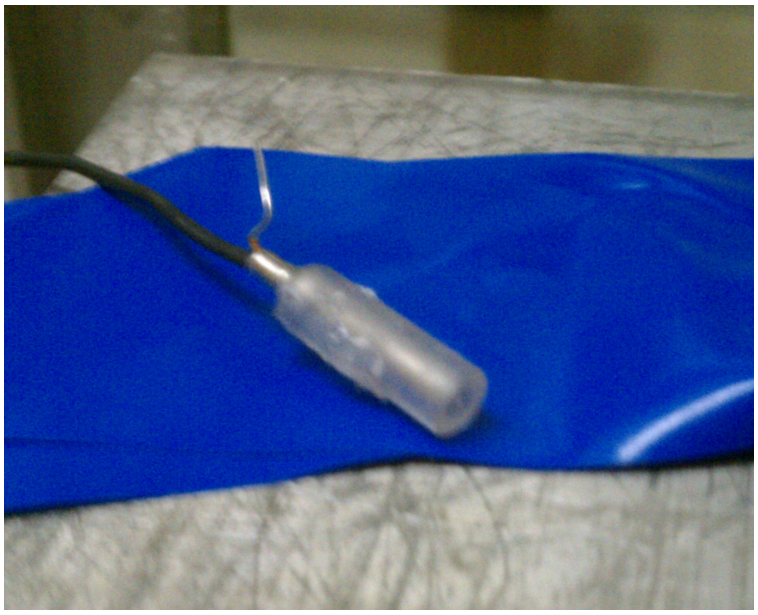

Figure 2.9: An Endevco miniature piezoresistive pressure transducer inside a 0.5 mm pinhole mask

Varano[22]. Two Endevco 8507C-2 Miniature Piezoresistive Pressure Transducers were used. The transducers have a flat frequency response from 0 to 70 kHz with a sensitivity of 130 mV/psi and full scale output (FSO) of 300 mV. The transducers have a four-arm strain gage bridge that requires a nominal 10 V excitation voltage.

The transducers were excited and their signals were amplified by two Measurements Group model 2310 strain gage conditioning amplifiers. A gain of 165 was used to amplify the signals. The amplifiers fed into a National Instruments PCI-6013 16-bit data acquisition board. The board sampled at a rate of 65536 Hz for a length 8 seconds recording 524288 total samples. The data were recorded and stored on a PC using LABView software. A MATLAB code used FFT on the time signals to calculate the power spectrum of the signals.

The pressure transducers were inserted into a pin hole mask with a diameter of 0.5 mm. This pin hole limited spatial averaging over the face of the transducer. Spatial averaging occurs with this size pin hole at frequences greater than 40 kHz. Resonent frequency

peaks occured at frequencies greater than 20 kHz. For the scope of this research, pressure fluctuations above 20 kHz are negligible; therefore, the resonent frequencies and spatial average had no effect on the measurements. Calibrations for these pressure transducers can be found in Goody[8].

The pin hole masks have an outer diameter that fits snugly into the roughness patches as described in the next section. The masks were mounted flush the the surface of the roughness patch. The holes in the patches where the masks were not located were covered with cellophane tape. The tapes thickness of 0.03 mm did not have a significant effect on the boundary layer due to being much thinner than the viscous sublayer.

To isolate the surface pressure fluctuations due to the turbulent boundary layer, a subtraction method described by McGrath and Simpson[13] is used. The procedure assumes that the wind tunnel acoustic and vibrational signals are correlated in the spanwise direction, and since the two microphones are placed at the same streamwise location and at an adequate spanwise distance from one another where the turbulent contributions are uncorrelated, the unwanted signals will cancel out when subtracting one signal from the other. This will leave only the wall generated turbulent component of the surface pressure spectrum. The signals from the microphones for a given frequency and same bandwidth are given as:

$$p_1\left(t\right) = p_{1a} + p_{1t} \tag{2.8}$$

$$p_2\left(t\right) = p_{2a} + p_{2t} \tag{2.9}$$

where p is the pressure signal, t denotes turbulent boundary layer contribution, and a represents the acoustic and vibrational part. The mean square of these signals when sub-

tracted is:

$$\overline{(p_1 - p_2)^2} = \overline{[(p_{1a} + p_{1t}) - (p_{2a} + p_{2t})]^2} \tag{2.10}$$

Since the two microphones are placed at the same streamwise location and the spanwise acoustic signal is correlated, such that $p_{1a} = p_{2a}$, the acoustic contributions from both signals subtract out. This leaves only the turbulent signals, and carrying out the mean square gives:

$$\overline{(p_1 - p_2)^2} = \overline{(p_{1t}^2 + p_{2t}^2 - 2p_{1t}p_{2t})} \tag{2.11}$$

Because the microphones are an adequare distance spanwise from one another, the turbulent signals are uncorrelated, or $2p_{1t}p_{2t} = 0$. Also, due to symmetry of the flow, the turbulent signals should be equivalent at each microphone, $\overline{p_{1t}^2} = \overline{p_{2t}^2}$. This leaves:

$$\overline{(p_1 - p_2)^2} = 2\overline{p_{1t}^2} \tag{2.12}$$

This subtraction method works for measurement locations which are an adequate distance apart to ensure the turbulent signals are not correlated, such as those on the outside of the roughness patch. However, measurements were also made along the center of the patch, where this isn't necessarily the case. To isolate the turbulent surface pressure fluctuations for these locations, a different yet similar method is used. One microphone is kept at an outer location where the turbulent fluctuations have already been determined from a previous measurement. The other microphone is moved to a location in the center of the patch, and its signal is:

$$p_3(t) = p_{3a} + p_{3t} \tag{2.13}$$

Taking the mean square of this signal gives:

$$\overline{p_3^2} = \overline{(p_{3t} + p_{3a})^2} = \overline{p_{3t}^2} + 2\overline{p_{3t}p_{3a}} + \overline{p_{3a}^2} \tag{2.14}$$

Solving for $\overline{p_{3t}^2}$ to isolate the turbulent contribution, and noting that $2\overline{p_{3t}p_{3a}} = 0$ because the acoustic and turbulent signals are not correlated, gives:

$$\overline{p_{3t}^2} = \overline{p_3^2} - \overline{p_{3a}^2} \tag{2.15}$$

To measure the value of $\overline{p_{3a}^2}$, one must assumed that $p_{1a} = p_{2a} = p_{3a}$. To find the acoustic signal at locations 1 and 2, the signals are added and squared:

$$\overline{(p_1 + p_2)^2} = \overline{(p_{1a} + p_{2a})^2} + 2\overline{(p_{1a} + p_{2a})(p_{1t} + p_{2t})} + \overline{(p_{1t} + p_{2t})^2} \tag{2.16}$$

The first signals in the first term are equivalent and reduce to four times the square of the acoustic signal. The middle term is equal to zero since the acoustic and turbulent signals are not correlated. The turbulent signals at 1 and 2 are not correlated so their mean product is zero, leaving:

$$\overline{(p_{1a} + p_{2a})^2} = 4\overline{p_{1a}^2} \tag{2.17}$$

$$2\overline{(p_{1a} + p_{2a})(p_{1t} - p_{2t})} = 0 \tag{2.18}$$

$$\overline{(p_{1t} + p_{2t})^2} = \overline{p_{1t}^2} + \overline{p_{2t}^2} \tag{2.19}$$

$$\overline{p_{1a}^2} = \left[\overline{(p_1 + p_2)^2} - 2\overline{p_{1t}^2}\right]/4 \tag{2.20}$$

The acoustic signals are assumed to be equivalent at each station, and Equation 2.13 can be entered into Equation 2.8 to solve for the turbulent signal at the 3rd location.

All calculations are done using MATLAB softare. The MATLAB programs first read the raw data from the Labview output. The signals have their amplification removed and are multiplied by a calibration coefficient to get the proper pressure signals from the voltage readings. Next, the mean of the signals are subtracted out so that each signal has a mean of zero. Then the various subtraction methods above are utilized before running the discrete time series data through a version of a Fast Fourier Transform. The pwelch script in MATLAB takes a discrete time series and returns the power spectral density for the frequency domain using Welch's averaged modified periodogram method.

The data from the pwelch is bin averaged to smooth out the apperance of the data and to better define peaks. Fifty bins are used on a log scale to smooth the data.

2.4 Roughness Patches

Type	$k(mm)$	$s(mm)$	$A_f(mm^2)$	$A_p(mm^2)$	λ^{-1}
Hemisphere	3.0	16.5	14.13	272.25	19.26
Cube	3.0	16.5	9	272.25	30.25

Table 2.3: Roughness types

2.4.1 Hemispheres

The hemispherical roughness patch consists of 3 mm height hemispheres placed in a 6x7 (spanwise x streamwise) array. The hemispheres are placed 16.5 mm in apart in both directions. The hemispheres were created by placed 6 mm diameter chrome spheres into a rectangular piece of aluminum. The aluminum had precise holes drilled into it by the

Figure 2.10: Hemispherical roughness plate

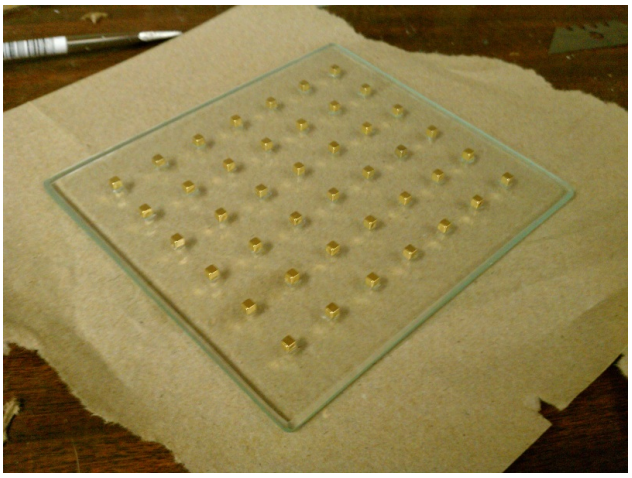

Figure 2.11: Cubical roughness plate

AOE Machine Shop. The holes were drilled using a CNC machine to the create an accurate and consistent 6x7 array. For each hole, two concentric holes were drilled. The larger hole on the top was the size of the sphere, while at the bottom of the patch a smaller hole was drilled to ensure that the sphere did not fall through the patch.

Before placing the spheres into the piece of aluminum, the metal was first polished to a mirror finish. This was done by sanding the metal using 200 grit up to 1500 grit sandpaper. The aluminum was then polished with Mother's Mag and Aluminum Polish on a microfiber towel with a random-orbit sander to create a mirror finish. The spheres were placed into the holes and affixed using 24 hour epoxy. When the spheres rested in the holes, they created the 3 mm high hemispherical elements.

The mirror finish was used to determine the wall position for the LDV measurements. The hemispherical roughness plate is shown in Figure 2.10.

2.4.2 Cubes

The cubical roughness patch consists of 3 mm height cubes in the same 6x7 array and spacing as the hemisperical patch. Two different approaches were used to create the cu-

bical roughness fetches. First, a block of aluminum was CNC machined to create the roughness pattern. The machine surfaces were polished first using sandpaper. To get a mirror finish, a Dremel rotary tool with polishing bits was using with Mother's Mag and Aluminum Polish. However, this method of polishing was unable to create an acceptable level of mirror finish. Instead, an entirely different method was used to create the cubical roughness. 3x3x3 mm^2 magnetic cubes were purchased from the internet retailer Gaussboys Super Magnets. These cubes were positioned in the 6x7 array by using a template produced by the 3D printer. This template allowed for an exact placement of the cubes to ensure proper spacing and alignment. The cubes were glued to the glass plate using Gorilla Glue 5 minute epoxy. The cubical roughness plate is shown in Figure 2.11.

2.4.3 SPF Roughnesses

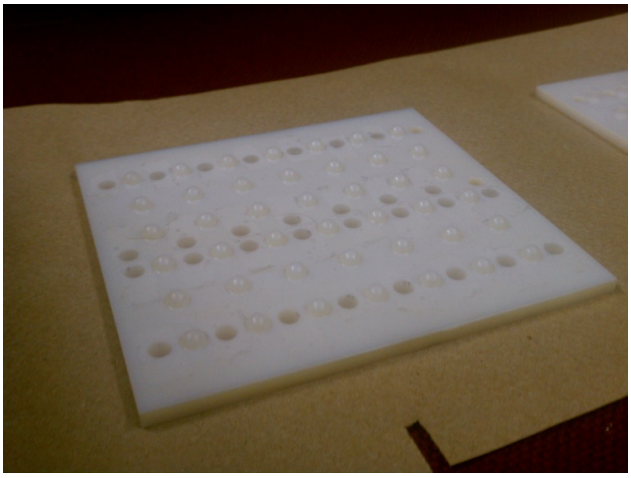

Figure 2.12: Roughness plate produced by the 3D printer for SPF measurements on the hemispherical elements

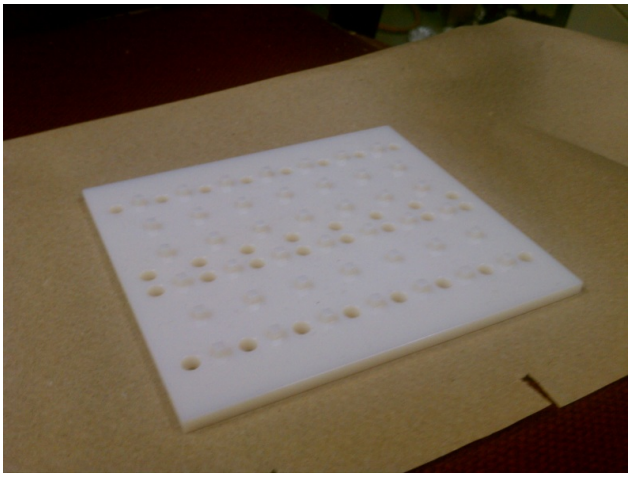

Figure 2.13: Roughness plate produced by the 3D printer for SPF measurements on the cubical elements

The roughness patches for both the hemispherical and cubical patches for the surface pressure fluctuation measurements were made entirely using the 3D printer. These patches are shown in Figures 2.12 and 2.13. Three-dimensional models of the patches were created in Autodesk Inventor and sent to the 3D printer for construction. The models had

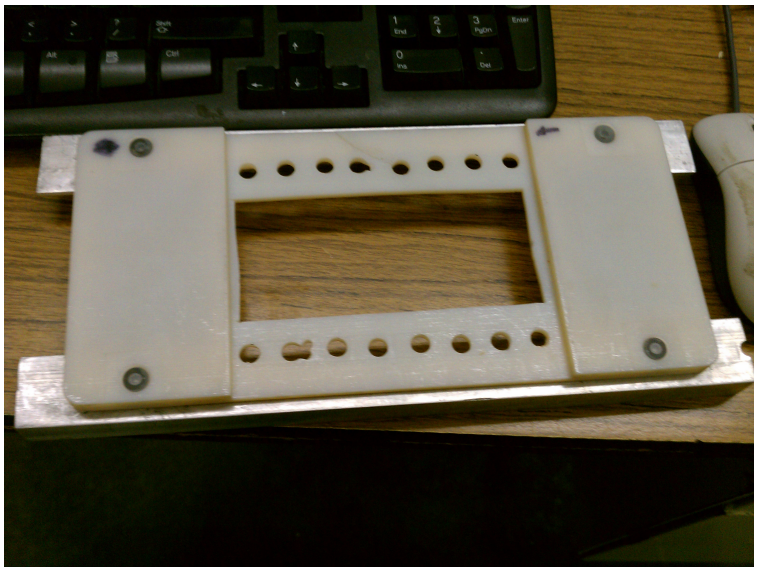

Figure 2.14: Roughness holder created by the 3D printer. This holder was used for all measurement patches, and fit snugly into the ceiling of the boundary layer wind tunnel.

holes located in the patches that fit the microphone houses snugly. When holes were not in use for a measurement, they were covered with scotch tape to prevent flow from passing through them. The 3D printer is able to produce the smoothness of the hemisphere as well as the sharpness of the cube corners with high precision.

2.5 Roughness Holder

The roughnesses were placed on the ceiling of the wind tunnel for measurement. The plexiglass ceiling of the wind tunnel has a removeable access hatch where the roughnesses were located. A special holder was created for the roughness cases that is the same shape as the usual plexiglass hatch. This special holder was made of plastic using a 3D printer. The holder had a recessed void where the different roughness patches could be taped. The holder and patches were designed so that they were flush with the wind tunnel ceiling. The roughness holder could be removed after measurements to clean the glass floor of the wind tunnel.

Chapter 3

Laser Doppler Velocimetry Results

3.1 Full Boundary Layer Profiles

3.1.1 Measurement Locations

Full boundary layer profile measurements were taken on both roughness patches in 16 distinct locations. A profile was taken behind each row of elements in two locations, in-between elements (or the centerline of the patch), and directly behind an element (or the centerline of the element).

For the hemispherical case, approximately 23 data points were measured in the wall-normal direction, starting around 850 microns and increasing until the edge of the boundary layer around 60000 microns. Four points were also measured "through" the mirrored surface and used to locate the wall. These data points are not plotted in this results section. Refer to Varano[22] and Hopkins[9] for an example of this method.

For the cubical case, approximately 30 data points were measured in the wall-normal direction. More data points were taken in these cases due to measurements being able to be taken closer to the wall due to the glass plate used to create the cubical roughness. For

the measurements between elements, data points start around 100 microns, and behind the elements at about 300 microns.

3.1.2 Mean Velocities

The profiles for the mean streamwise velocity U are presented in Figure 3.1. The profiles located between the roughness elements, and not directly behind the elements, display the gradual reduction of streamwise velocity that the roughness patch causes. The zero row profile, located before any roughness begins, mimics a smooth wall turbulent boundary layer. In both the hemispherical and cubical cases, the first row profile is extremely similar to the zero row profile. This profile is taken after the first row of elements, but because it is located in-between two columns of elements, the roughness has not had enough distance to affect the stream-wise velocity.

After the second row of elements, the flow between the roughness has begun to slow down. The profile behind the second row merges back to the free-stream values about 6 mm above the wall, or 2k. The third and fourth rows of data continue to show the decrease in streamwise velocity between the elements. As the flow moves downstream, the velocity profiles merge with the freestream at a higher and higher location from the wall. By the fifth row, it appears that the flow is approaching an equilibrium. The fifth, sixth, and seventh row profiles all show a similar structure in magnitude. These three rows appear to merge with the stream-wise velocity around 10-11 mm, or slightly over 3k. The flow structure and progression is between the elements is very similar for both the hemispheres and cubes. Both roughness types show the gradual deceleration of the boundary layer and the profiles appear to merge with the freestream about 3.5k above the wall in both cases.

The stream-wise velocity flow is drastically affected for the measurements taken directly behind the roughness elements. Behind the first row of elements, there is a large veloc-

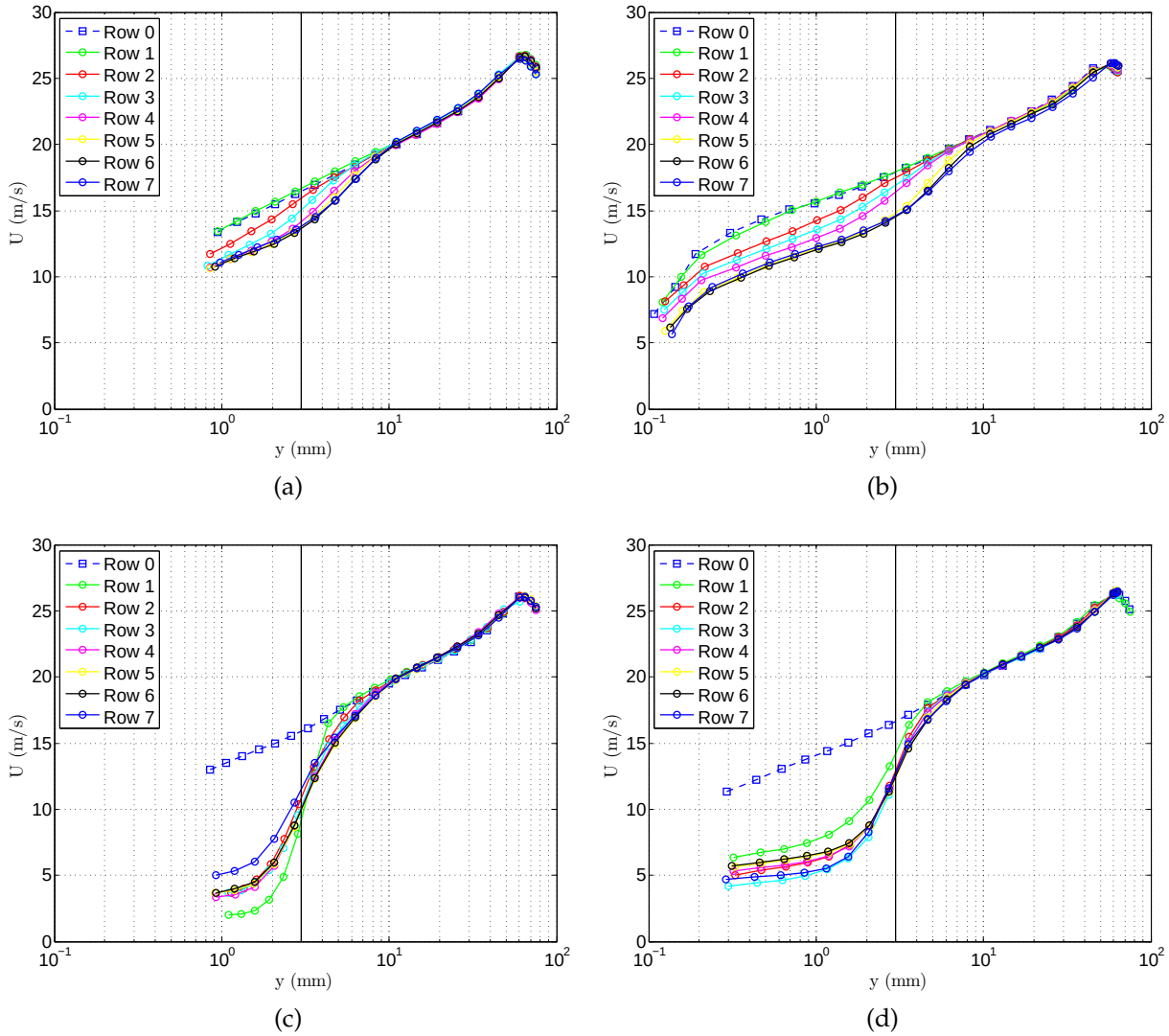

Figure 3.1: Mean streamwise U velocity profiles: (a) between hemispheres; (b) between cubes; (c) behind hemispheres; and, (d) behind cubes

ity defect below the height the height of the elements. In the case of the hemispheres, the flow behind the first row is the slowest out of all measurements taken on that patch. Interestingly, the flow behind the first row of cubes is faster than the other rows in the cubical roughness patch. One explanation for this is the large physical size of the hemispherical roughness elements. The backflow region for the hemisphere is larger than that of the cube. Also, the relative turbulence intensities, as will be seen in coming sections, are larger for the hemishperes. The backflow region behind the first row is the largest of any row for the hemispherical case, and this could cause the large velocity defect. In the case of the cubical roughness patch, the opposite is possibly true. The backflow region is not as large, and neither are the turbulence intensities. The reason the first row streamwise velocity is larger than the other rows is because the overall streamwise flow begins to slow down after passing over the elements.

Below the element height, the profiles for rows 2-6 of the hemispherical roughness all collapse to around 3.5 m/s at 900 microns. As explained above, the first row behind the hemispheres is slower than the other rows. Interestingly, the seventh row is noticeably faster than the other rows. This is likely due to the flow rushing over the seventh row of hemispheres towards the wall without having to adjust for an eight row. That is, since there is not another row of roughness behind the seventh, the higher speed flow stays near the wall and the entire boundary layer begins to slowly transforms back to a smooth wall flow.

The cubical roughness profiles behave similarly to hemispheres behind the roughness elements. The main difference is the row at the beginning of the patch, as described above. The flow behind the cubes does not decelerate as much as behind the hemispheres.

All profile measurements behind the elements appear to have merged with the upstream outer layer around the 10 mm mark. The profile behind the first row of elements merges lower, around 5-6 mm, for both roughness cases.

Inner Layer Growth

Figures 3.2 and 3.3 show plots depicting the growth of the inner layer through the roughness patches. The streamwise velocity U is normalized by the freestream value and plotted versus $y^{1/2}$. When plotted in this manner, the two layers appear as distinct lines of different slope. The joint where these lines meet is a good estimate of the inner layer thickness. The inner layer contains fluid that is affected by the wake of the first roughness element and the generated turbulence from the entire rough surface, while the outer layer contains traits from the upstream boundary layer.

Antonia and Luxton[4] plotted this half-power trend and found that the inner layer growth is similar to the growth of a two-dimensional bluff body wake. This growth rate is $\delta_i \sim x^{0.50}$.

The stream-wise boundary layers are plotted in Figures 3.2 and 3.3. These plots show the knee joint locations for each row of the roughness patches. Note that the profile behind the first row of cubes shows an unintuitive joint location, as it is located higher than joints downstream. This is an experimental error that Antonia also experienced. His first measurement downstream of the first roughness element deviate from the $\delta_i \sim x^{0.50}$, and he concluded this is due to the large separation bubble downstream of the first row of elements. This error is less apparent for profiles behind the hemispheres in this study, but is more noticeable when plotting inner layer thickness versus streamwise location.

The location of the joints in Figures 3.2 and 3.3 was recorded and plotted in Microsoft Excel. A power trendline was fit through the data. The joint location behind the first row of elements is plotted as a red square, and these data points were not included in the trendline calculation due to the error discussed above. These data are presented in Figures 3.4 and 3.5.

The inner layer for the hemispherical patchs grows as $\delta_i \sim x^{0.522}$ and the cubical element grows as $\delta_i \sim x^{0.520}$. These numbers agree closely to those that Antonia measured.

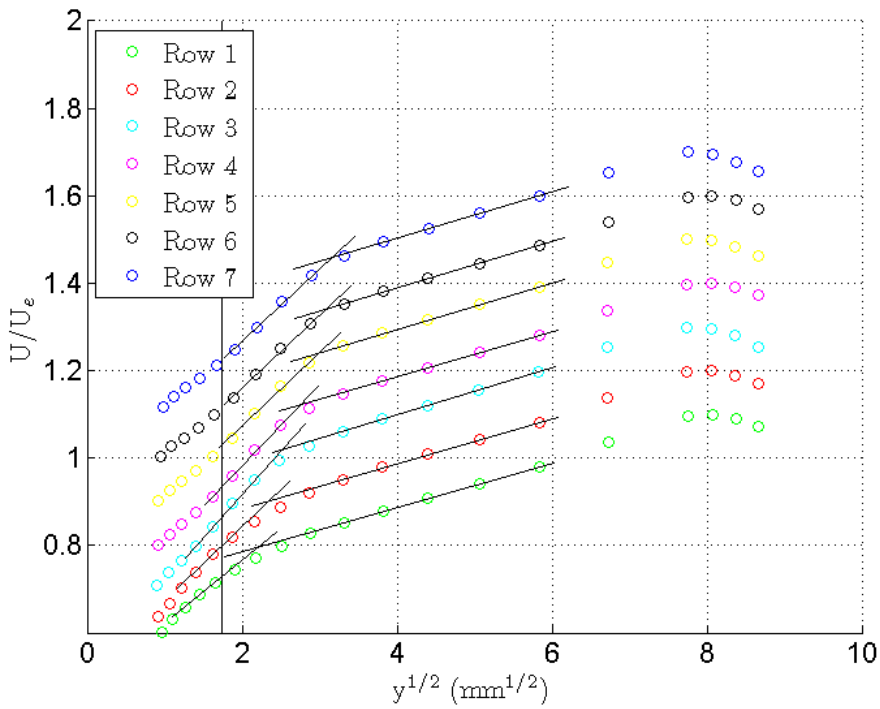

Figure 3.2: Streamwise velocity U profiles for the hemispherical roughness normalized on the freestream velocity and plotted vs. $y^{1/2}$ to show the inner and outer layer thicknesses.

Antonia's measurements were made on cubical roughness elements 3.175 mm in height, although at a much slower speed (6 m/s) than the current study. The results of his study and the current study show that the inner boundary layer formed due to a step change in roughness will grow at the same rate that of a two-dimensional wake originating from a bluff body.

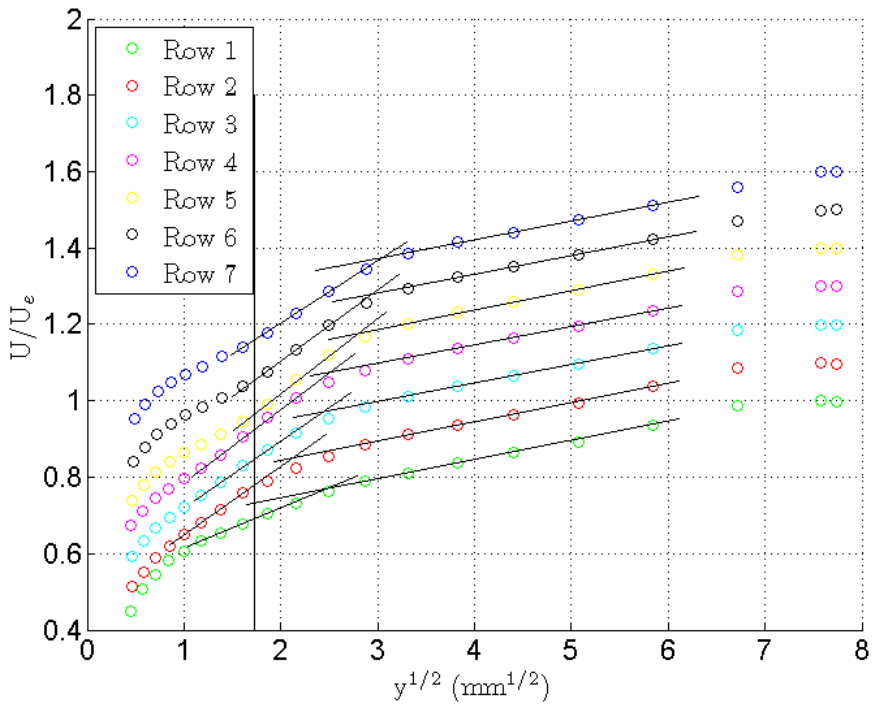

Figure 3.3: Streamwise velocity U profiles for the cubical roughness normalized on the freestream velocity and plotted vs. $y^{1/2}$ to show the inner and outer layer thicknesses.

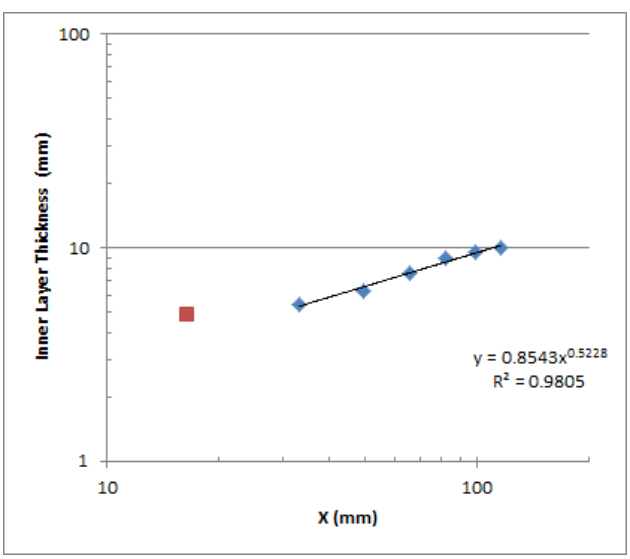

Figure 3.4: Inner layer growth behind hemispherical patch

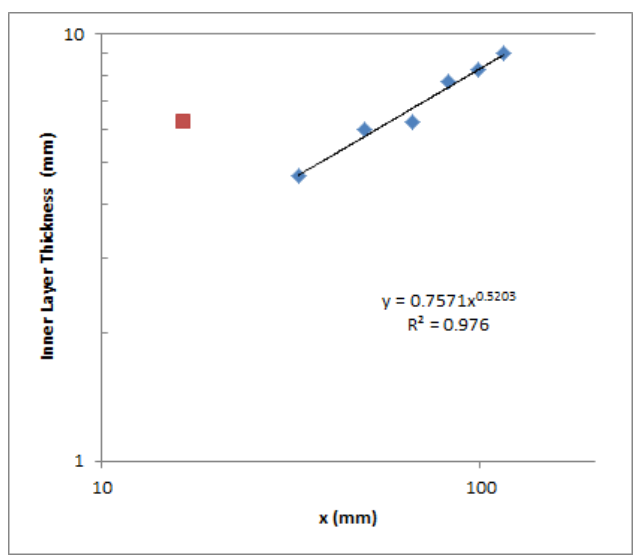

Figure 3.5: Inner layer growth behind cubical patch

The profiles for the mean wall-normal velocity are presented in Figure 3.6. The wall-normal flow in-between the roughness elements shows two distinct peak maxima for both cases. Below the roughness heights, around 2 mm, the wall-normal velocity gradually increases as flow passes through the fetches until reaching a maximum after the 4th row of elements. The magnitude of the wall-normal velocity then slowly decreases until the end of the fetch. This trend is apparent in both the hemispherical and cubical cases. The flow below and in-between the elements reacts slowly to the presence of the roughness. This gradual effect was also seen in the mean streamwise velocity plots as well. By the time the flow has reached the 5th row of elements, the mean boundary layer flow has mostly adapted to the presence of the roughness and the wall-normal velocity magnitude decreases. The boundary layer above the height of the elements acts differently for the profiles in-between the roughness. The largest magnitudes of upward wall-normal velocity occur at the very beginning of the fetch, before the roughness even begins, and decreases as the flow travels across the roughness patch. This peak of wall-normal velocity occurs between 20-40 mm above the wall. The flow in this region predicts presence of the wall downstream and begins adjusting even before the roughness begins. This causes the large wall-normal upward velocity for the measurement location in front of the first row of roughness. The opposite of this effect is shown for the measurements behind the 7th and last row of roughness elements. Because the roughness patch has ended, the flow begins to travel back toward the wall. This is shown in the areas of negative wall-normal flow behind the 7th row of elements for both roughness cases.

The wall-normal velocity flow behaves drastically different for the measurement locations directly behind the roughness elements. These plots show that the flow acts similarly behind each row of elements for both cases. There is a large downward velocity just below the roughness element height due to the flow rushing over the elements and down toward the wall. This downward wall-normal velocity is largest for the locations behind the first and last row of elements. The first row of roughness elements encounters the fastest streamwise flow; therefore, it makes sense that the largest downward flow behind

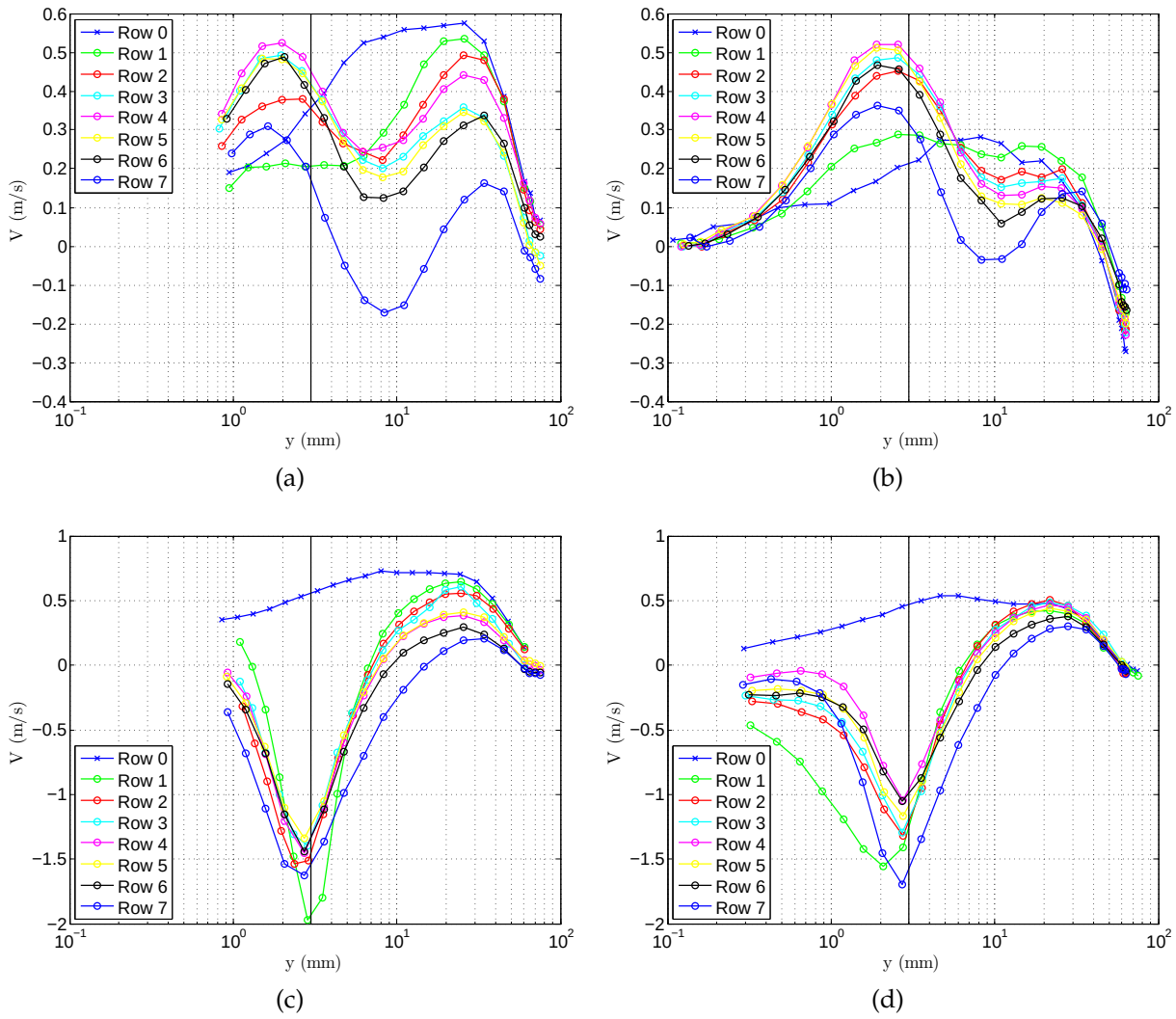

Figure 3.6: Mean wall-normal V velocity profiles: (a) between hemispheres; (b) between cubes; (c) behind hemispheres; and, (d) behind cubes

the elements would occur behind the first row. The large downward flow behind the 7th row of elements can be explained using the same logic discussed above. That is, the boundary layer is reacting to the end of the roughness patch by flowing back toward the wall and adjusting to the smooth wall conditions.

The magnitudes of the downward wall-normal velocity between the two different roughness cases are similar. The hemispherical patch has slightly higher magnitudes compared to the cubes. Above the height of the roughness elements, the flows for both cases behave similarly.

The profiles for the mean spanwise velocity are presented in Figure 3.7. In the locations that measurements were taken for these velocity profiles, the spanwise velocity profiles would ideally be equal to zero through the boundary layer. The difficulty of aligning the laser Doppler velocimeter measurement volume directly in the center between two elements or the centerline of a single element causes an uncertainty in the measurements. The uncertainty of locating the LDV directly behind an element is approximately $\pm 200\mu m$. This uncertainty is not a large factor for measurements in-between elements, as seen in the top two charts of 3.7. The spanwise flow for these profiles is nearly zero. The uncertainty does have an effect when attempting to line the LDV up directly behind a roughness element. This is shown in the bottom two graphs, where there is some spanwise flow shown beneath the height of the roughness element. The hemispheres have less scatter and or overall closer to zero, as the hemispheres have a width of 6mm and an uncertainty of 0.2 mm is not considerable. However for the cube measurements, the elements are only 3 mm wide and the 0.2 mm location uncertainty causes more scattering of the spanwise velocity measurements.

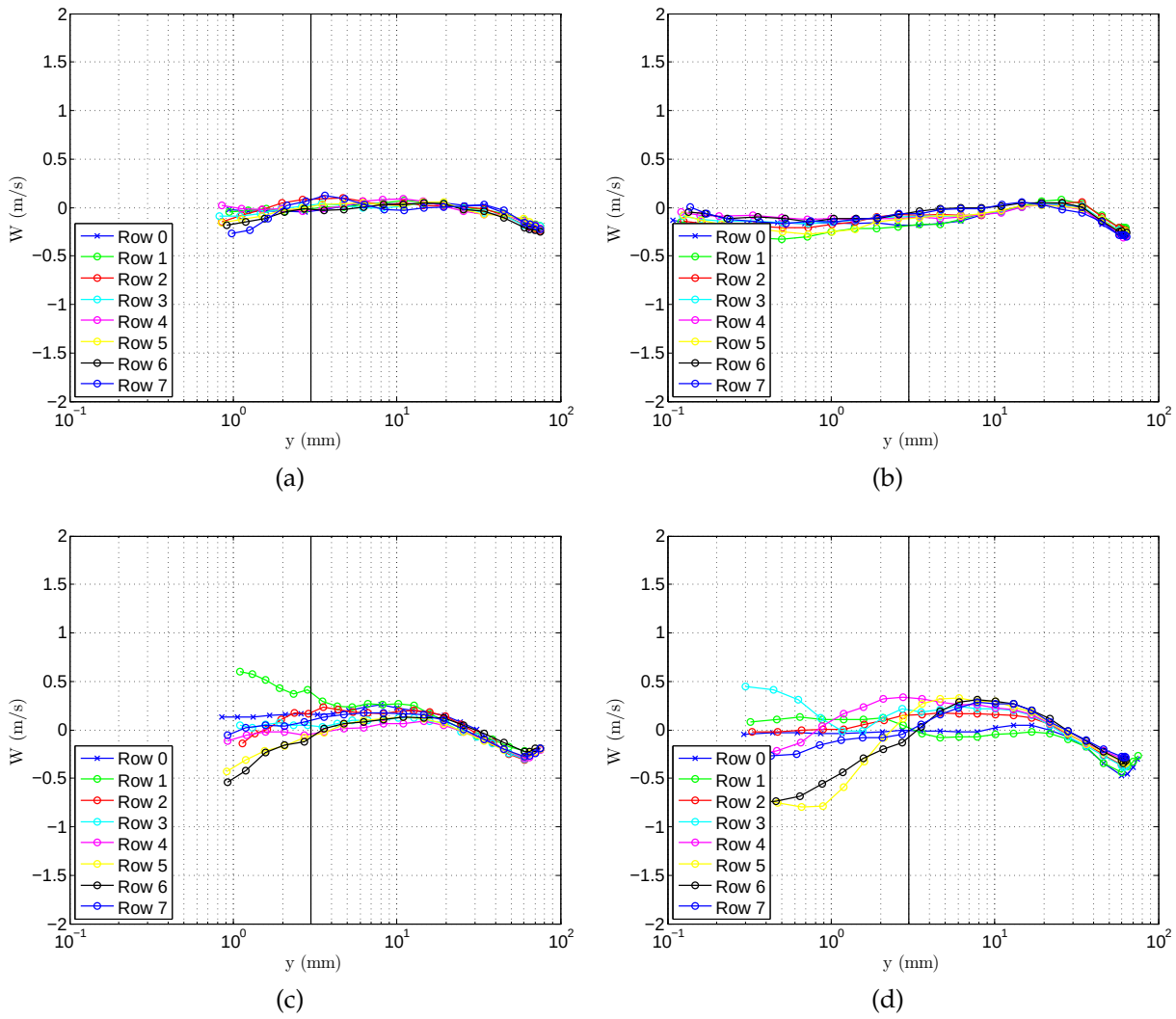

Figure 3.7: Mean spanwise W velocity profiles: (a) between hemispheres; (b) between cubes; (c) behind hemispheres; and, (d) behind cubes

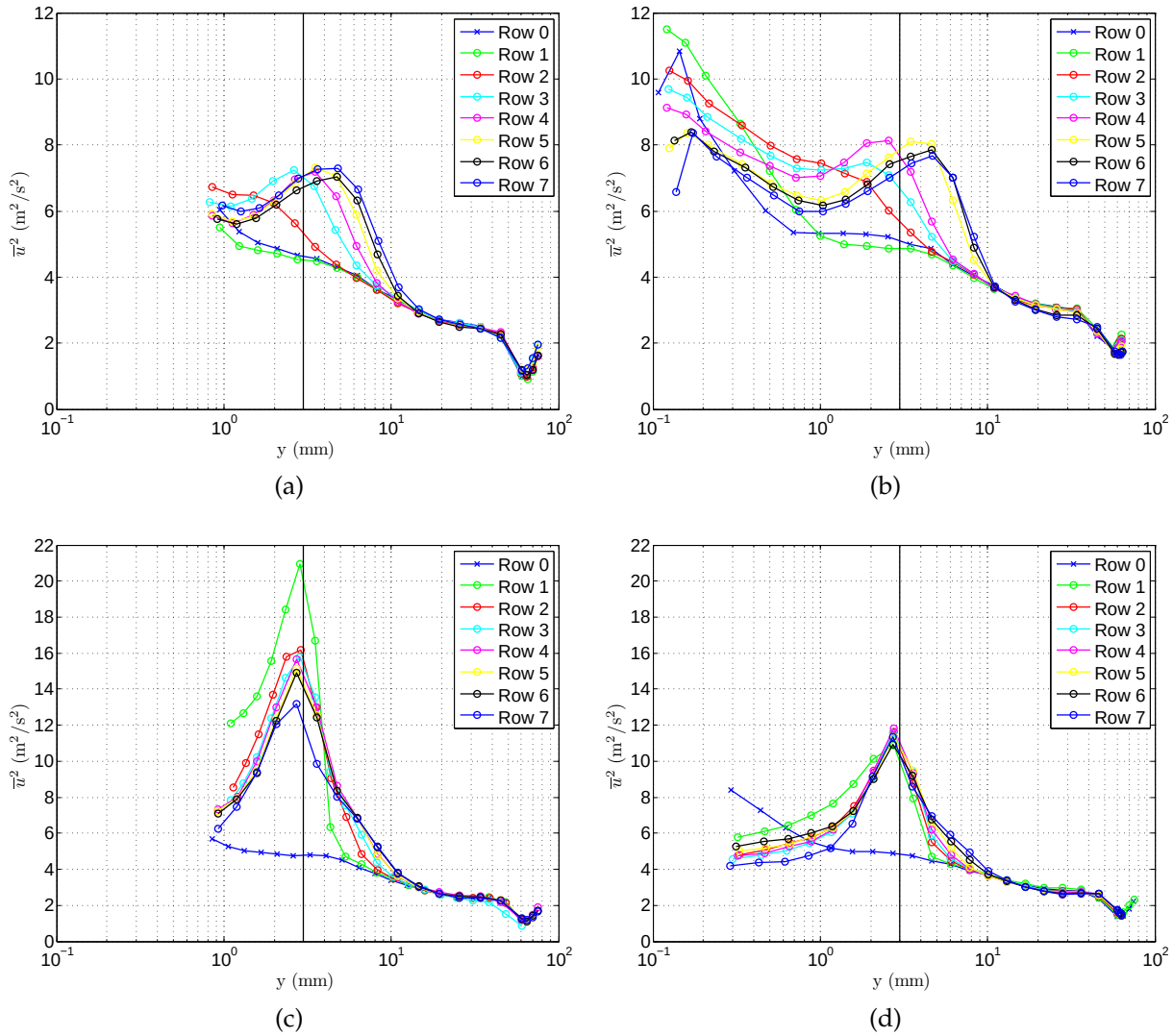

Figure 3.8: $\overline{u^2}$ normal stress profiles: (a) between hemispheres; (b) between cubes; (c) behind hemispheres; and, (d) behind cubes

3.1.3 Reynolds Stresses

The profiles for the mean streamwise normal stress are presented in Figure 3.8. For the flow in-between the elements, the $\overline{u^2}$ stress gradually increases near the roughness height at the flow moves downstream on the roughness patch. Eventually, a peak of $\overline{u^2}$ stress is formed slightly above the roughness height, around 4-5 mm. This peak is experienced by both roughness types, with the cube patch actually causes a slightly larger peak $\overline{u^2}$ magnitude for measurements in-between the elements. Due to the use of the glass plate, points closer to the wall were taken for the cube roughness. In this chart on the top right of Figure 3.8, the characteristic peak of $\overline{u^2}$ near the wall in a smooth wall boundary layer is present.

Directly behind the elements, a large peak of $\overline{u^2}$ is present right at the roughness element height. The $\overline{u^2}$ stresses behind the hemispheres reach a large maximum behind the first row and decrease as the flow moves streamwise along the roughness patch. The $\overline{u^2}$ behind the first hemisphere is about 21 m^2/s^2 while behind the 7th row it has dropped to 13 m^2/s^2. This reduction of the $\overline{u^2}$ stress as the flow moves streamwise over the hemispheres is in stark contast to that of the cubical case. The $\overline{u^2}$ stress behind the cubes is about 11-12 m^2/s^2 for all rows. It appears that each cube is capable of producing the same amount of $\overline{u^2}$ turbulence regardless of its location.

For the flow directly behind the elements, the near wall region of peak $\overline{u^2}$ turbulence is destroyed by the presence of the roughness. This is typical for rough wall cases.

The profiles for the mean wall-normal stress are presented in Figure 3.9. The $\overline{v^2}$ stress acts in a similar manner to that of the $\overline{u^2}$ stress in-between the elements. The stress gradually increases as the flow moves streamwise along the roughness patch. The measurement location after the first row of roughness elements is very similar to the location in front of the entire roughness patch for both roughness types. After the second row of elements, the flow starts adjusting to the turbulence produced by the elements and the $\overline{v^2}$ stress

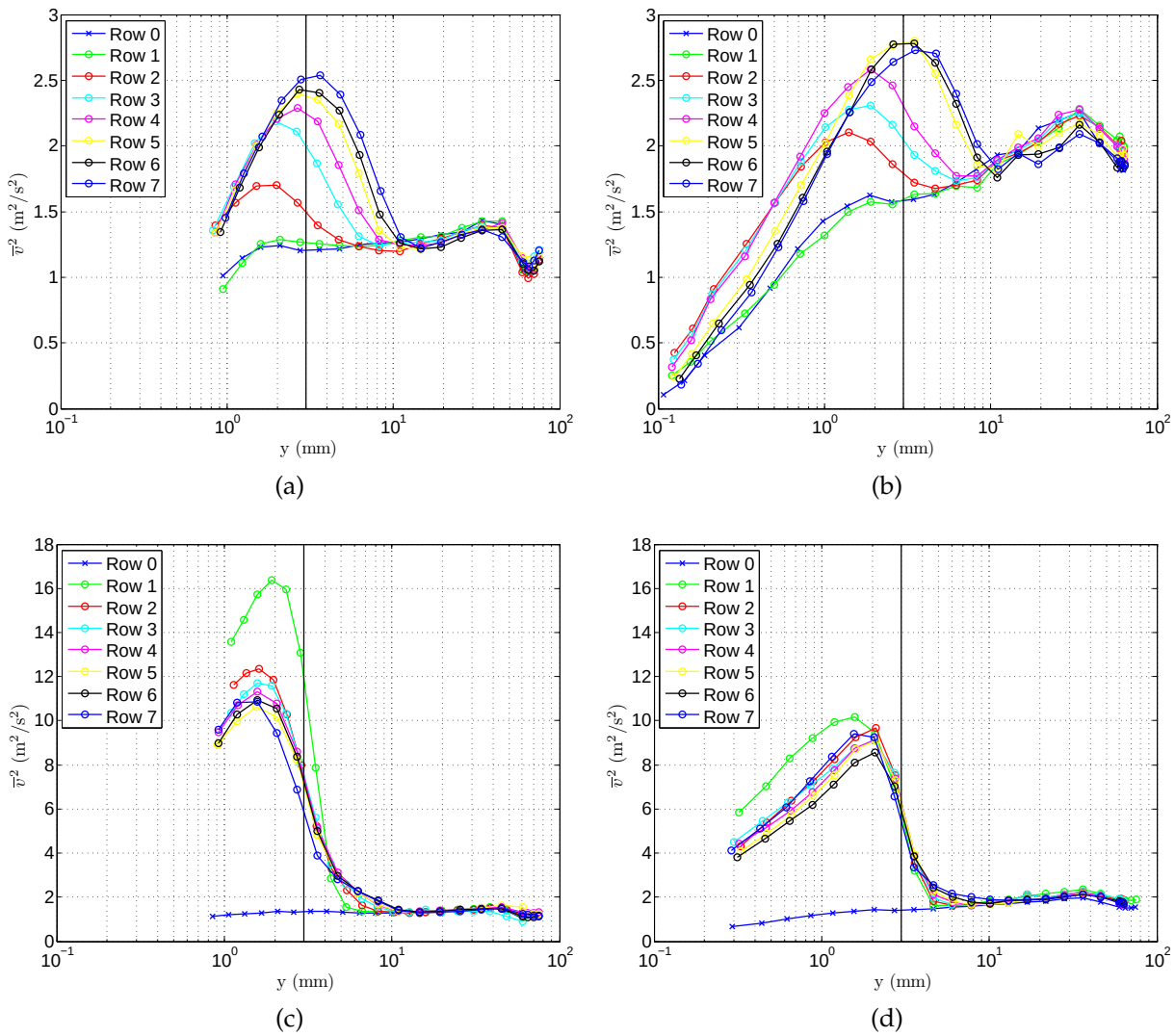

Figure 3.9: $\overline{v^2}$ normal stress profiles: (a) between hemispheres; (b) between cubes; (c) behind hemispheres; and, (d) behind cubes

starts increasing. The stress increases until reaching a maximum at the end of the roughness patch. One interesting thing to note about the peak $\overline{v^2}$ in-between the elements is that y location of the peak starts below the element height and slowly moves upward to slightly above the element height. This $\overline{v^2}$ peak behind the second row of elements occurs around 1.4 mm above the wall for both roughness cases. The location of the peak moves upward until it is around 3.5 mm above wall at the end of the roughness patch. Similarly to the $\overline{u^2}$ stress, the cubes have a slightly higher $\overline{v^2}$ stress magnitude in-between the roughness elements.

For measurement locations directly behind the roughness elements, the flow is characterized by a large $\overline{v^2}$ peak around 2 mm above the wall. The location behind the first row of roughness elements for both cases shows the largest magnitudes of $\overline{v^2}$ stress. The $\overline{v^2}$ behind the first hemisphere is significantly larger than any other stress level measured, reaching about 16.5 m^2/s^2. The stresses decrease significantly after the first row and then gradually from the 2nd to final row of elements. The cubical roughness patch shows a similar pattern; however, the $\overline{v^2}$ stress behind the first row is not significantly larger than the rest of the normal stresses. Overall, the $\overline{v^2}$ stresses behind the hemispherical elements vary between 10.5 and 16.5 m^2/s^2 while the cubical elements produce stresses between 8.5 and 10 m^2/s^2.

The profiles for the mean spanwise normal stress are presented in Figure 3.10. The flow between the roughness elements is characterized by a peak $\overline{w^2}$ stress value that occurs well below the height of the roughness elements.. The peak is close enough to the wall that it is only defined on the cube element plot on the top right of Figure 3.10. The $\overline{w^2}$ stress reaches a maximum around 0.7 mm behind each row and in-between elements on the cubical roughness patch. The hemispherical roughness patch shows a similar trend in-between elements, but a true maximum is not defined due to not being able to measure that closely to the wall. Rows 0 and 1 do not show a large $\overline{w^2}$ stress peak as seen in previous turbulence figures. The stress begins to increase after the 2nd row elements. In the case of the cubes, the spanwise normal stress behind the final row of elements is

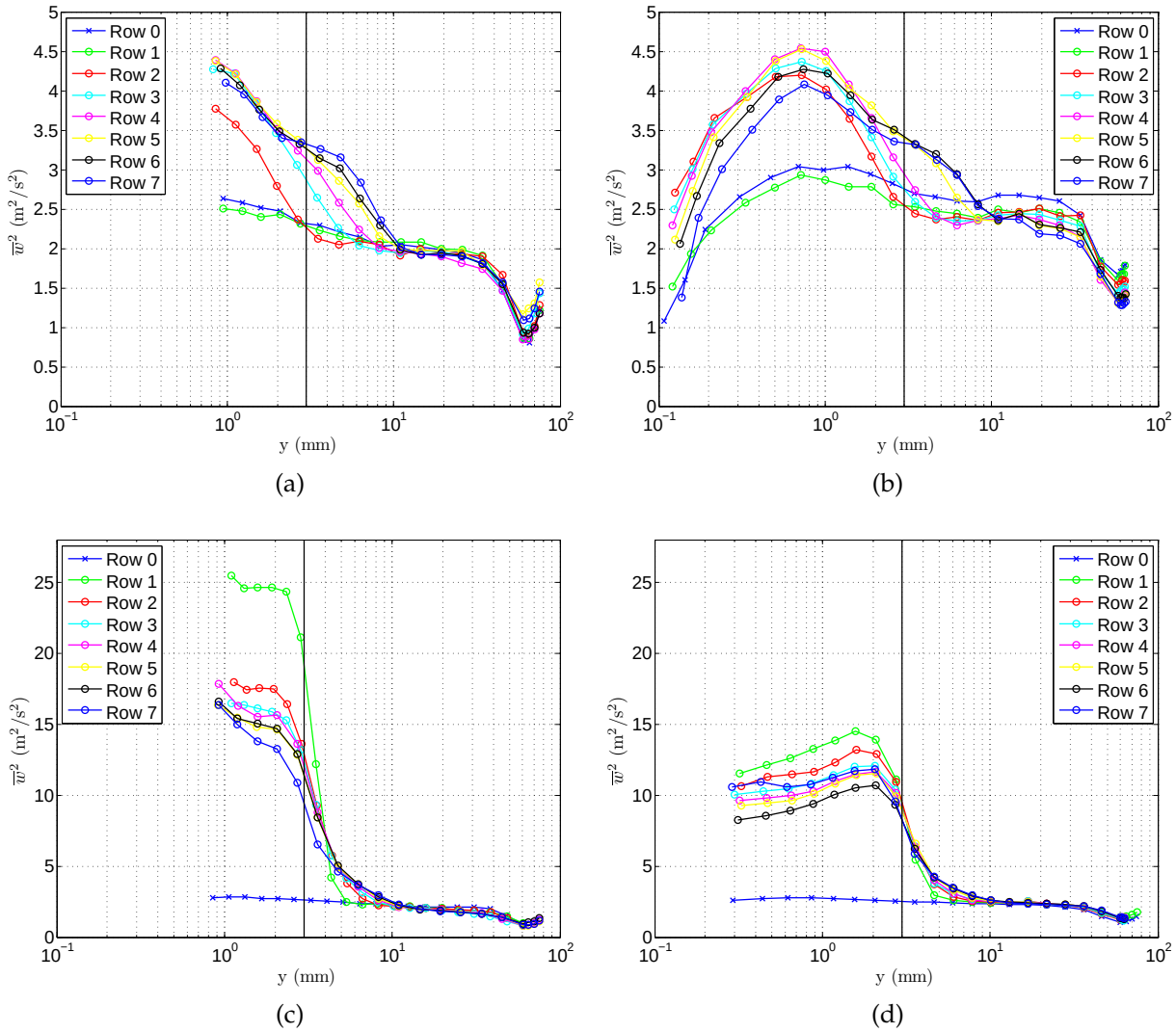

Figure 3.10: $\overline{w^2}$ normal stress profiles: (a) between hemispheres; (b) between cubes; (c) behind hemispheres; and, (d) behind cubes

slightly less than the rest of the rows. Otherwise, the $\overline{w^2}$ stress in-between the roughness elements is similar for rows 3 through 7. The strength of the turbulence is similar between the hemispherical and cubical roughness patches.

Behind the elements, the $\overline{w^2}$ stress also peaks below the roughness height. In the case of the cubes, this peak is well defined at around 1.5-2 mm above the wall, similar to the peak $\overline{v^2}$ stress. The first row of cubes produces the largest $\overline{w^2}$ stress at around 14.5 m^2/s^2, and then the stress decreases as the flow moves streamwise down the roughness patch. In the case of the hemispherical elements, there is not a defined peak of $\overline{w^2}$ stress behind the elements. There is a brief leveling off of stress around the 1.5 mm mark; however, below that level, the stress appears to start increasing again. Unfortunately, due to limitations in measuring very close to the wall, there is not further data on the $\overline{w^2}$ stresses behind the hemisphere closer to the wall. The $\overline{w^2}$ stress behind the first row of hemispheres is significantly larger than the stress behind other elements, reaching above 25 m^2/s^2. This stress decreases as the flow moves streamwise over the hemispherical patch.

The profiles for the Reynolds shear stress $\overline{-uv}$ are presented in Figure 3.11. In a smooth wall and fully developed rough wall turbulent boundary layer, the $\overline{-uv}$ shear stress is typically a constant maximum value in the log region of the boundary layer. For these cases, this constant shear stress region is only apparent on the measurement locations in front of the entire patch and the location after the first row of elements. The $\overline{-uv}$ shear stress between the elements increases in a similar manner to the $\overline{v^2}$ normal stress. There is a gradual increase starting after the second row of roughness elements and reaching a maximum at the end of the patch. The y location of this peak also moves upward in a similar manner to the $\overline{v^2}$ stress. The magnitude of the $\overline{-uv}$ shear stress in-between the cubes is slightly higher than that of the hemispheres, but not significantly.

The $\overline{-uv}$ shear stress directly behind the elements peaks at a location just slightly below the roughness height. Behind the hemispheres, the $\overline{-uv}$ shear stress after the first row reaches the largest peak around 9 m^2/s^2. The stress then decreases behind the elements

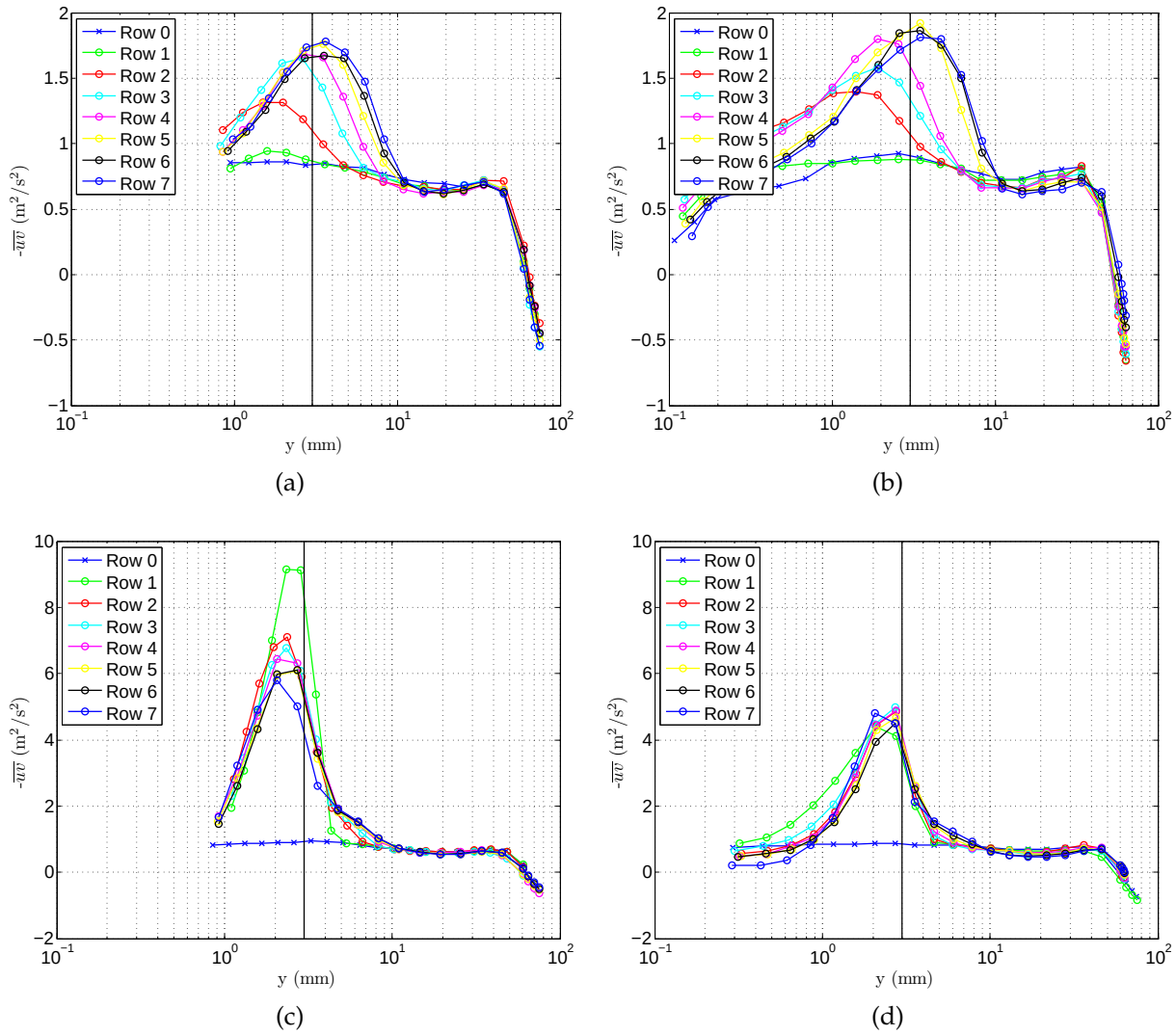

Figure 3.11: $\overline{-uv}$ shear stress profiles: (a) between hemispheres; (b) between cubes; (c) behind hemispheres; and, (d) behind cubes

as the flow moves downstream. In contrast, the shear stress behind the cube elements is similar along the entire length of the roughness patch. The maximum $\overline{-uv}$ shear stress for the cubes ranges between 4-5 m^2/s^2 for rows 1-7. As witnessed in some other turbulent measurements, it is possible that each cubical roughness produces a similar amount of turbulence behind it no matter the streamwise position. However, the hemispherical elements have shown a gradual decrease in turbulence behind elements as the flow moves downstream.

The profiles for the Reynolds shear stresses $\overline{uw}$ and $\overline{vw}$ are presented in Figures 3.12 and 3.13. These values should be equal to zero in a symmetric flow location. In-between the roughness elements, these shear stress values are very near zero, indicating little spanwise velocity fluctuations. However, directly behind the elements, there is some scatter of the shear stresses below the height of the roughness elements. As explain above in the mean spanwise velocity section, this scatter is due to uncertainty in positioning the LDV measurement volume directly behind a roughness element.

Full velocity profiles for all 10 variations of triple products are provided in Appendix A. They are not discussed in this section because they are analyzed in Section 3.2.4.

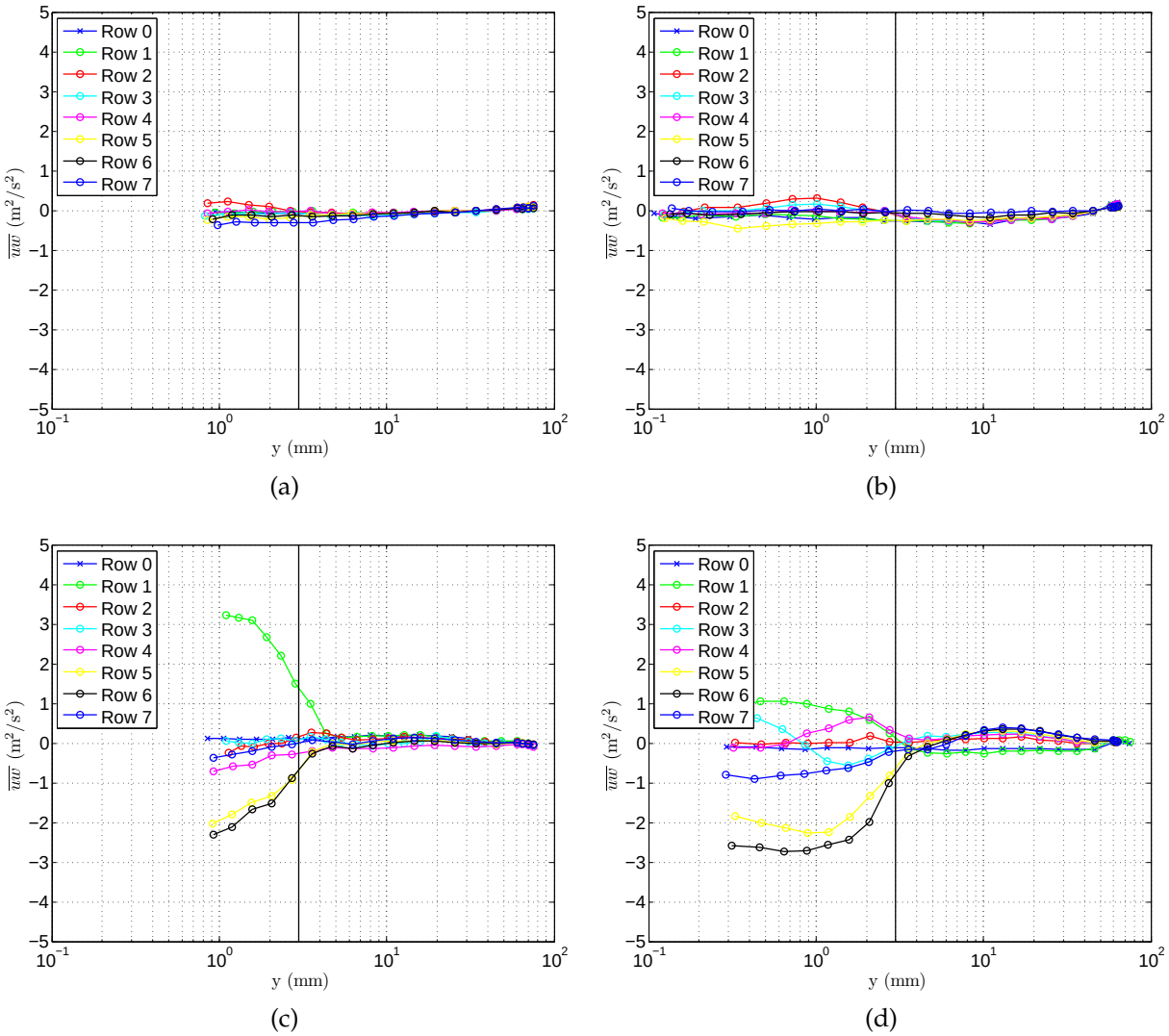

Figure 3.12: $\overline{uw}$ shear stress profiles: (a) between hemispheres; (b) between cubes; (c) behind hemispheres; and, (d) behind cubes

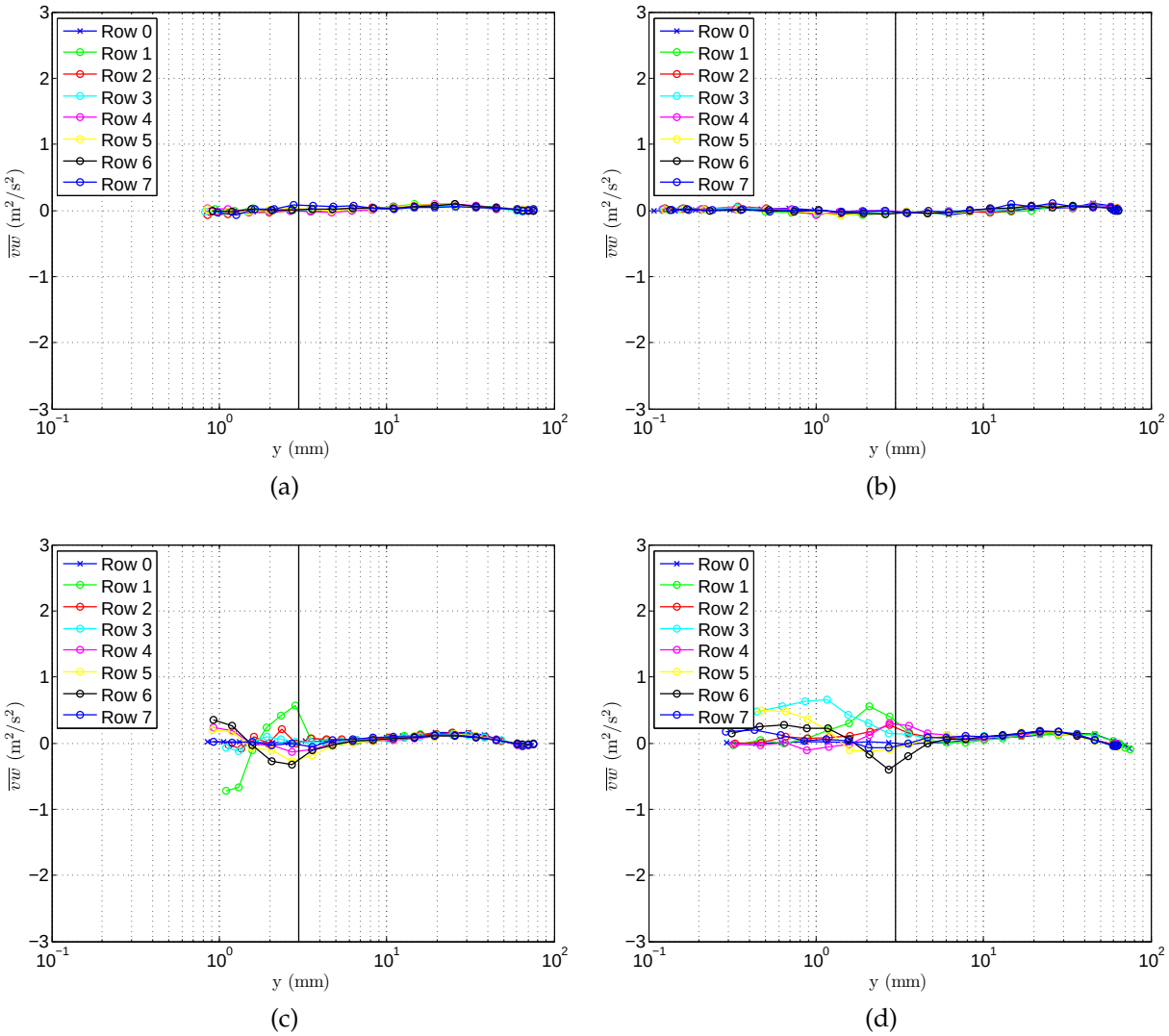

Figure 3.13: $\overline{vw}$ shear stress profiles: (a) between hemispheres; (b) between cubes; (c) behind hemispheres; and, (d) behind cubes

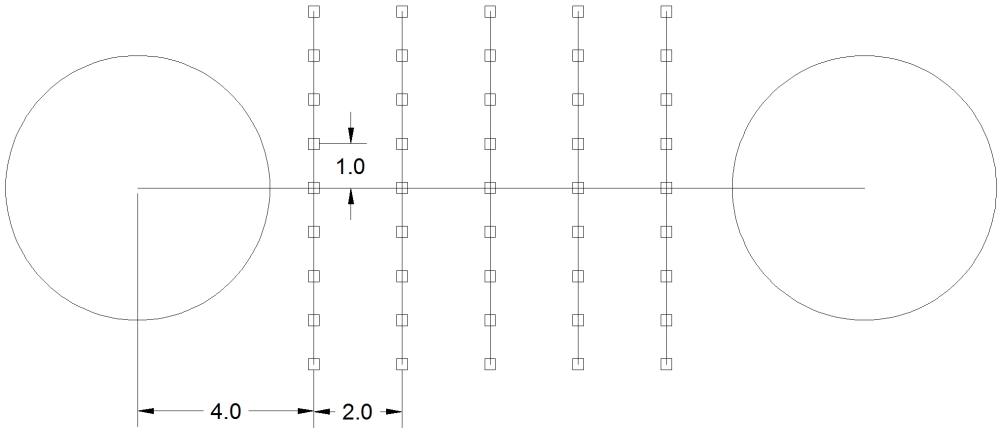

Figure 3.14: Measurement locations where partial boundary layer profiles were measured for contour plots

3.2 Local Flow Behavior Around Elements

3.2.1 Measurement Locations

To investigate the turbulent flow structure around the roughness elements, 45 partial boundary layer profiles were taken behind specific elements. These profiles were taken behind a central element of each patches' first and sixth rows of roughness. The measurement locations are presented in Figure 3.14. Axis labels on the figures are given in microns. Distances in the streamwise and spanwise direction are referenced to the center of the roughness element. Note that the first contour plane for both roughness elements is located at x = 4 mm. The base of the hemisphere covers +/- 3 mm in both directions while the cube covers just $\pm$ 1.5 mm. This means that the first contour plane measurements are taken 1 mm from the aft of the hemisphere and 2.5 mm from the aft of the cube. Measurements could not be taken closer to the hemisphere due to flare and to the cube due to the angle of the LDV beams. The plots for the hemispherical case includes 585 distinct LDV measurement points and the cubical case contains 720 points.

3.2.2 Mean Velocities

The mean stream-wise velocity contour plots (Figure 3.15) show the drastic drop in U velocity due to the presence of the roughness element. A large backflow region is present immediately behind both sets of elements due to the separation of the flow. A large velocity gradient is present where the backflow region meets the flow traveling around the elements. The direction of this gradient is perpendicular to the outline of both element types. The flow above the roughness height approaches that of the turbulent boundary layer in front of the element. The effect of the roughness elements in front of the sixth row is shown in those contour plots with the lower magnitude velocity flowing over the tops of the elements. Flow has reattached by the center of the spacing between the elements and begins to smooth out before it meets the next row of elements. The hemispherical and cubical cases show very similar results with the mean stream-wise velocity contours. The main difference is the shape of backflow and high velocity gradient regions directly behind the elements, where each region takes on the shape of the roughness elements projection.

The mean wall-normal velocity contours (Figure 3.16) again show the separation region directly behind the elements with a positive mean value. Up-wash from near the base of the element is sucked back into the large amount of fluid rushing over the element. In the hemispherical case, the proximity of the first contour to the edge of the element only shows this large upwash region behind the first row. The next contour at x = 6 mm shows the large region of flow heading towards the wall. In the cubical case, both the upflow from the separated region and the negative velocity flow from the top of the element are show in the first streamwise contour. Behind the sixth row of elements, velocity magnitudes are slightly smaller for both roughness cases. The upflow region behind the row 6 hemisphere is noticeably smaller while the row 6 cube is roughly the same size and magnitude as the first row. The last streamwise contour for each of the hemispherical cases show a slight positive wall-normal velocity as the fluid prepares to climb over the next

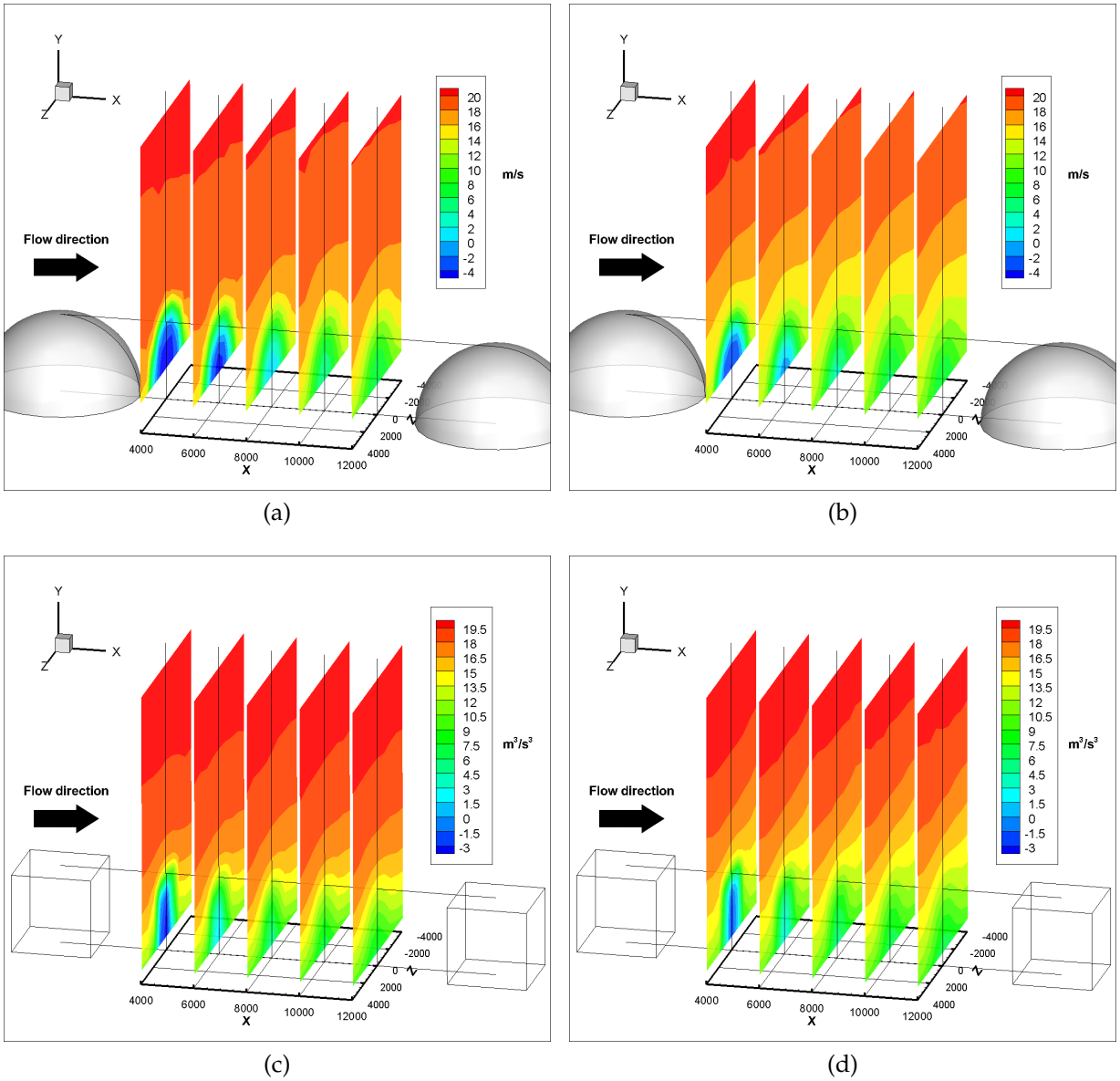

Figure 3.15: Contour plots of mean stream-wise U velocity behind: (a) first row of hemispheres; (b) sixth row of hemispheres; (c) first row of cubes; and, (d) sixth row of cubes

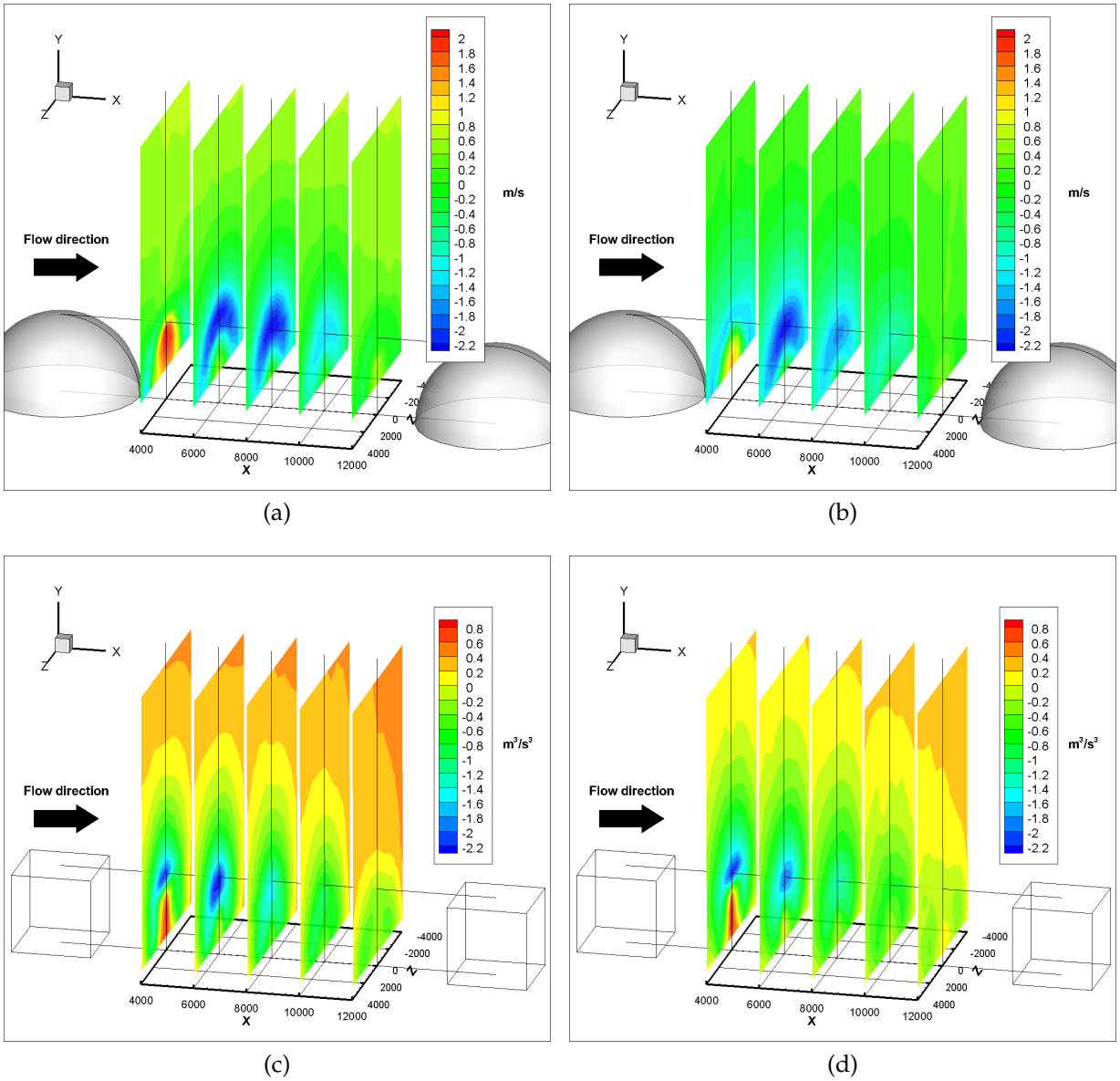

Figure 3.16: Contour plots of mean wall-normal V velocity behind: (a) first row of hemispheres; (b) sixth row of hemispheres; (c) first row of cubes; and, (d) sixth row of cubes

element. This is not apparent in the cubical cases, as the flow is still headed toward the wall at a low velocity at x = 12 mm.

The mean spanwise velocity contour plots (Figure 3.17) show the fluid attempt to return to the center of the element after flowing around its sides. The separated region behind the hemisphere shows very little spanwise velocities, but at x = 6 mm the flow from the sides of the element is rushing back towards the center of the element. Velocities of the magnitude $\pm$ 3 m/s are seen behind the hemispherical elements. The flow behind the row 6 of hemispheres is similar in pattern, but lower in magnitude than the first row. The spanwise contour plots can confirm flow symmetry behind the elements.

3.2.3 Reynolds Stresses

The turbulent structure behind the roughness elements will now be examined by discussing the Reynolds stresses downstream of the elements. The stream-wise Reynolds normal stress $\overline{u^2}$ (Figure 3.18) reach a maximum value around the height of the roughness element, as seen by George, Bennington, and Varano. The hemispheres have a region of high normal stress in the shape of the edge of the hemisphere about 6mm downstream from the center of the element. The cube's high stress region is limited to the element height about 4 mm downstream. The magnitude of the stresses behind the first row hemisphere is nearly double the values behind the cube. George states this is due to the vortex structure flowing over the top of the elements, and that these vortices are larger over the hemisphere due to it's larger frontal area. The larger vortices produce a larger normal stress. Bennington[5] also noted smaller $\overline{u^2}$ values behind cubes, and stated this is attributed to the flow blockage from the cubes. This blockage reduces mixing immediately behind the cube, and the lower stress values are due to a lower of amount of mixing by the shear layers. The flow behind the sixth row of roughness elements is similar in shape to that of the first row. The main difference in these measurements is a reduction in the magnitude of the stresses. Interestingly, the highest normal stress behind the sixth row

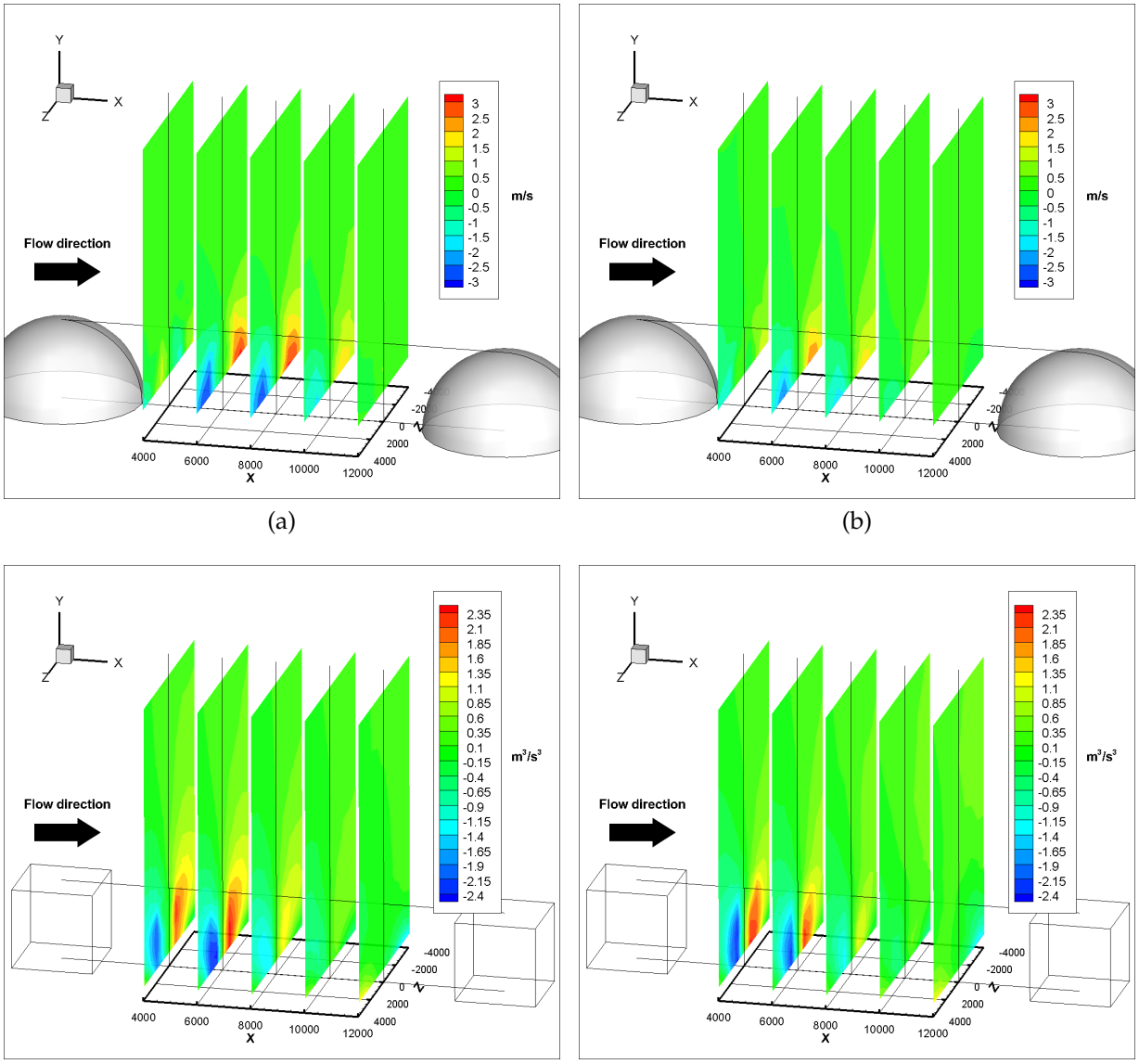

Figure 3.17: Contour plots of mean spanwise W velocity behind: (a) first row of hemispheres; (b) sixth row of hemispheres; (c) first row of cubes; and, (d) sixth row of cubes

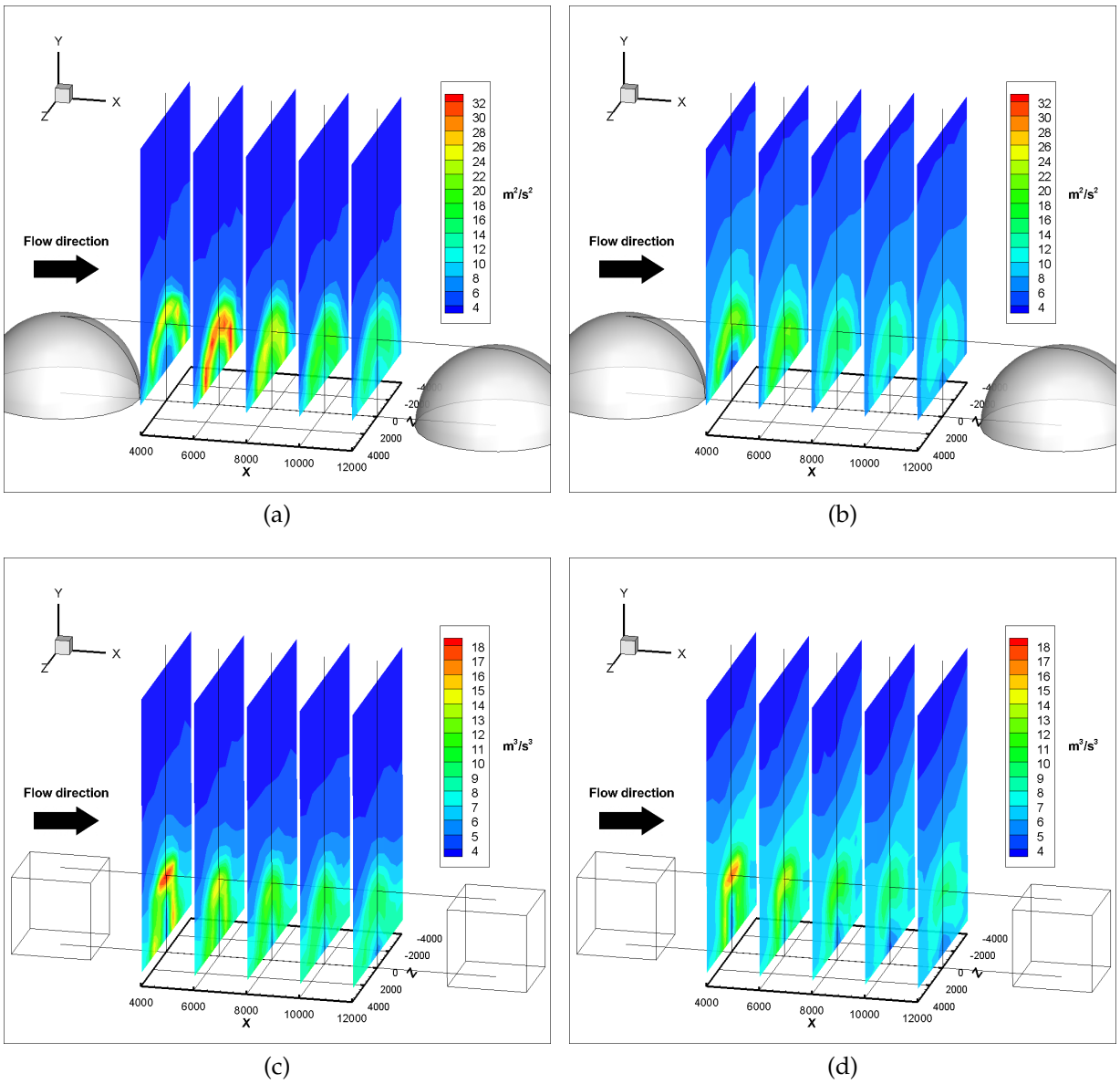

Figure 3.18: Contour plots of $\overline{u^2}$ normal stress behind: (a) first row of hemispheres; (b) sixth row of hemispheres; (c) first row of cubes; and, (d) sixth row of cubes

cube element only dropped a slight percentage in comparison to the first row. However, the stresses behind the sixth row hemisphere are significantly lower than that of the first, dropping by nearly 25%.

The contour plots for the wall-normal Reynolds normal stress $\overline{v^2}$ are shown in Figure 3.19. The hemispherical element produces a large region of normal stress 6 and 8 mm downstream from the center of the element as flow rushes over the surface of the hemisphere towards the wall. The highest normal stress for the cubical element occurs 6 mm downstream and is much smaller in size than that of the hemisphere. Both cases produce maximum values slightly below the element heights, which agrees with the findings of George and Varano. These wall-normal stresses are produced by the shear layers from the top surface vortex structures rushing fluid toward the wall as well as the downwash produced from the horseshoe vortex structures from the bottoms of the elements. The structure behind the sixth row of elements is similar to that of the first row, but lower in magnitude.

The spanwise Reynolds normal stress $\overline{w^2}$ (Figure 3.20) contour plots are very similar to the $\overline{v^2}$ plots. The same core of stress is located in the same locations for both the hemispherical and cubical cases. These stresses are produced by the same flow mechanisms as the wall-normal stresses. The flow rushes around the roughness elements and is pushed toward the centerline by the vortex structures. One key difference between the $\overline{v^2}$ and $\overline{w^2}$ plots are their relative magntitudes. The $\overline{w^2}$ stresses are larger than the $\overline{v^2}$ stresses because the spanwise fluctuations are not affected by the presence of the wall.

The Reynolds shear stress $\overline{-uv}$ is depicted in Figures 3.21. Large $\overline{-uv}$ shear stresses are created when the fluid experiences a sweep $(u > 0, v < 0)$ or ejection $(u < 0, v > 0)$ event. The flow immediately behind the elements experiences large sweeping motions over the top of the element from the vortex structures. The highest levels of shear stress are at or slightly below the element height in both cases. The cubical cases have a very small core where the shear stresses are large, while the hemispherical elements produce a consider-

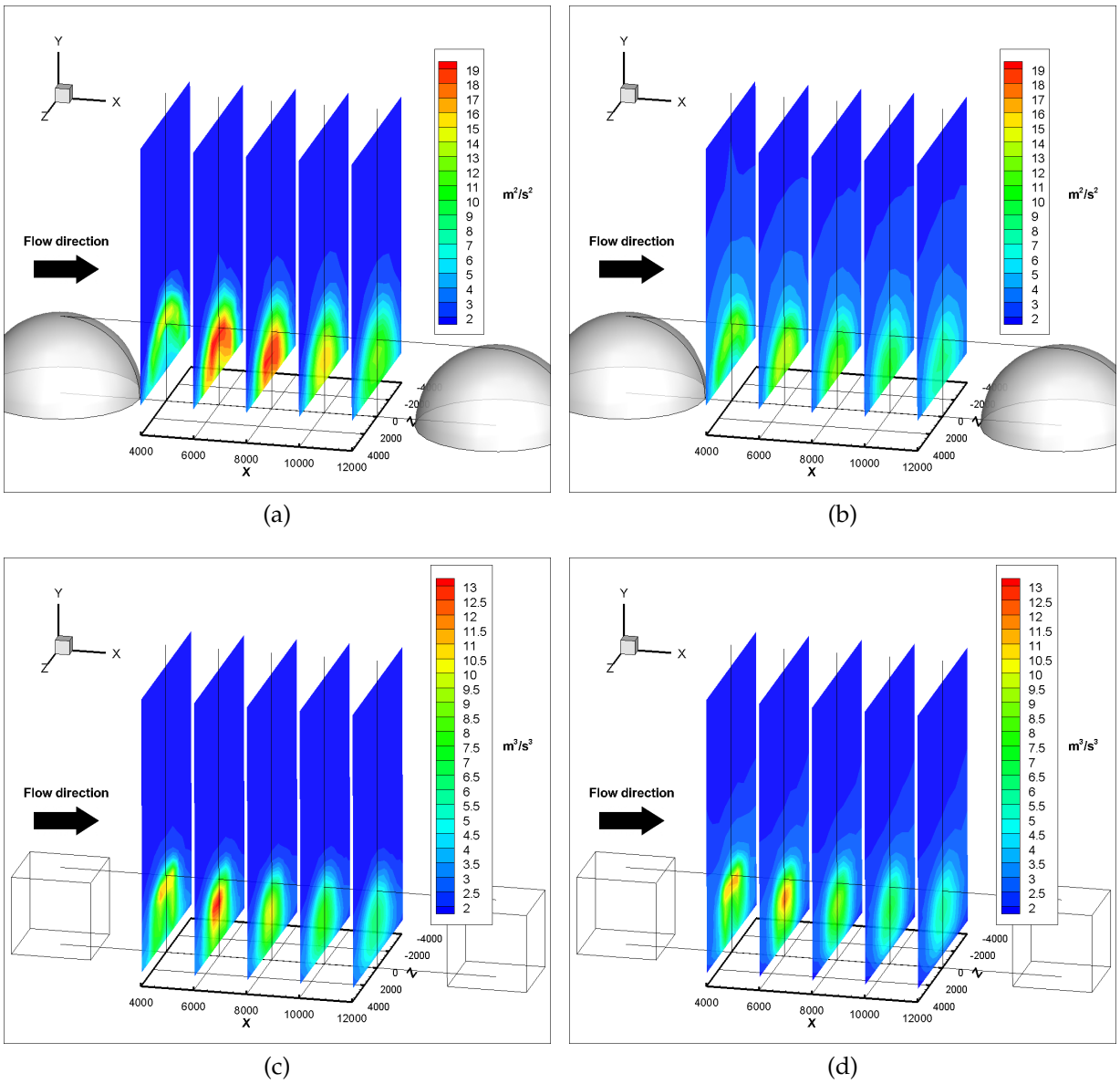

Figure 3.19: Contour plots of $\overline{v^2}$ normal stress behind: (a) first row of hemispheres; (b) sixth row of hemispheres; (c) first row of cubes; and, (d) sixth row of cubes

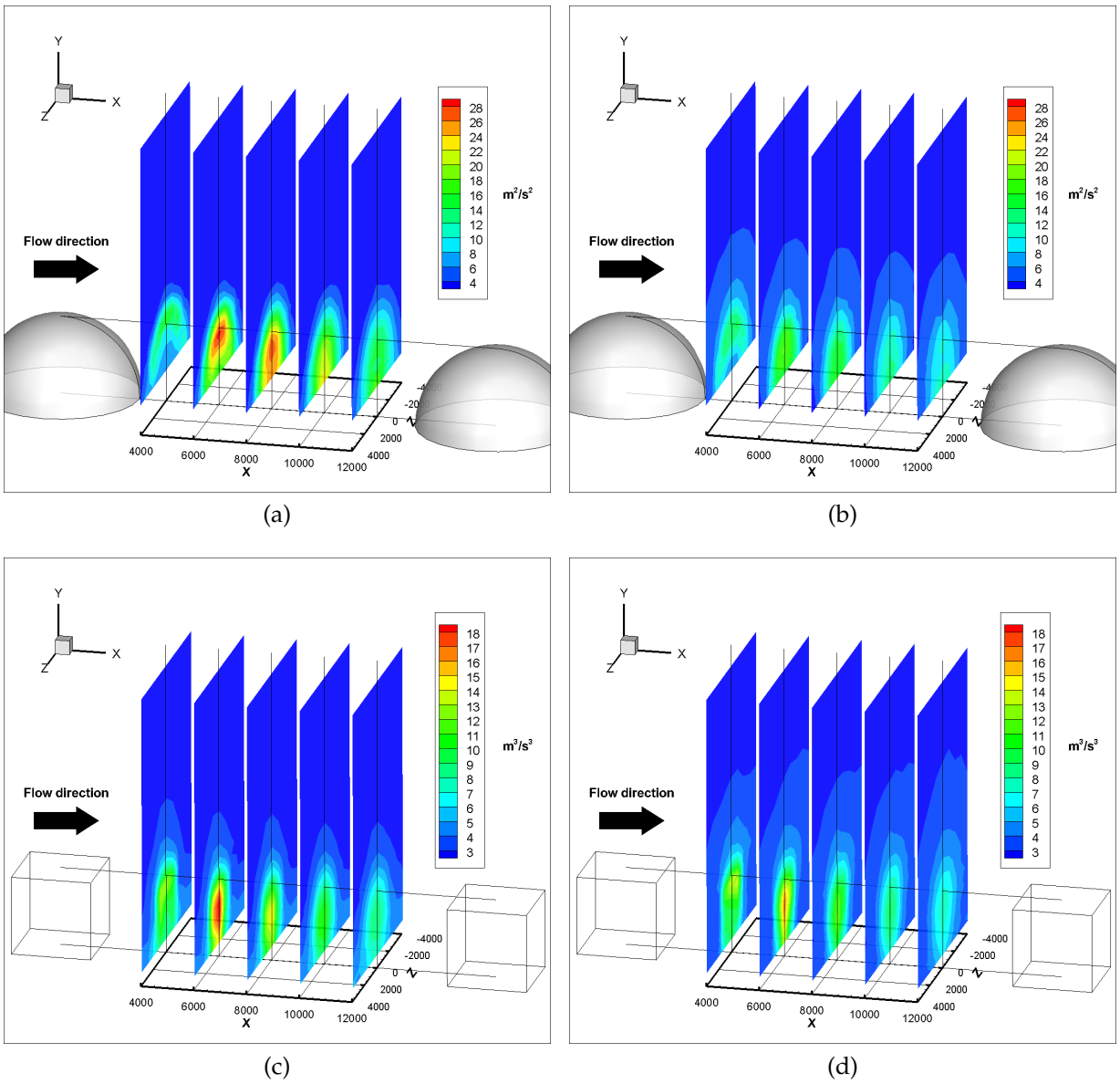

Figure 3.20: Contour plots of $\overline{w^2}$ normal stress behind: (a) first row of hemispheres; (b) sixth row of hemispheres; (c) first row of cubes; and, (d) sixth row of cubes

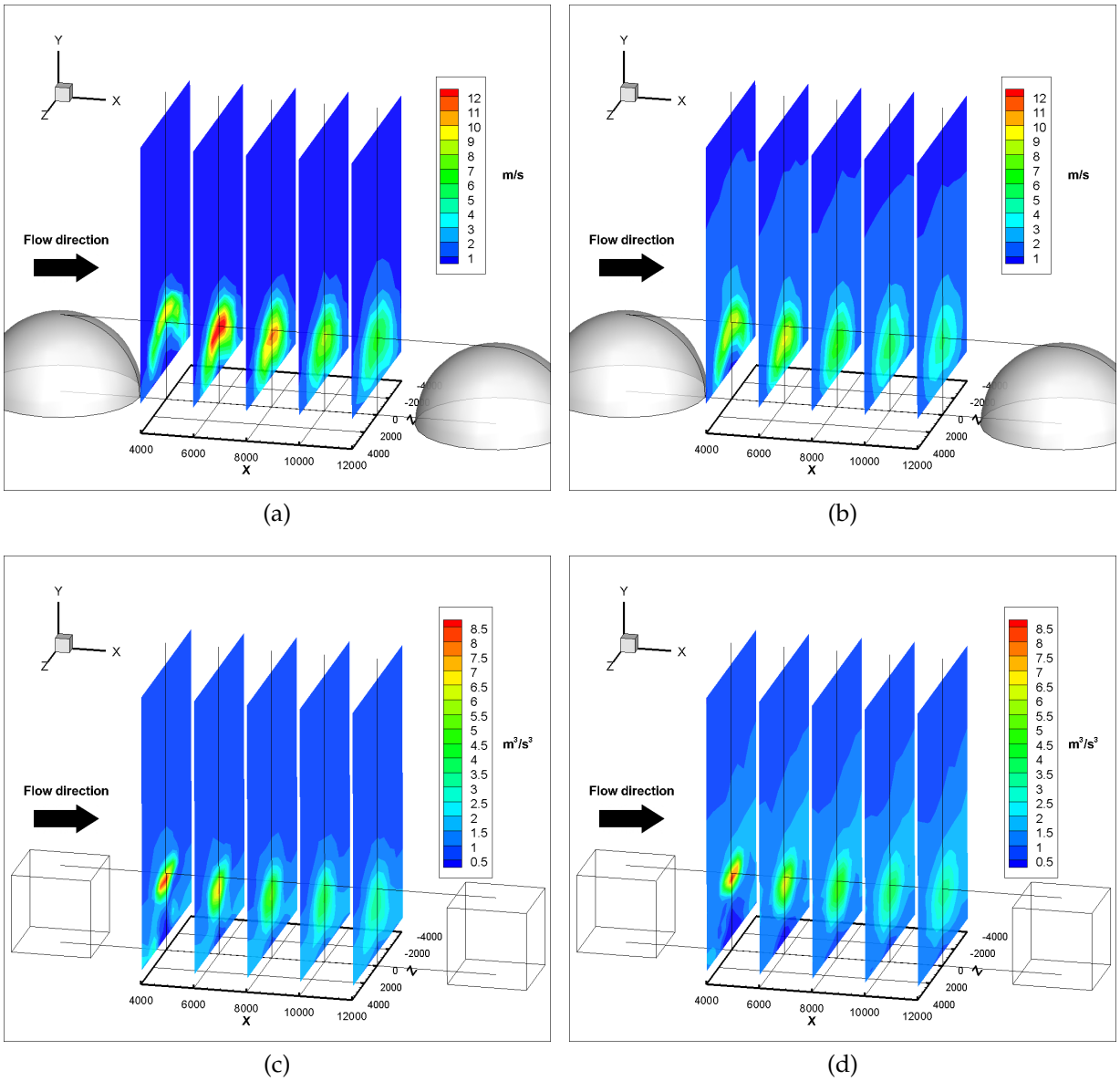

Figure 3.21: Contour plots of $\overline{uv}$ shear stress behind: (a) first row of hemispheres; (b) sixth row of hemispheres; (c) first row of cubes; and, (d) sixth row of cubes

ably larger area of stress. George states that this core of high shear stress is formed by the merging of separate shear layers from the tops of the elements. The fluid below these cores of stress, near the wall, show very little amounts of $\overline{-uv}$ shearing stress. The hemispheres produce a larger value of shear stress than the cubes as in the other Reynolds stresses. Also apparent in this case as well as the others is that the cube creates nearly the same amount of turbulence behind the first and sixth rows, while the hemisphere produces a significant amount less of turbulence behind the sixth row.

The Reynolds shearing stresses $\overline{uw}$ (Figure 3.22) and $\overline{vw}$ (Figure 3.23) convey the three-dimensionality and symmetry of the flow. These stresses should be zero along the centerline of the elements due to the mean spanwise velocity equaling zero. For the $\overline{uw}$ stress, the cubical contour plots show thin regions of large positive and negative stresses that coincide with the edge of the cube and are approximately the same height as the cube. The regions for the hemispherical elements are slightly broader in width. The hemispheres again create the larger values of stress in the case of $\overline{uw}$. For $\overline{vw}$, the cores of high shear stress occur slightly below the element height and are smaller circles in shape.

Reynolds Stress Production

The production term, $v^2 \frac{du}{dy}$, for the streamwise Reynolds shear stress $\overline{-uv}$ is shown in Figure 3.24. Extremely large values of the production term are present immediately behind the first row of roughness elements. The hemisphere appears to produce the $\overline{-uv}$ shear stress at the height of the roughness element, while the cube produces it slightly lower than the roughness height. Most of the production occurs in the two planes right behind the elements, at x = 4mm and x =6 mm. There is little production elsewhere in the flow. The large values occur due to the extremely large $\frac{dU}{dy}$ gradient located behind the elements. The separated flow region has a low value for the U streamwise velocity, and where this region meets the flow rushing over the top of the element there is a very large velocity gradient.

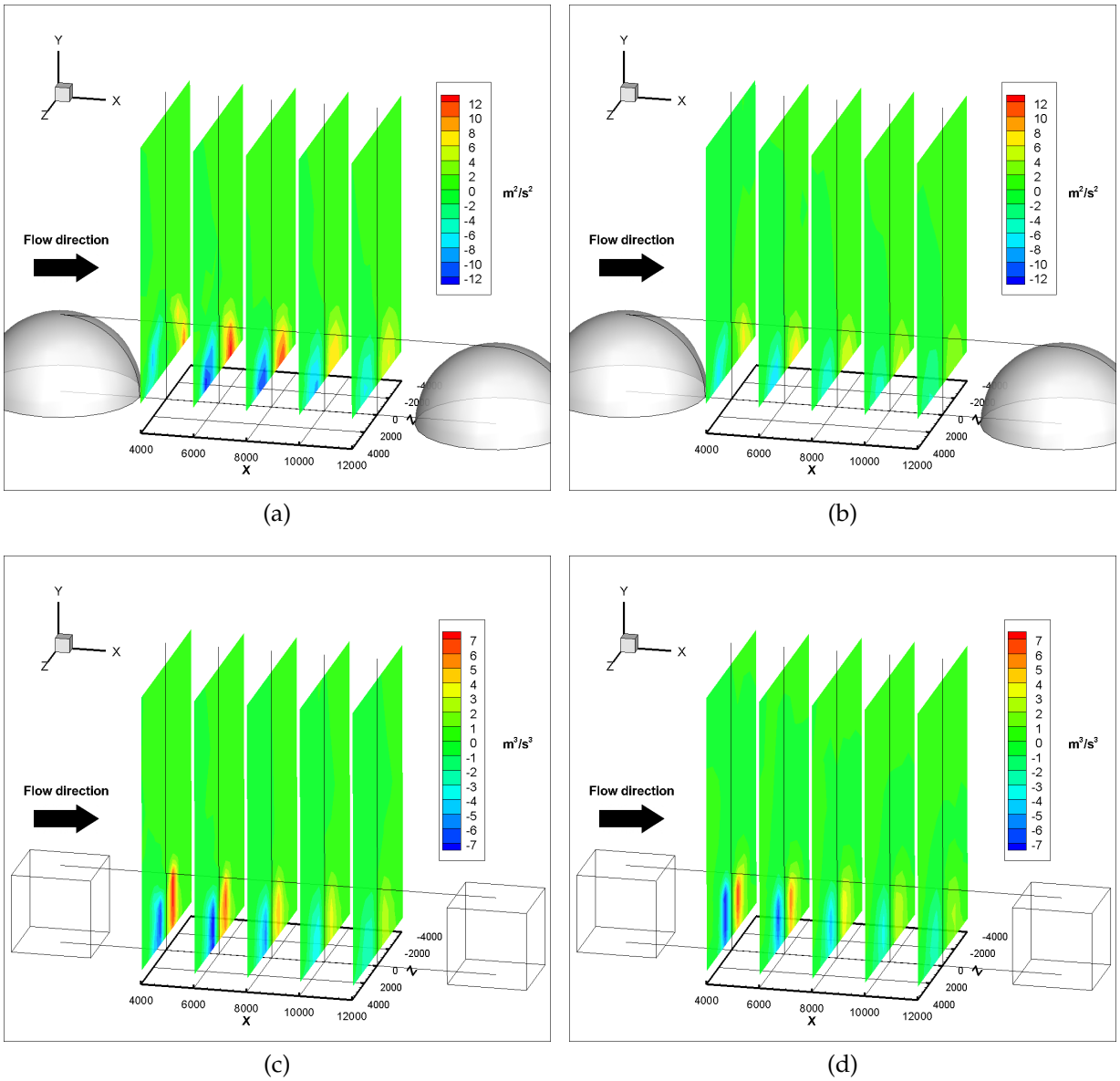

Figure 3.22: Contour plots of $\overline{uw}$ shear stress behind: (a) first row of hemispheres; (b) sixth row of hemispheres; (c) first row of cubes; and, (d) sixth row of cubes

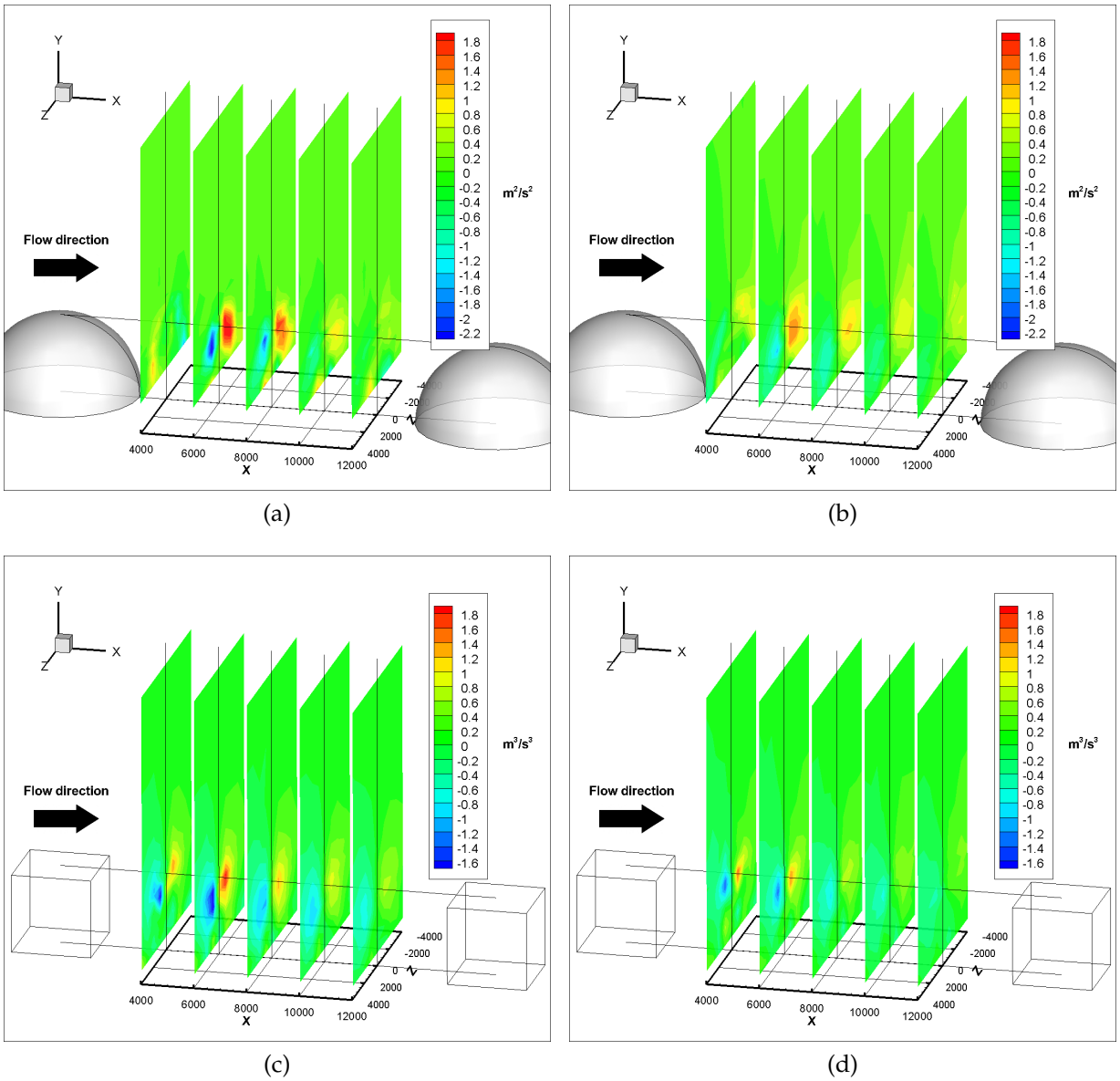

Figure 3.23: Contour plots of $\overline{vw}$ shear stress behind: (a) first row of hemispheres; (b) sixth row of hemispheres; (c) first row of cubes; and, (d) sixth row of cubes

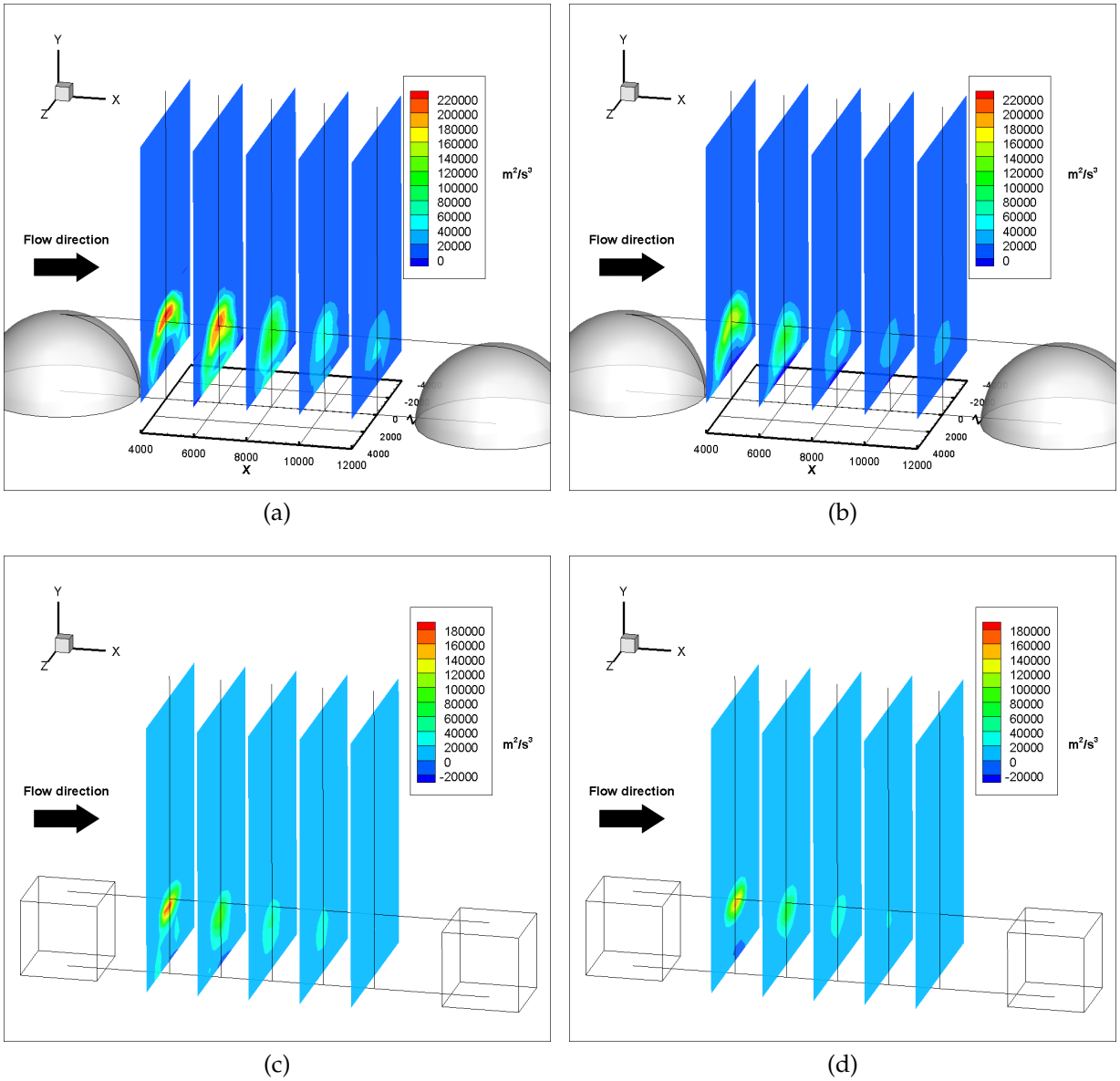

Figure 3.24: Contour plots of Reynolds shear stress production behind: (a) first row of hemispheres; (b) sixth row of hemispheres; (c) first row of cubes; and, (d) sixth row of cubes

3.2.4 Triple Products

The turbulent triple products are represented in summation notation as $\overline{u_i u_j u_k}$. All ten variations of triple products are plotted in Figures 3.25 - A.14. The triple products are mostly used to analyze the transport of the Reynolds stresses. The $\overline{u^3}$ and $\overline{u^2 v}$ triple products describe whether $\overline{u^2}$ turbulent fluctuations are being brought toward the wall in a sweeping manner or ejected away from the wall. For the hemispherical case, there is a core of positive $\overline{u^3}$ along the centerline due to sweeps and below the element height. This core of positive $\overline{u^3}$ is surrounded by negative $\overline{u^3}$ where ejections are occuring. For $\overline{u^2 v}$, these signs are changed, and there is a negative core surrounded by positive $\overline{u^2 v}$. This shows that near the wall directly behind the element, the $\overline{u^2}$ fluctuations are being swept toward the wall because u' is positive and v' is negative. Around this core of fluid sweeping toward the wall is fluid that is ejecting away from the wall. There is a similar pattern with the cubical elements, except that the shape of the regions are less defined. It appears that the region of ejecting $\overline{u^2}$ is located at the cube roughness height, while there is a very small point below the element height where $\overline{u^2}$ is sweeping toward the wall. The $\overline{u^2 w}$ plots depict the $\overline{u^2}$ fluctuations getting pushed toward the centerline of the element due to the flow rushing around the sides of the roughness.

The $\overline{v^2 u}$, $\overline{v^3}$, and $\overline{v^2 w}$ contour plots show a similar pattern to those attributed to the u2 fluctuation. In these cases, there is a region below the element height where v2 fluctuations are being swept toward the wall due to a $u' > 0$ and $v' < 0$ motion. There is also the region above and around the sweeping region that contains ejections of $\overline{v^2}$. For the hemisphere, the shape of these regions is very similar to the shape of the $\overline{v^2}$ fluctuations. For the cube, the region of sweeping $\overline{v^2}$ is more defined and larger in shape than the region of sweeping $\overline{u^2}$. The $\overline{v^2 w}$ plots again show the tendency of the $\overline{v^2}$ fluctuations to be pushed toward the centerline due to the flow coming around the sides of the roughness elements.

The behavior of the triple products is similar to what George measured. Behind the elements and slightly below the roughness height is dominated by sweeping motions to-

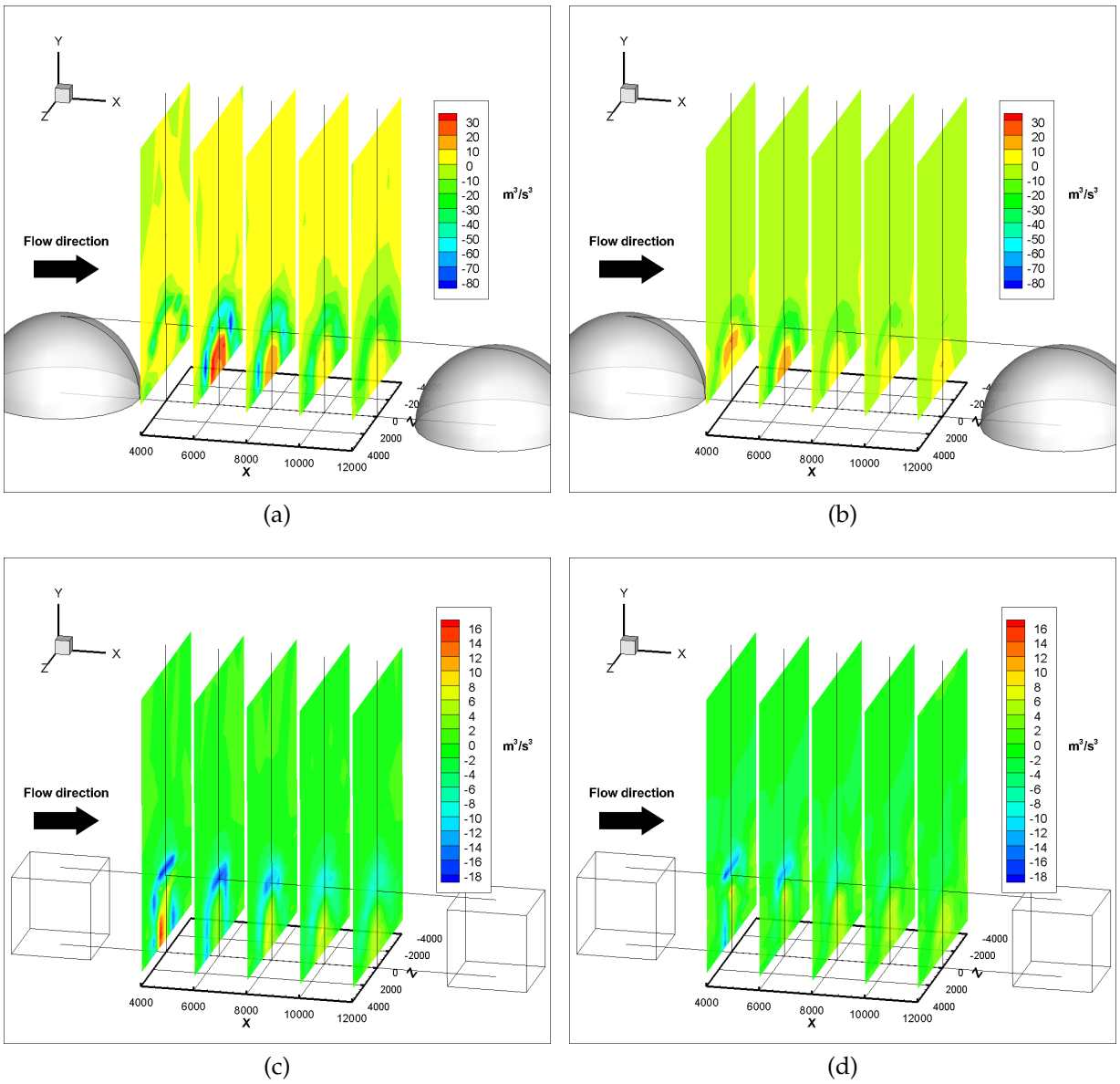

Figure 3.25: Contour plots of $\overline{u^3}$ behind: (a) first row of hemispheres; (b) sixth row of hemispheres; (c) first row of cubes; and, (d) sixth row of cubes

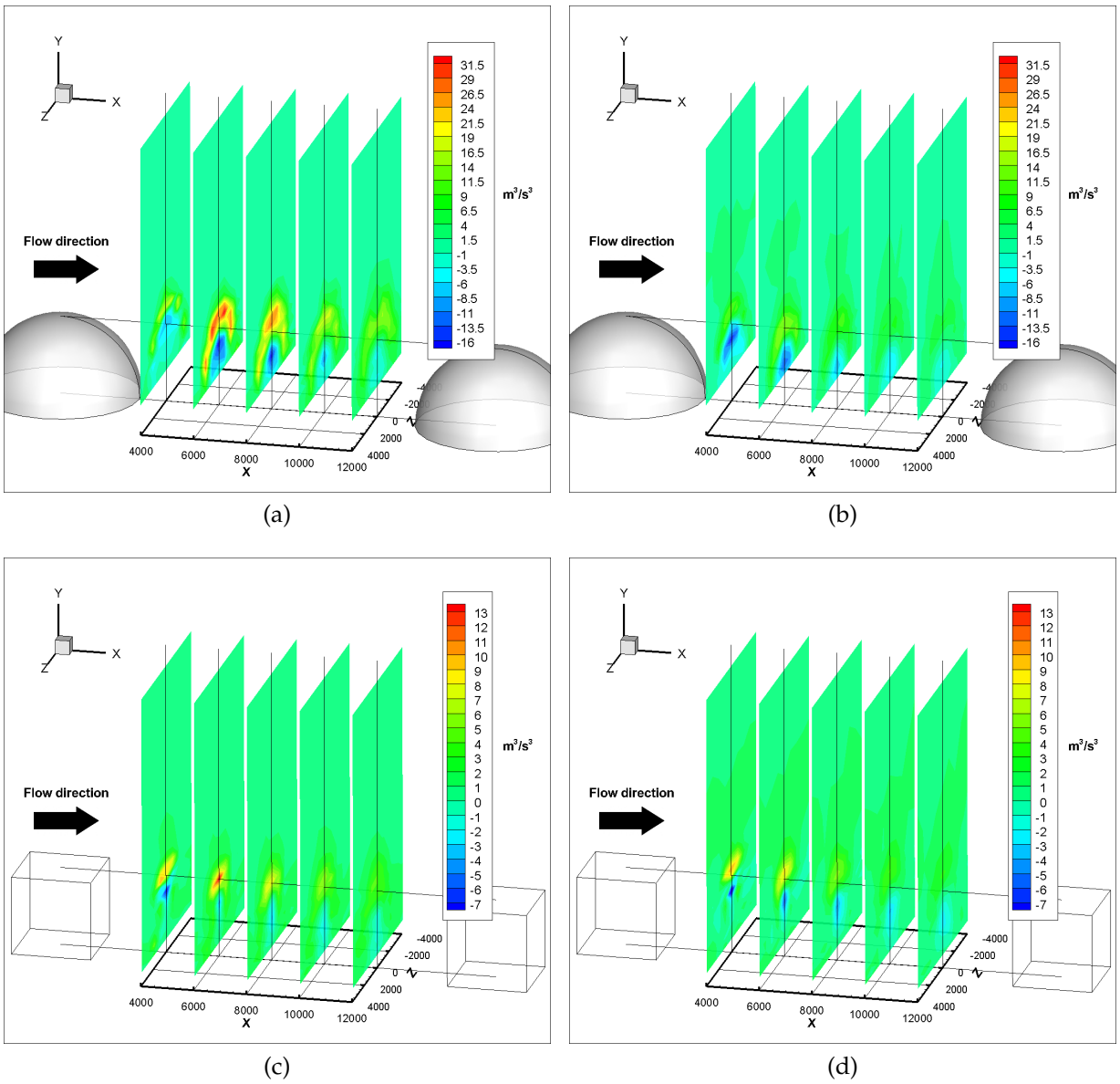

Figure 3.26: Contour plots of $\overline{u^2v}$ behind: (a) first row of hemispheres; (b) sixth row of hemispheres; (c) first row of cubes; and, (d) sixth row of cubes

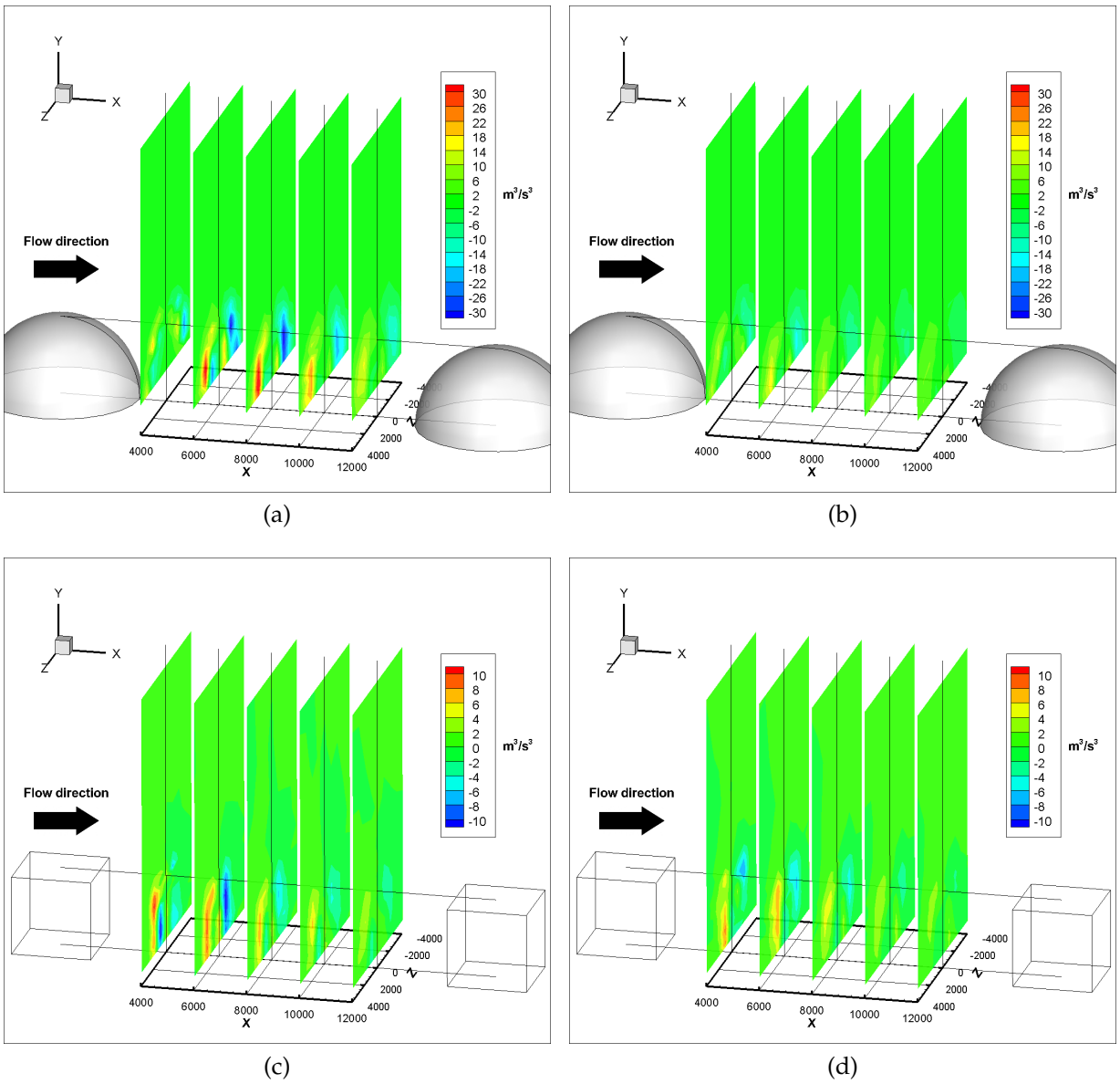

Figure 3.27: Contour plots of $\overline{u^2 w}$ behind: (a) first row of hemispheres; (b) sixth row of hemispheres; (c) first row of cubes; and, (d) sixth row of cubes

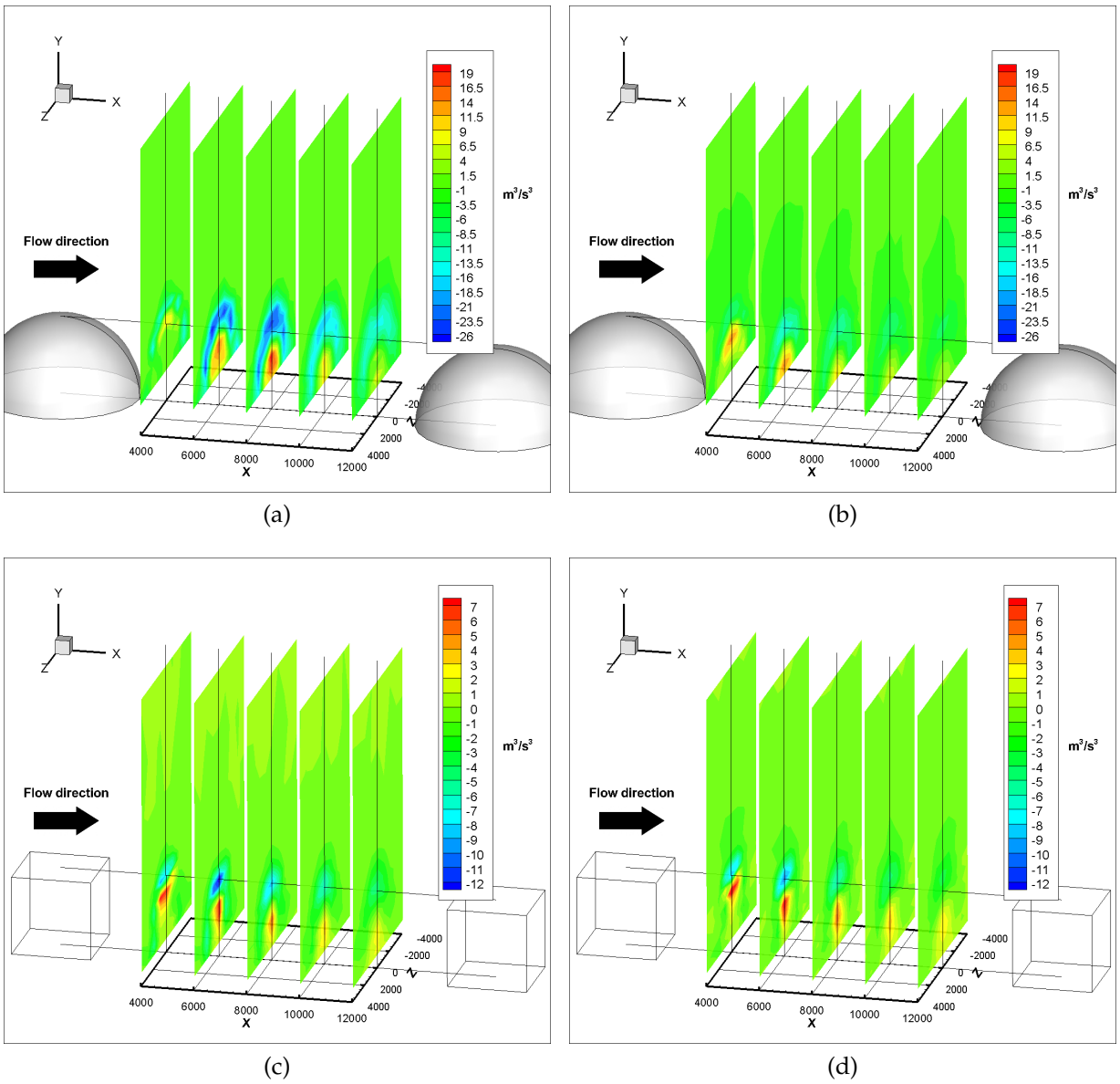

Figure 3.28: Contour plots of $\overline{v^2u}$ behind: (a) first row of hemispheres; (b) sixth row of hemispheres; (c) first row of cubes; and, (d) sixth row of cubes

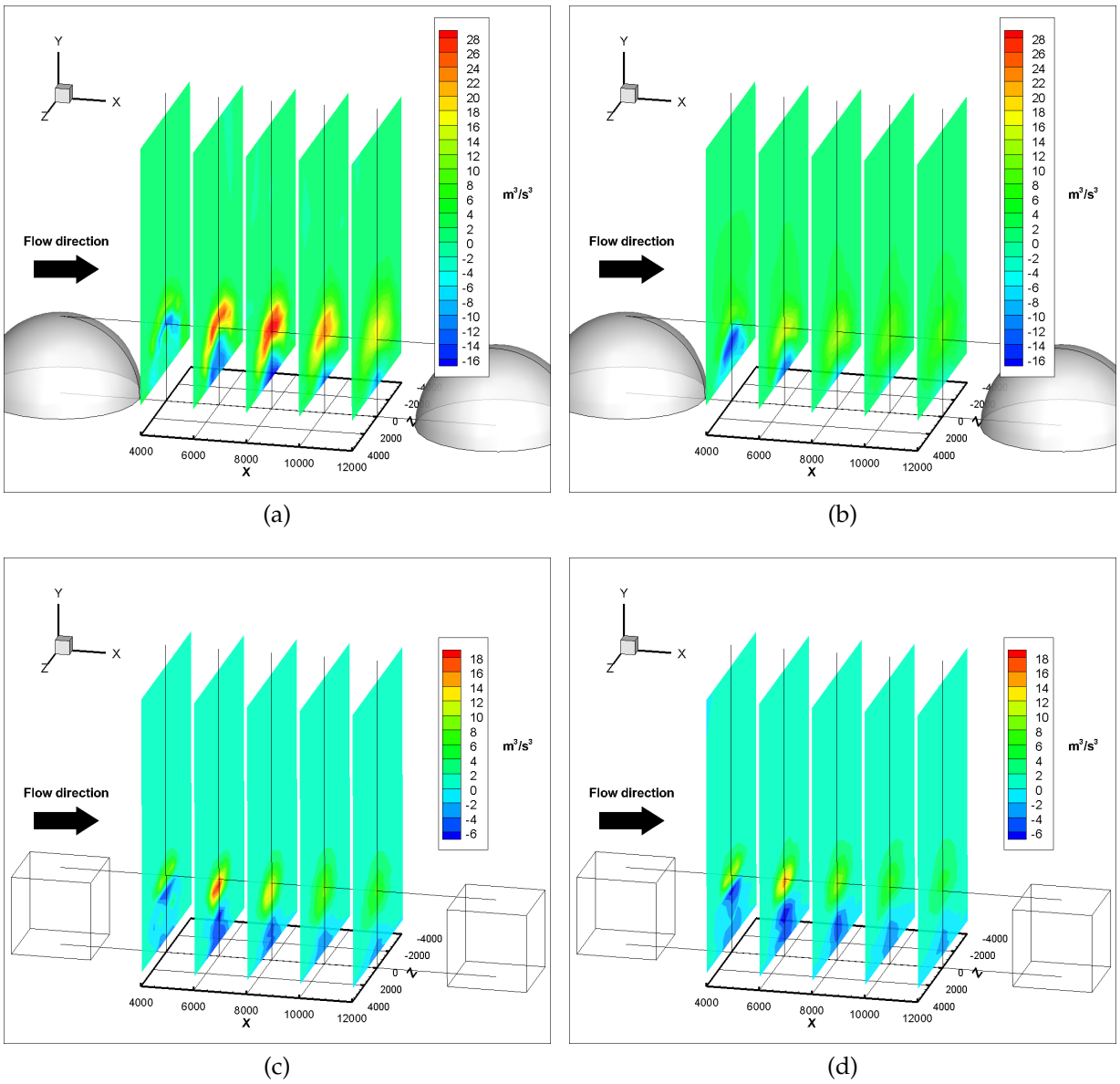

Figure 3.29: Contour plots of $\overline{v^3}$ behind: (a) first row of hemispheres; (b) sixth row of hemispheres; (c) first row of cubes; and, (d) sixth row of cubes

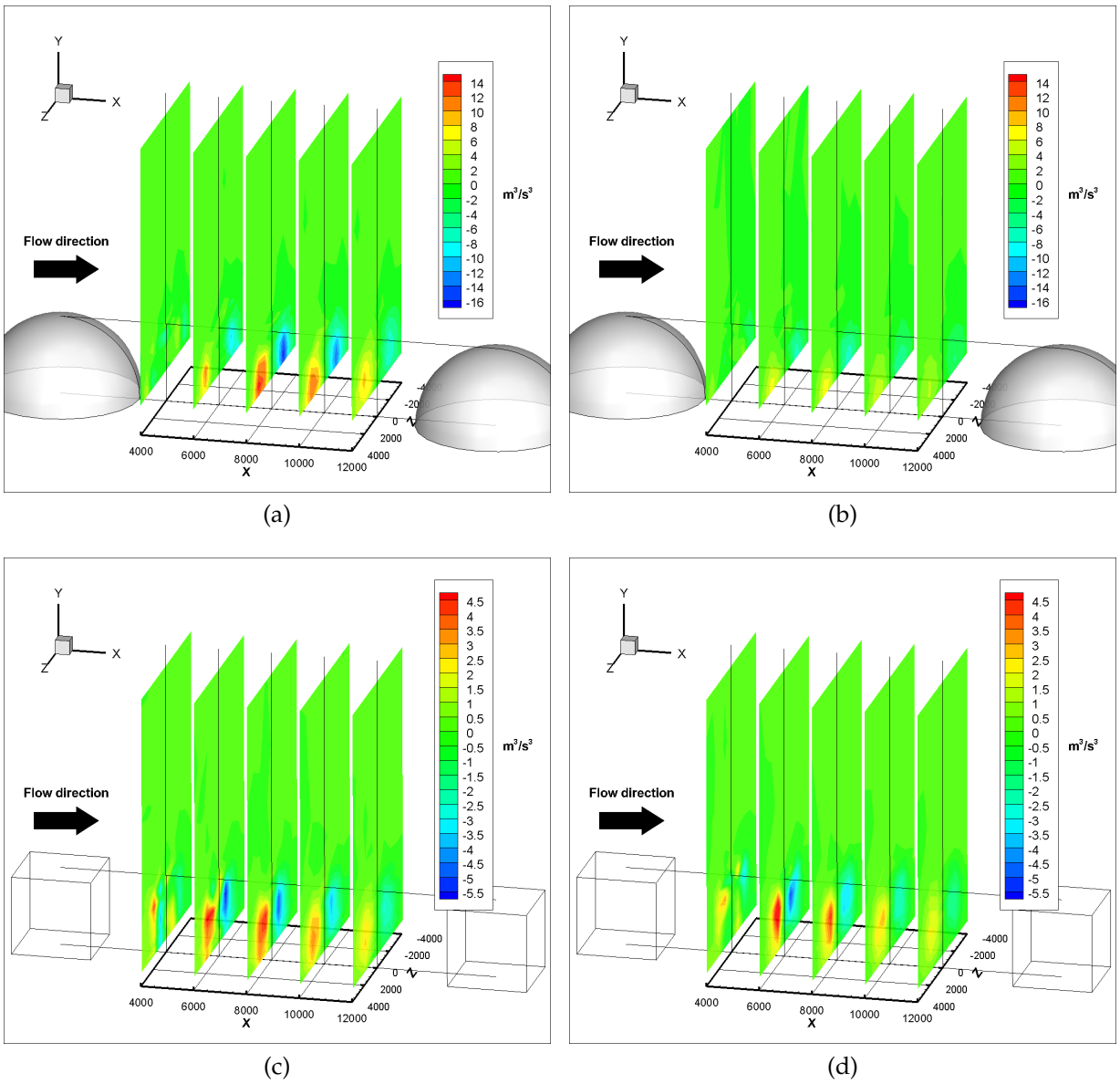

Figure 3.30: Contour plots of $\overline{v^2 w}$ behind: (a) first row of hemispheres; (b) sixth row of hemispheres; (c) first row of cubes; and, (d) sixth row of cubes

ward the wall. Slightly above that region is a larger region of fluid which is ejecting away from the wall and into the upper boundary layer.

A full quadrant analysis will now be done to examine the magnitudes of the sweep and ejection events behind the roughness elements.

3.2.5 Sweep and Ejection Events

To analyze how different turbulent motions affect the structure of the flow, the contour data taken behind the sixth row of the hemispherical and cubical roughness patches were conditionally averaged. The data were averaged based on the streamwise and wall-normal velocity fluctuations to extract sweep and ejection events. Sweep events are characterized by a positive streamwise u′ fluctuation and a negative wall-normal v′ fluctuation. Ejection events are the opposite, with a negative u′ and positive v′ component. All other events, where the fluctuations have the same sign, are called interactions. Interactions are relative weak motions, and produce only a slight amount of positive uv shear stress. The sweep and ejection events are what drive the large shear stresses in the flow. In a smooth wall flow, sweeps and ejections occur each about 10% of the time. In a rough wall flow, sweep and ejection events occur much more frequently, up to roughly 38% each in the case of this study. Figure 3.46 shows that the two events are most likely to occur behind the elements right at the roughness height.

Figure 3.31 shows the mean stream-wise velocity after conditional averaging. There is little difference between the two separate events because the stream-wise velocity has such a large positive magnitude in the first place. The only difference is that the sweep motions have a slightly higher mean stream-wise velocity, and this result is trivial because sweep events are defined as having a faster stream-wise velocity than the mean. Figure 3.32 shows the wall-normal velocities, and since this mean velocity is close to zero everywhere, the conditional averaging has an effect on the sign of averaged data. For the sweep events, a large negative velocity value appears behind the element at the roughness height as the fluid rushes over the elements and toward the wall. The ejection events show maximum wall-normal velocity in the separated region behind the elements. The last contour plane also shows the upward ejections of the flow as it approaches the next row of roughness elements from the front. The spanwise mean velocity is shown in Figure 3.33, and there is little new information in these plots except that the spanwise velocity

has larger magnitudes for the sweeping motions.

Figures 3.34 through 3.36 show the conditionally averaged turbulent normal stresses. There is not a significant difference between the sweep and ejection events for these values, except that the sweep events create their maximum normal stresses around 2/3 of the roughness height, while the ejections create maximum normal stresses just slightly below the roughness height. These plots also show that the sweep and ejection events produce similar magnitudes of normal stress levels, as Varano [22] also measured.

The Reynolds shear stresses are provided in Figures 3.37 through 3.39. There is very little difference between the two turbulent events in these cases. The sweep and ejection events produce the same magnitude of shearing stresses.

Figures 3.40 through 3.45 show contours of turbulent triple products conditionally averaged. The $\overline{u^3}$, $\overline{u^2v}$, and $\overline{u^2w}$ terms are equal in magnitude but opposite in sign for the sweep and ejection events. This is a result that Varano [22] also measured. The $\overline{v^3}$, $\overline{v^2u}$, and $\overline{v^2w}$ terms show a similar trend, except that the sweep events create this triple products slightly lower than the ejection events. Varano[22] stated that these triple products based off of $\overline{v^2}$ had larger magnitudes for the sweeping motions, however that was not witnessed in these measurements.

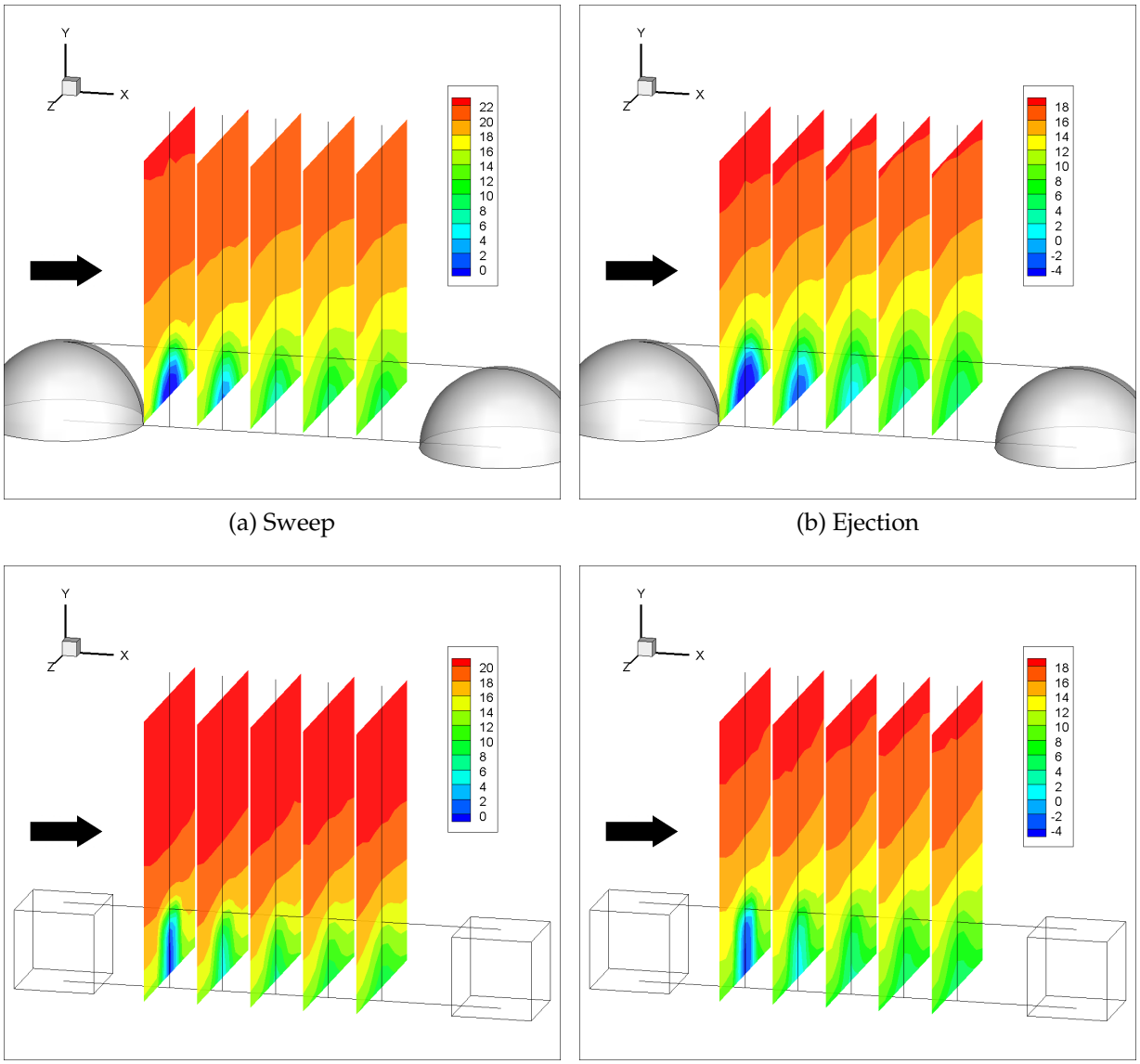

(a) Sweep (b) Ejection

(c) Sweep (d) Ejection

Figure 3.31: Contour plots of mean streamwise velocity for data conditionally averaged to show sweep and ejection events

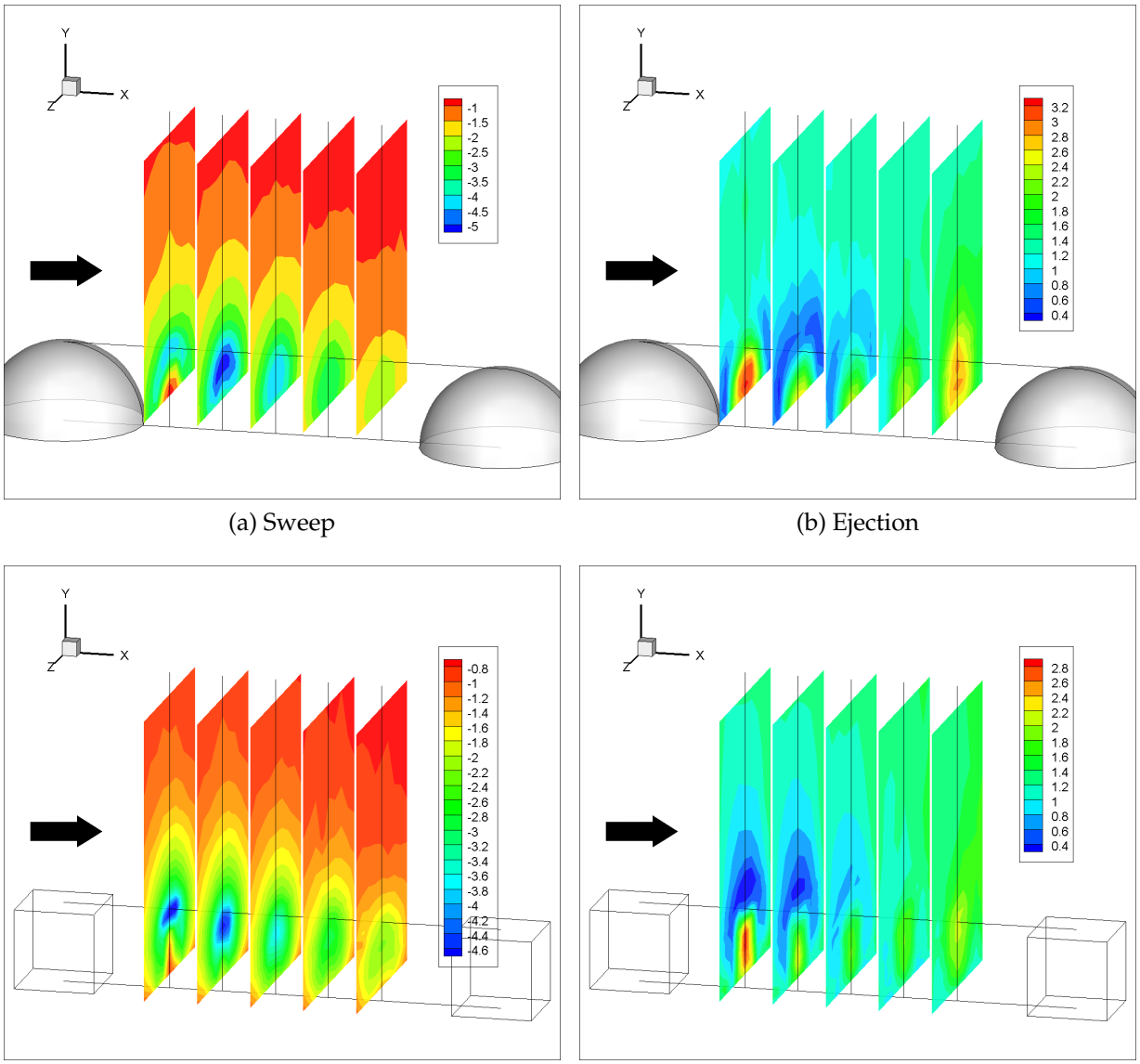

(a) Sweep (b) Ejection

(c) Sweep (d) Ejection

Figure 3.32: Contour plots of mean wall-normal velocity for data conditionally averaged to show sweep and ejection events

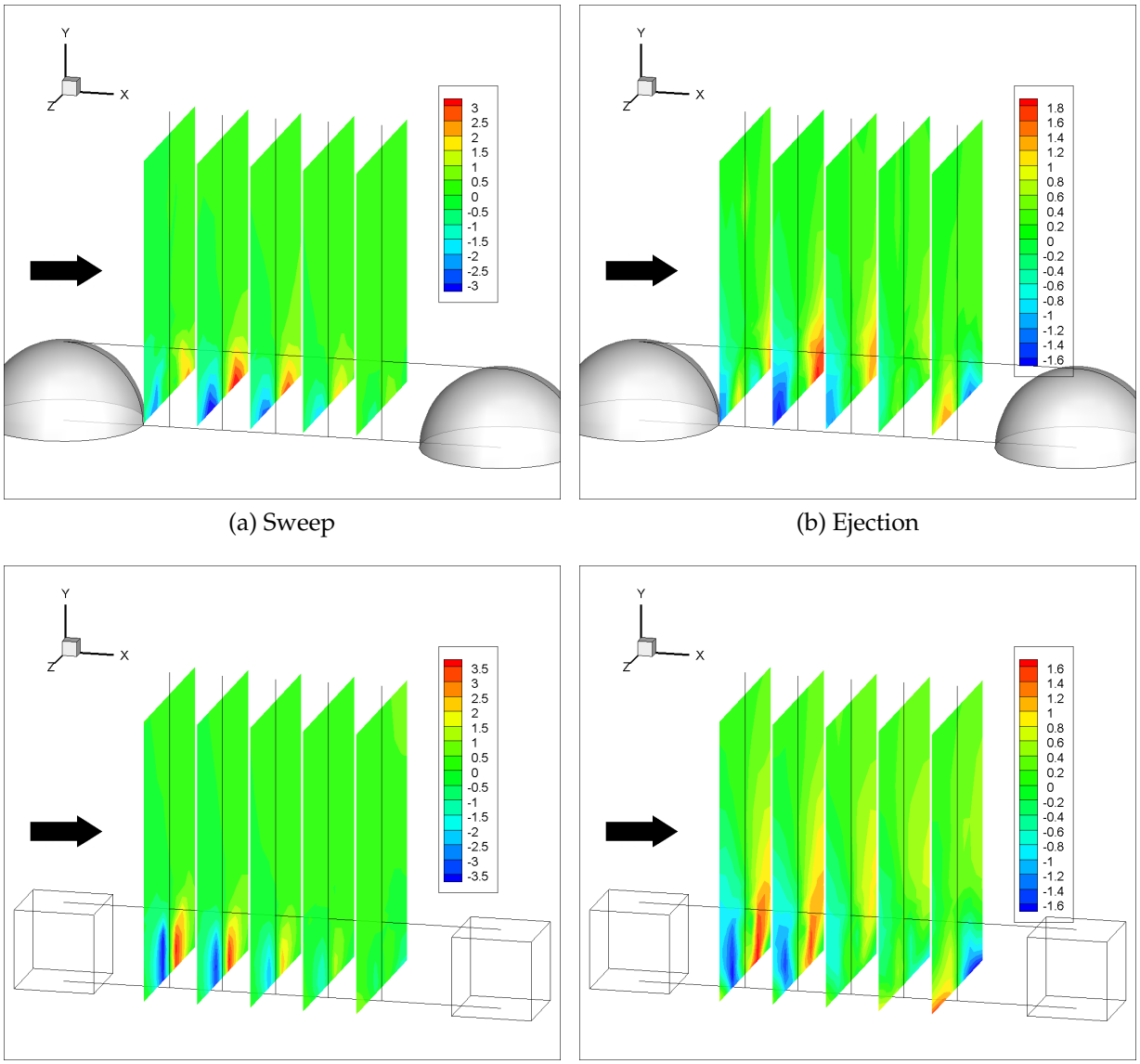

(a) Sweep (b) Ejection

(c) Sweep (d) Ejection

Figure 3.33: Contour plots of mean spanwise velocity for data conditionally averaged to show sweep and ejection events

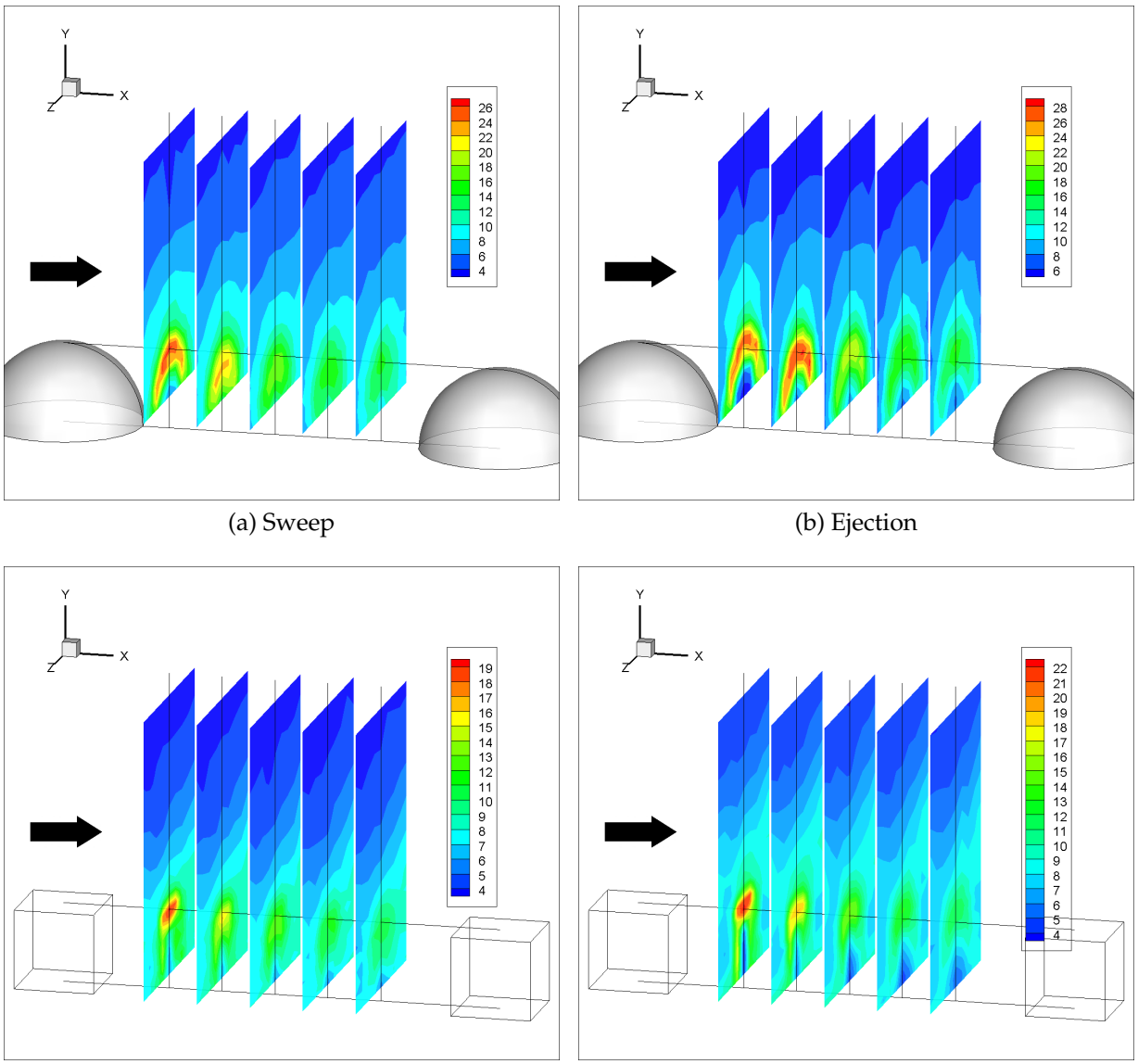

(a) Sweep

(b) Ejection

(c) Sweep

(d) Ejection

Figure 3.34: Contour plots of $\overline{u^2}$ normal stress for data conditionally averaged to show sweep and ejection events

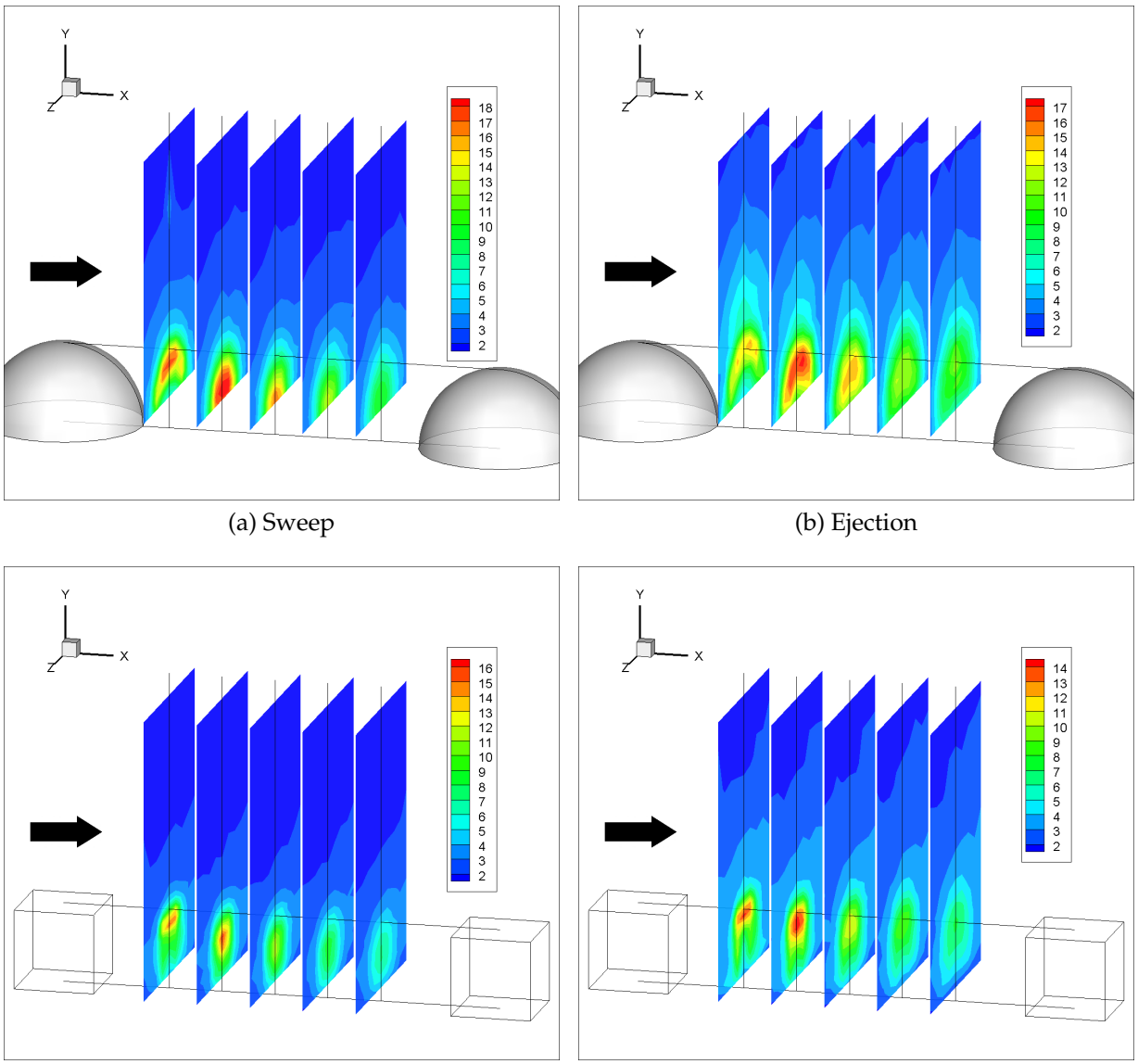

(a) Sweep (b) Ejection

(c) Sweep (d) Ejection

Figure 3.35: Contour plots of $\overline{v^2}$ normal stress for data conditionally averaged to show sweep and ejection events

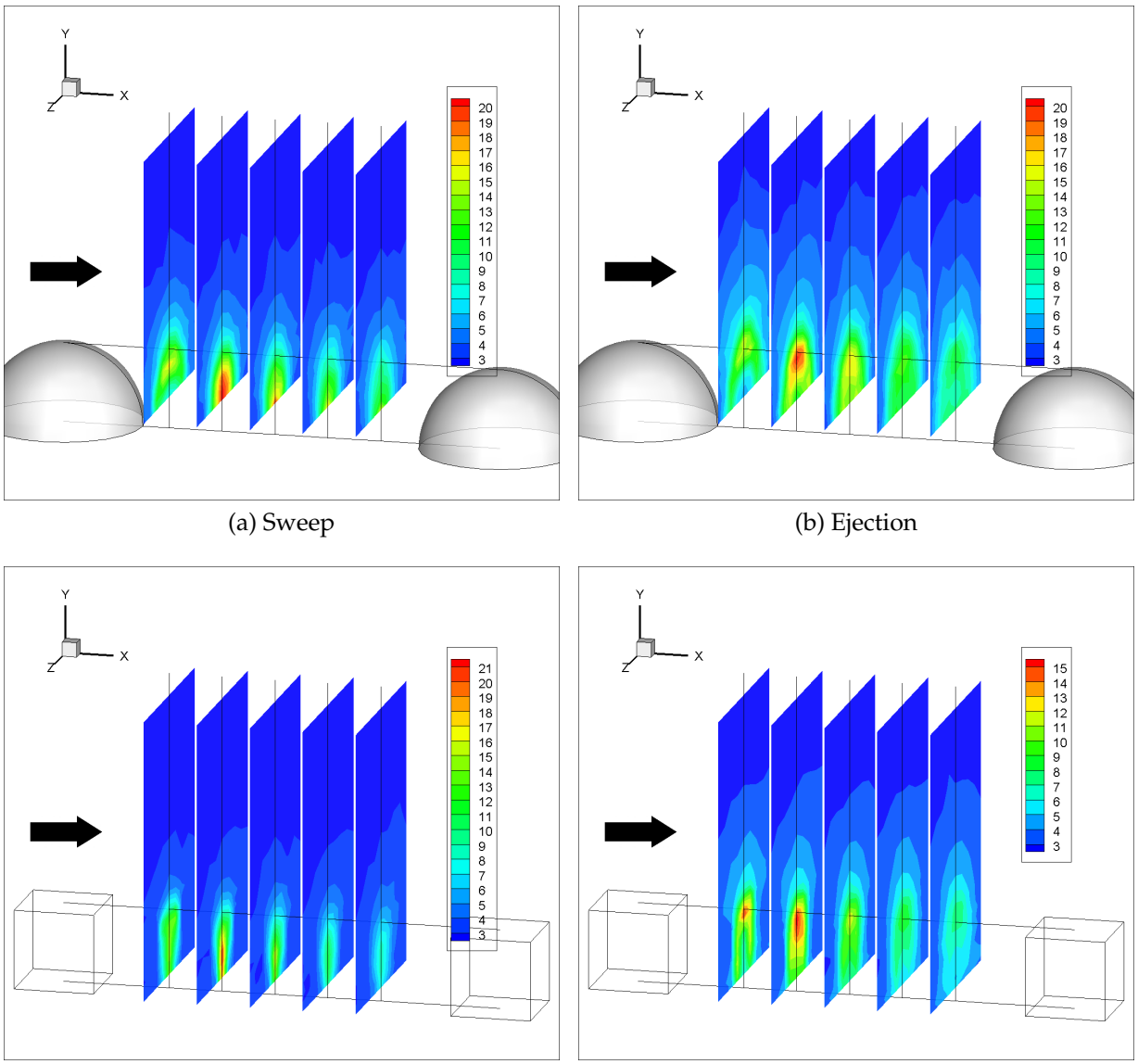

(a) Sweep (b) Ejection

(c) Sweep (d) Ejection

Figure 3.36: Contour plots of $\overline{w^2}$ normal stress for data conditionally averaged to show sweep and ejection events

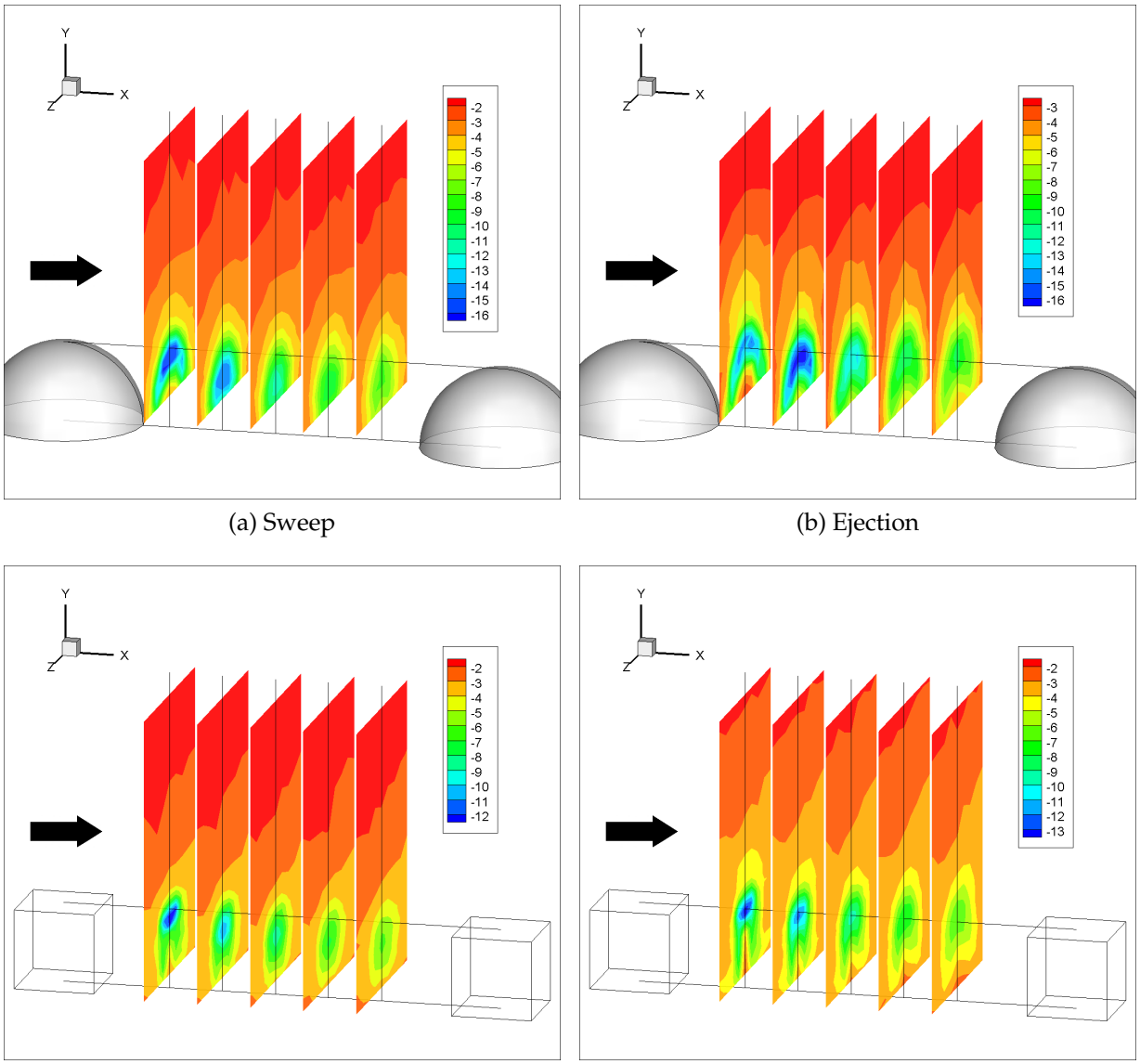

(a) Sweep (b) Ejection

(c) Sweep (d) Ejection

Figure 3.37: Contour plots of $\overline{uv}$ shear stress for data conditionally averaged to show sweep and ejection events

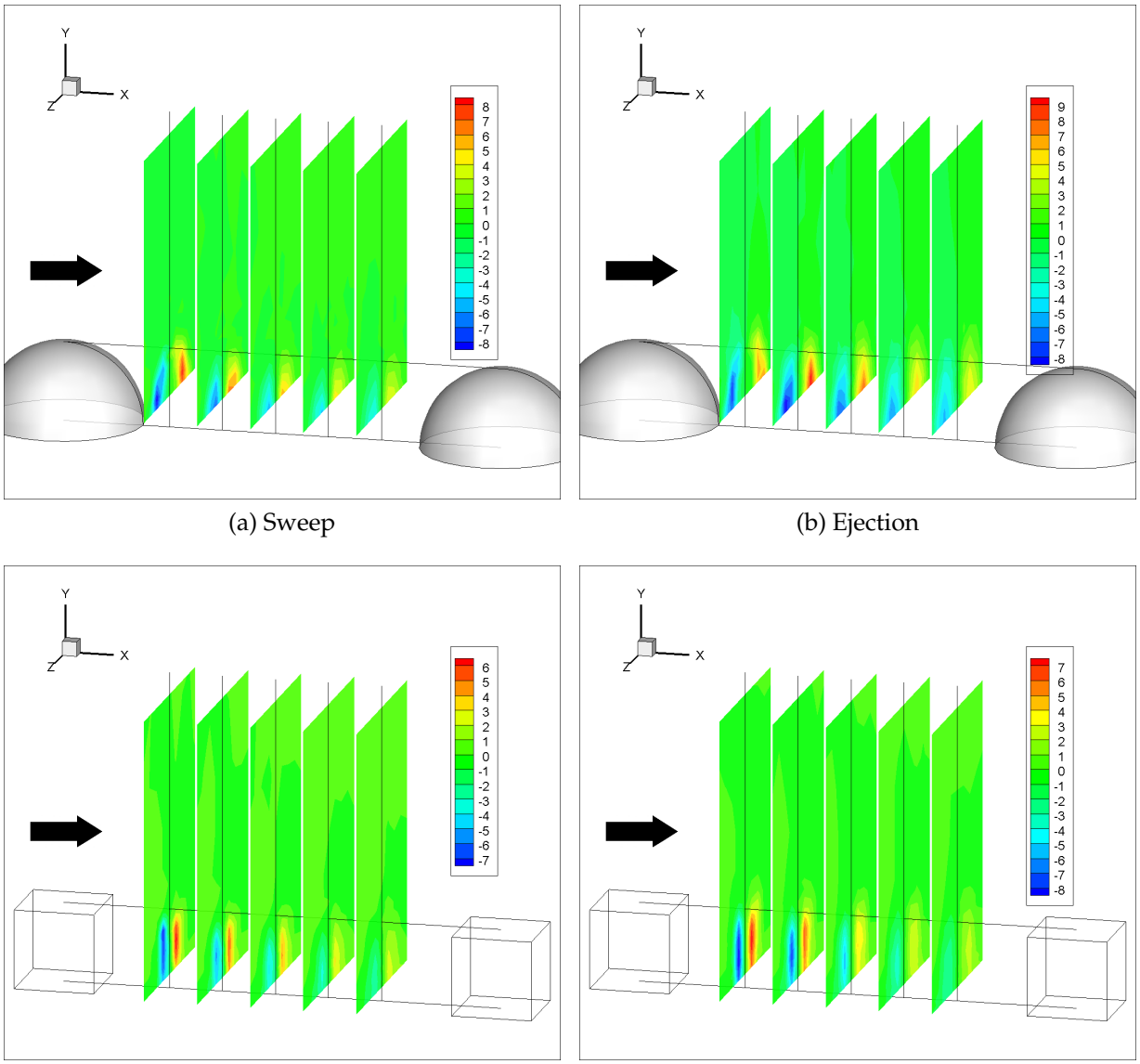

(a) Sweep

(b) Ejection

(c) Sweep

(d) Ejection

Figure 3.38: Contour plots of $\overline{uw}$ shear stress for data conditionally averaged to show sweep and ejection events

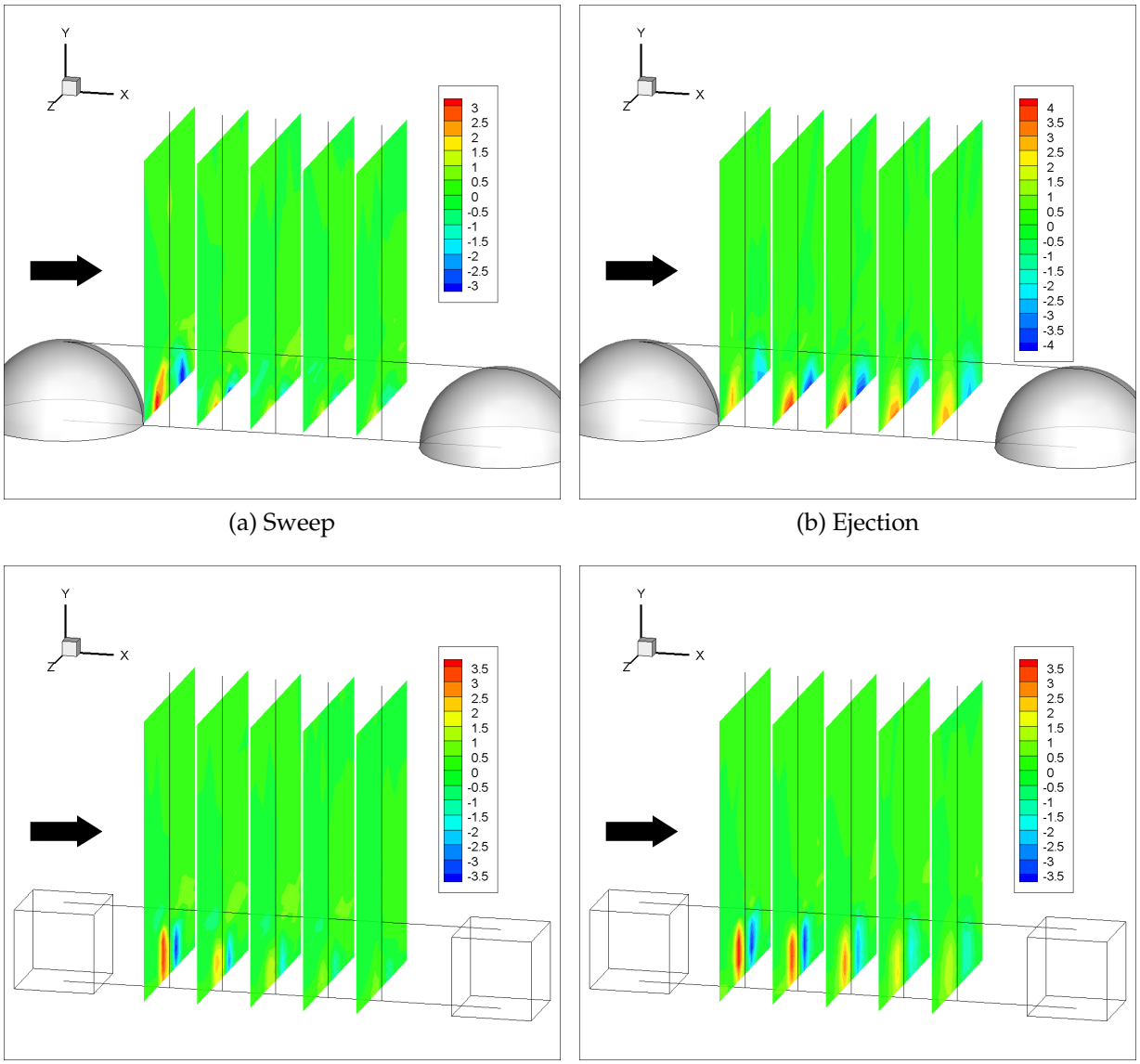

(a) Sweep

(b) Ejection

(c) Sweep

(d) Ejection

Figure 3.39: Contour plots of $\overline{vw}$ shear stress for data conditionally averaged to show sweep and ejection events

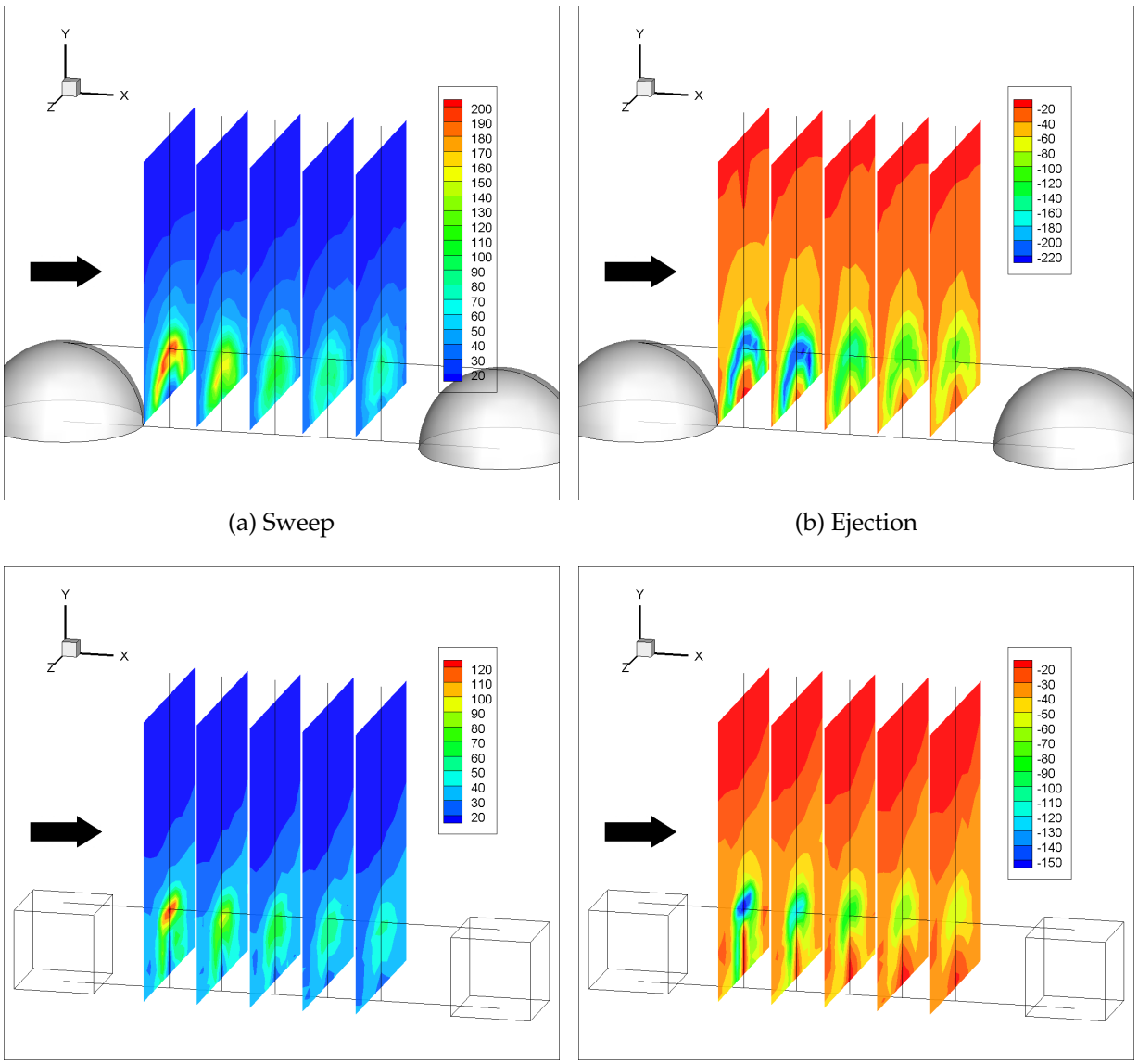

(a) Sweep (b) Ejection

(c) Sweep (d) Ejection

Figure 3.40: Contour plots of $\overline{u^3}$ triple product for data conditionally averaged to show sweep and ejection events

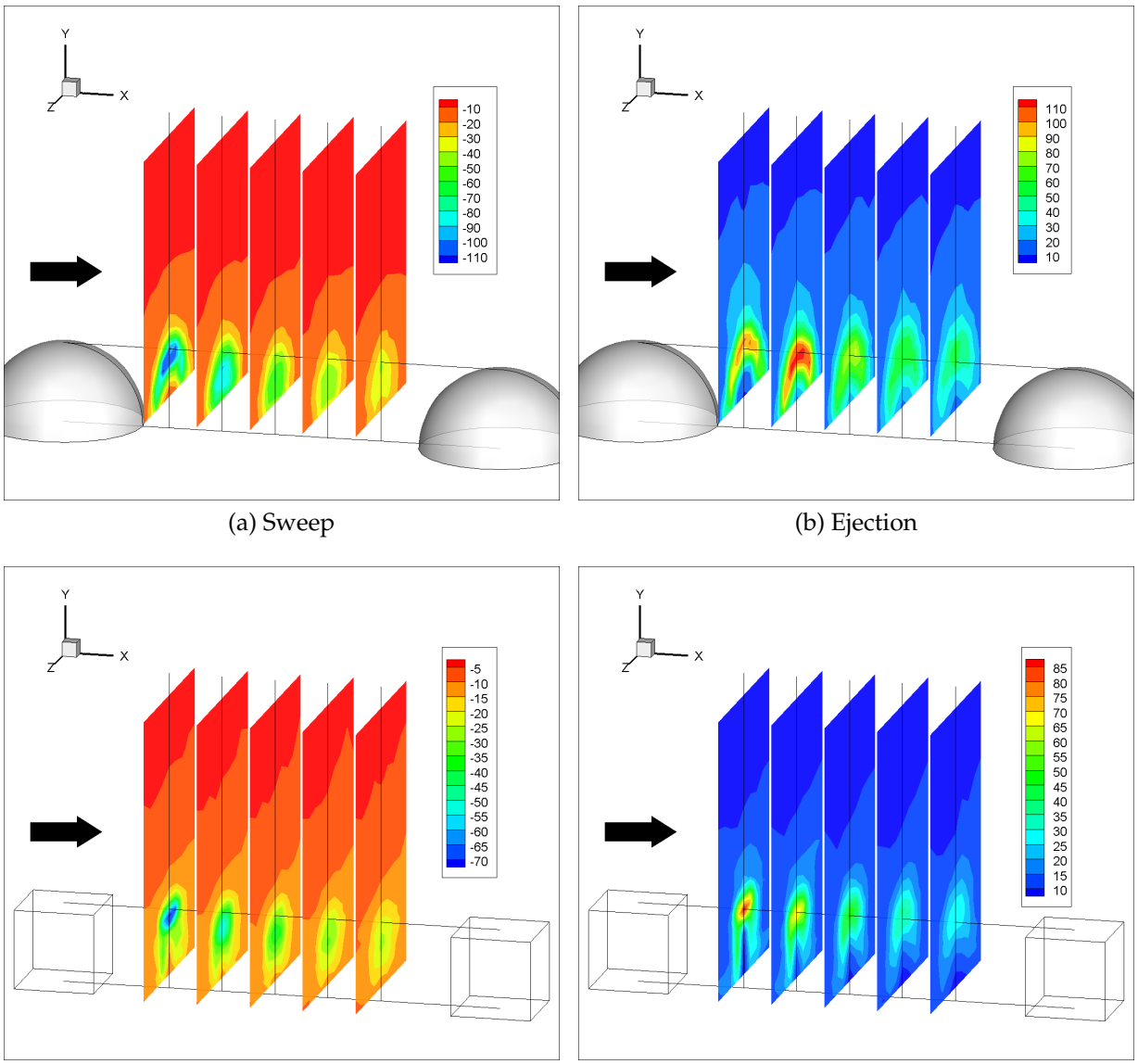

(a) Sweep (b) Ejection

(c) Sweep (d) Ejection

Figure 3.41: Contour plots of $\overline{u^2 v}$ triple product for data conditionally averaged to show sweep and ejection events

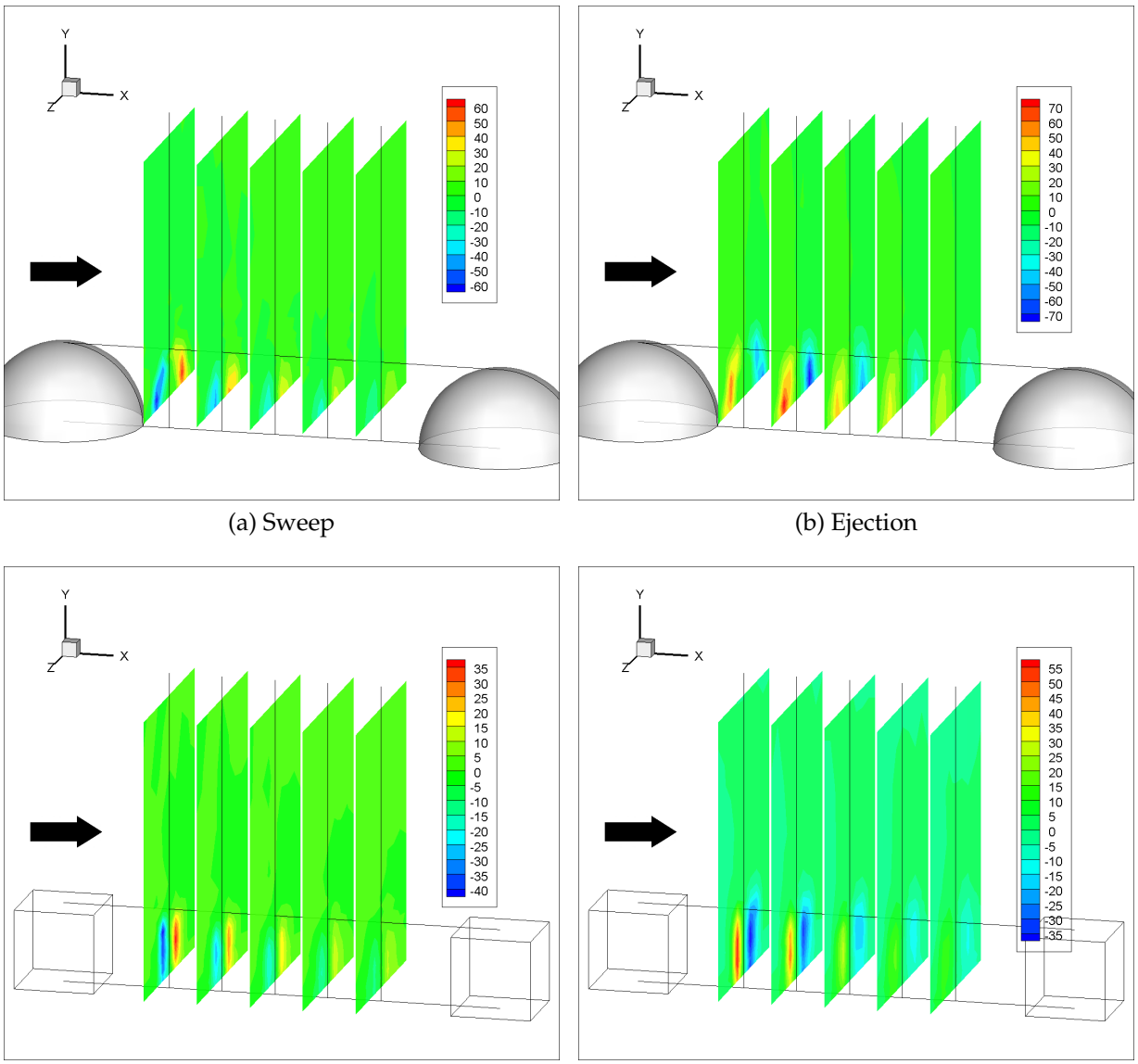

(a) Sweep (b) Ejection

(c) Sweep (d) Ejection

Figure 3.42: Contour plots of $\overline{u^2 w}$ triple product for data conditionally averaged to show sweep and ejection events

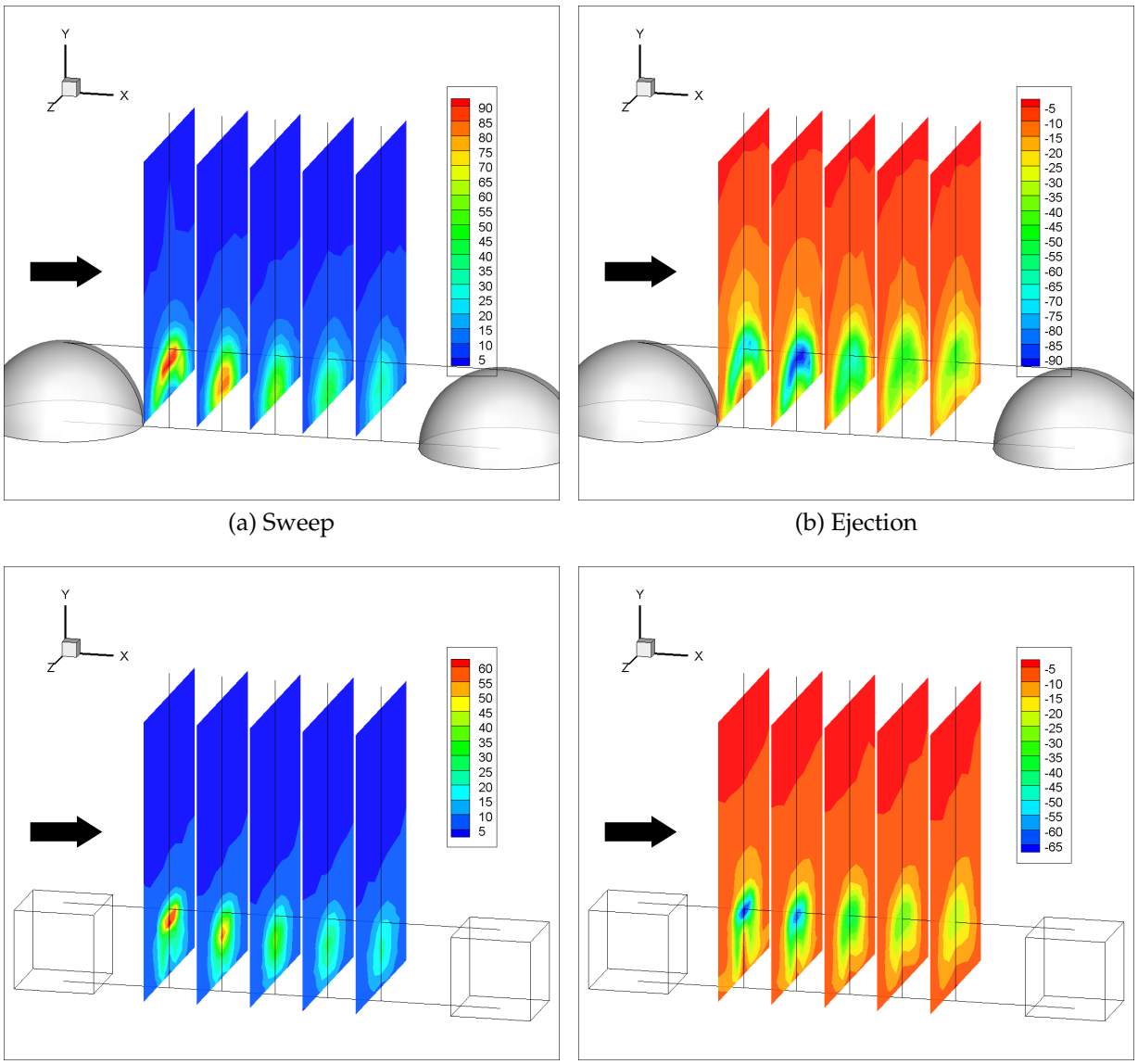

(a) Sweep (b) Ejection

(c) Sweep (d) Ejection

Figure 3.43: Contour plots of $\overline{v^2u}$ triple product for data conditionally averaged to show sweep and ejection events

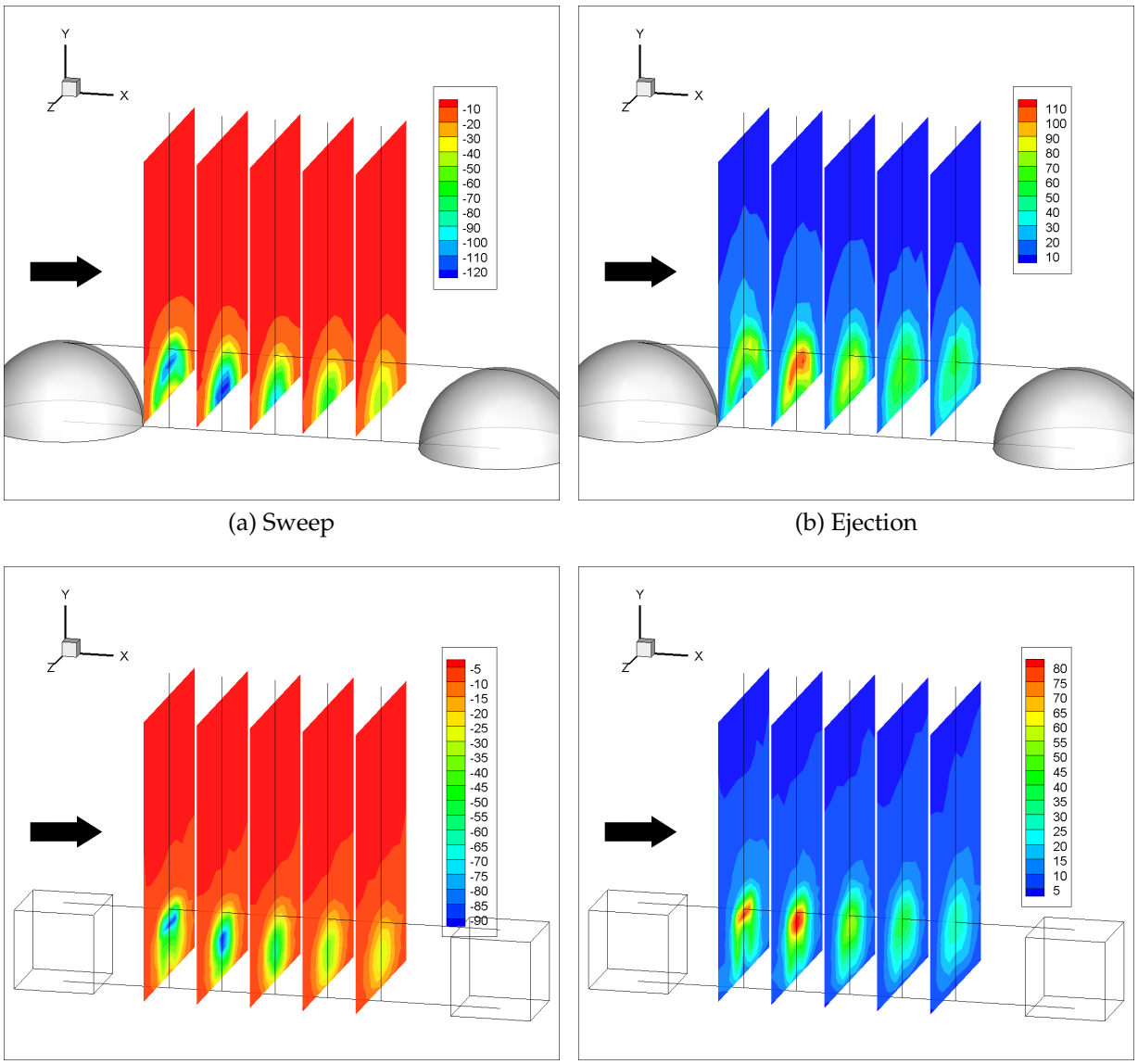

(a) Sweep (b) Ejection

(c) Sweep (d) Ejection

Figure 3.44: Contour plots of $\overline{v^3}$ triple product for data conditionally averaged to show sweep and ejection events

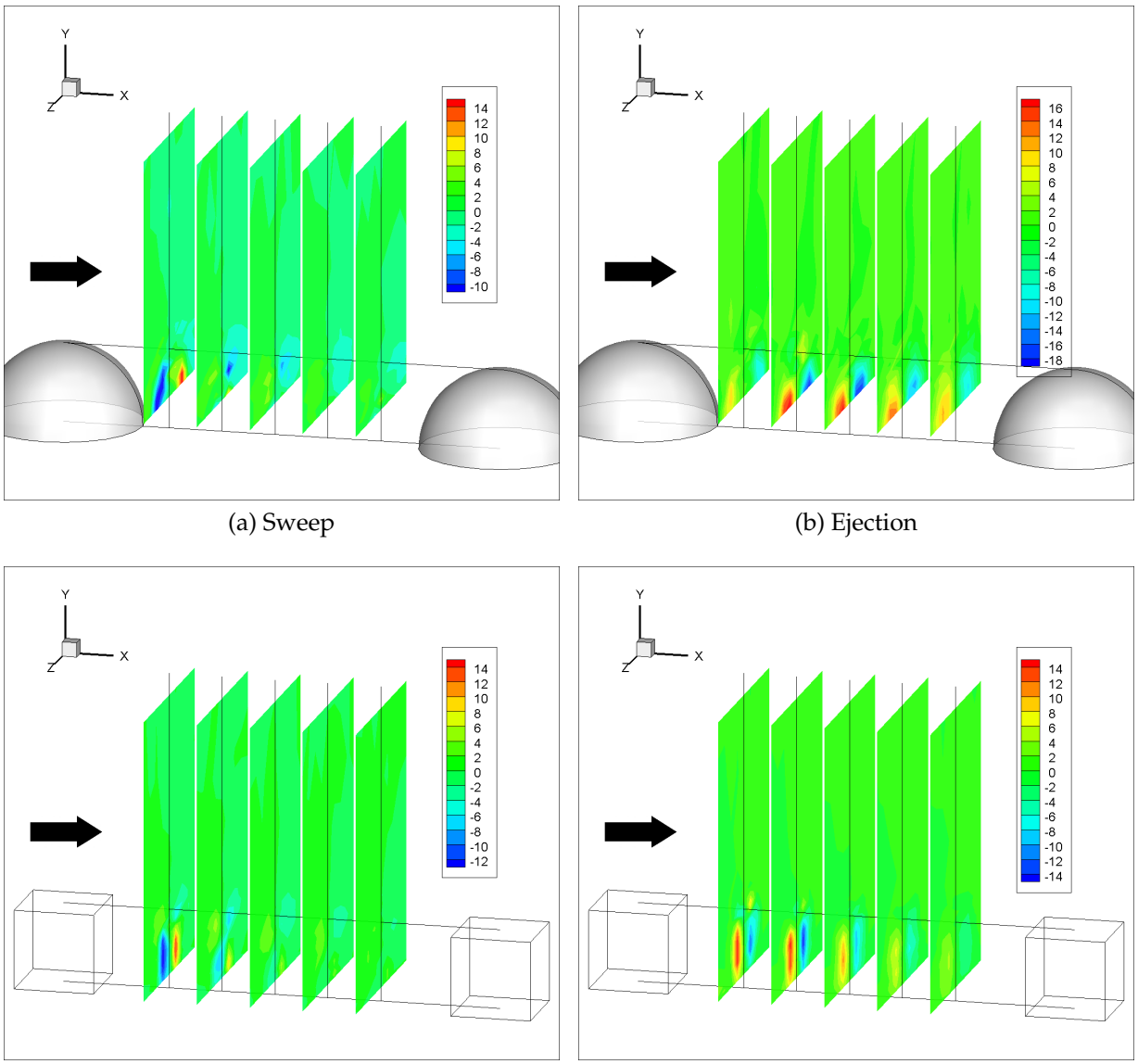

(a) Sweep (b) Ejection

(c) Sweep (d) Ejection

Figure 3.45: Contour plots of $\overline{v^2 w}$ triple product for data conditionally averaged to show sweep and ejection events

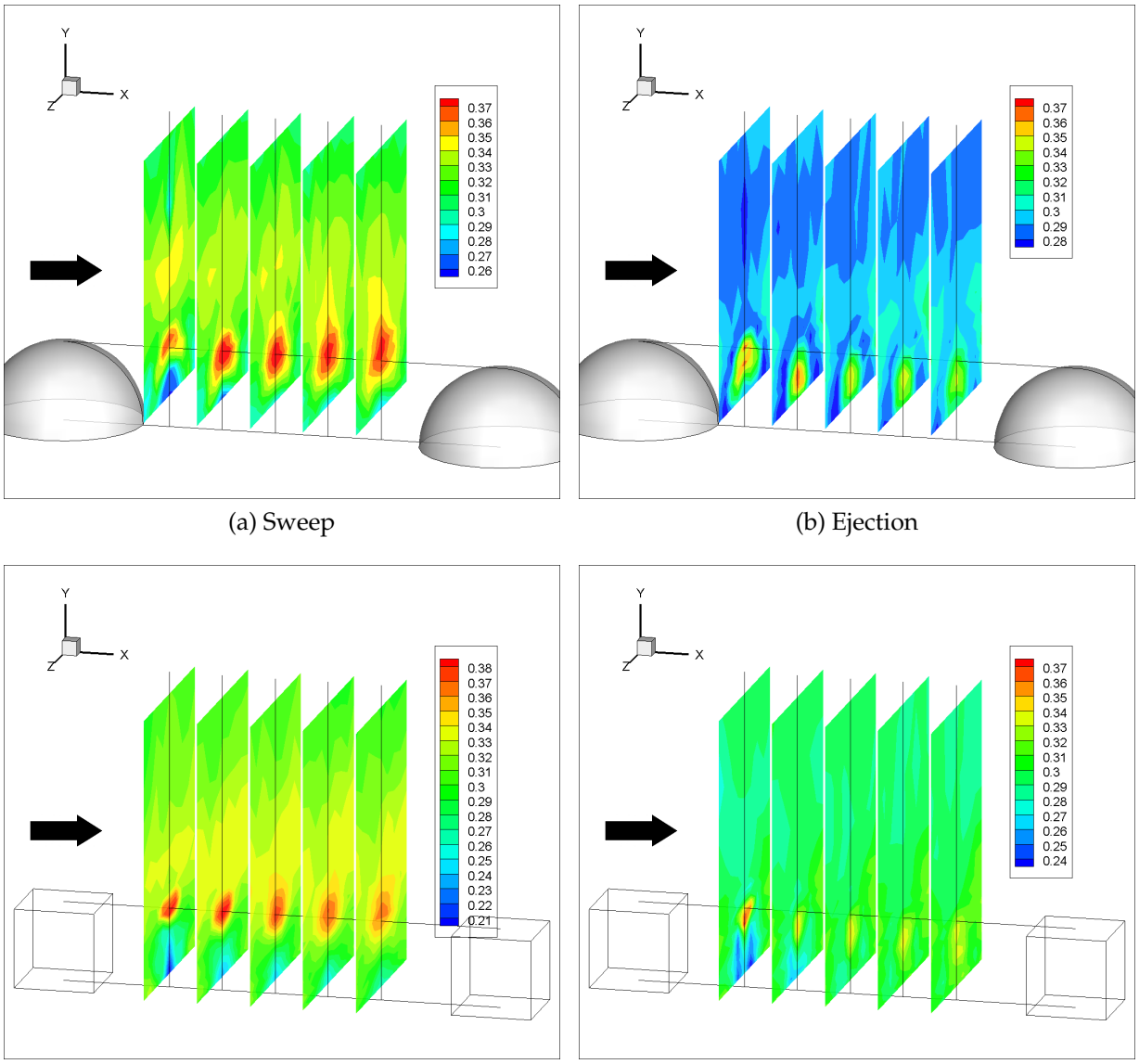

(a) Sweep

(b) Ejection

(c) Sweep

(d) Ejection

Figure 3.46: Contour plots of the percentage of event occurances for data conditionally averaged to show sweep and ejection events

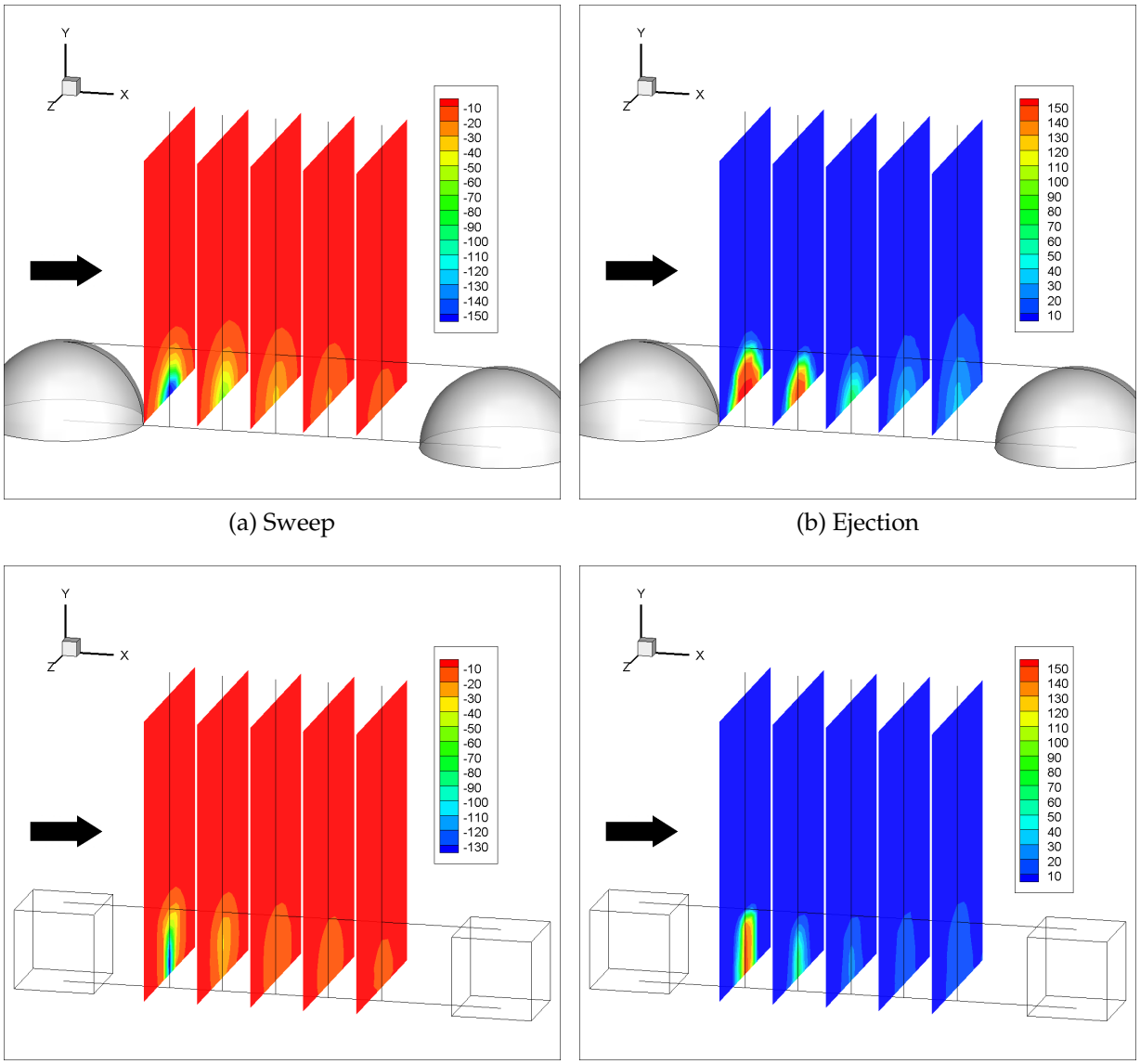

(a) Sweep (b) Ejection

(c) Sweep (d) Ejection

Figure 3.47: Contour plots of mean flow angle ($\tan^{-1}(V/U)$) for data conditionally averaged to show sweep and ejection events

3.2.6 Turbulent Kinetic Energy

The turbulent kinetic energy (TKE) of the flow is shown In Figure 3.48. The turbulent kinetic energy is calculated as half the sum of the Reynolds normal stresses, or TKE = $\frac{1}{2}(\overline{u^2} + \overline{v^2} + \overline{w^2})$. High levels of TKE are measured just below the element height approximately 6 mm downstream of both the cubical and hemispherical roughness elements. As seen in George and Bennington's data, the TKE diffuses outward in a radial direction as it progresses along in the streamwise direction. The hemisphere produces a larger amount of TKE due to its larger frontal area. The production of TKE is due to both horseshoe vortices sweeping fluid toward the wall and the shear layers created by the separated region mixing with the flow rushing over the tops of the elements. Again, as noted in previous turbulence measurements, it appears that the sixth row cube produces just slightly less turbulence levels than the first row, while the sixth row hemisphere produces nearly 25% less turbulence than its first row counterpart.

The dominant term in the production of turbulent kinetic energy is $\overline{-uv}\frac{dU}{dy}$. This value is plotted in Figure 3.49. As in the case with the Reynolds shear stress production term, the TKE production term shows extremely large values just 4 mm downstream of the element and at the height of the element for both cases. This large value is due to the velocity gradient dU/dy being large where the separated region meets the flow rushing over the top of the element. A large production term immediately behind the element translates to high TKE levels downstream. Turbulent diffusion from the location of TKE production leads to large amounts of TKE just downstream of the location of production. The regions of large TKE production are small in comparison to other turbulence values that have been studied. The cubical case is just a small point of large production at the roughness height. The production region behind the hemisphere is larger than that of the cube, but it is still smaller than regions associated with other types of turbulence.

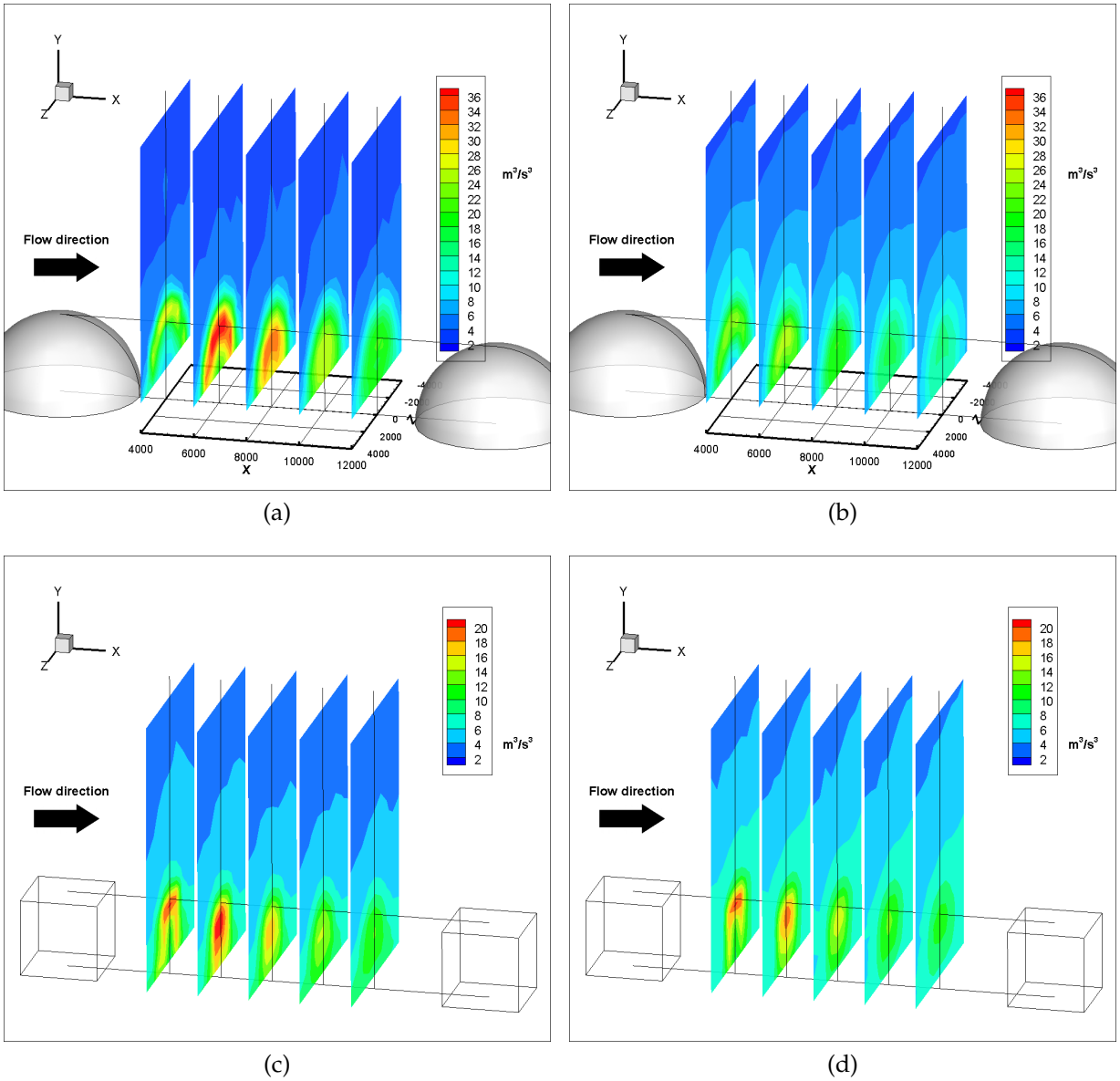

Figure 3.48: Contour plots of turbulent kinetic energy behind: (a) first row of hemispheres; (b) sixth row of hemispheres; (c) first row of cubes; and, (d) sixth row of cubes

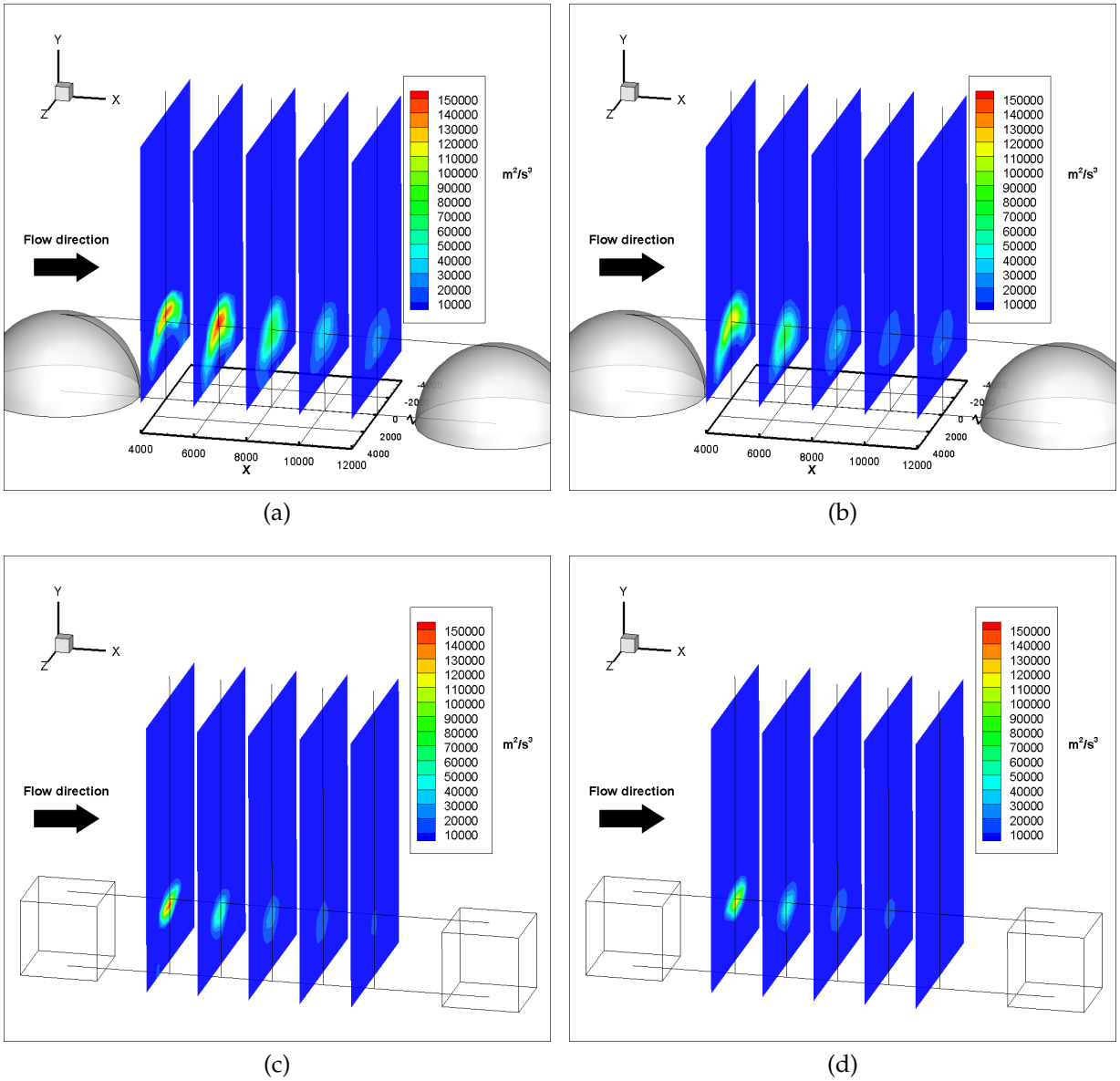

Figure 3.49: Contour plots of turbulent kinetic energy production behind: (a) first row of hemispheres; (b) sixth row of hemispheres; (c) first row of cubes; and, (d) sixth row of cubes

3.2.7 Vorticity

To analyze the production of horseshoe vortices created at the base on the roughness elements, the streamwise vorticity is plotted in Figure 3.50. The vorticity of a flow, and the stream-wise component, are defined as:

$$\vec{\Omega} = curl\vec{V} = \begin{vmatrix} e_x & e_y & e_z \\ \partial/\partial x & \partial/\partial y & \partial/\partial z \\ U & V & W \end{vmatrix} \tag{3.1}$$

$$\vec{\Omega_x} = \frac{\partial W}{\partial y} - \frac{\partial V}{\partial z} \tag{3.2}$$

The space between the measurement points was finely interpolated and differentiated using the Tecplot 360 program.

The contour plots behind the cube elements depict the formation of the horseshoe vortices better than the hemisphere element plots. This is due to the measurement locations being closer to the wall for the cubical roughness patch as well as the reduced width of the element itself. The horseshoe vortices are present for the hemishperical case are present outside the width of the measurement volume.

For the cubical roughness patch, the horseshoe vortices show up just at the bottom outside corners of the contour plots. The direction of their vorticity implies that fluid is traveling toward the wall and closer to the centerline of the element. A portion of the large negative mean wall-normal V velocities can be attributed to the rotation of the horseshoe vortices located behind the elements. The cubical elements are particularly good at forming the horseshoe vortices. In Bennington's[5] work, he found that his two cubical cases produced the largest horseshoe vortices.

The strength of the horseshoe vortices dissipate as they move downstream. Their proximity to wall creates an 'image' vortex that forms directly above the wall. Due to image vortex, as well as proximity to the wall in general, the viscosity of the fluid plays a large role in dissipating the strength vortices.

Flow behind the sixth row of cubes shows that horseshoe vortices due form on each row of elements; however, the strength of the vortices formed downstream are less than that created by the first row of elements. This is a result that Yang and Wang[23] observed in their LES study. For their study, the cubes produced the highest strength horseshoe vortices. These vortices stuck close to the sides of the cubes as the moved downstream and behind the elements. The horseshoe vortices created by the hemispheres and cylinders in Yang's work were smaller in magnitude and traveled further outward in the spanwise direction. The horseshoe vortices behind the hemispheres of the current study are not visible in the contour plots.

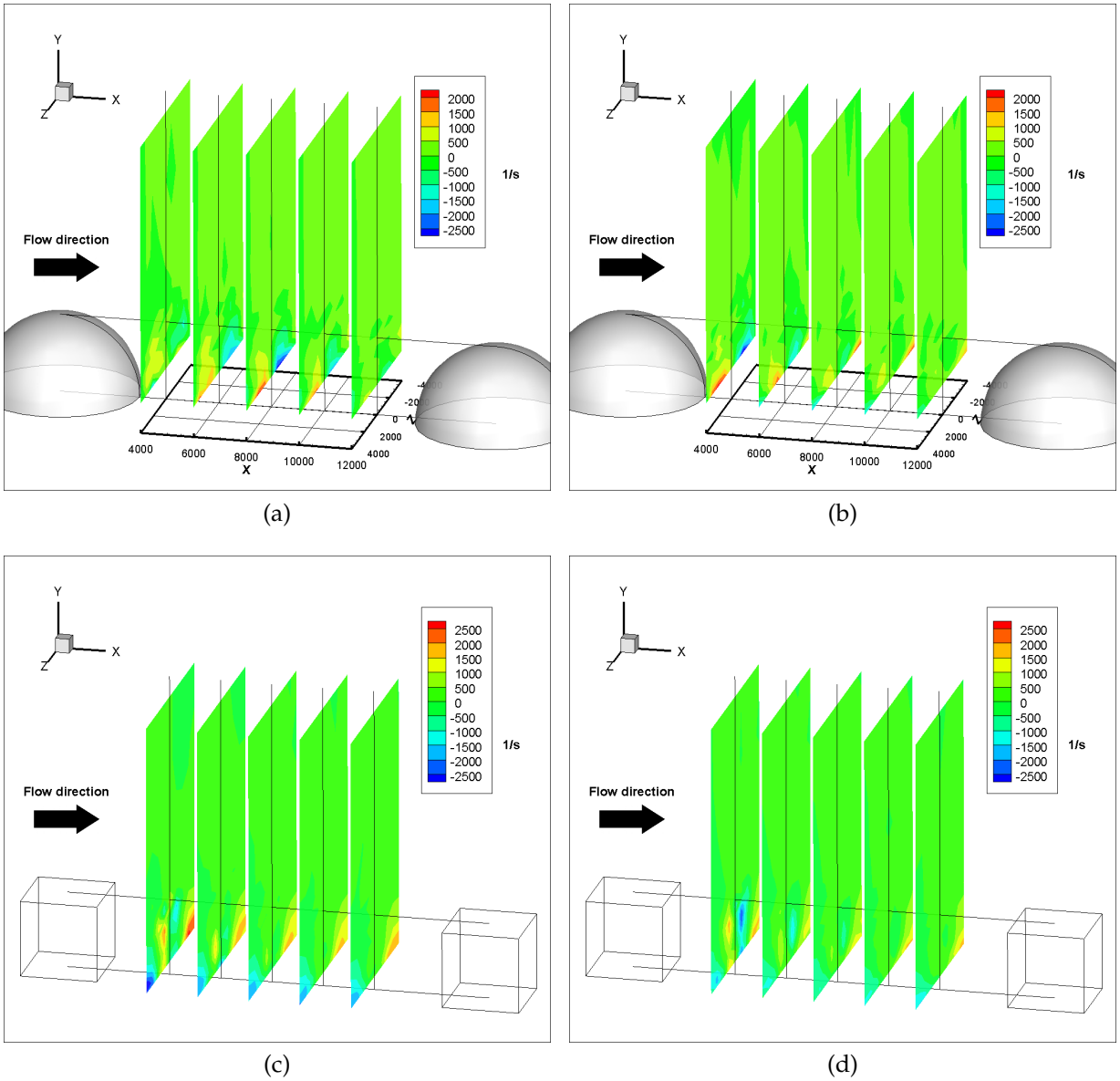

Figure 3.50: Contour plots of vorticity behind: (a) first row of hemispheres; (b) sixth row of hemispheres; (c) first row of cubes; and, (d) sixth row of cubes

3.3 Velocity Spectra

Velocity spectra' measurements were made on the cubical roughness patch behind the first and sixth row of elements. The velocity frequency spectrum is defined as:

$$E_{ij}(\omega) = \frac{1}{\pi}\int_{-\infty}^{\infty} R_{ij}(\tau)exp(-i\omega\tau)d\tau \tag{3.3}$$

Where $R_{ij}(\tau)$ is a time delay correlation between u_i and u_j. Kolmogorov's (1941) theory states that as energy of large eddies is transferred to smaller and smaller ones, the time scales of the large wave numbers (smaller eddies) must be much smaller than the time scales of the larger energy-containing eddies. So much so that the motion of the large wavenumber eddies is considered close to an equilibrium state. This leads to "Kolomogorov's 5/3 law", which states that there is an inertial subrange of the energy spectrum where the cascade of energy is uniquely determined by the wavenumber scale k and the energy dissipation rate ϵ_0. The formula for this is:

$$E(k) = C\epsilon_0^{2/3}k^{-5/3} \tag{3.4}$$

This -5/3 region is apparent in many turbulent boundary layer flows, and a line with that slope is plotted below on the energy spectra plots below. Lumley [12] derived a similar theory to Kolomogorov's for the Reynolds shear stress energy spectrum. His result is of the form:

$$E(k) = -CS\epsilon_0^{1/3}k^{-7/3} \tag{3.5}$$

A -7/3 slope line is plotted below on the Reynolds shear stress plots for comparison. The coherency of the velocity spectra data can be computed to correlate the turbulent motions of the flow and the production of shear stresses over the range of frequencies that are

measured. The formula for the coherency of the Reynolds shear stress energy spectrum is:

$$\gamma_{uv}^2 = \frac{\mid E_{uv} \mid^2}{E_{uu}E_{vv}} \tag{3.6}$$

The coherency is a function that ranges from 0 to 1. A low coherency near 0 signifies that the turbulent energy at that frequency range is uncorrelated and not producing a significant amount of stress. This information is important to know when attempting large eddy simulation studies, as uncorrelated turbulence at higher frequencies can be modeled instead of simulated.

The first set of plots presented in Figures 3.51-3.54 are measured directly behind the cubical element an equal distance between the rows, that is 8.25 mm behind the center of the element. Measurements were made at y locations of 1.5, 3, 4.5, 7.5, 12, and 18 millimeters above the wall surface. After making these measurements behind the first and sixth rows of data, more measurements were made at locations that exhibited very large turbulence when examining the local flow contour plots. Additional measurements were made 4 mm behind the element at a height of 3 mm, and 6 mm behind the element at heights of 2 and 3 mm. These results are presented to analyze the velocity spectra energy at areas of extremely large turbulence.

The energy spectra for the streamwise normal stress is presented in Figure 3.51. The locations below, at, and slightly above the roughness element show higher levels of energy at the higher frequencies compared to the flow further out in the boundary layer. The flow behind the first cube shows a similar amount of energy for y locations of 1.5 and 3 mm. The locations higher in the boundary layer, experiencing mostly freestream flow, show a good agreement with the -5/3 decay rate.

There is significant difference between the first point and sixth point measurements. The energy at the height of the roughness element, 3 mm, appears the same in both cases.

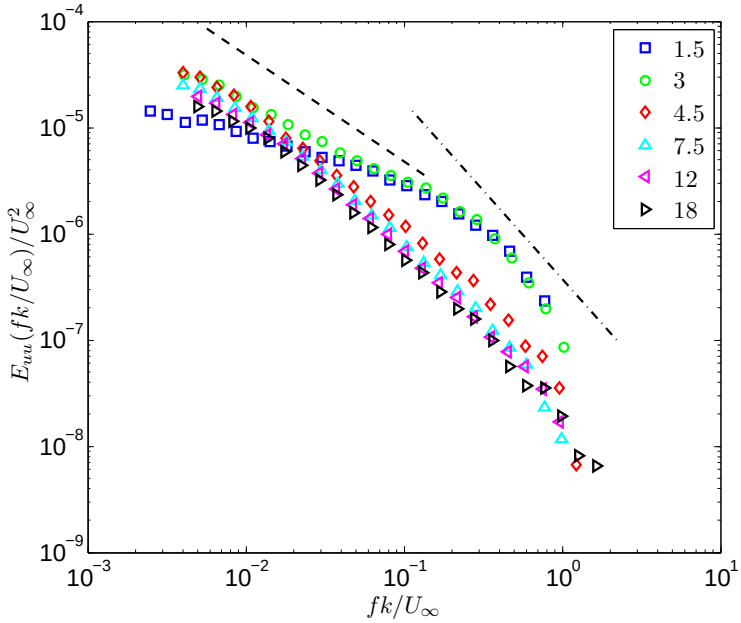

(a)

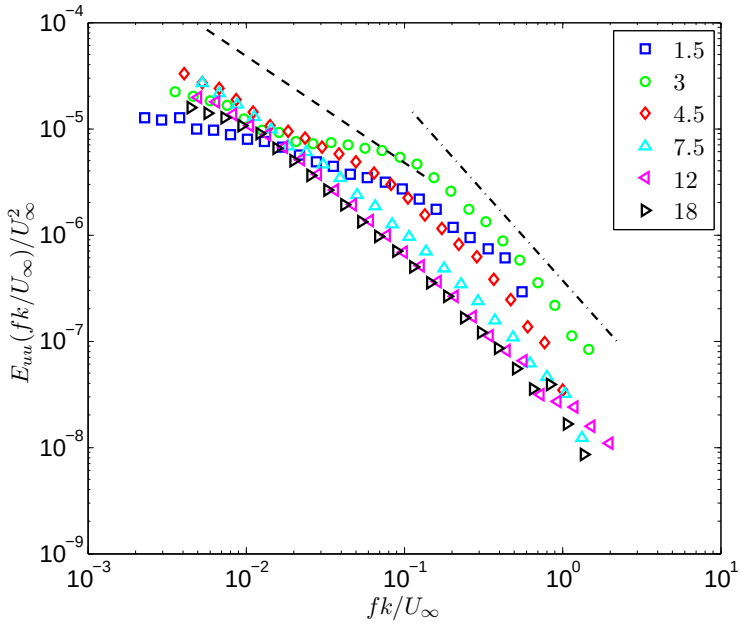

(b)

Figure 3.51: Energy spectra for streamwise normal stress. The dashed lines are slopes of f^{-1} and $f^{-5/3}$. The plots show measurements behind: (a) first row; and, (b) sixth row. The legend shows measurement locations in distance above the wall, y (mm).

However, the energy below the element height, at 1.5 mm, has decreased after the sixth row compared to the first. The energy at y locations of 4.5 mm and 7.5 mm has increased as the flow travels over the roughness patch. Smaller eddies produced behind the elements have convected and ejected upward into the boundary layer, causing this increase in energy above the element height. The energy below the element height has reduced likely due to the decleration of the flow and production of less turbulence behind the sixth row element as compared to the first row.

The energy spectra for the wall-normal normal stress is presented in Figure 3.52. For the first row, the location below the element height at 1.5 mm produces the largest amount of energy across the spectrum. The energy peaks near $fk/U_\infty \approx 0.1$ and decays after that point. The flow at 3 mm follows a similar trend, but the magnitude is significantly less. The energy spectra for points above the element are similar in magnitude. It appears that the 4.5 mm and 7.5 mm locations have less energy at lower frequencies than the flow higher in the boundary layer.

The flow behind the sixth row cube appears similar to the first row. The 1.5 and 3 mm points have lost some overall energy as compared to the first row. The 4.5 mm location has increased energy at higher frequencies, which is similar to that observed in the streamwise normal stress energy spectrum. The energies at all locations appear to decay at a rate near -5/3 at the higher frequencies.

The energy spectra for the spanwise normal stress is presented in Figure 3.53. Behind the first row, the spanwise normal stress energy is largest below the element height at 1.5 mm. This energy peaks at a frequency of $fk/U_\infty \approx 0.07$ and quickly decays after that. The flow at 3 mm does not show the same significant peak, but does contain elevated energy across the spectrum. At the higher frequencies, the 1.5 and 3 mm locations have similar magnitude of energy. The four locations above the element height all appear very similar across the energy spectrum, which the 4.5 mm location having just slightly elevated energy levels at higher frequencies.

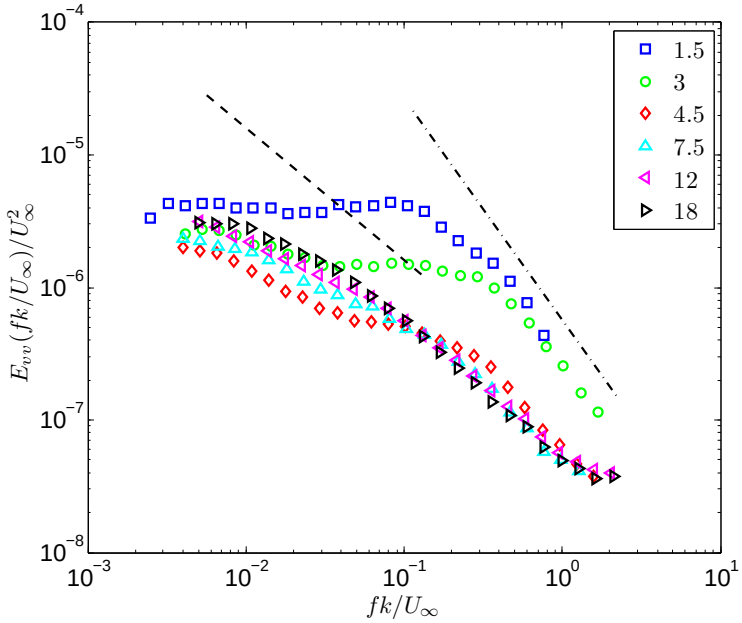

(a)

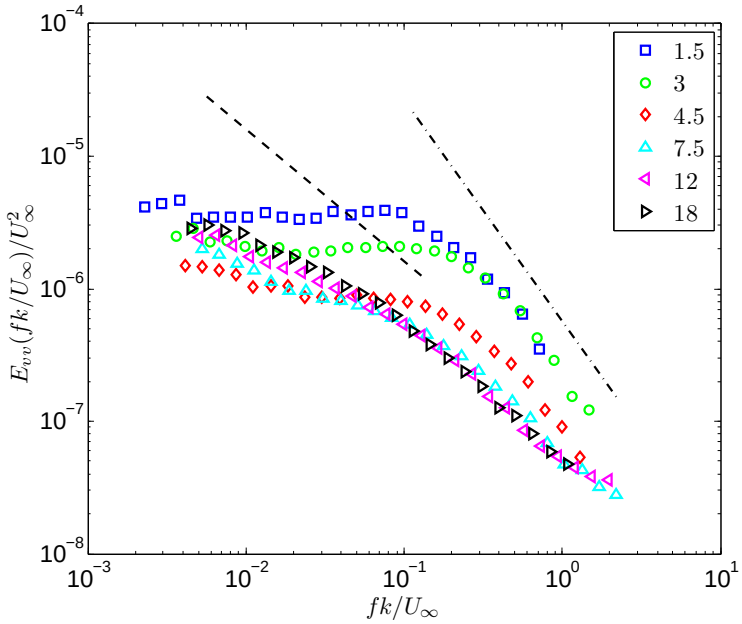

(b)

Figure 3.52: Energy spectra for wall-normal normal stress. The dashed lines are slopes of f^{-1} and $f^{-5/3}$. The plots show measurements behind: (a) first row; and, (b) sixth row. The legend shows measurement locations in distance above the wall, y (mm).

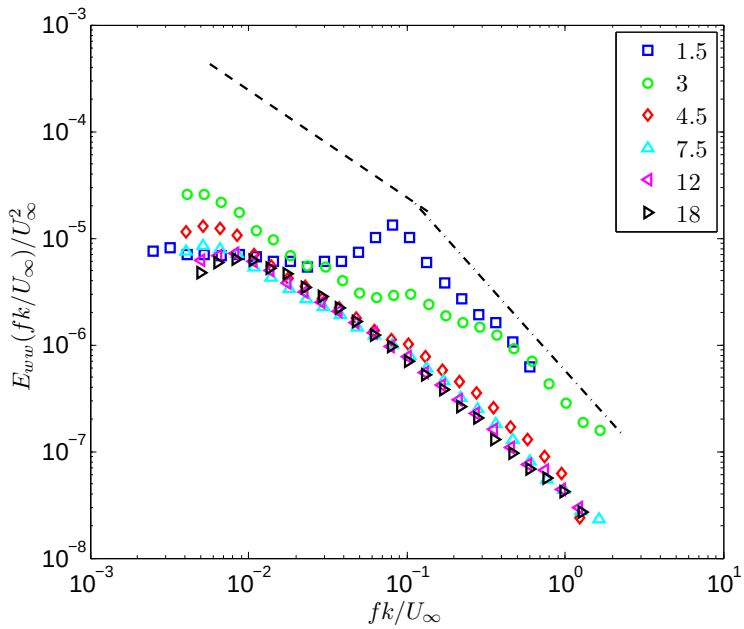

(a)

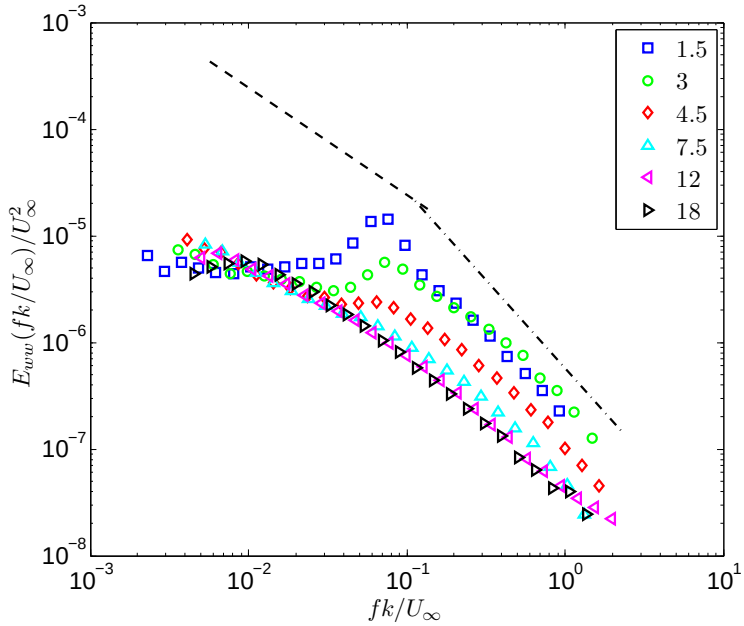

(b)

Figure 3.53: Energy spectra for spanwise normal stress. The dashed lines are slopes of f^{-1} and $f^{-5/3}$. The plots show measurements behind: (a) first row; and, (b) sixth row. The legend shows measurement locations in distance above the wall, y (mm).

The sixth row energy spectra for the spanwise normal stress show the same peak energy level that was witnessed behind the first row. This peak behind the sixth row has the same magnitude as the first row and is also located at $fk/U_\infty \approx 0.07$. The 3 mm location also begins to show a peak energy in this region, though lower in magnitude than the 1.5 mm location. The energy has increased for the 4.5 and 7.5 mm locations at higher frequencies as the eddies are ejected up into the boundary layer. The locations behind the first and sixth row appear to decay at a rate close to -5/3 for the spanwise normal stress.

The peak in the spanwise normal stress at $fk/U_\infty \approx 0.07$ is a feature that Lowe[11] also witnessed. He observed this unsteady motion at $fk/U_\infty \approx 0.05$, and used the work of George[7] to explain a possible reasoning behind this. He states that this peak of energy at a specific frequency is due to the intense mean vortex structure that is shed from the top of a large roughness element. George labeled this the roughness top vortex structure (RTVS), and the two legs of this structure coming from either side of the element fluctuate between pulling fluid momentum from the wall and the separated region.

The energy spectra for the Reynolds shear stress is presented in Figure 3.54. For the first row, the shear stress energy level is much higher at the 1.5 and 3 mm locations. Both locations show a similar energy level across the spectrum. The four locations above the element height show similar energy levels at frequencies less than $fk/U_\infty \approx 0.03$, but then diverge at higher frequencies. The energy of the Reynolds shear stress decreases as the measurement location moves further from the wall. The energy levels behind the first row appear to decay at a slightly slower rate than the -7/3 slope line.

Behind the sixth row, there is a distinct difference between all six measurement locations. The energy level right at the roughness height, 3mm, is higher across the entire frequency spectrum. The 1.5 mm location has the next highest energy level, and has decreased slightly from the levels it contained behind the first row. The 4.5 mm location has significantly increased its Reynolds shear stress energy across the entire spectrum. It near contains the same amount of energy as the flow beneath the roughness height. Similarly,

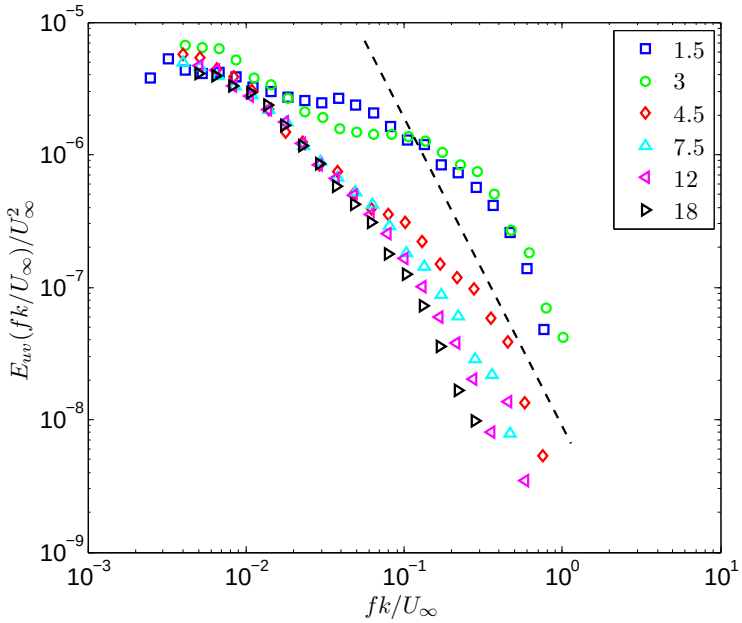

(a)

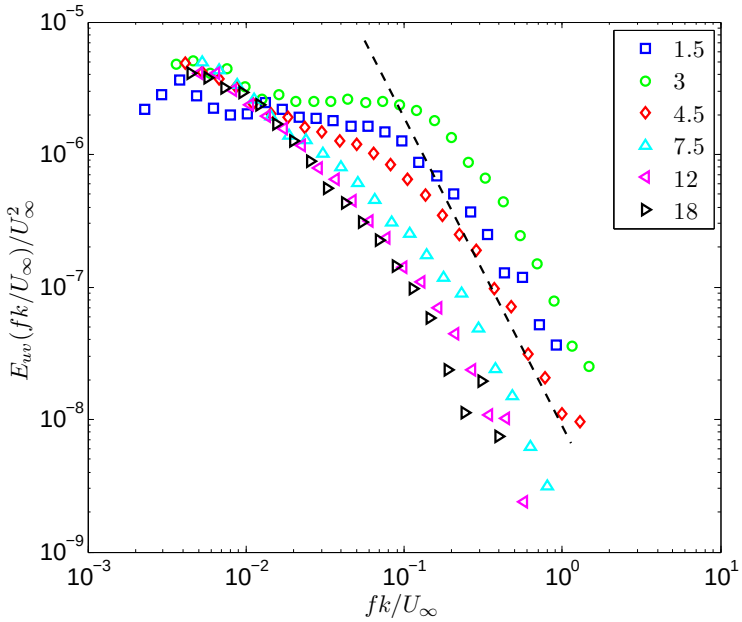

(b)

Figure 3.54: Energy spectra for Reynolds shear stress. The dashed line is slope of $f^{-7/3}$. The plots show measurements behind: (a) first row; and, (b) sixth row. The legend shows measurement locations in distance above the wall, y (mm).

the 7.5 mm location has also increased energy levels. The 12 and 18 mm locations appear to have not changed significantly from the first row to the sixth row, but the 12 mm location contains a slightly higher amount of energy than the 18 mm location. All locations behind the sixth row show good agreement with the -7/3 decay rate.

Figure 3.55 shows the four stresses discussed above for the locations containing high levels of turbulence. Examining 3.55a shows that the streamwise normal stress is largest at the 'a' locations. This location is located immediately behind the cube element (x = 4 mm), and right at the roughness height. This area is characterized as the region where the separated flow behind the cube merges with the high velocity flow rushing over the top of the elements. High streamwise normal stresses would be present at this area. Figure 3.55b shows the wall-normal normal stress energy spectrum. The 'b' locations contain the most energy across the spectrum for this turbulence. The 'b' locations correspond to a point 6 mm downstream of the element and at a height of 2 mm. This is an area of large wall-normal fluctuations due to sweep and ejection events occurring near the wall. Figure 3.55c shows the spanwise normal stress energy, and again the 'b' locations contain the most amount of energy. This area is where a lot of flow is merging together, producing intense amounts of energy. The flow rushing around the sides meets with the flow rushing over the top of the cube element and separated region. The flow is sweeping towards the wall at this point, creating the large energies in the wall-normal and spanwise normal stresses. The Reynolds shear stress energy levels shown in Figure 3.55d show similar levels for all measurement locations. The 'a' locations have slightly elevated levels than the others, likely due to the large amount of Reynolds shear stress production located directly behind the element at the roughness height. This small but intense region of shear stress production is also apparent in the local flow contour plots.

Coherency measurements for the Reynolds shear stress for all cases are presented in Figures 3.56 and 3.57. Immediately apparent is the large correlation for measurements taken right at the roughness height. Behind both the first and sixth row, there is a peak coherency around $fk/U_\infty \approx 0.1$ for 3mm measurement location. At low frequencies, below

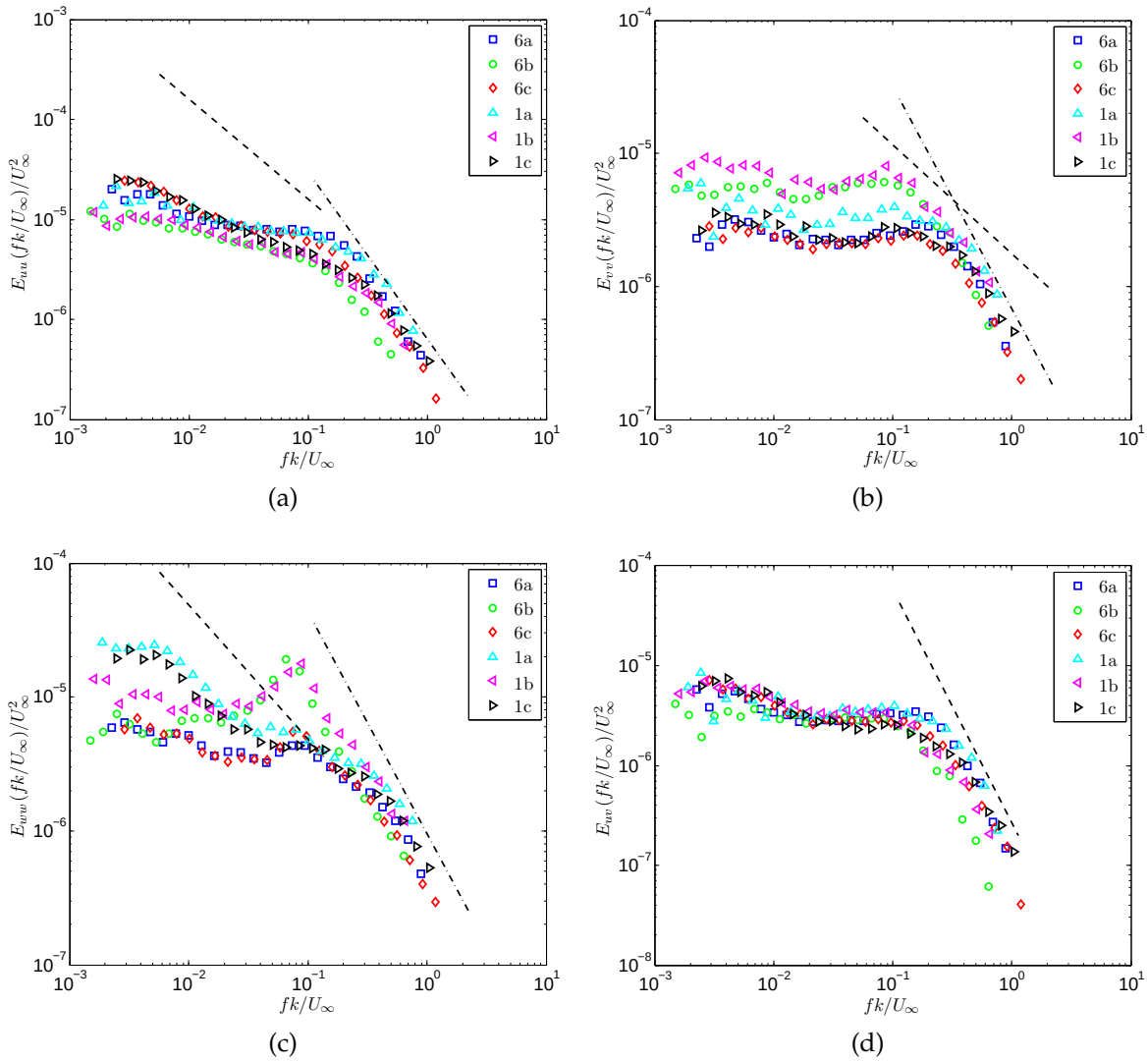

Figure 3.55: Energy spectra for various quantities at locations of high turbulence behind the roughness elements. The charts show: (a) streamwise normal stress; (b) wall-normal normal stress; (c) spanwise normal stress; and, (d) Reynolds shear stress

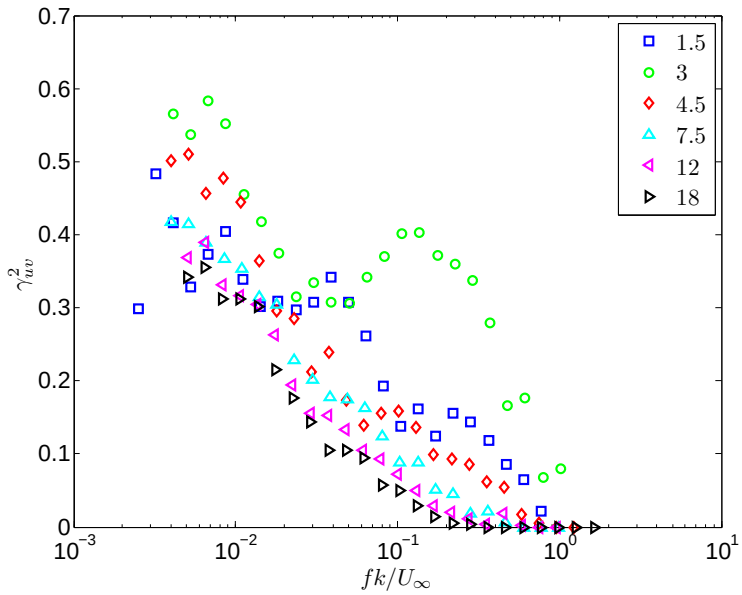

(a)

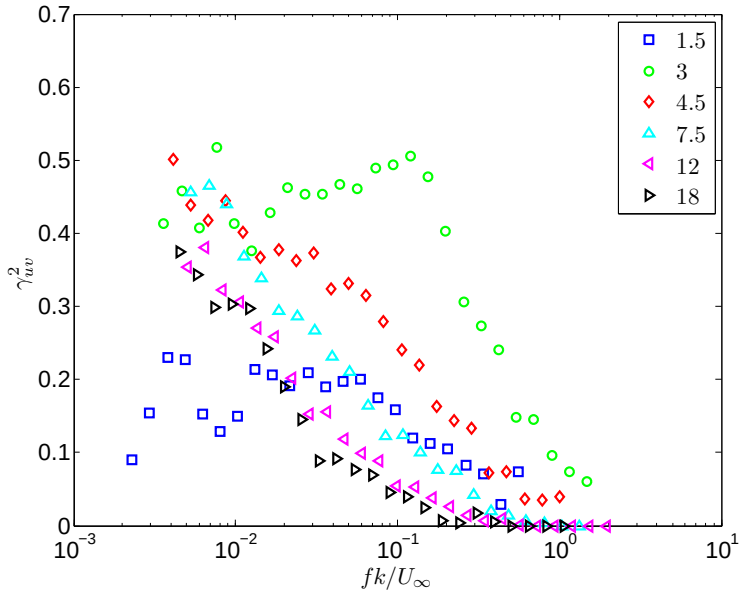

(b)

Figure 3.56: Coherency measurements of the Reynolds shear stress. The plots show measurements behind: (a) first row; and, (b) sixth row. The legend shows measurement locations in distance above the wall, y (mm).

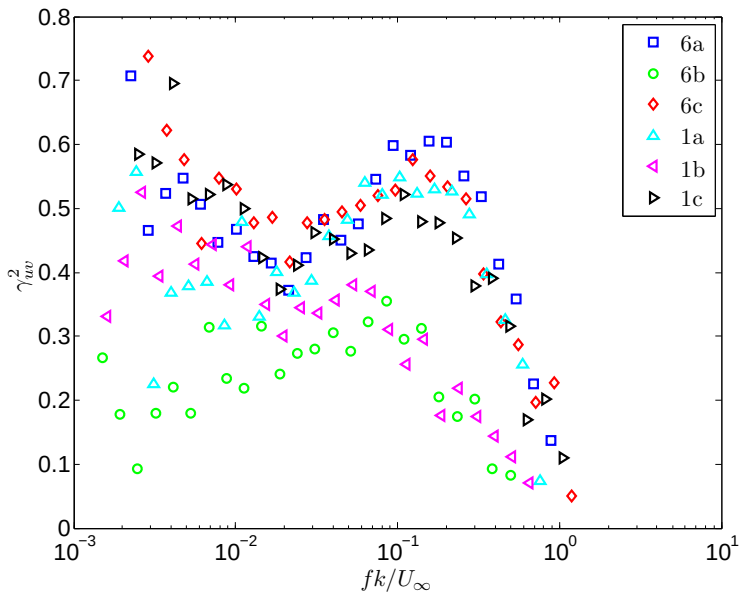

Figure 3.57: Coherency measurements of the Reynolds shear stress for various quantities at locations of high turbulence behind the roughness elements.

$fk/U_\infty \approx 0.1$, all locations show significant coherence levels. At higher frequencies, the locations further out in the boundary layer, show minimal correlation and could likely be modeled instead of simulated in a LES simulation. However, the flow near the roughness elements, especially below and at the roughness height, show good correlation between turbulence and shear stress production, and therefore would have to be simulated.

Behind the sixth row of elements, the coherency values are magnified for the 3, 4.5, and 7.5 mm locations. Coherency for the location below the element height appears to have lessened, especially at lower frequencies. There is little change for the 12 and 18 mm locations.

Figure 3.57 shows that there is a large correlation between turbulence and shear stress production across the frequency spectrum for all of the special locations. These locations were selected because of their high turbulence characteristics, so it only makes sense that this is the case. These areas could never be modeled and must be simulated in some way.

Chapter 4

Surface Pressure Fluctuation Results

Pressure fluctuations were measured on the surface of both roughness patches. The data were reduced as described in Section 2.3. Measurements were made in three distinct spanwise locations on the patches, and 8 distinct streamwise locations. The spanwise locations are along the center of the patch in-between two elements, directly behind an element in the center, and directly behind an element on the outside of the patch. The locations on the outside of the patch were measured to use as a reference when subtracting the acoustic and vibrational noise from the signals. Refer to Figure 4.1 for a picture of the measurement locations. The data is presented as a sound pressure level (SPL), with the reference sound pressure as 20 μPa, which is considered as the threshold of human hearing.

The first two graphs, Figures 4.2 and 4.3, depict the surface pressure fluctuations in-between the roughness elements on the center of the roughness patches. For the cubical case, the spectrum below 3 kHz shows a slight trend of increasing energy as the flow moves streamwise over the elements. The zeroth, first, and second rows show this increase in energy. By the fourth row, the energy is nearly the same across the remaining rows. However, above about 3 kHz, this order is opposite. It appears the rows at the beginning of the fetch have higher energy at higher frequencies than those at the end of the

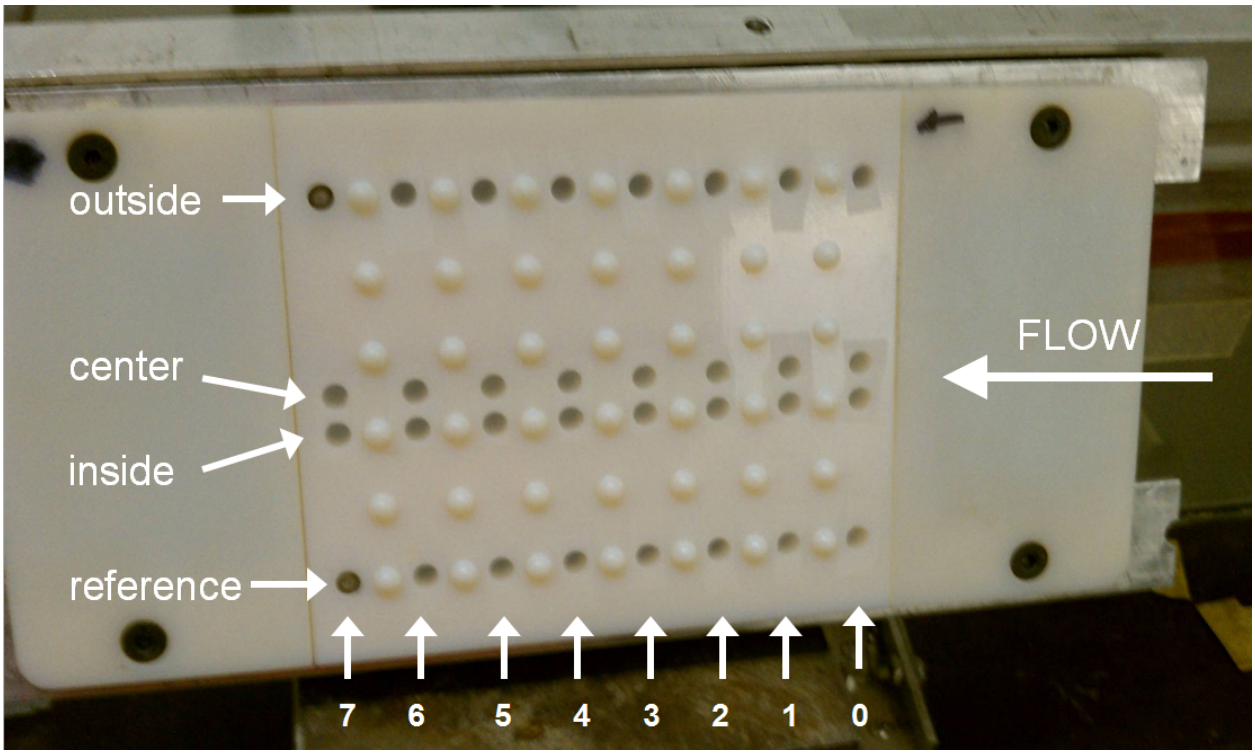

Figure 4.1: Location of surface pressure fluctuation measurements

fetch. It is likely that by the end of the fetch, some energy from the turbulence upstream has transferred towards the outer layer of the boundary layer and at lower frequencies. The hemispherical case shows a slight similarity to the cubical case, except the energies are much closer in magnitude to each other. Both roughness cases have a "knee" point at roughly 3 kHz, where the energy decay rates changes. Below 3 kHz, the energy decays slightly slower than the f^{-1} rate that is commonly witnessed. For the spectrum greater than 3 kHz, the energy decays at a slower rate than the f^{-5} region that is often measured.

Figures 4.4 and 4.5 depict the surface pressure fluctuations directly behind a central element of the flow. For the cubical case, there is no apparent pattern to the SPF energy directly behind an element. The measurement location in front of all the roughness elements measures about 7 dB lower than the rest of the roughness patch. At higher frequencies the row 0 energy eventually merges with the other spectra. The only difference with the hemispherical roughness is that the row 0 energy is about 8-9 dB lower than the

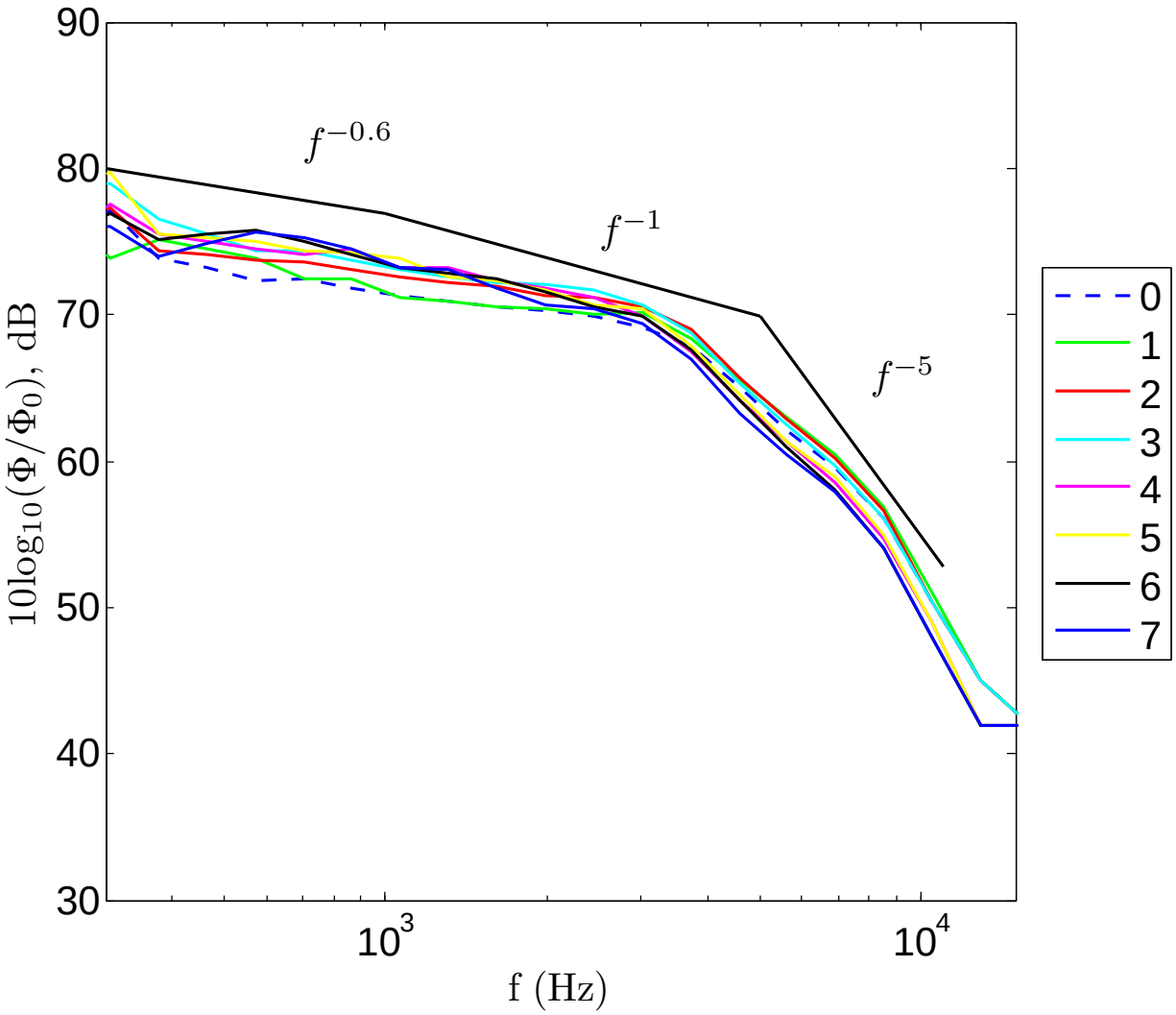

Figure 4.2: Surface pressure fluctuation spectra measurements taken in-between elements in the center of the cubical roughness patch, $\Phi_0 = (20\text{x}10^{-6})^2\text{Pa}^2\text{s}$

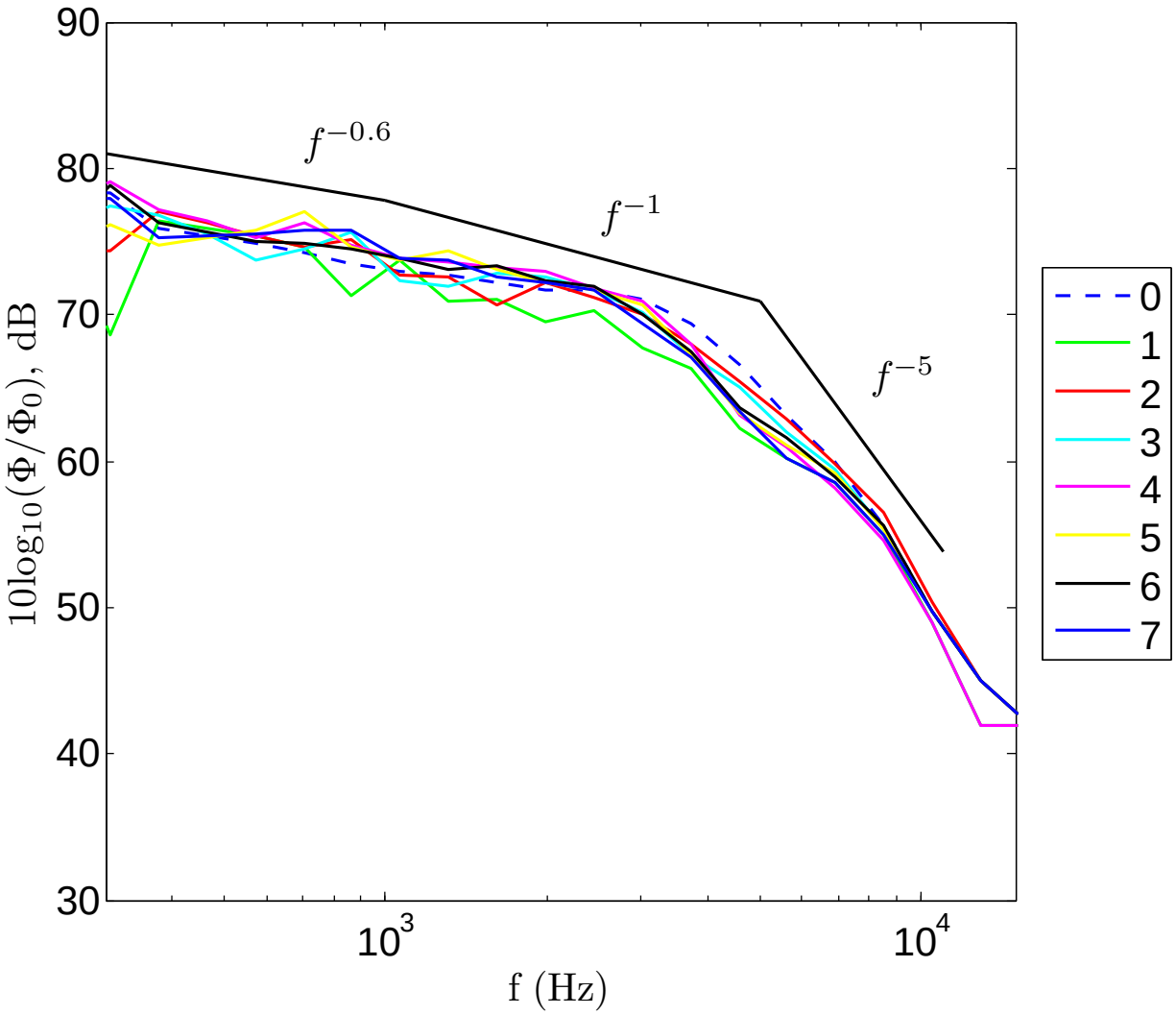

Figure 4.3: Surface pressure fluctuation spectra measurements taken in-between elements in the center of the hemispherical roughness patch, $\Phi_0 = (20\text{x}10^{-6})^2\text{Pa}^2\text{s}$

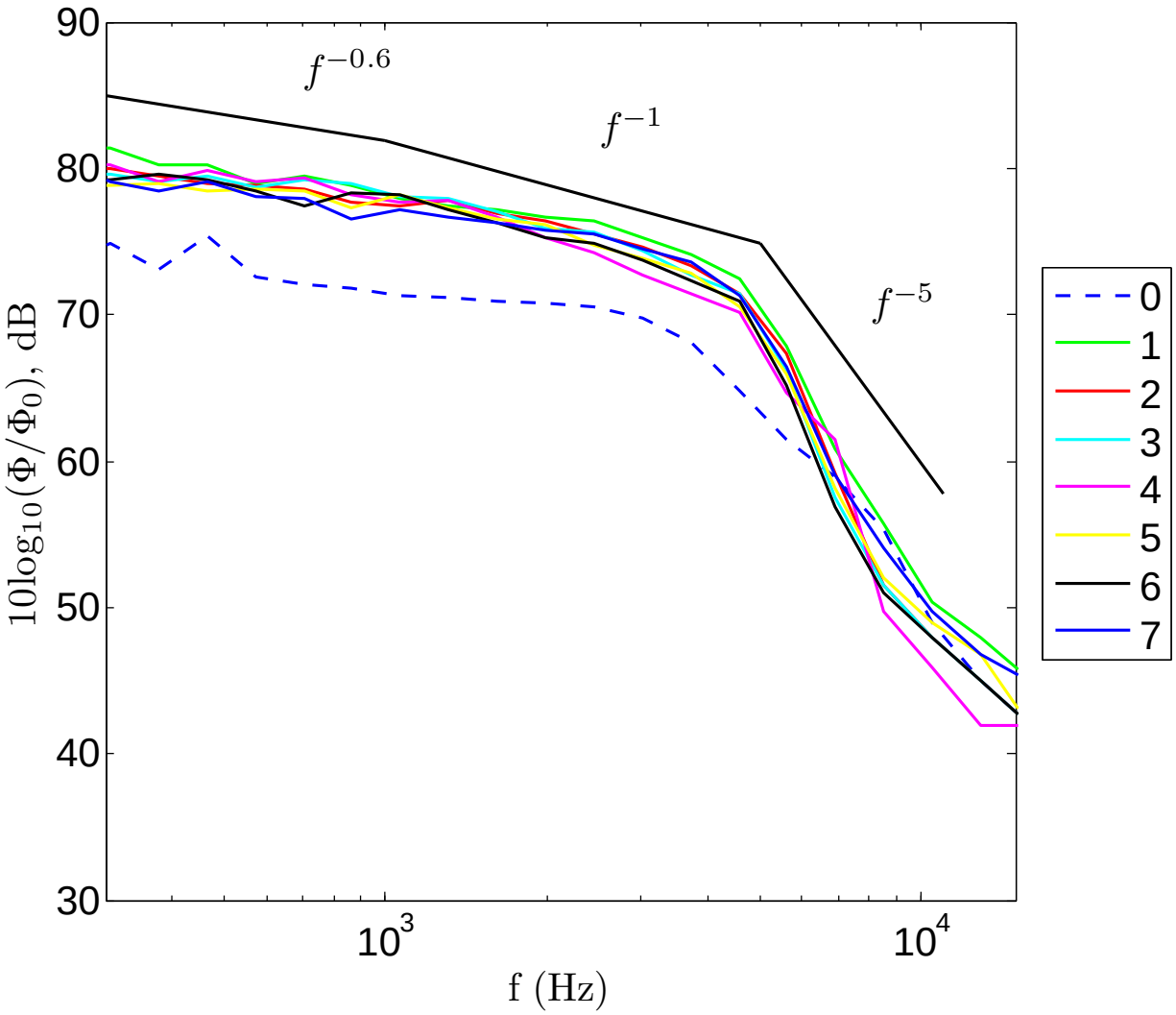

Figure 4.4: Surface pressure fluctuation spectra measurements behind an element in the center of the cubical roughness patch, $\Phi_0 = (20\text{x}10^{-6})^2\text{Pa}^2\text{s}$

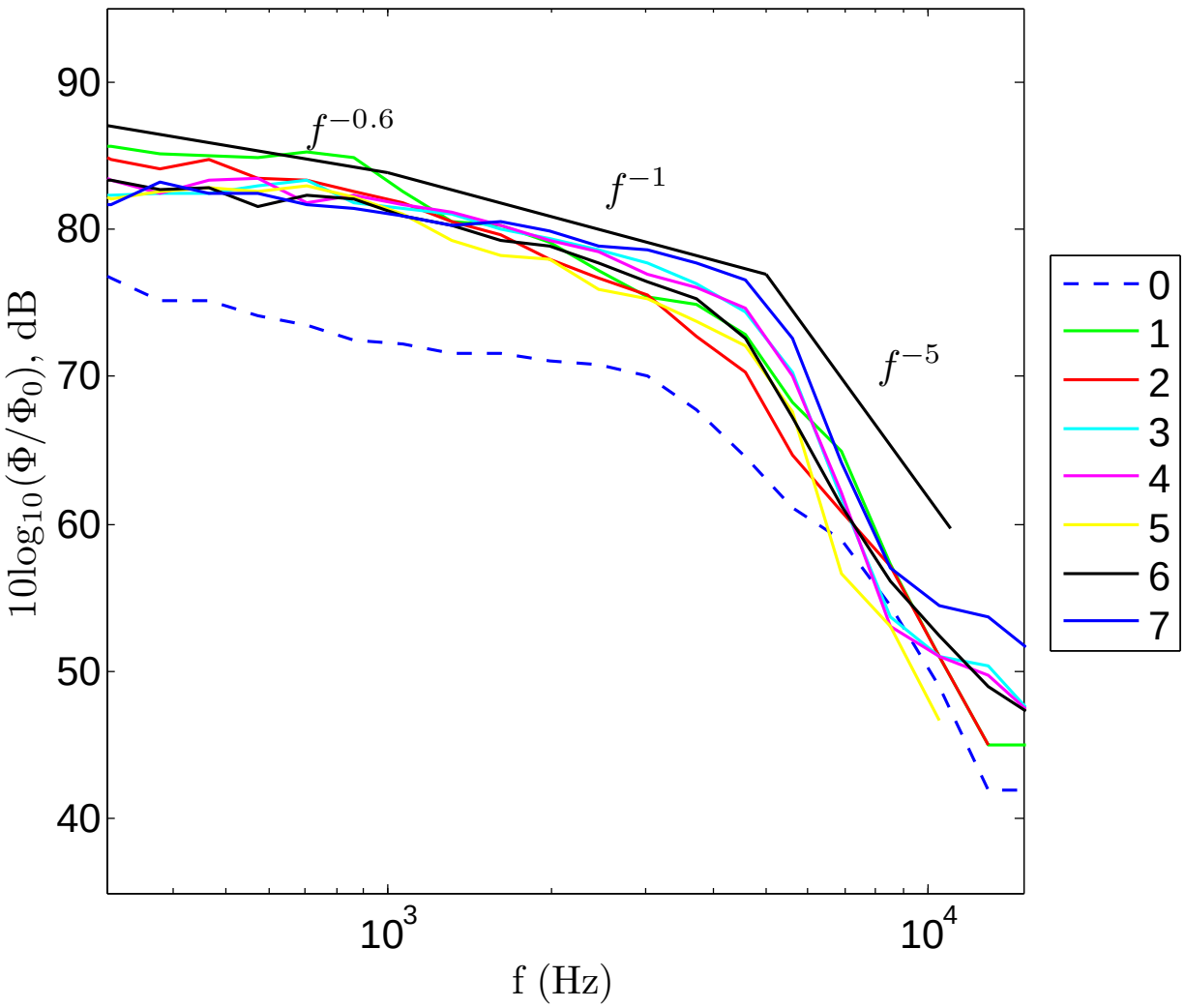

Figure 4.5: Surface pressure fluctuation spectra measurements behind an element in the center of the hemispherical roughness patch, $\Phi_0 = (20\text{x}10^{-6})^2\text{Pa}^2\text{s}$

rest of the roughness patch. There againi is no real pattern for the energy of the flow from rows 1 through 7. Both roughness cases exhibit the knee joint around 4-5 kHz. Below that range, the low frequency energy decays with good agreement at f^{-1}. The high frequency region appears to decay at a rate faster than the typical f^{-5}.

The surface pressure fluctuations for the elements on the outside of the roughness patch are presented in Figures 4.6 and 4.7. The data for these two measurements appear much cleaner due to the symmetrical placement of the microphones in the flow. For the cubical case, the location behind the first row of elements has the largest amount of energy over the entire spectrum. After that location, rows 2-7 show a nearly equivalent amount of energy across the spectrum. The row 0 location shows a energy deficit of between 5 and 8 dB in the low frequencies before merging with the other locations around 7 kHz. The hemispherical case shows similar trends as the cubical case. The first contains the most energy across the entire spectrum, and there is little differentiating the other rows. The difference between the zeroth row and the other rows reaches as large as 10 dB for the hemispherical case. For both roughness cases, the low frequency spectrum's energy shows good agreement with a decay of f^{-1} and the high frequency spectrum decays very near the typical f^{-5}.

Figure 4.8 shows the different spanwise sound pressure levels for both roughness cases at the same streamwise row. All rows show a similar pattern, so only row 6 has presented for analysis. First, the locations located on the inside of the roughness patch in-between elements show the lowest energy levels below 7 kHz. Both the cubical and hemispherical cases show equivalent energies for this location. Next in energy is the location behind a center cube element. With slightly higher energy than that location is the outer cube location. Finally, the inside hemisphere and outer hemisphere provide the largest amount of energy across the spectrum. These results show that the hemispherical elements produce a larger surface pressure fluctuation behind them than the cube and that the outer elements produce a higher SPL than elements on the inside. The larger noise level from the hemisphere matches agrees with what was analyzed by the LDV results. The hemi-

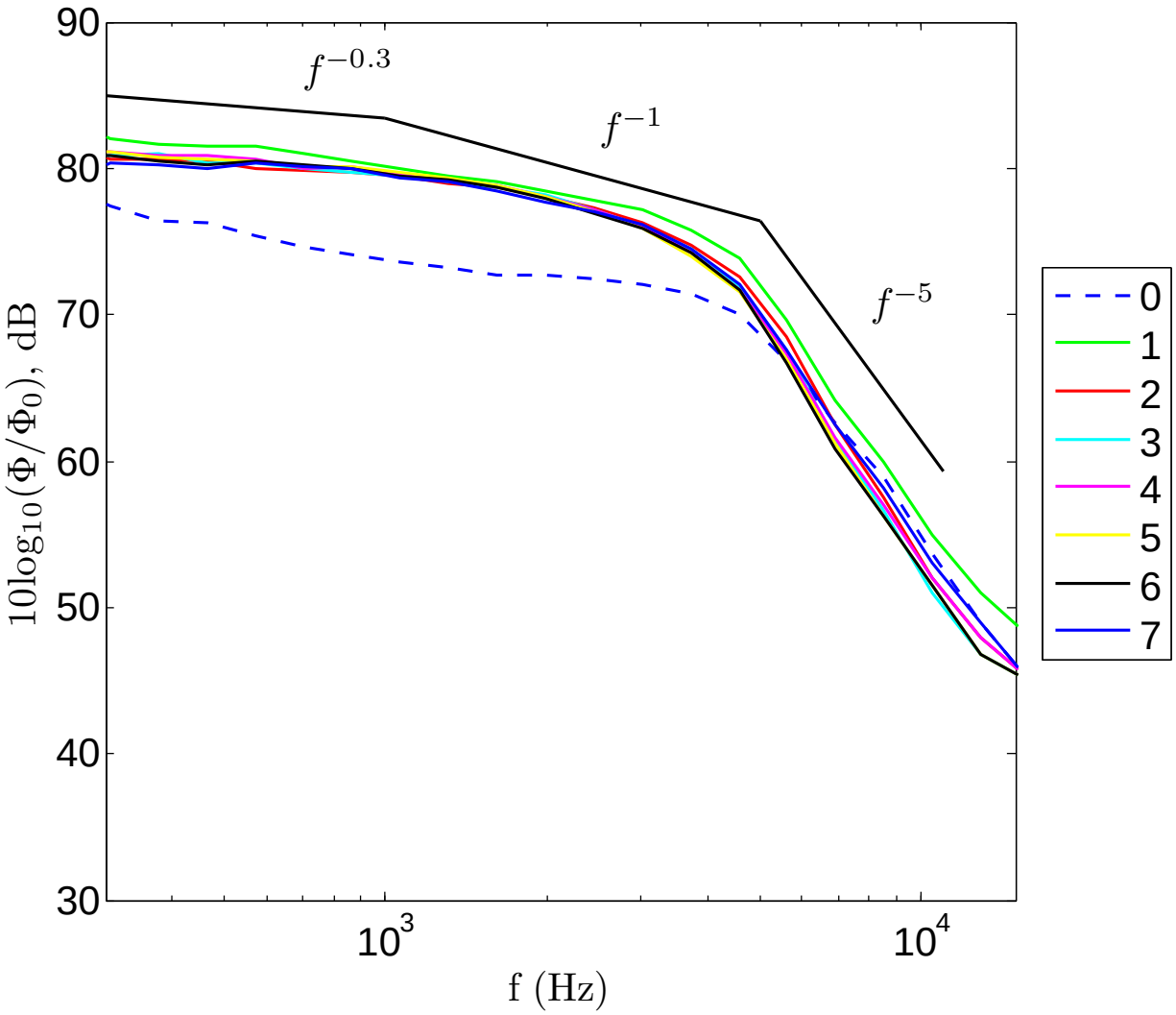

Figure 4.6: Surface pressure fluctuation spectra measurements behind an element on the outside of the cubical roughness patch, $\Phi_0 = (20\text{x}10^{-6})^2\text{Pa}^2\text{s}$

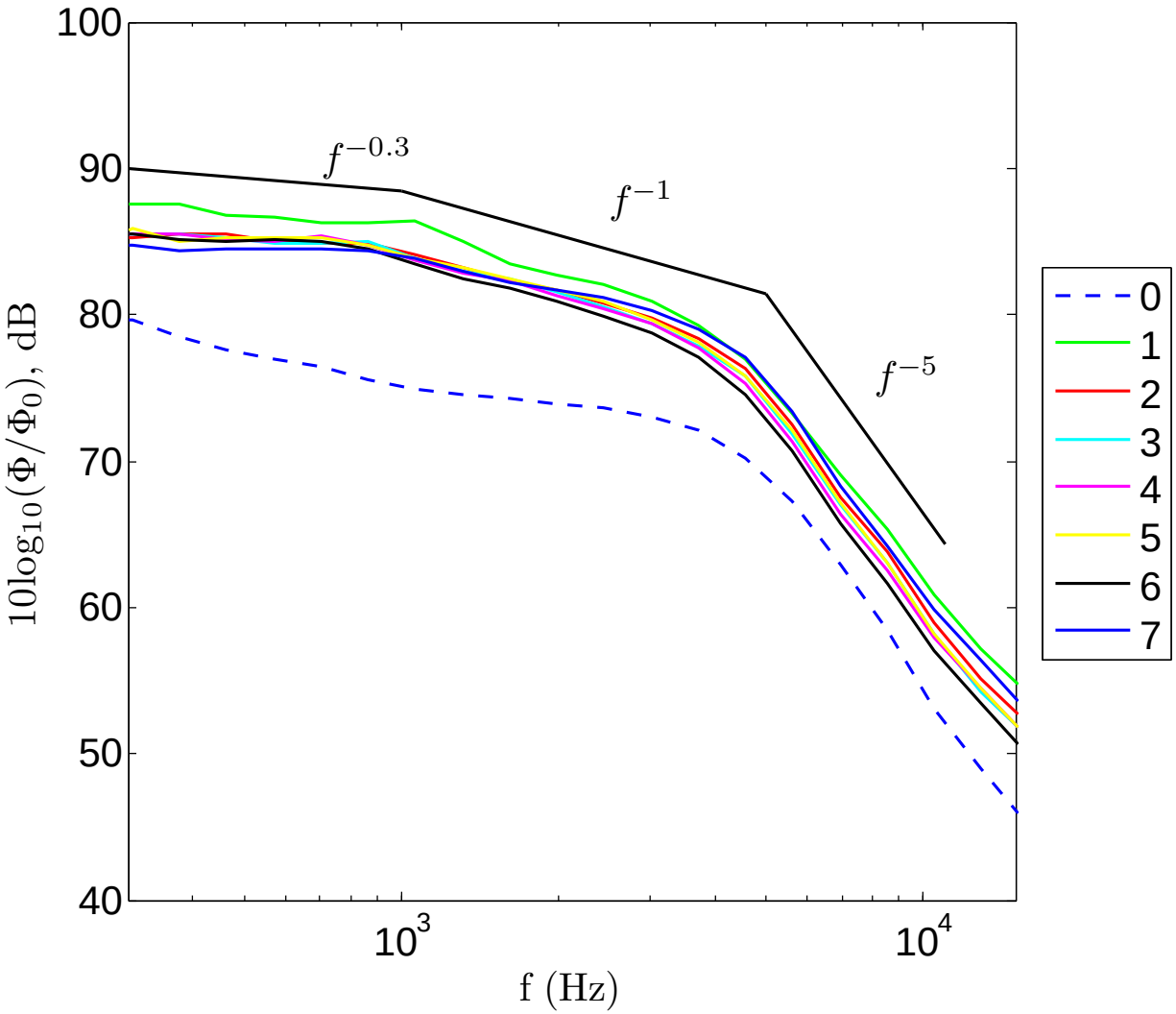

Figure 4.7: Surface pressure fluctuation spectra measurements behind an element on the outside of the hemispherical roughness patch, $\Phi_0 = (20\text{x}10^{-6})^2\text{Pa}^2\text{s}$

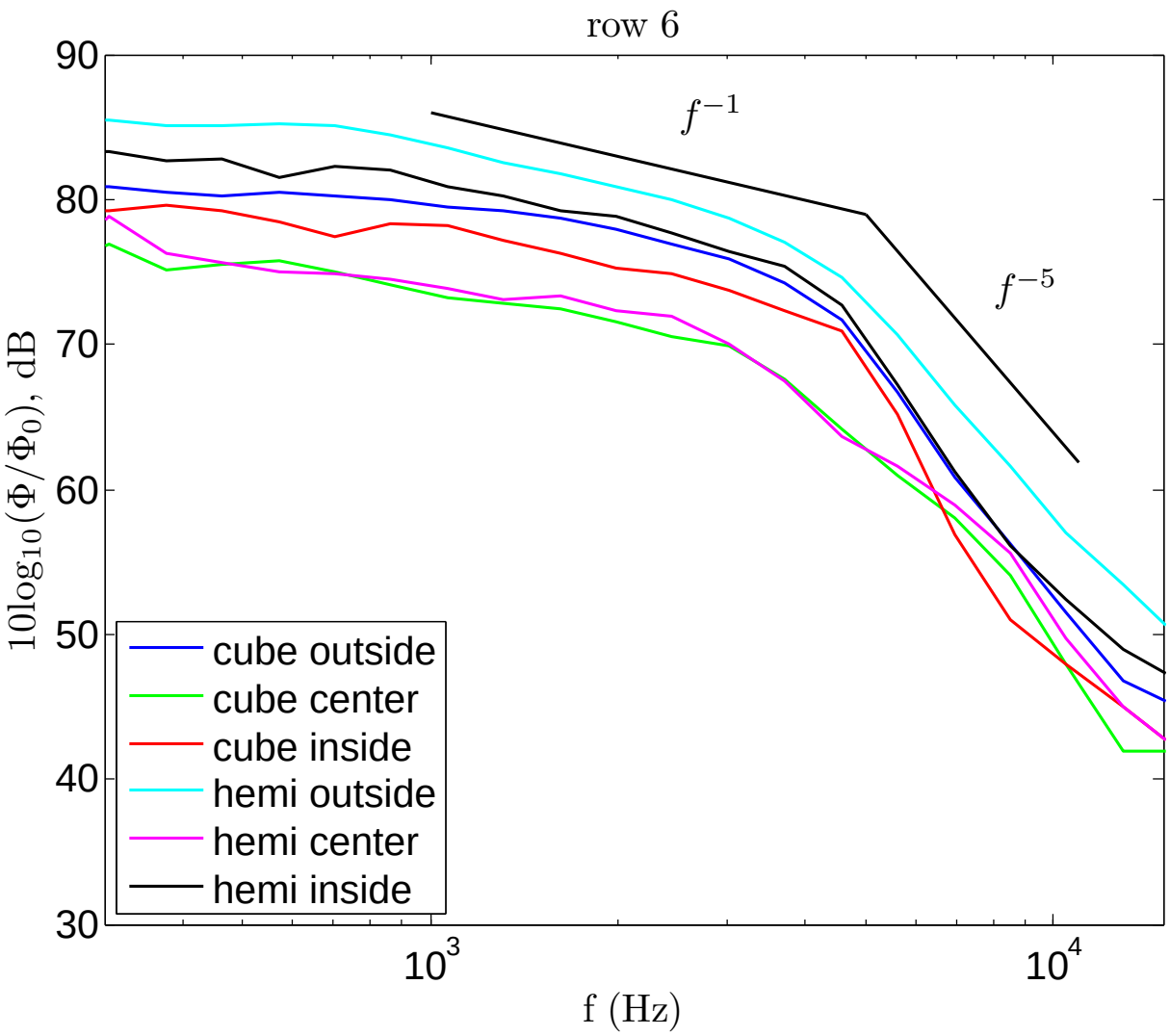

Figure 4.8: Surface pressure fluctuation spectra measurements at different spanwise locations behind the sixth row of hemisphere and cube elements, $\Phi_0 = (20\text{x}10^{-6})^2\text{Pa}^2\text{s}$

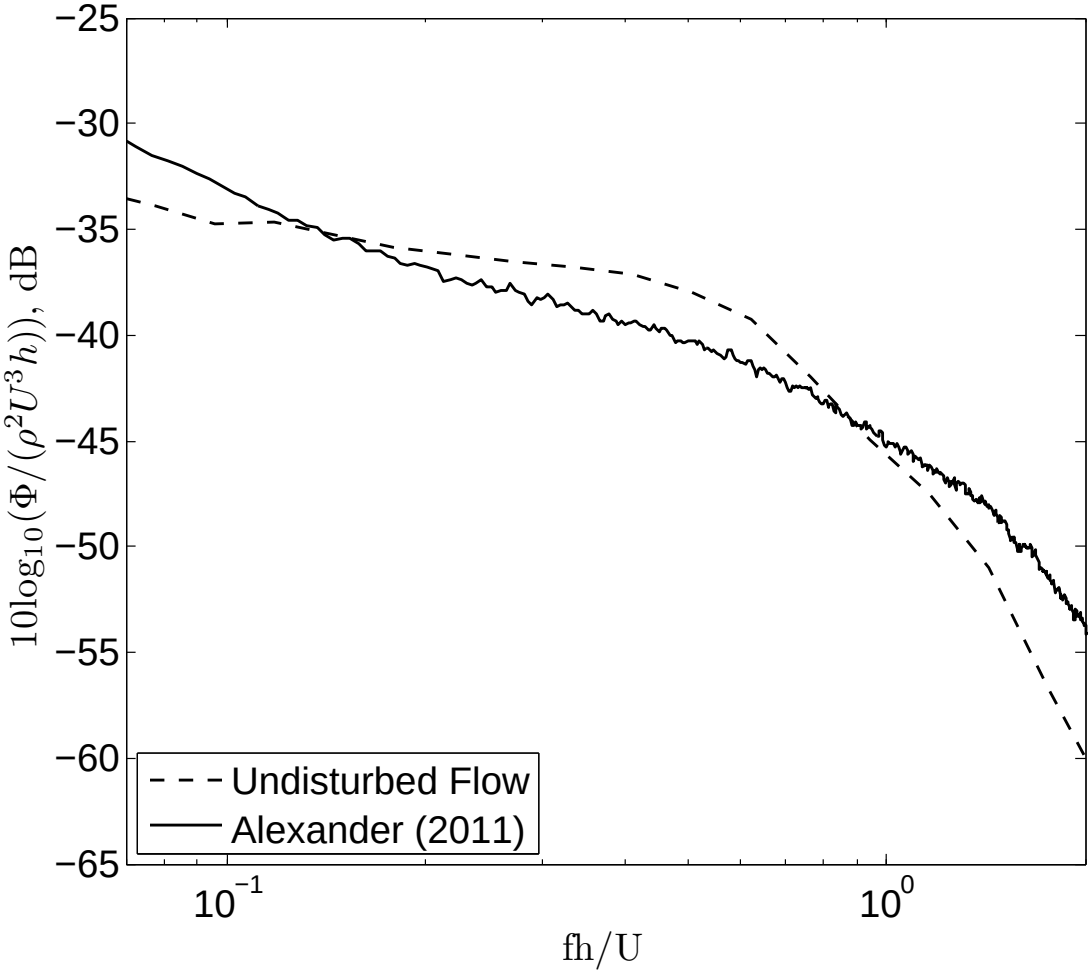

Figure 4.9: Comparison between current data and Alexander (2011) for an undisturbed smooth wall location. Data is normalized on the local velocity at the roughness height, the density, and the roughness height.

spheres create a significantly larger amount of turbulence behind themselves, and this correlates to a larger surface pressure fluctuation. A possible explanation for the outer elements producing more noise energy than the inner elements is that the outside elements on the edge face higher speed flow from one of their sides. This higher speed flow could cause more turbulence to occur on the edge of the roughness than inside of the roughness where other elements have an effect on the flow.

Figures 4.9-4.11 show a comparison for surface pressure fluctuations measured for this

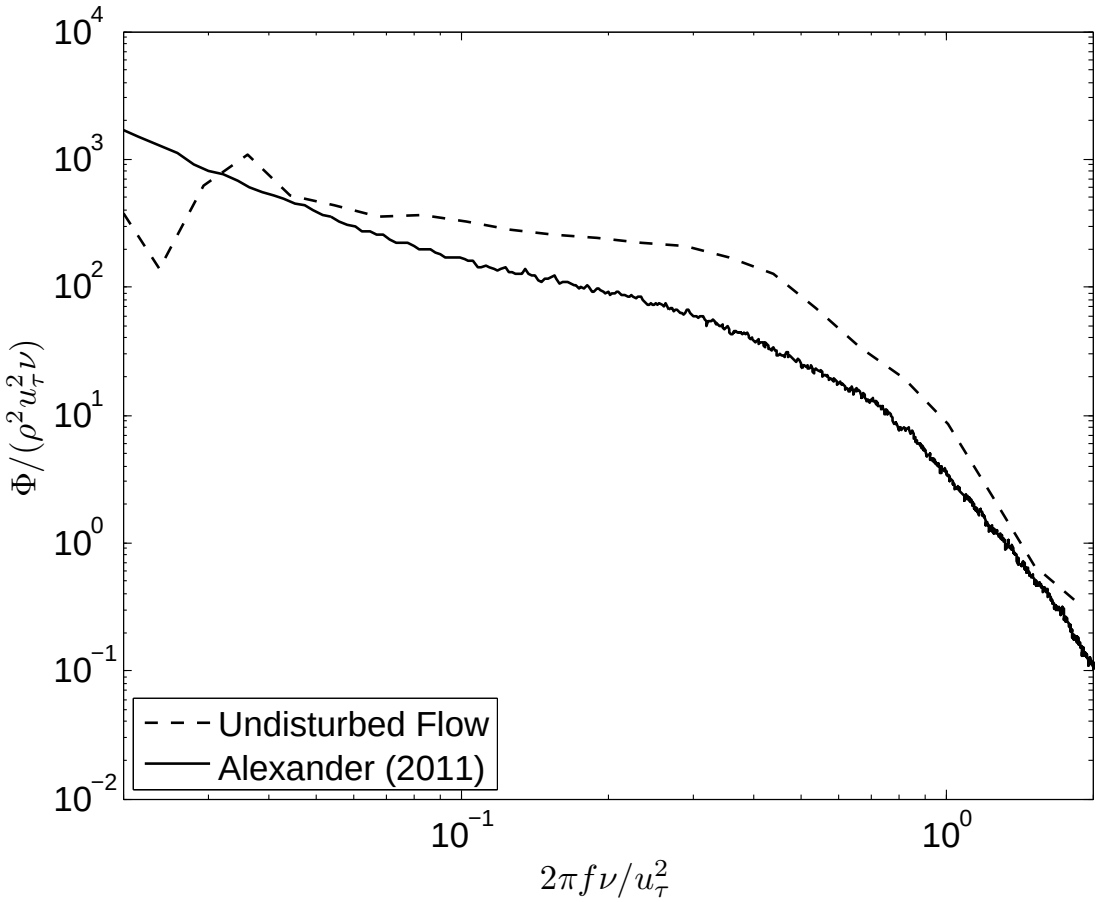

Figure 4.10: Comparison between current data and Alexander (2011) for an undisturbed smooth wall location. Data is normalized on the friction velocity and kinematic viscosity.

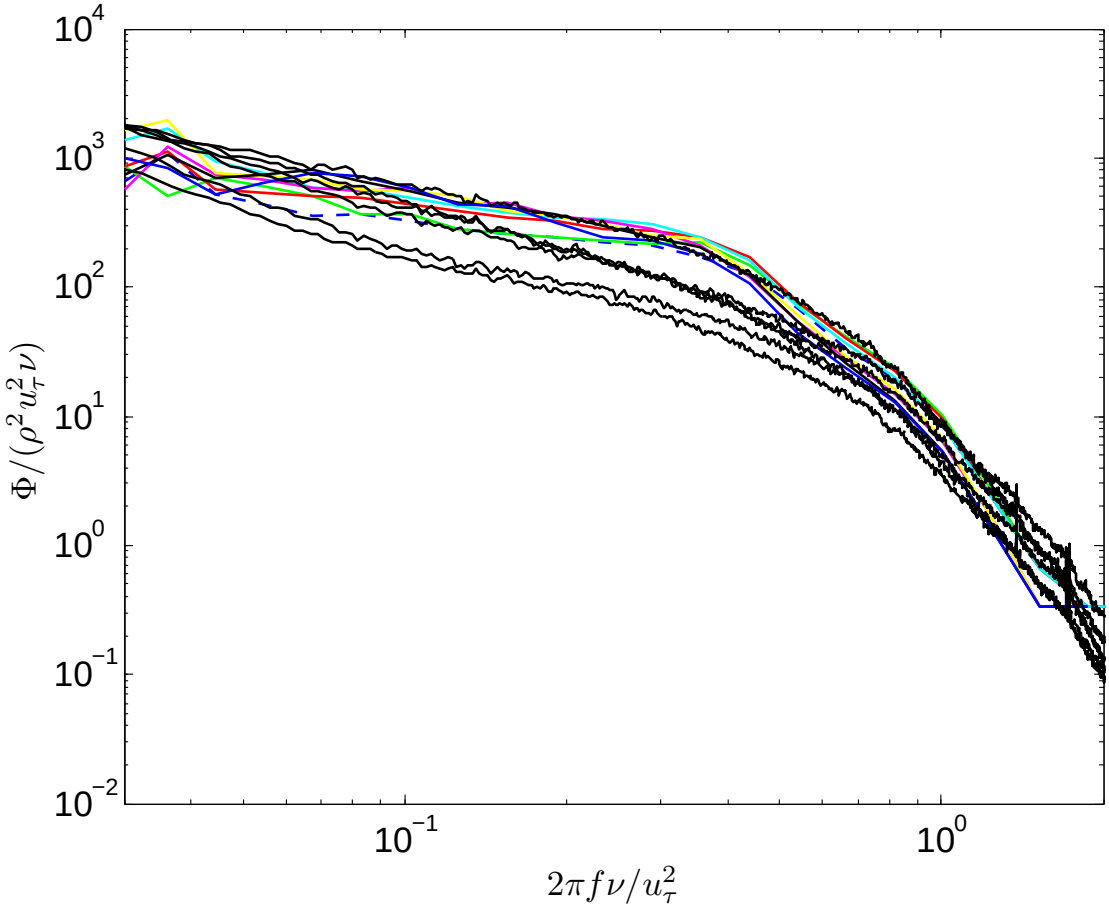

Figure 4.11: Comparisons between current data and Alexander (2011) for a variety of locations down the center of the cubical roughness patch. Data is normalized on the friction velocity and kinematic viscosity at a smooth wall location. Colored lines shows the current study's results, while black line show results of Alexander.

study and the measurements of Alexander[1]. The pressure fluctuations are normalized by two separate set of variables. The first plot is normalized by the density of the flow squared, a characteristic velocity cubed, and the roughness element height. The characteristic velocity used for this comparison was the velocity of the freestream flow at height of the roughness elements. The normalized variables are plotted as a function of the Strouhal number, $St = fh/U$. The other set of variables are based on the friction velocity and kinematic viscosity at an undisturbed smooth wall location for both types of flow.

The wall-jet SPF of Alexander's study decay at a faster rate for the lower frequencies due to the mixing layer of the wall-jet compared to the turbulent boundary layer of this study. The wall-jet SPF decay on the order of f^{-1} for lower frequencies while the current data decay around $f^{-0.6}$. Both sets of data approach an f^{-5} region for higher frequencies. The pressure levels of Alexander's data is lower in mid-frequencies in comparison to the current data, but have higher levels at the low and high frequency ranges.

Chapter 5

Discussion and Conclusions

An experimental study has been conducted on two roughness patches containing sparsely-spaced large hemisphere and cube elements in a zero pressure gradient turbulent boundary layer. Boundary layer profiles and velocity spectra using laser Doppler velocimetry were measured at a number of locations on each patch. Surface pressure fluctuations were measured at similar locations using a two microphone setup, and the data were compared.

The results show that the flow field for the hemispherical patch is very unique to the cubical patch, and that the turbulent structure is continuously changing over the entire streamwise length of the patches. The smooth wall boundary layer approaches the roughness patches, hits the first row of elements, and then begins to adjust to the new boundary conditions. This adjustment continues over the length of the patches until the flow passes over the final row of elements. By the time the flow has reached the last row of elements, it has not yet fully adjusted to the roughness, but now it must flow back toward the smooth wall boundary behind the patches.

The flow down the centerline of the roughness patches, not directly behind any elements, is characterized by a gradual deceleration of the streamwise flow and the gradual increase

of turbulence quantities. Turbulent quantities in-between elements after the first row are similar to the values in front of the patch. The flow begins to slow and turbulence increases after the second row. This trend continues streamwise along the patch until the fourth and fifth rows, when the inner boundary layer begins to approach an equilibrium state. The fifth, sixth, and seventh row locations in-between the elements have similar mean velocity and turbulent quantities. However, this does not signify that the boundary layer has completely adjusted; it only shows that front of the roughness patches encounter larger flow changes that taper off as the flow moves streamwise. Also, the inner layer of boundary layer is still growing even as the flow passes over the final row of elements.

The differences in the flows between elements for the hemispherical and cubical patches are minimal. Both patches show the same turbulent structure for these locations and the flow adjusts to the roughness in a similar manner. The only difference is that the cubes produce a slightly higher magnitude of turbulence for some of the terms. This observation is likely caused by the blunt windward faces of the cubes. Flow likely hits the front of these faces and ejects in all directions, including off to the side. This would cause a slight increase in turbulence as compared to the hemishperes since that flow reaches into the centerline between elements.

Flow directly behind the roughness elements is not similar in any manner to the flow in-between elements. The flow behind elements is characterized by extremely strong turbulent structures located behind the first row of both patches. The high speed smooth wall boundary layer encounters the first row of elements, separates from the surfaces as it flows over the first elements, and creates a large separation region behind the element. Just downstream of this separated region is an area where flow rushing over the top and around the sides of the elements merges. The large velocity gradients present between this area and the separation zone create intense shearing stresses. The flow over the elements downstream of the first row shows similar structures, with slight differences between the two types of roughness.

The shape of the turbulent structure behind the two type of elements is different. The hemispherical elements produce turbulent regions that are arch-like shapes. These arch-like regions contain strong magnitudes of turbulence, which shows that the flow over the direct top as well as some flow around the side of the hemisphere produces similar amounts of turbulence in a large region. This is in contrast to the cubical elements, which produce most turbulence from flow directly over the top of the element. The turbulent regions behind the cube occur just below the height of the roughness element, and these areas are much smaller in size than the hemispherical elements.

The turbulent quantities behind the hemispheres are of significantly higher magnitude than those behind the cubes. This is likely due to the hemispheres large frontal area, which is nearly 60% larger than that of the cubes. This difference means that the flow must travel a longer distance around the body of the hemisphere, and when it merges back toward the centerline of the element, it will carry more momentum, creating higher turbulent values. There is another difference when comparing the turbulent values as the flow progresses over the patches. For the hemispheres, the turbulent intensities decreases at downstream measurement locations. The cause of this is likely due to the deceleration and drag of the flow near the wall, which reduces momentum for the flow before reaching elements downstream. However, the cubical elements at different streamwise rows produce a similar amount of turbulence for many of the terms. This shows that the individual cubes have less influence on one another than the hemispheres do. Since a similar amount of turbulence is created upstream as is downstream, the reduced amount of blockage must not impede the flow as well.

The sweep and ejection events that occur behind the elements produce a similar amount of turbulent intensity. Most sweep and ejection events occur close to or just below the element height. The sweeping motions occur as the fluid rushes over the elements and towards the wall. Ejection events occur closer to the separated zone behind the elements, as well as near the front of the oncoming row of elements. Interactions occur less frequently in the turbulent areas behind the elements, and create little shear stress values of

significance.

Velocity spectral results show that behind the first row, elevated levels of normal stress energy are produced at and below the roughness height across the frequency spectrum. Behind the sixth row, some energy has convected upward into the boundary layer, as the levels are also elevated at locations above the roughness elements. For the normal stresses, the cascade of energy agrees with Kologormov's -5/3 decay power law. Energy spectra for the Reynolds shear stress are elevated across the spectrum after the sixth row in comparison to the first row. The Reynolds shear stress spectra decay with good agreement at the -7/3 rate defined by Lumley[12]. Coherence plots show significant correlation between the turbulent motions and the production of shear stress, particularly right at the roughness height. In the areas below and just above the roughness element, the flow shows coherency below 10 kHz, and a large eddy simulation is necessary to analyze this flow. However, flow a couple roughness heights above the wall is not significantly correlated above around 2 kHz.

Surface pressure fluctuation measurements show little difference between rows of the roughness patches. There is a slight pressure level increase at lower frequencies over the first couple rows on the roughness patches, but overall the difference is insignificant. Alexander[1] also found that after the first couple of rows, changes in surface pressure were minimal. The hemispherical and cubical patches produced the same amount of surface pressure fluctuations in-between elements down the centerline. The hemispherical elements produced significantly larger levels directly behind elements in comparison to the cubes. This result agrees with the LDV findings of higher turbulence quantities located behind the hemispheres. A comparison between the current study results and Alexander's [1] show similar magnitudes of pressure level when scaling on the flow velocity, density, and roughness height. The wall-jet flow of Alexander decays at a faster rate than the wind tunnel flow of this study for the lower Strouhal numbers.

The study of Yang and Wang [23] show that most far field noise is produced by the cubes'

front facing flat surfaces. Alexander[1] also found that the far field noise produced by the cubes is significantly louder than that of the hemispheres. Unfortunately for this study, it was not possible to measure the flowfield directly in front of the cubical elements due to laser flare from the surface. Yang's large eddy simulation results due show the formation of horseshoe vortices at the base of the roughness elements. The presence of these horseshoe vortices was measured behind the elements and displayed in the streamwise vorticity contour plots. The strength of the horseshoe vortex formed on the first row of elements is larger than other vortices produced downstream in the flow.

Bibliography

[1] W.M. Alexander and W. Devenport. Aerodynamic noise from sparse surface roughness. In *17th AIAA/CEAS Aeroacoustics Conference*, 2011.

[2] J. Andreopoulos and D.H. Wood. The response of a turbulent boundary layer to a short length of surface roughness. *Journal of Fluid Mechanics*, 118:143–164, 1982.

[3] R. A. Antonia and R. E. Luxton. The response of a turbulent boundary layer to a step change in surface roughness Part 1. Smooth to rough. *Journal of Fluid Mechanics*, 48(4):721–761, 1971.

[4] R.A. Antonia and R.E. Luxton. The response of a turbulent boundary layer to and upstanding step change in surface roughness. *Journal of Basic Engineering*, pages 22–34, March 1971.

[5] J. L. Bennington. Effects of various shaped roughness elements in two-dimensional high reynolds number turbulent boundary layers. Master's thesis, Virginia Polytechnic Institute and State University, 2004.

[6] W.P. Elliott. The growth of the atmospheric internal boundary layer. *American Geophysical Union Transactions*, 39:1048–1054, 1958.

[7] J. George. *Structure of 2-D and 3-D Turbulent Boundary Layers with sparsely Distributed Roughness Elements*. PhD thesis, Virginia Polytecnic Institute and State University, 2005.

[8] M. Goody. *An Experimental Investigation of Pressure Fluctuations in Three-Dimensional Turbulent Boundary Layers*. PhD thesis, Virginia Polytechnic Institute and State University, 1999.

[9] A. M. R. Hopkins. *Fluid Dynamics and Surface Pressure Fluctuations of Two-Dimensional Turbulent Boundary Layers Over Densely Distributed Surface Roughness*. PhD thesis, Virginia Polytechnic Institute and State University, 2010.

[10] J. Jimnez. Turbulent Flows over Rough Walls. *Annual Review of Fluid Mechanics*, 36:173–196, 2004.

[11] K. T. Lowe. *Design and application of a novel Laser Doppler Velocimeter for turbulence structural measurements in turbulent boundary layers*. PhD thesis, Virginia Polytechnic Institute, 2006.

[12] J.L. Lumley. Similarity of the turbulent energy spectrum. *Phys. Fluids*, 10:855–858, 1967.

[13] B.E. McGrath and R.L. Simpson. Some features of surface pressure fluctuations in turbulent boundary layers with zero and favorable pressure gradients. Technical report, NASA, 1986.

[14] Semih M Olcmen and Roger L Simpson. A five-velocity-component laser-doppler velocimeter for measurements of a three-dimensional turbulent boundary layer. *Measurement Science and Technology*, 6:702–716, June 1995.

[15] H.A. Panofsky and A.A. Townsend. Change of terrain roughness and the wind profile. *Royal Meteorological Society Quarterly Journal*, 90:147–155, 1964.

[16] M.B. Rasnick. The noise of a boundary layer flowing over discrete roughness elements. Master's thesis, Virginia Polytecnic Institute and State University, 2010.

[17] M. P. Schultz and K. A. Flack. The rough-wall turbulent boundary layer from the hydraulically smooth to the fully rough regime. *Journal of Fluid Mechanics*, 580:381–405, 2007.

[18] K. A. Shinpaugh, R. L. Simpson, A. L. Wicks, S. M. Ha, and J. L. Fleming. Signal-processing techniques for low signal-to-noise ratio laser Doppler velocimetry signals. *Experiments in Fluids*, 12:319–328, 1992.

[19] A.J. Smits, S.T.B. Young, and P. Bradshaw. The effects of short regions of high surface curvature on turbulent boundary layers. *Journal of Fluid Mechanics*, 94(2):209–242, 1979.

[20] D. O. Stewart. Effects of spacing and geometry of distributed roughness elements on a two-dimensional turbulent boundary layer. Master's thesis, Virginia Polytechnic Institute and State University, 2005.

[21] A.A. Townsend. Self preserving flow inside a turbulent boundary layer. *Journal of Fluid Mechanics*, 22:773–797, 1965.

[22] N. D. Varano. *Fluid Dynamics and Surface Pressure Fluctuations of Turbulent Boundary Layers Over Sparse Roughness*. PhD thesis, Virginia Polytechnic Institute and State University, 2010.

[23] Q. Yang and M. Wang. Statistical analysis of acoustic-source field in rough-wall boundary layers. In *17th AIAA/CEAS Aeroacoustics Conference*, 2011.

Appendix A

Additional Figures

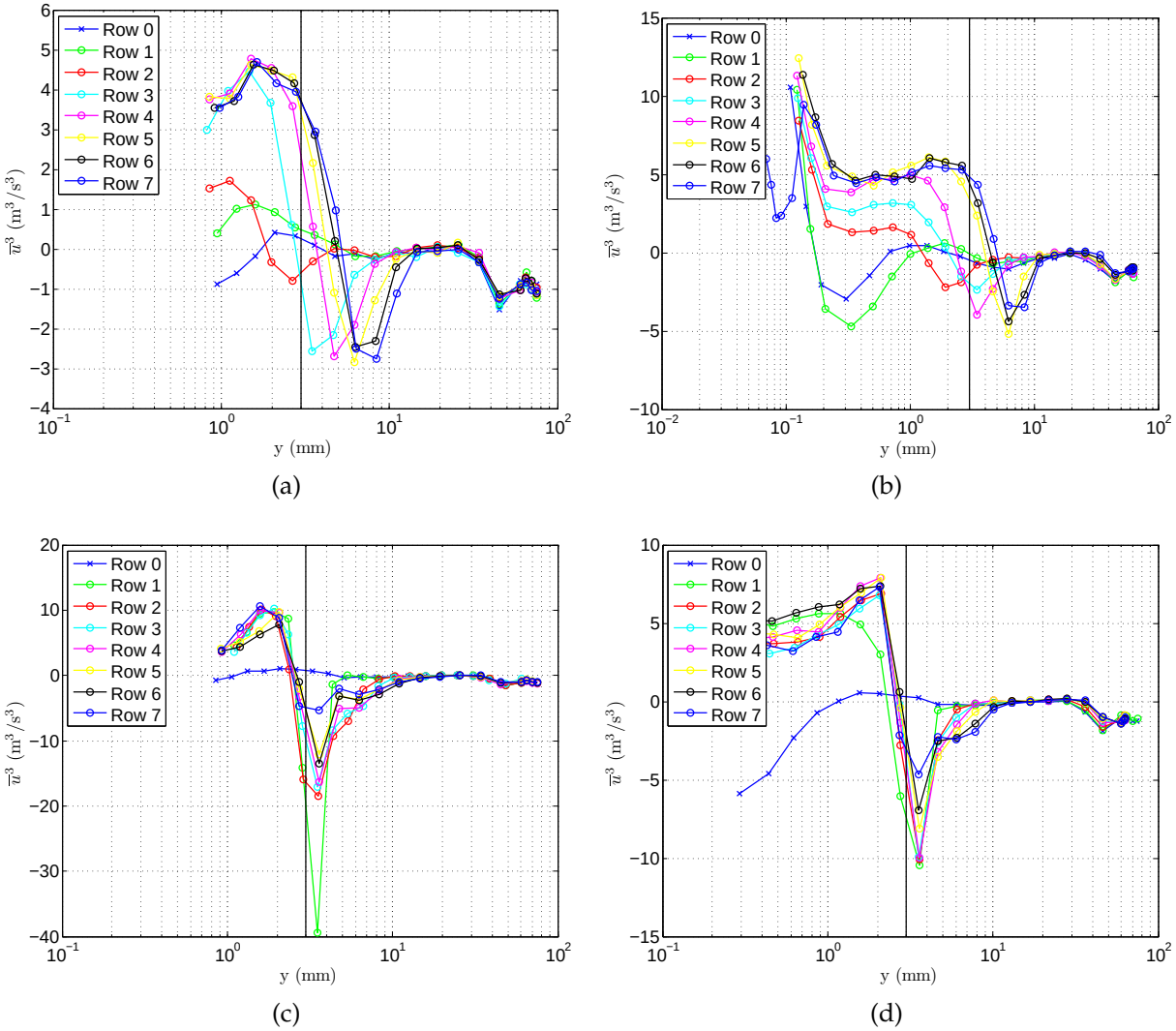

Figure A.1: $\overline{u^2u}$ triple product profiles: (a) between hemispheres; (b) between cubes; (c) behind hemispheres; and, (d) behind cubes

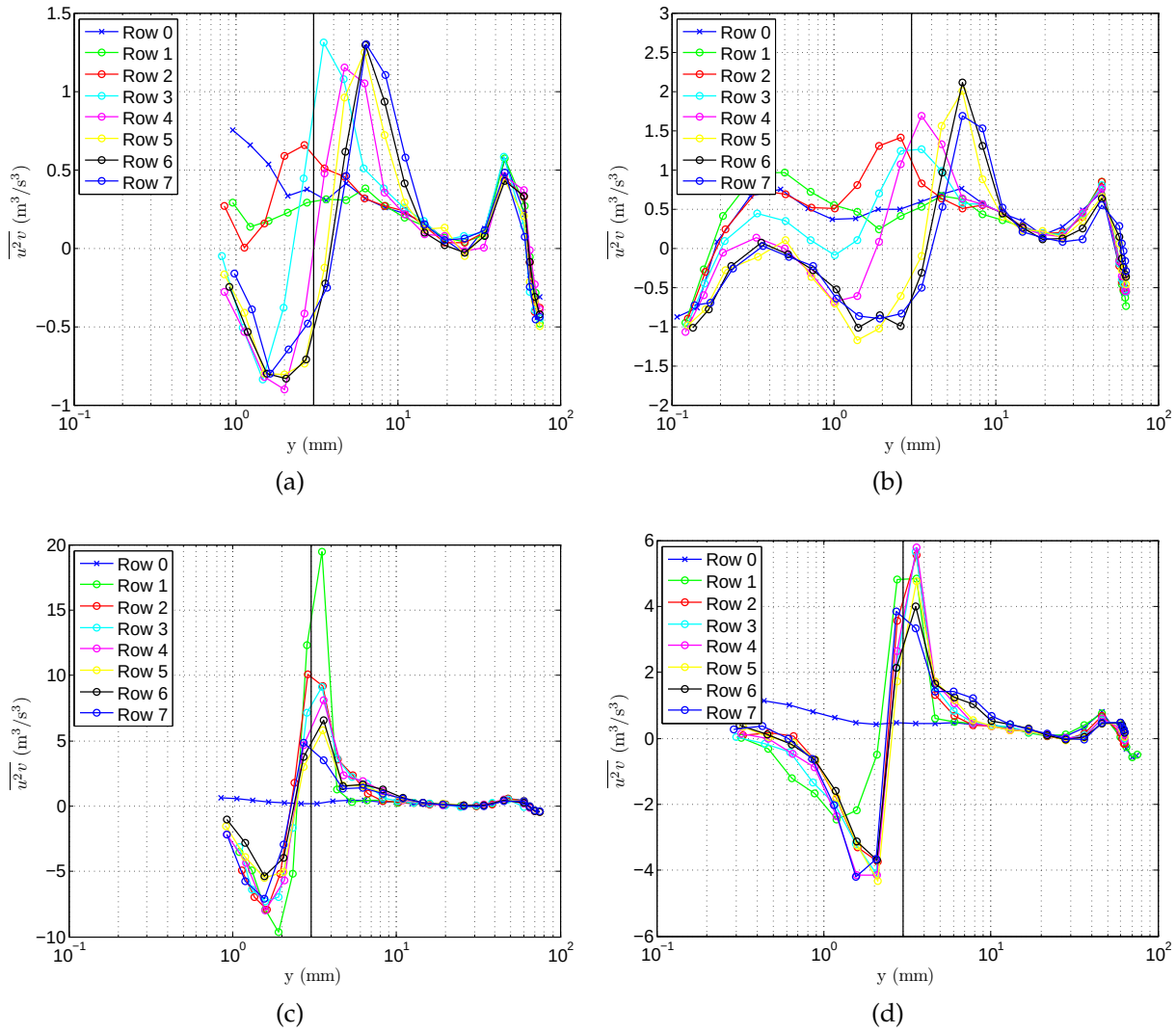

Figure A.2: $\overline{u^2v}$ triple product profiles: (a) between hemispheres; (b) between cubes; (c) behind hemispheres; and, (d) behind cubes

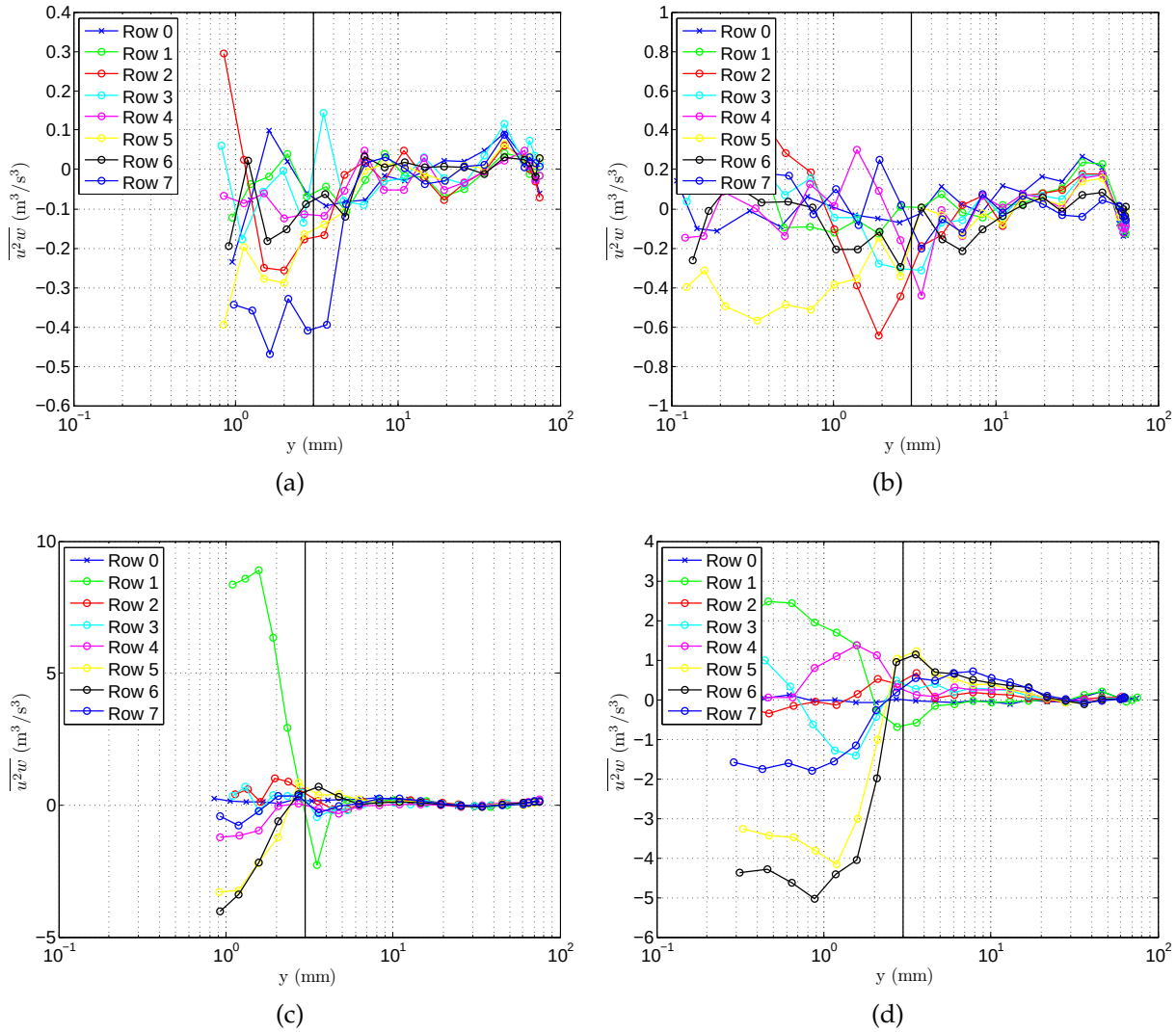

Figure A.3: $\overline{u^2w}$ triple product profiles: (a) between hemispheres; (b) between cubes; (c) behind hemispheres; and, (d) behind cubes

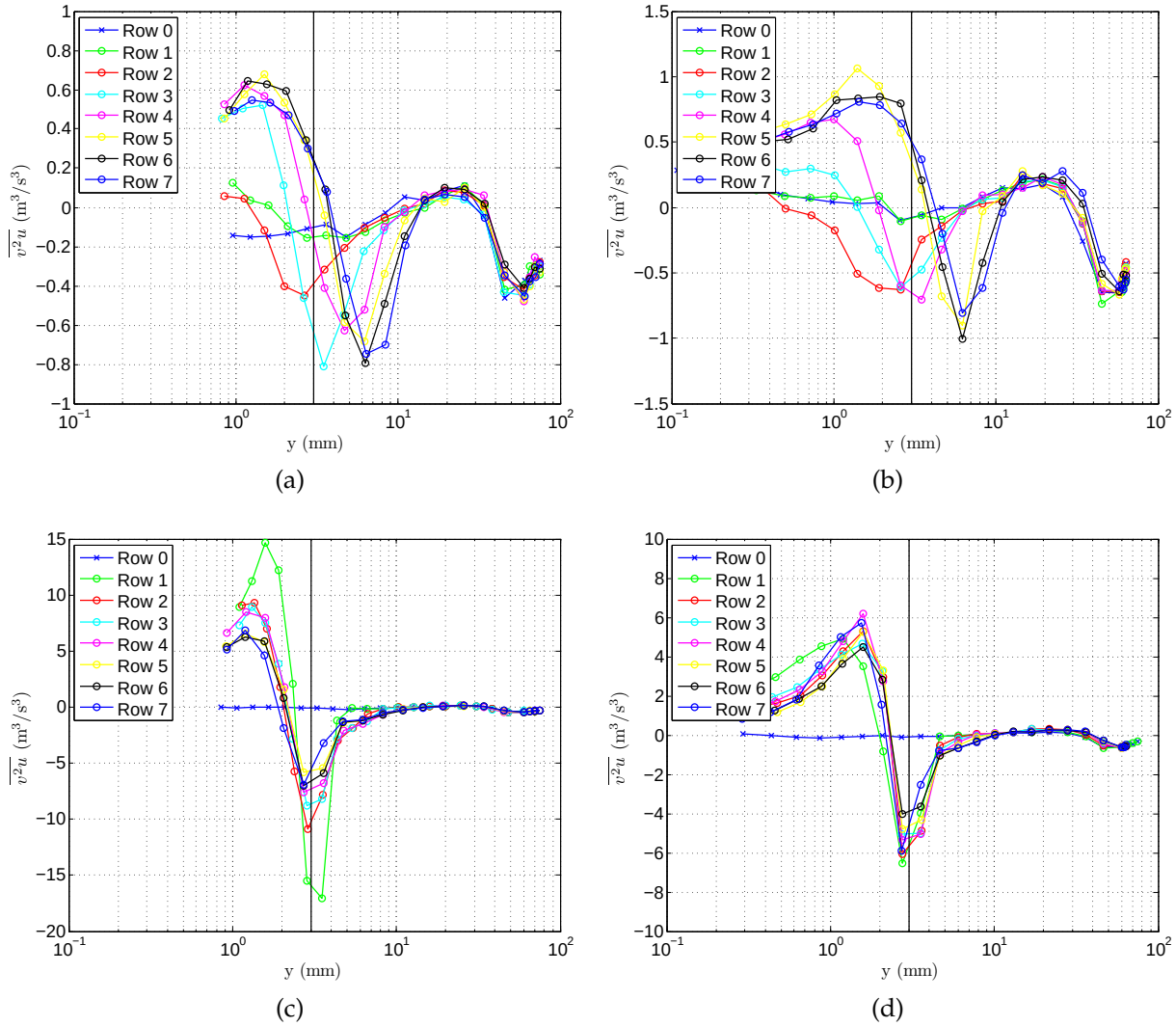

Figure A.4: $\overline{v^2u}$ triple product profiles: (a) between hemispheres; (b) between cubes; (c) behind hemispheres; and, (d) behind cubes

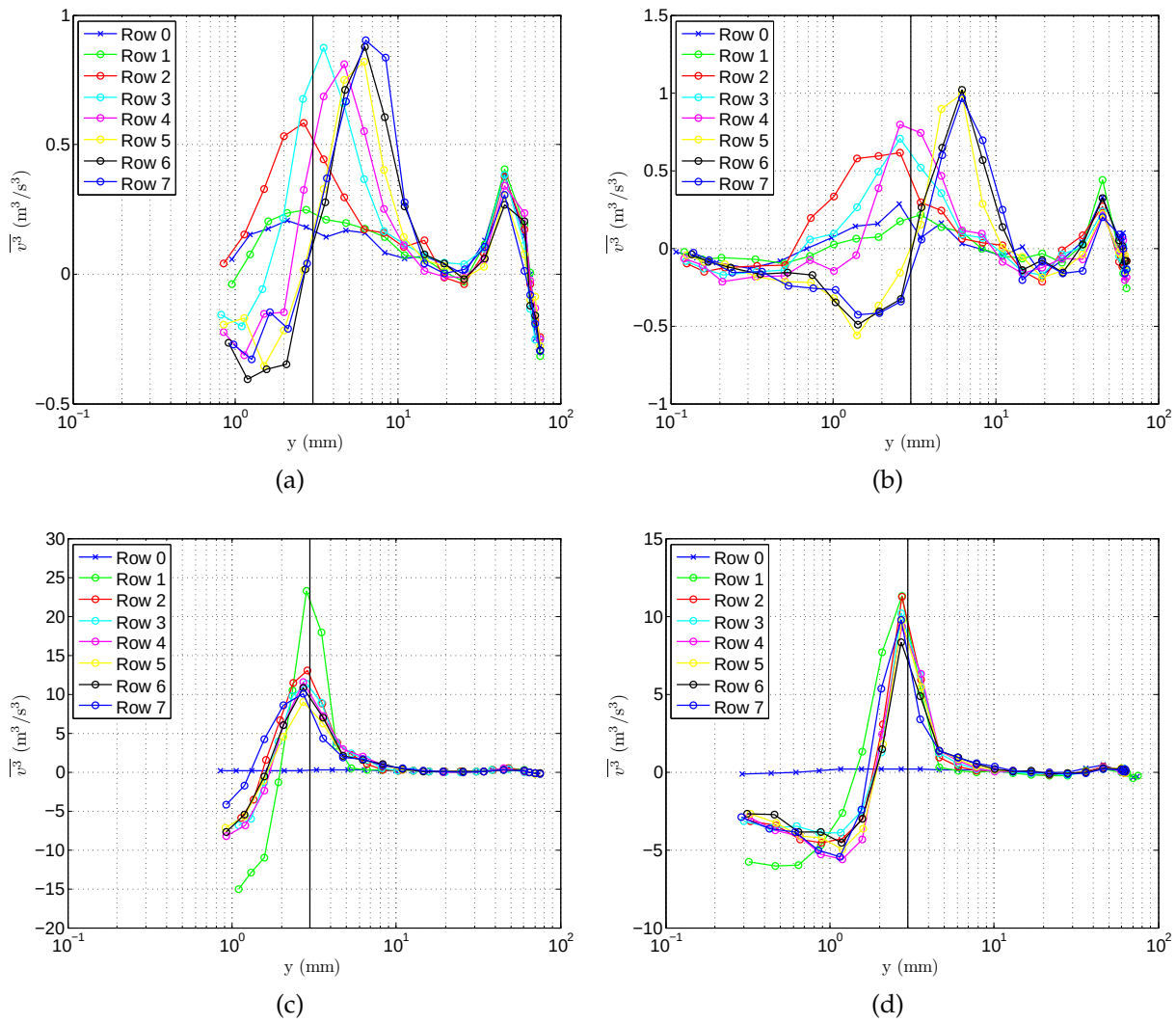

Figure A.5: $\overline{v^3}$ triple product profiles: (a) between hemispheres; (b) between cubes; (c) behind hemispheres; and, (d) behind cubes

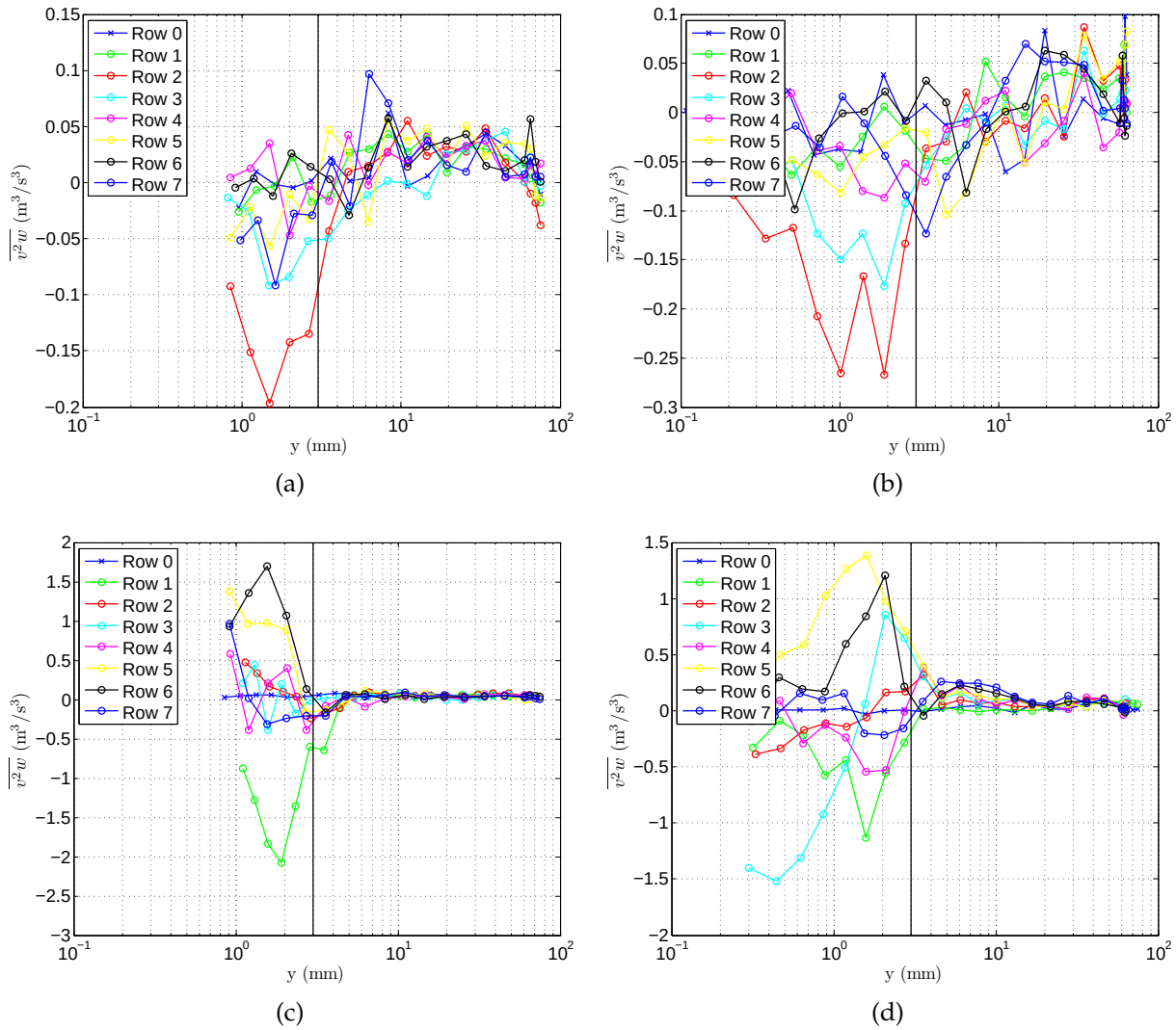

Figure A.6: $\overline{v^2w}$ triple product profiles: (a) between hemispheres; (b) between cubes; (c) behind hemispheres; and, (d) behind cubes

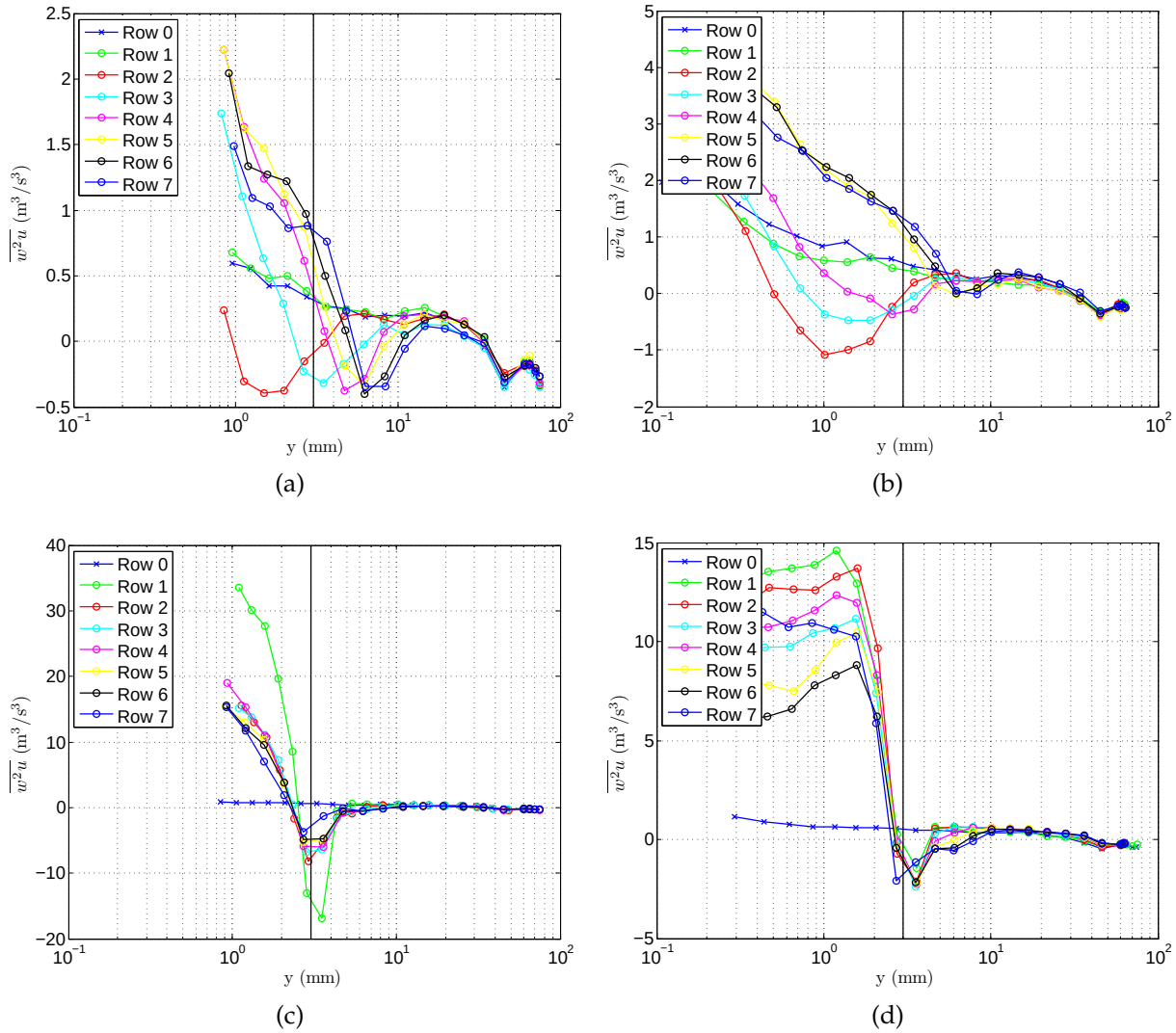

Figure A.7: $\overline{w^2u}$ triple product profiles: (a) between hemispheres; (b) between cubes; (c) behind hemispheres; and, (d) behind cubes

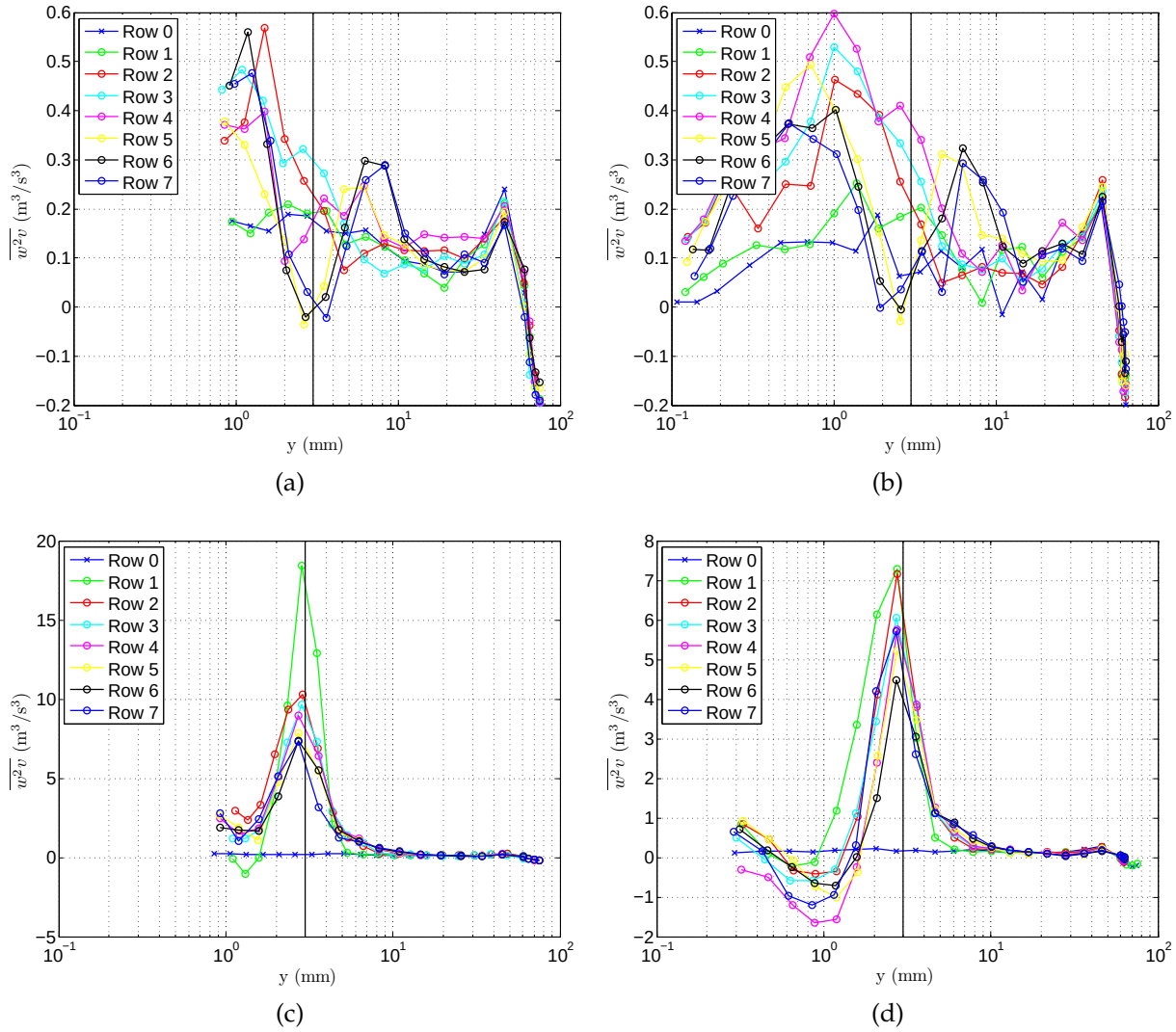

Figure A.8: $\overline{w^2v}$ triple product profiles: (a) between hemispheres; (b) between cubes; (c) behind hemispheres; and, (d) behind cubes

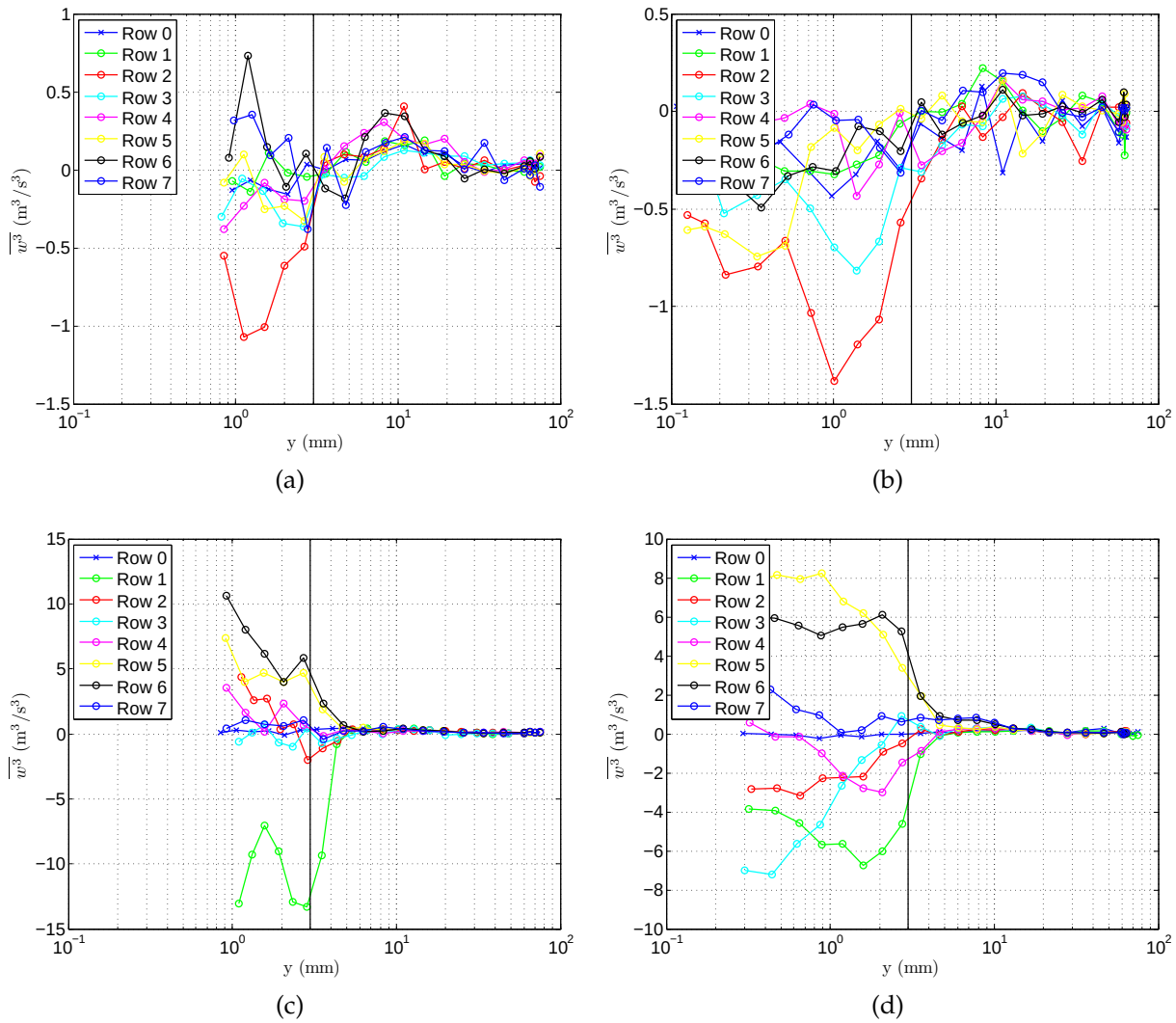

Figure A.9: $\overline{w^3}$ triple product profiles: (a) between hemispheres; (b) between cubes; (c) behind hemispheres; and, (d) behind cubes

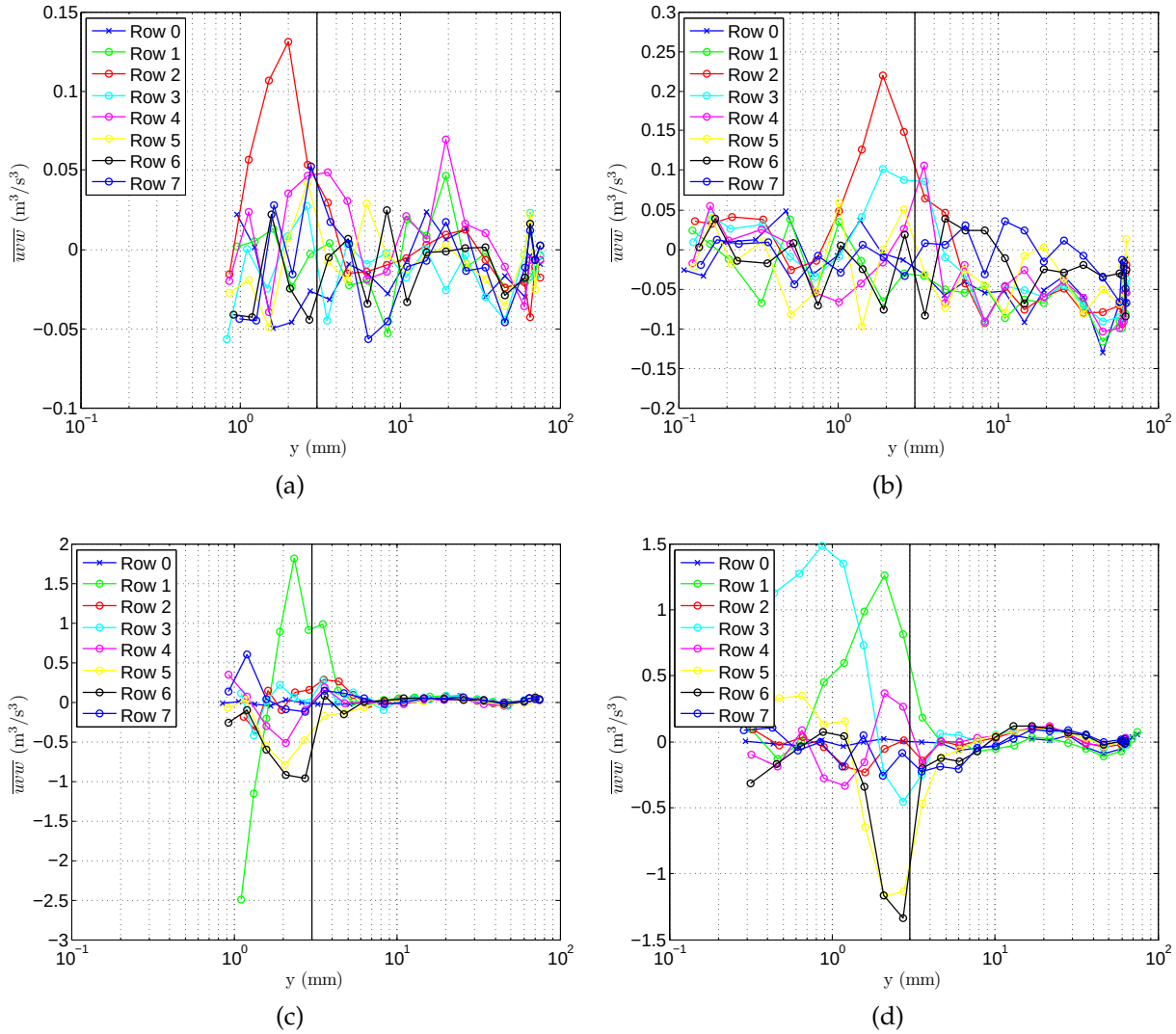

Figure A.10: $\overline{uvw}$ triple product profiles: (a) between hemispheres; (b) between cubes; (c) behind hemispheres; and, (d) behind cubes

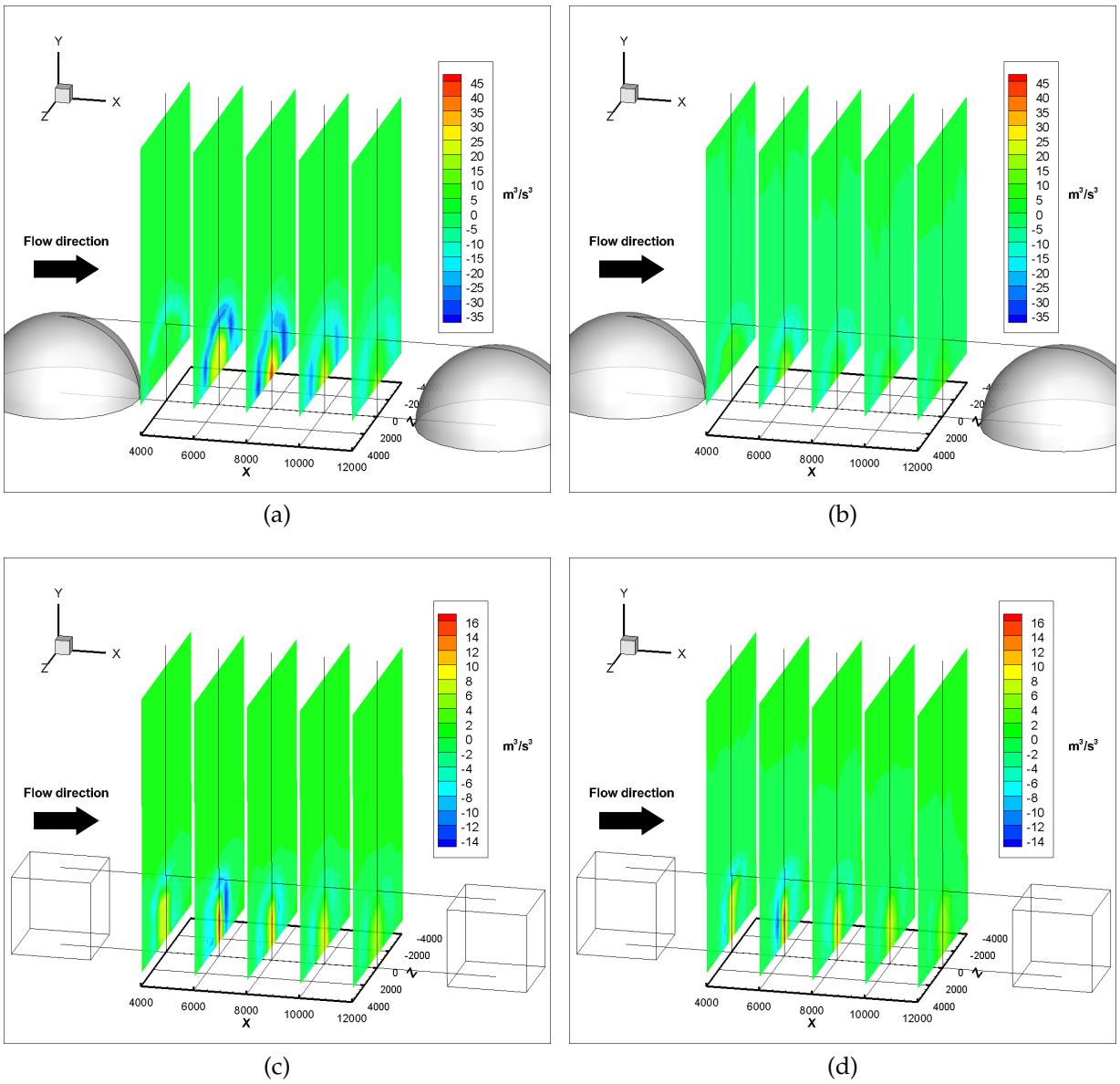

Figure A.11: Contour plots of $\overline{w^2u}$ behind: (a) first row of hemispheres; (b) sixth row of hemispheres; (c) first row of cubes; and, (d) sixth row of cubes

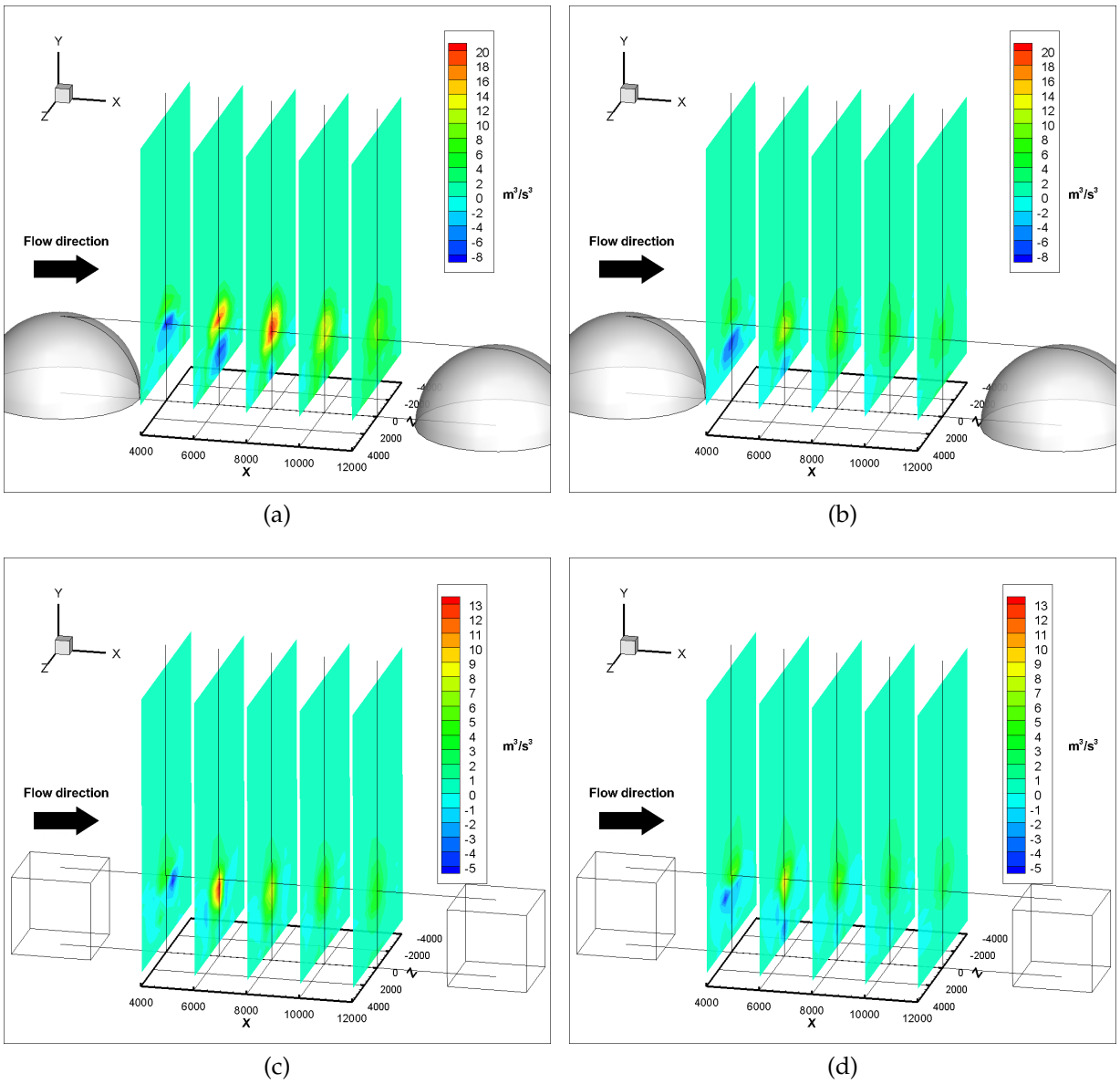

Figure A.12: Contour plots of $\overline{w^2 v}$ behind: (a) first row of hemispheres; (b) sixth row of hemispheres; (c) first row of cubes; and, (d) sixth row of cubes

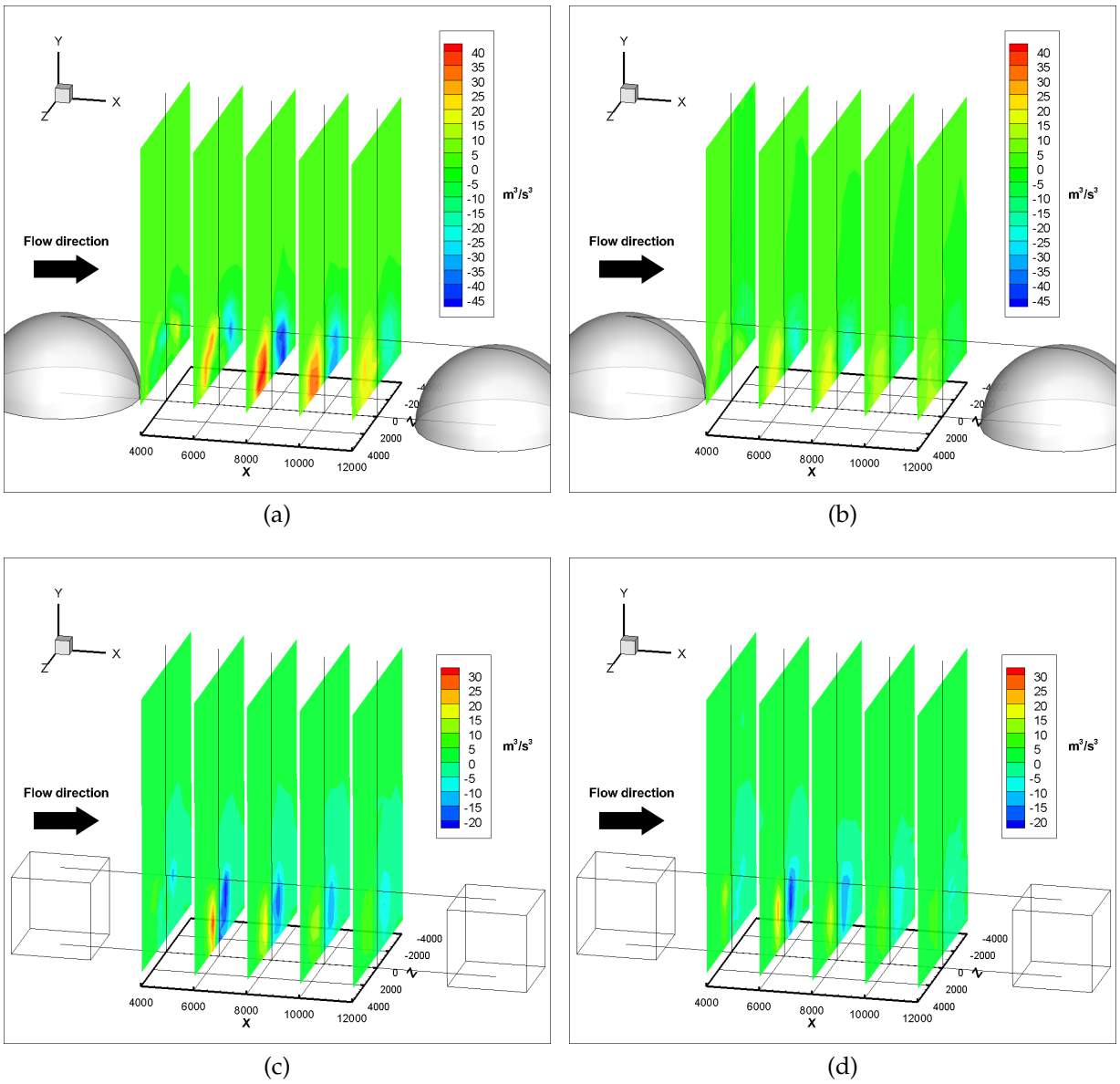

Figure A.13: Contour plots of $\overline{w^3}$ behind: (a) first row of hemispheres; (b) sixth row of hemispheres; (c) first row of cubes; and, (d) sixth row of cubes

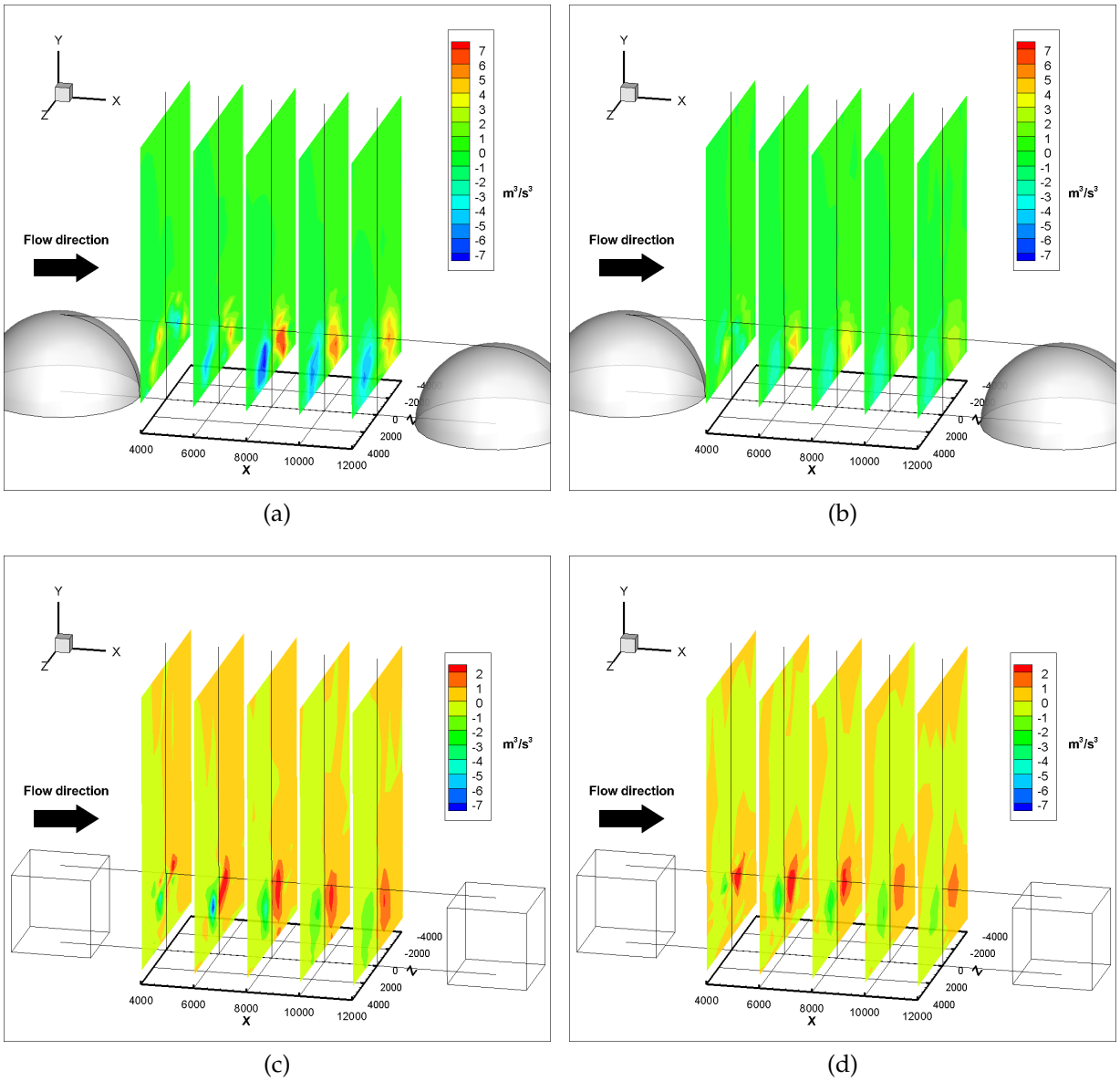

Figure A.14: Contour plots of $\overline{uvw}$ behind: (a) first row of hemispheres; (b) sixth row of hemispheres; (c) first row of cubes; and, (d) sixth row of cubes

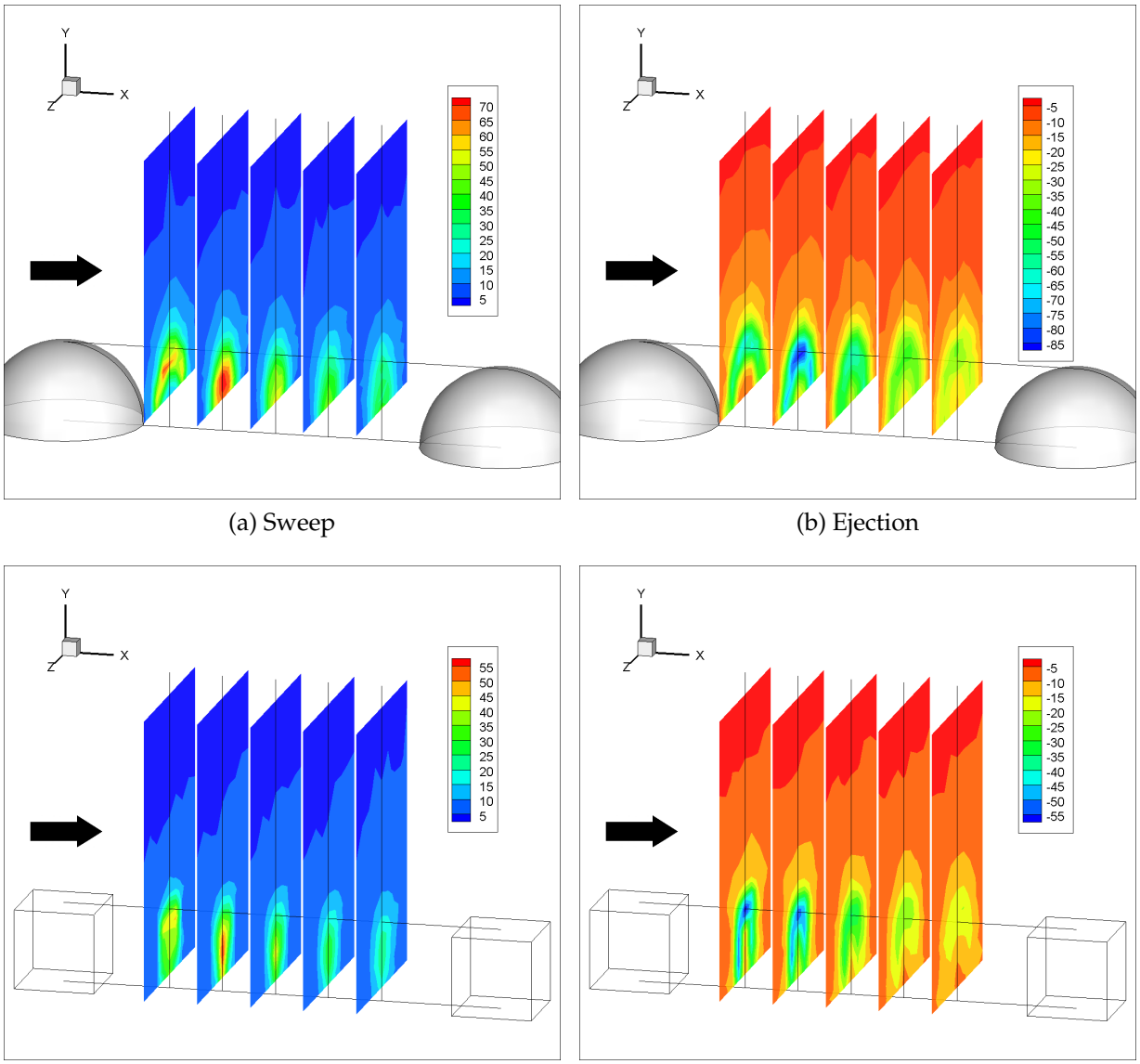

(a) Sweep (b) Ejection

(c) Sweep (d) Ejection

Figure A.15: Contour plots of mean streamwise velocity for data conditionally averaged to show sweep and ejection events

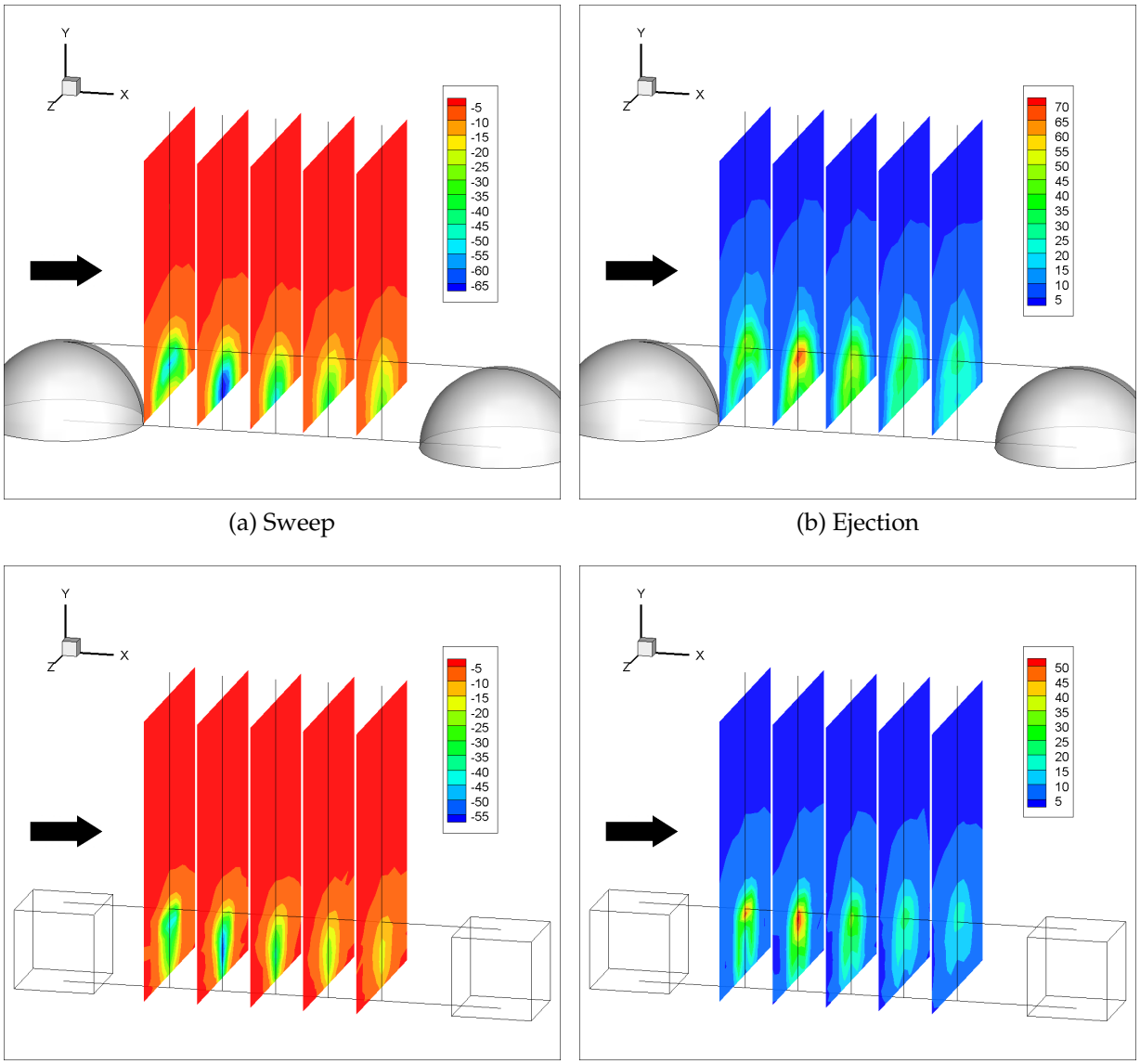

(a) Sweep

(b) Ejection

(c) Sweep

(d) Ejection

Figure A.16: Contour plots of mean streamwise velocity for data conditionally averaged to show sweep and ejection events

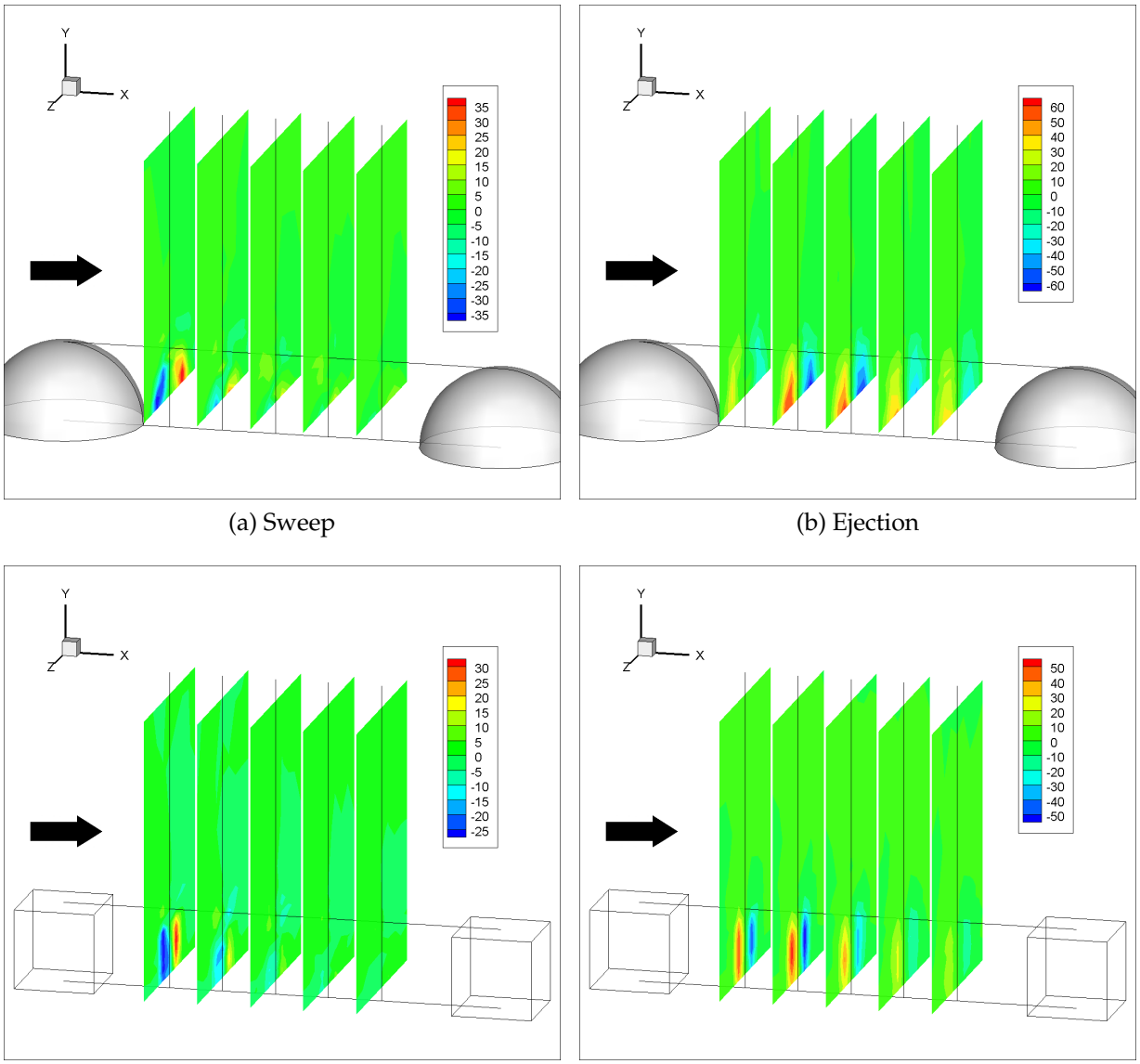

(a) Sweep (b) Ejection

(c) Sweep (d) Ejection

Figure A.17: Contour plots of mean streamwise velocity for data conditionally averaged to show sweep and ejection events

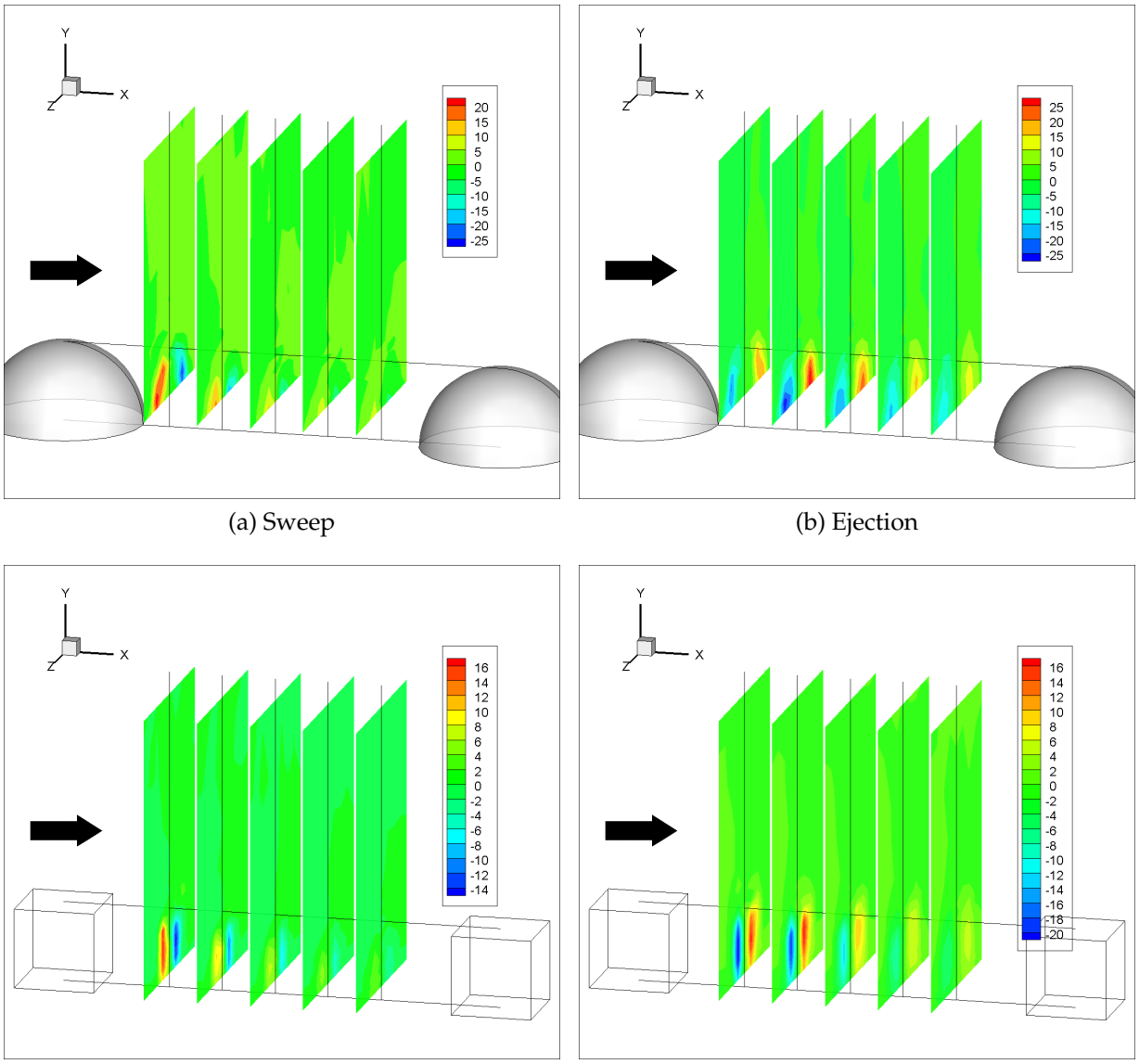

(a) Sweep (b) Ejection

(c) Sweep (d) Ejection

Figure A.18: Contour plots of mean streamwise velocity for data conditionally averaged to show sweep and ejection events

Appendix B

Long System DNS Comparisons

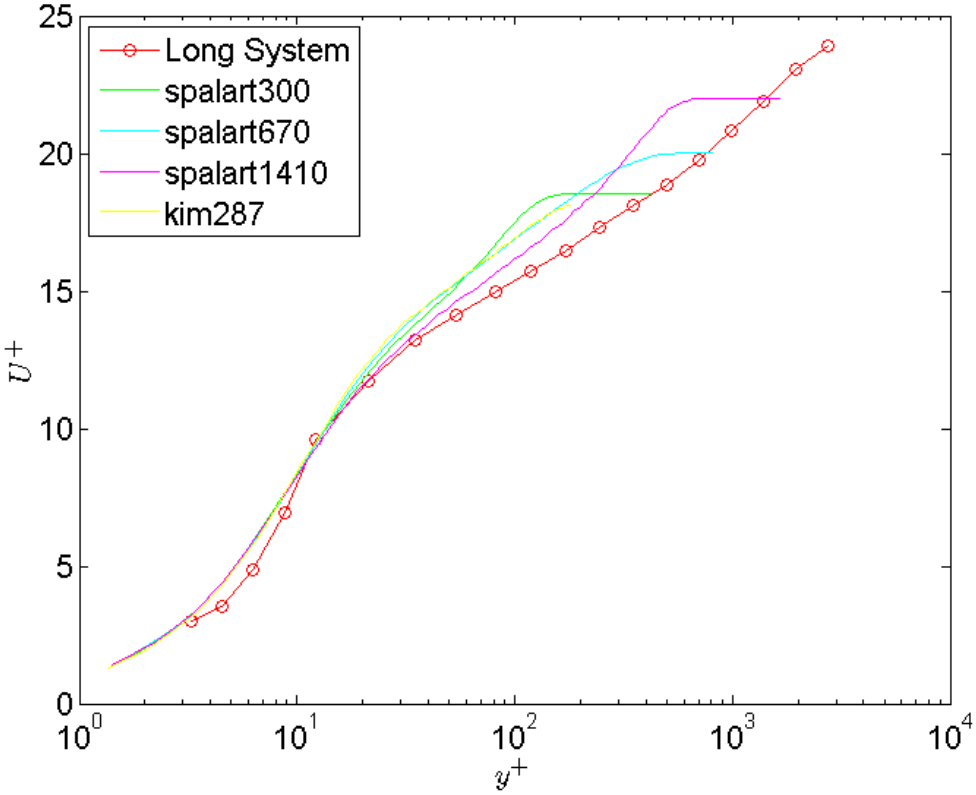

Figure B.1: Non-dimensional mean streamwise velocity comparison between Long System smooth wall data and various DNS results

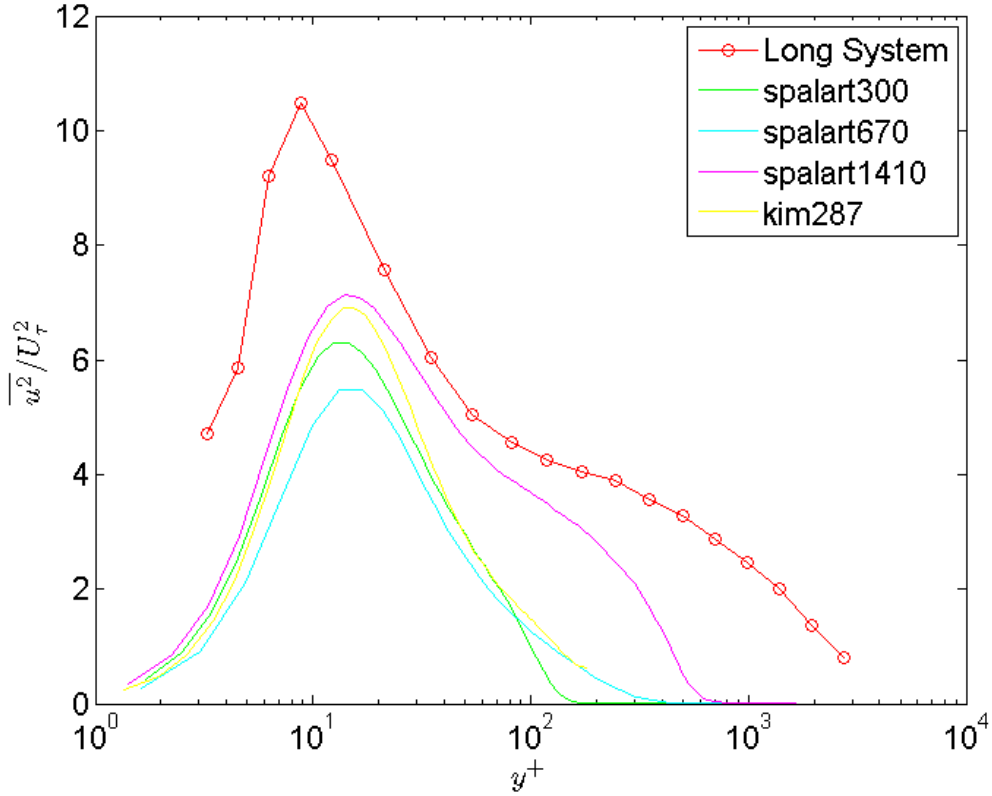

Figure B.2: Non-dimensional mean streamwise normal stress comparison between Long System smooth wall data and various DNS results

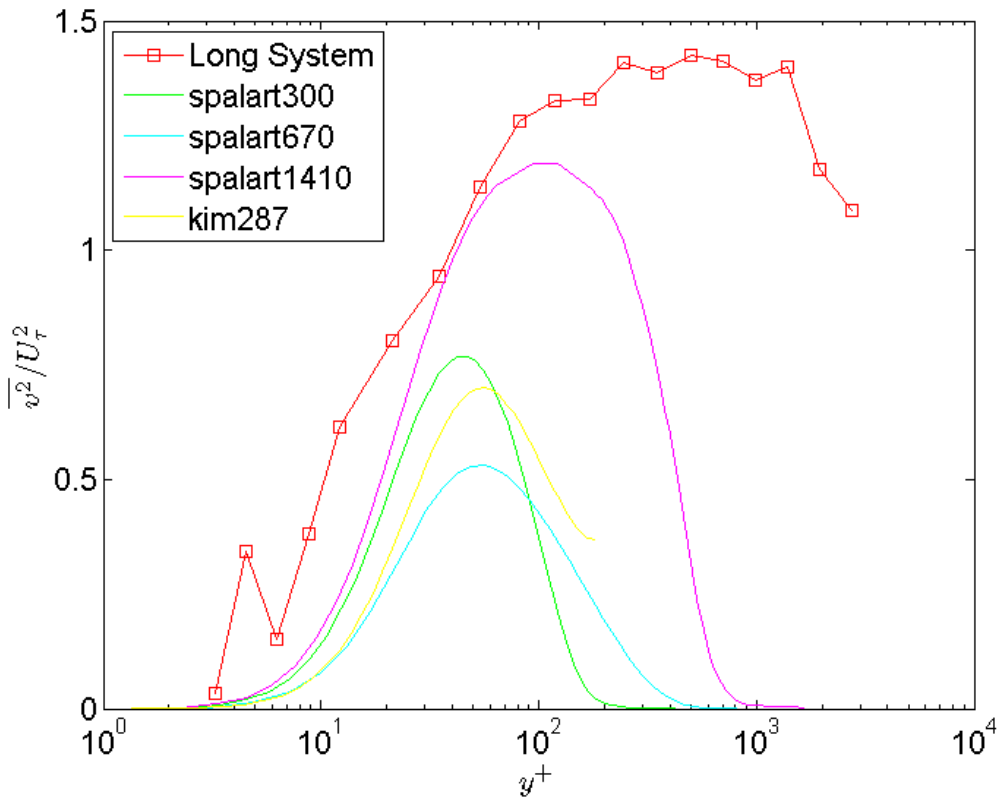

Figure B.3: Non-dimensional mean wall-normal normal stress comparison between Long System smooth wall data and various DNS results

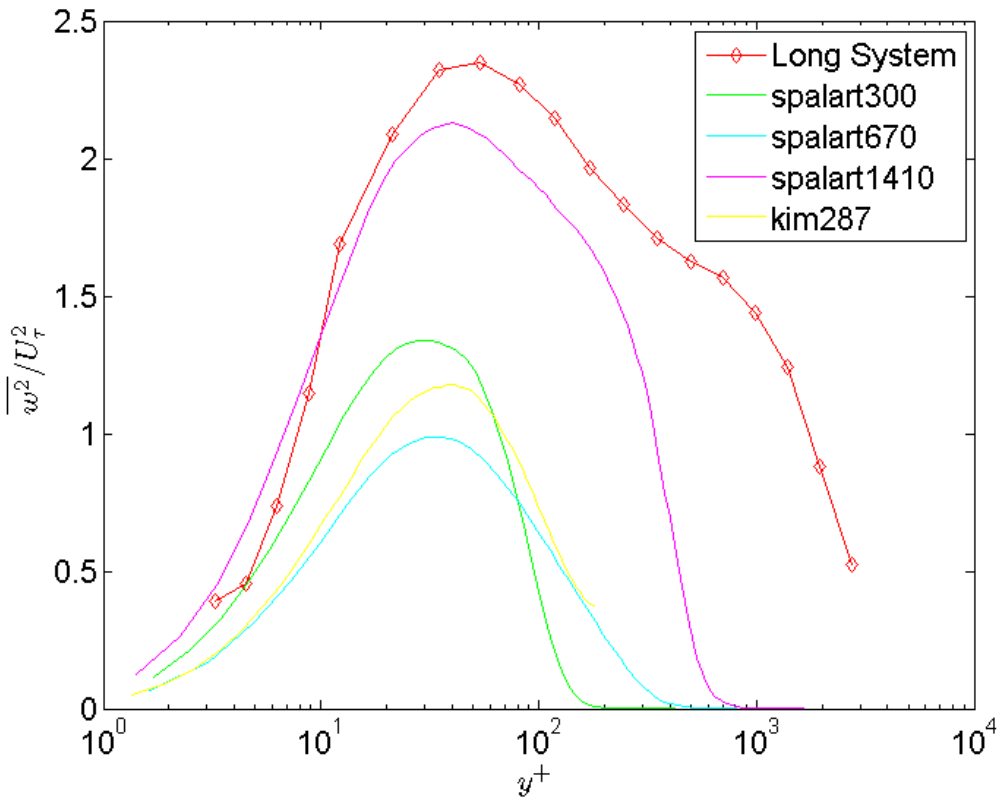

Figure B.4: Non-dimensional mean spanwise normal stress comparison between Long System smooth wall data and various DNS results

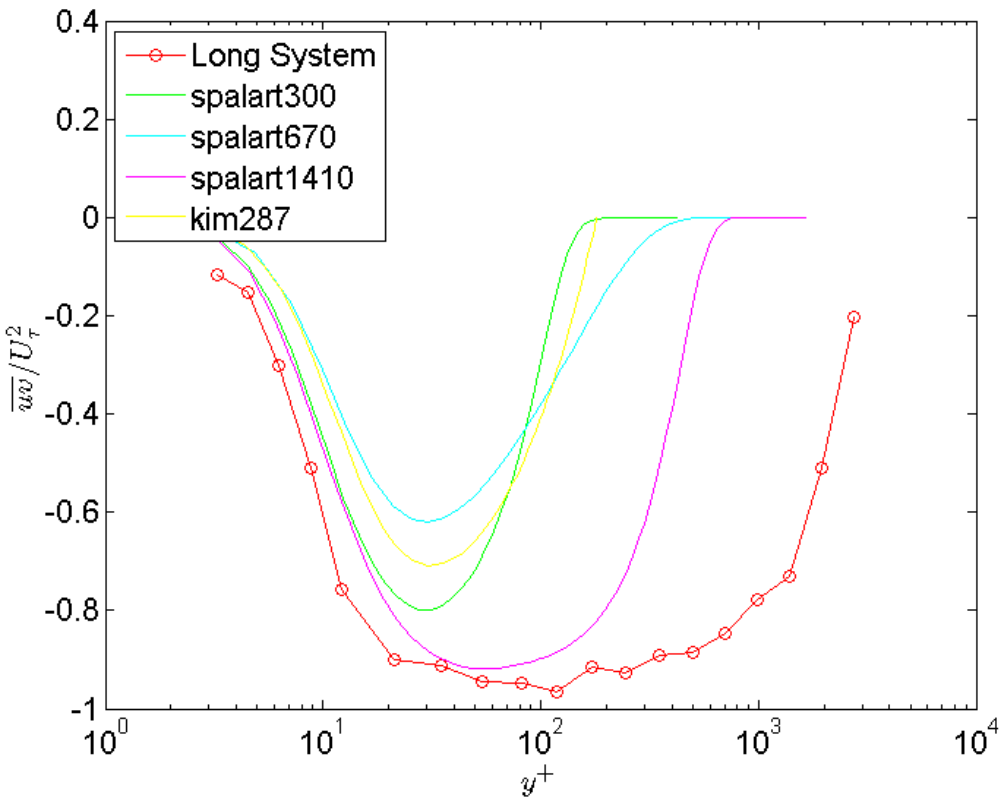

Figure B.5: Non-dimensional mean Reynolds shear stress comparison between Long System smooth wall data and various DNS results